# The Calibration of the Super-Kamiokande Outer-Detector and Particle Kinematics Reconstruction in Hyper-Kamiokande

Gao, Joanna

*Awarding institution:*
King's College London

King's College London

Department of Physics

# The Calibration of the Super-Kamiokande Outer-Detector and Particle Kinematics Reconstruction in Hyper-Kamiokande

Jingyuan Gao

A thesis submitted for the degree of

***Doctor of Philosophy***

August 2024

# Acknowledgement

Since embarking on this endeavour four years ago, I have encountered many generous individuals who have lent their support during my journey, for which I am profoundly thankful. It may not be possible to name everyone, but I would like to first extend my deepest gratitude to my supervisor, Dr Teppei Katori, for his constant encouragement, insightful comments, and invaluable advice throughout my time at KCL. His expertise and mentorship have been instrumental in shaping the content of this thesis. Equally memorable are the tales and lessons learned from our many gatherings at the pub.

I owe a debt of gratitude to the entire WatChMaL group, especially Dr Nicholas Prouse and Professor Patrick de Perio, for they have provided me with the tools I needed for the machine-learning analysis and given me patient guidance, insightful feedback and constructive critiques, which have been pivotal to the development of my thesis.

The Super-Kamiokande calibration group's endless support made my work on the outer detector (OD) calibration feasible. Special thanks to Dr Shunichi Mine, Dr Hidekazu Tanaka and Dr Byeongsu Yang for their profound knowledge of the detector, which granted me insight into its complex functions. Gratitude is also due to Dr Baran Bodur from Duke University, who dedicatedly engaged with me online each week for half a year to get me started on the OD calibration activities. In addition, I would like to thank Dr Shige Matsuno from Hawaii University, Professor Neil McCauley and Balint Bodgan from Liverpool University, Dr Amelle Zair from KCL and Dr Benjamin Richards from Warwick University for their generous help along my quest to find a replacement laser for the OD; without their extensive knowledge on the topic I would have been on a detoured to no end.

Life at KCL would have felt incredibly solitary without the Experimental Parti-

cle and Astro-particle Group. Thanks to Zhenxiong Xie, my gym companion, coffee enthusiast peer and conversation buddy, for my increasingly healthy body, more sophisticated taste and stronger mind; and to Rogan Clark, Ewan Miller, Nahid Bhuiyan, Rory Ramsden, Sania Lewis and others for the camaraderie and laughter in the office, at conferences or somewhere in Japan. Additionally, I offer a heartfelt acknowledgement to Dr Alexander Goldsack, whose unwavering encouragement and mentorship have helped me immensely along this journey.

Though my time at Kamioka, Japan, was short, I have had some of the best times in my life. Words cannot express how much I enjoyed Hiroki Kouchi-kun and Yoshino Kaminaga-san's companionship, which was like a ray of sunshine enveloping my star-dimmed, moonless nights. I will forever cherish the memories of the 3 am Kajikara sessions, the heavenly feeling of standing in the cold, swift-flowing stream on a hot summer afternoon, the sparkles of Hanabi into the darkening evening, and that perfectly sunny afternoon at the Amaharashi-kaigan. These memories will ground me for the years to come.

I must also extend my thanks to my dear friends beyond the confines of KCL. Thanks to Dr Jonathan Nelsson-Hallén and Kenza Tazi, my pillars of emotional support and academic inspiration, for their attentive ears and for refining all my academic writings (including this one); without whom my English writings would not be close to as good. I am equally thankful to William Richards, Trenton Delahaye, Bernadette Fernandes, Abby Wong and Lauran Chan for occasionally drawing me out of the realm of physics.

On a personal note, I wish to express my deepest appreciation to my parents and family, who have supported my independent journey since the age of 16. My adventures through life so far would not have been possible otherwise. Last but not least, a huge thank you to my partner and confidant, Thomas Zhu, who patiently accompanied me through the thick and thin since the start of COVID in 2020, and continuously inspiring me with his vast amount of knowledge.

# Declaration

The work presented in this thesis is the work of the author, except as noted here or where other work has been cited.

In Chapter 3, the foundational OD PMT gain and timing calibration methods were introduced by members of the Super-K calibration group. The author refined these methods, established a daily monitoring system, and created a dedicated webpage. The plots in this thesis use existing code for visualisation, but the data and analysis — including the study on geomagnetic coil failure effects on OD PMTs — are the author's contributions.

Chapter 4 explores the Super-K OD laser data, a joint effort with the Super-K calibration group. The author modified a legacy Fortran script for data extraction, developed new data-reduction cuts, and performed all subsequent analyses, including power measurements. Laser wavelength measurements were conducted by group members, but photon loss calculations and simulations were primarily the author's work, with some input from the supervisor.

In Chapters 5 and 6, the author adapted the machine learning framework from the WatChMaL collaboration to suit the HybridHK geometry, generated the dataset, and independently analyzed the results, showcasing a blend of collaboration and individual innovation.

***Jingyuan Gao***

**Abstract**

Super-Kamiokande (Super-K) is a water Cherenkov detector nestled in the mountains of Gifu Prefecture in Japan. With over 27 years of history, it has studied neutrinos from diverse origins. Building on its legacy, the construction of Hyper-Kamiokande (Hyper-K) commenced in 2020. A significantly larger detector, Hyper-K aims to improve upon the Super-K results.

This thesis is divided into two sections. The first focuses on the calibration of the Super-K Outer Detector (OD) Photomultiplier Tubes (PMTs). It reports the OD PMT constants calculation techniques, results, and the impact of geomagnetic compensation coil failures in 2023 on those constants. Furthermore, it provides a detailed account of the current OD laser light injection system. The analysis of SK-VII laser data highlights a significant drop in laser light intensity, emphasising the need for an immediate laser replacement. It concludes with an evaluation of alternative light sources and the photon output required for an effective replacement.

The second section explores particle classification (distinguishing between $e^-$ and $\mu^-/\pi^0/\gamma$) and kinematics reconstruction (momentum and vertex positions for $e^-$ and $\mu^-$) within Hyper-K, utilising PointNet, a machine learning model. The study analyses data of 3 million events per particle type, simulated with Hyper-K's event simulation software, WCSim, which uses a tank geometry that consists of both 20-inch diameter PMTs and multi-PMT (mPMT) modules.

In comparison with FiTQun, a statistical reconstruction tool adapted from Super-K, PointNet demonstrates comparable efficacy in particle classification. Specifically, PointNet and FiTQun achieve similar performance in $e^-/\mu^-$ (99.7% and 99.8%) and $e^-/\pi^0$ (94.4% and 92.5%) discriminations, though both struggle to differentiate $e^-$ from $\gamma$. However, PointNet significantly outpaces FiTQun, being at least seven orders of magnitude faster in processing time. While PointNet surpasses FiTQun in momentum reconstruction for energies above 100 MeV, it falls short in accurately reconstructing vertex positions. Notably, the simulation geometry led to an overly optimistic position resolution with FiTQun, highlighting an area for future research improvement.

# Contents

# List of Figures

# List of Tables

# List of Acronyms and Abbreviations

| | |
|---|---|
| **ADC** | Analogue-to-Digital Converter |
| **AI** | Artificial Intelligence |
| **ANN** | Artificial Neural Network |
| **BBN** | Big Bang Nucleosynthesis |
| **CC** | Charge Current |
| **CNB** | Cosmic Neutrino Background |
| **CNN** | Convolutional Neural Network |
| **CNO** | carbon-nitrogen-oxygen |
| **CR** | Cosmic Ray |
| **CW** | continuous wave |
| **DONUT** | Direct Observation of the Nu Tau |
| **DSNB** | Diffuse Supernova Neutrino Background |
| **FC** | Fibre Connector |
| **FWHM** | Full Width at Half Maximum |
| **Gd** | Gadolinium |
| **Hyper-K** | Hyper-Kamiokande |
| **IBD** | inverse beta decay |
| **ID** | Inner Detector |
| **IMB** | Irvine-Michigan-Brookhaven |
| **IWCD** | Intermediate Water Cherenkov Detector |
| **Kamiokande** | Kamioka Nucleon Decay Experiment |

| | |
|---|---|
| **KamLand** | Kamioka Liquid-scintillator Anti-Neutrino Detector |
| **LArTPC** | Liquid Argon Time Projection Chamber |
| **LBL** | long-baseline |
| **LSI** | Laser Science, Inc. |
| **LTB** | LaserTechnik Berlin |
| **MC** | Monte Carlo |
| **ML** | Machine Learning |
| **MLP** | Multi-layer perceptron |
| **MSW** | Mikheyev-Smirnov-Wolfenstein |
| **mPMT** | multi-PMT |
| **NC** | Neutral Current |
| **NLL** | Negative Log-Likelihood |
| **OD** | Outer Detector |
| **p.e.** | photoelectron |
| **PID** | particle identification |
| **PMNS** | Pontecorvo-Maki-Nakagawa-Sakata |
| **PMT** | Photomultiplier Tube |
| **pp** | proton-proton |
| **QE** | quantum efficiency |
| **ROC** | Receiver Operating Characteristic |
| **SAGE** | Soviet–American Gallium Experiment |
| **SLAC** | Stanford Linear Accelerator Centre |
| **SM** | Standard Model |
| **SMA** | SubMiniature version A |
| **SN** | Supernova |
| **SNO** | Sudbury Neutrino Observatory |
| **s.p.e.** | single-photoelectron |
| **ST** | Straight Tip |

| | |
|---|---|
| **Super-K** | Super-Kamiokande |
| **T2K** | Tokai to Kamioka |
| **TEA** | Transversely Excited at Atmospheric pressure |
| **ToF** | time of flight |
| **TTL** | Transistor-Transistor Logic |
| **TVT** | Training, Validating, and Testing |
| **UV** | ultraviolet |
| **WCSim** | Water Cherenkov Simulator |

# Chapter 1

# Introduction

## 1.1 The Birth of Neutrinos

In 1911, Lise Meitner, a pioneer in the study of beta decay, conducted an experiment on observing the decay product of a radioactive source that emitted beta particles. Using a magnetic spectrometer, she provided the first evidence of neutrinos [1]. Her groundbreaking discovery revealed that the energy spectrum of the emitted electrons was continuous, which was against the common belief at the time that when a neutron decayed at rest, it would result in only an electron and a proton, and the energy spectrum of those electrons should be a discrete one according to the conservation of energy. This seemingly blatant violation of the established energy conservation law puzzled physicists of that generation, including Wolfgang Pauli [2].

At last, Pauli proposed a new particle to the 'Radioactive Ladies and Gentlemen' attending the Gauverein meeting in December 1930 as a 'desperate remedy' for saving the law of conservation of energy [3]. Initially termed a 'neutron', this theoretical particle was described as electrically neutral with a half-integer spin, adhering to Pauli's exclusion principle, moving just slower than light, with a mass akin to an electron, purportedly emitted alongside electrons in beta decay to conserve total energy. However, its name was soon replaced when James Chadwick discovered a significantly heavier particle and named it the neutron [4]. Subsequently, in 1931, Enrico Fermi rechristened Pauli's particle as 'neutrino', meaning 'little neutral one' in Italian, a name more fitting

for its characteristics. The beta decay can now be expressed as

$$n \rightarrow p + e^{-} + \bar{\nu}_e, \tag{1.1}$$

where $\nu$ is a neutrino. Conversely, a neutrino can also be detected through the inverse beta decay (IBD)

$$\bar{\nu}_e + p \rightarrow e^{+} + n. \tag{1.2}$$

Detecting a neutral, and possibly massless, particle was no easy task. According to Hans Bethe and Rudolf Peierls' calculation in 1934, the interaction cross-section of a beta-decay-produced neutrino is less than $10^{-44}$ cm$^2$ [5]. Hence, for the successful detection of these fission-emitted neutrinos, a large number of interaction targets, as well as a vast amount of produced neutrinos, are essential.

Then, in 1956, Clyde L. Cowan and Frederick Reines made the first observation of electron anti-neutrinos using coincident signals, one from the annihilation of IBD positrons and atomic electrons and the other from the additional energy release from IBD neutrons captured on cadmium molecules [6]. The experiment reported increased coincidences correlating with the nuclear reactor's operational periods, signifying the detection of neutrinos. This observation also verified the neutrino cross-section prediction made by Bethe and Peierls.

In 1962, Leon Lederman, Melvin Schwartz and Jack Steinberger made their discovery of the next generation of the lepton family at the Brookhaven Alternating Gradient Synchrotron [7]. They bombarded beryllium targets with protons producing charged pions, which subsequently decayed into muons, $\mu$, and muon neutrinos, $\nu_\mu$.

The tau-neutrino concept emerged following the tau lepton's discovery at the Stanford Linear Accelerator Centre (SLAC) in 1978 [8]. Initial indications of this third neutrino type were deduced from observations of momentum and energy discrepancies in tau lepton decays, akin to the methods employed in detecting electron neutrinos. Subsequently, in 1991, experiments at the Large Electron-Positron Collider (LEP) established the existence of only three particle families by studying the decay width of the $Z$ boson. Finally, the Direct Observation of the Nu Tau (DONUT) experiment observed the tau neutrino in 2000 by observing its decay product tau using a high-

resolution emulsion detector [9]. Thus, the final piece of the lepton puzzle had been found.

## 1.2 Neutrinos in the Standard Model

The Standard Model (SM) stands as a remarkably successful framework within particle physics, effectively interpreting a wide array of experimental outcomes from both accelerator-based and non-accelerator sources. This comprehensive theory delineates the interactions between matter's fundamental constituents — fermions, which are spin-1/2 particles - and the carriers of fundamental forces, bosons, which have a spin of 1. In addition, it also contains the Higgs boson, a spin-0 particle that grants mass to the weak force bosons through spontaneous symmetry breaking in the electroweak theory, and gives rise to the masses of charged fermions through Yukawa coupling. Figure 1.1 displays every particle described by the Standard Model, its electric charge, mass and the force it interacts with.

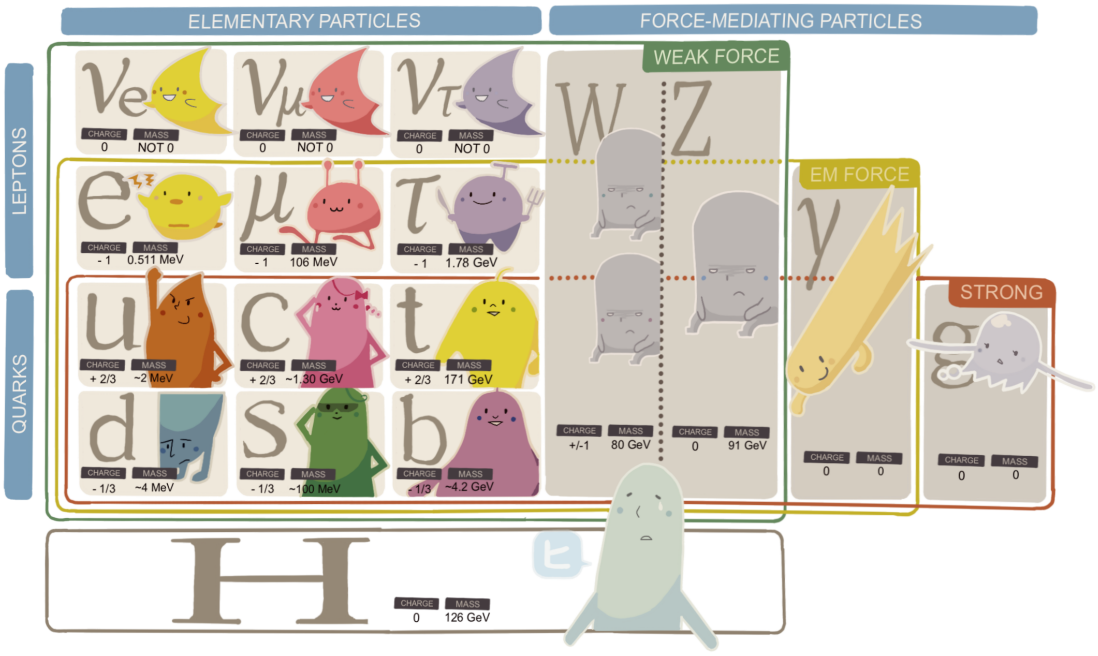


**Figure 1.1:** Particles in the Standard Model, their charges, masses and the forces they experience. The figure is traced from a folder sold in the KEK International Linear Collider shop [10].

As shown in the figure, fermions are categorised into quarks and leptons. Each of these groups is further structured into three flavours. On the other hand, bosons come in four types: photons, which mediate electromagnetic interactions; gluons, which are responsible for strong interactions; and the $W$ and $Z$ bosons, which govern weak interactions. Quarks, which have types up, down, charm, strange, top and bottom, are able to engage in all three types of interactions and naturally exist in the forms of composite particles known as baryons and mesons. Baryons consist of three quarks, while mesons are made up of a quark and an antiquark pair. An example of a meson is the neutral pion, $\pi^0$, a particle discussed in the results section of this thesis. The $\pi^0$ meson consists of two quark-antiquark pairs in superposition, expressed as $\pi^0 = (u\bar{u} - d\bar{d})/2$. It has a mass of $134.9770 \pm 0.0005$ MeV$/c^2$ and an average lifespan of $8.52 \pm 0.18 \times 10^{-17}$ s [11].

On the other hand, the charged leptons — electrons, muons, and tauons — interact through both electromagnetic and weak forces. Neutrinos, which are their neutral counterparts, interact exclusively via the weak force. Within this force, the interactions are mediated by $W^{\pm}$ and $Z^0$ bosons, corresponding to charged current (CC) and neutral current (NC) interactions, respectively. Figure 1.2 are example Feynman diagrams of CC and NC interactions. These diagrams depict neutrinos of any flavour interacting with quarks within the nuclei of the target materials. During a CC interaction, the exchanging of a $W$ boson results in a change in flavour. This transformation can occur from a neutrino to its respective charged lepton or from an up quark with a $+2/3$ charge to a down quark carrying a $-1/3$ charge. For a neutrino to engage in CC interactions, it must possess sufficient energy to create its corresponding charged lepton. Conversely, in an NC interaction where a $Z$ boson is exchanged, there is no alteration in the flavour of the participating particles.

In the SM, neutrinos were originally theorised as massless particles. This prediction stems from the concept of chirality and helicity. Chirality, or helicity (handedness) in the massless particle regime, refers to the symmetry (or lack thereof) of a particle's spin and its momentum. A particle is said to be right-handed if its spin and momentum are aligned in the same direction and vice versa. In the realm of the SM, only the left-handed particles and right-handed anti-particles can have weak force interactions.

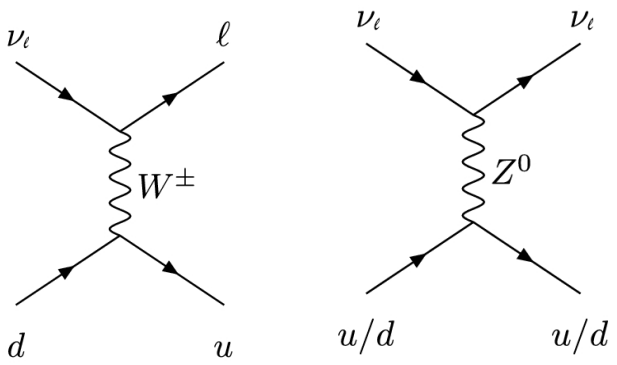


**(a)** **(b)**

**Figure 1.2:** Example Feynman diagrams of neutrino (a) CC Quasi-Elastic and (b) NC interactions [12]. The initial-state particles are on the left and the final-state particles are on the right in both diagrams. In (a), a neutrino exchanges a $W$ boson with a quark from a nucleus and turns into its corresponding charged lepton, while the quark changes type. In (b), a neutrino scatters with a quark through the exchange of a $Z^0$ boson, with the final state particles remaining the same.

Thus, the neutrinos are exclusively left-handed, and the antineutrinos are strictly right-handed.

Every SM particle interacts with the Higgs bosons to gain mass, and the more interactions there are, the heavier the particle [13]. According to Quantum Field Theory and Lorentz invariance, the helicity of a particle would inverse every time it collides with the Higgs boson. If neutrinos were massive, the SM would require them to interact with the Higgs, inevitably inversing their helicity, creating right-handed neutrinos and left-handed antineutrinos, which is forbidden. Consequently, the existence of neutrino mass is evidence for beyond the Standard Model physics.

## 1.3 Neutrino Mass and Oscillations

Although neutrino detection capabilities were improving throughout the middle to late 20th century, new problems arose. In the 1960s, the Homestake experiment was the first to observe solar neutrinos, and it reported a strange deficit in the observed electron neutrino number compared to expectation [14]. Moreover, in the 1980s, similar deficits were detected in the muon neutrinos of atmospheric sources [15]. Proposed explanations for the observed anomalies included neutrino decay and miscalculations of

expected rates, but it was the findings from Super-Kamiokande (Super-K) [16] and the Sudbury Neutrino Observatory (SNO) [17] that ultimately affirmed neutrino oscillation as the definitive answer. Super-K observed a deficit of atmospheric muon neutrinos arriving from below the detector, a phenomenon not seen in muon neutrinos from above or in electron neutrinos from all directions [15]. Similarly, SNO reported a deficit in solar neutrinos, which will be discussed further in the next section.

Importantly, the oscillation property of neutrinos requires their mass to be non-zero, which is shown in the following derivations.

In 1957, Bruno Pontecorvo was the first to propose the idea of neutrino oscillations [18]. It was later refined into a mathematical formulation by Ziro Maki, Masami Nakagawa and Shoichi Sakata in 1962 [19]. It was proposed that the three flavour eigenstates of neutrinos, $|\nu_\alpha\rangle = (|\nu_e\rangle, |\nu_\mu\rangle, |\nu_\tau\rangle)$, has to be expressed in terms of the mass eigenstates $|\nu_i\rangle = (|\nu_1\rangle, |\nu_2\rangle, |\nu_3\rangle)$ when propagating through space and time since only the mass eigenstates are eigenstates of the Hamiltonian. The relationship can be written as

$$|\nu_\alpha\rangle = \sum_{i=1}^{3} U_{\alpha i} |\nu_i\rangle \tag{1.3}$$

where $U_{\alpha i}$ is an element in the Pontecorvo-Maki-Nakagawa-Sakata (PMNS) matrix, $\boldsymbol{U}$. Under the assumption that neutrinos and antineutrinos are distinct particles, and by imposing the condition that the matrix is unitary, $\boldsymbol{U}$ can be expressed as the product of three rotational matrices. Each of these matrices facilitates the mixing of two out of the three mass states and can be measured using neutrinos from different sources as indicated below:

$$\begin{aligned}\boldsymbol{U} &= \begin{pmatrix} U_{e1} & U_{e2} & U_{e3} \\ U_{\mu 1} & U_{\mu 2} & U_{\mu 3} \\ U_{\tau 1} & U_{\tau 2} & U_{\tau 3} \end{pmatrix} \\ &= \underbrace{\begin{pmatrix} 1 & 0 & 0 \\ 0 & \cos\theta_{23} & \sin\theta_{23} \\ 0 & -\sin\theta_{23} & \cos\theta_{23} \end{pmatrix}}_{\text{Atmospheric}} \underbrace{\begin{pmatrix} \cos\theta_{13} & 0 & \sin\theta_{13}\exp(-i\delta_{\text{CP}}) \\ 0 & 1 & 0 \\ -\sin\theta_{13}\exp(i\delta_{\text{CP}}) & 0 & \cos\theta_{13} \end{pmatrix}}_{\text{Nuclear Reactors}} \underbrace{\begin{pmatrix} \cos\theta_{12} & \sin\theta_{12} & 0 \\ -\sin\theta_{12} & \cos\theta_{12} & 0 \\ 0 & 0 & 1 \end{pmatrix}}_{\text{Solar}}\end{aligned} \tag{1.4}$$

where the $\theta_{ij}$ are the mixing angles, and $\delta_{\text{CP}}$ is a complex phase which determines

the amount of Charge-Parity (CP) violation within the neutrino sector of the SM; it is used to explore the potential asymmetries in neutrino and antineutrino interaction behaviours and explain the imbalance of matter and antimatter in the universe.

Following Equation 1.3, the flavour eigenstate after some propagation in spacetime ($x = 0, t = 0 \rightarrow x = x, t = t$) is given by

$$|\nu_\alpha(x,t)\rangle = \sum_{i=1}^{3} U_{\alpha i} \exp\left(-i\phi_i\right) |\nu_i(0,0)\rangle \,, \tag{1.5}$$

and $\phi_i = E_i t - \boldsymbol{p}_i \cdot \boldsymbol{x}$, where $E_i$ and $\boldsymbol{p}_i$ are the energy and momentum eigenvalues of the mass eigenstate $\nu_i$. The probability of observing flavour state $\nu_\beta$ at $x = x, t = t$ provided that it started as state $\nu_\alpha$ at the origin is then

$$\begin{aligned} P(\nu_\alpha \rightarrow \nu_\beta) &= |\langle \nu_\beta(x,t) | \nu_\alpha(0,0) \rangle|^2 \\ &= \left| \Big( \sum_{j=1}^{3} U^*_{\beta j} \exp\left(i\phi_j\right) \langle \nu_j(x,t)| \Big) \Big( \sum_{i=1}^{3} U_{\alpha i} \exp\left(-i\phi_i\right) |\nu_i(0,0)\rangle \Big) \right|^2 \\ &= \sum_{i=1}^{3} \left| U^*_{\beta i} U_{\alpha i} \right|^2 + \sum_{i \neq j} U_{\alpha i} U^*_{\beta i} U^*_{\alpha j} U_{\beta j} \exp\left(-i\Delta\phi_{ij}\right) \end{aligned} \tag{1.6}$$

where $\Delta\phi_{ij} = \phi_i - \phi_j = (E_i - E_j)t - (\boldsymbol{p}_i - \boldsymbol{p}_j) \cdot \boldsymbol{x}$. In the ultra-relativistic limit, $m \ll E \rightarrow p \approx E$ and using natural units leads to $E_i = \sqrt{m_i^2 + p_i^2} = E_i + m_i^2/2E_i$ and subsequently

$$\Delta E_{ij} = E_i - E_j = \frac{\Delta m^2_{ij}}{2E} \tag{1.7}$$

where $\Delta m^2_{ij} = m_i^2 - m_j^2$ and $E_1 \approx E_2 \approx E$. Substituting into the expression for $\Delta\phi_{ij}$ to get

$$\Delta\phi_{ij} = \frac{\Delta m^2_{ij}}{2E} t, \tag{1.8}$$

note that the momenta are equal in size in the ultra-relativistic regime and are thus cancelled.

Concretely, as an example, for a simple two-flavour oscillation, the matrix $\boldsymbol{U}$ reduces to a $2 \times 2$ matrix with a single mixing angle, $\theta$, i.e.

$$\boldsymbol{U} = \begin{pmatrix} \cos\theta & \sin\theta \\ -\sin\theta & \cos\theta \end{pmatrix} \tag{1.9}$$

and through trigonometry manipulations, Equation 1.6 becomes

$$P(\nu_\alpha \to \nu_\beta) = \sin^2(2\theta)\sin^2\Big(\frac{\Delta m^2_{21}}{4E}x\Big), \tag{1.10}$$

where, as a result of the ultra-relativistic nature of neutrinos, one can approximate $t$ as $x$.

For a distance $x = L$ [km], expressing the mass difference in [eV], the energy in [GeV] and returning the omitted $\hbar$'s and $c$'s, the two-flavour oscillation probability evolves to its final form

$$P(\nu_\alpha \to \nu_\beta) = \sin^2(2\theta)\sin^2\Big(1.27\frac{\Delta m^2_{21}[\text{eV}]L[\text{km}]}{E[\text{GeV}]}\Big), \tag{1.11}$$

which contains all the key parameters that govern the flavour-changing probabilities: $\theta$ quantifies the extent of flavour mixing, $\Delta m^2_{ij}$ dictates the oscillation frequency, and the travel distance (L) and $E$ determines the oscillation phase. As one can see from the above expression, the probability of observing a change in neutrino flavour is a function of $\Delta m^2_{21}$; therefore, if the neutrinos were massless, the oscillation would not have been possible. Extending this principle to three-flavour oscillations, the basic dependency on the mass-squared differences remains integral. In the three-flavour model, additional mixing angles and a CP-violating phase are introduced, modifying the oscillation pattern but not the underlying reliance on non-zero $\Delta^2_{ij}$ for oscillations to occur.

The oscillation probability derived under the two-flavour assumption still holds for the three-flavour scenario in most cases, specifically, when the mass-squared difference $\Delta m^2_{21}$ is either much greater or much smaller than $\Delta m^2_{32}$, a relationship corroborated by experimental data. However, in the propagation condition considered above, it is challenging to discern the sign of these differences due to the mass-squared differences appearing within a $\sin^2$ term in the derived oscillation probability. This ambiguity gives rise to the neutrino mass ordering problem, with two possible configurations: normal ordering (NO) where $m_3 \gg m_1/m_2$, and inverted ordering (IO) where $m_1/m_2 \gg m_3$, as indicated in Figure 1.3.

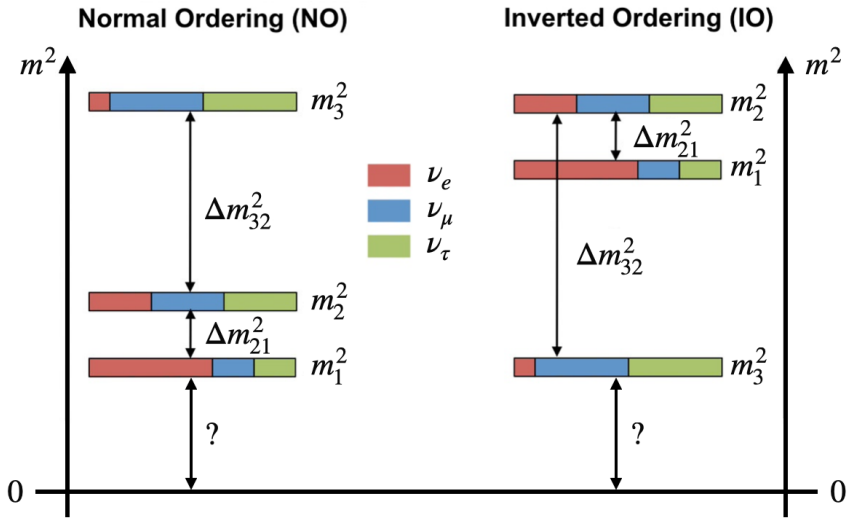


**Figure 1.3:** The normal and inverted mass ordering regimes of neutrino. Under normal mass ordering, $m_{\nu_3}$ is much larger than $m_{\nu_1}$ and $m_{\nu_2}$, and vice versa in the inverted ordering case.

### 1.3.1 The Matter Effect

When electron (anti)neutrinos traverse matter, they interact with both the atomic electrons and nucleons through CC and NC interactions, in contrast to the other neutrino flavours. This leads to the Mikheyev-Smirnov-Wolfenstein (MSW) effect, a distinct 'matter effect' that alters the potential within the electron neutrino part of the Hamiltonian. Consequently, this effect creates an asymmetry in oscillation probabilities for the electron (anti)neutrinos compared to other neutrino flavours, which only undergo NC interactions while going through matter. As a result, the matter effect changes the oscillation behaviour compared to that observed in a vacuum.

The modified electron neutrino Hamiltonian can be written as [20]

$$H_{\text{matter}} = H_{\text{vacuum}} + V_e = H_{\text{vacuum}} \pm \sqrt{2} G_f n_e \tag{1.12}$$

where $G_F$ is the Fermi coupling constant, and $n_e$ is the electron density in the material. The potential is positive for a neutrino and negative for an antineutrino.

This change in the Hamiltonian introduces explicit dependence on the sign of the mass-squared difference in the oscillation probability through matter.

A significant manifestation of the MSW effect is reported to be observed in solar

neutrinos by SNO in 2002 by comparing the total active solar neutrino flux and $\nu_e$-only flux [21]. The survival probability of $\nu_e$ travelling through the vacuum is calculated to be 1/2 to the leading order, however, the measured rate suggested a probability of closer to only 1/3. It was eventually understood that the oscillation probability of $\nu_e$ from the sun has been enhanced as these $\nu_e$'s satisfy the MSW resonance conditions of $E \sim 1$ MeV, $\Delta m^2_{21} \sim 10^{-5}$ eV$^2$ and $\Delta m^2_{21} > 0$. Through analysis of the data, it has therefore been established that $m_2 > m_1$, thereby providing a step forward in the study of neutrino mass hierarchies.

## 1.4 Neutrino Sources

The neutrino flux observed on Earth originates from an array of sources, spanning a broad spectrum of energies. As depicted in Figure 1.4, these sources include the Cosmic Neutrino Background (CNB), Big Bang Nucleosynthesis (BBN), solar processes, Earth-based sources like reactors, accelerators (not shown on the plot) and geoneutrinos, the Diffuse Supernova Neutrino Background (DSNB), the atmosphere, and cosmogenic processes. The graph illustrates neutrinos using solid lines, while antineutrinos are depicted through dotted or dashed lines. Sources that emit both neutrinos and antineutrinos are indicated by the superposition of solid and dashed lines. This Section categorises the neutrino sources into two groups: extragalactic sources, encompassing the CNB, BBN, DSNB, and cosmogenic origins, and the solar and terrestrial sources, which include solar, reactor, geological, atmospheric, and accelerator neutrinos.

### 1.4.1 Extragalactic Sources

#### Neutrino Backgrounds from the Early Universe

The Cosmic Neutrino Background (CNB), emerging approximately one second after the Big Bang, and neutrinos from Big Bang Nucleosynthesis (BBN), generated within the first few minutes of the universe, represent critical yet elusive elements of cosmological studies. The CNB is the most prevalent neutrino source on Earth, theorised to have a density of around 112 neutrinos per cubic centimetre for each flavour. These neutrinos,

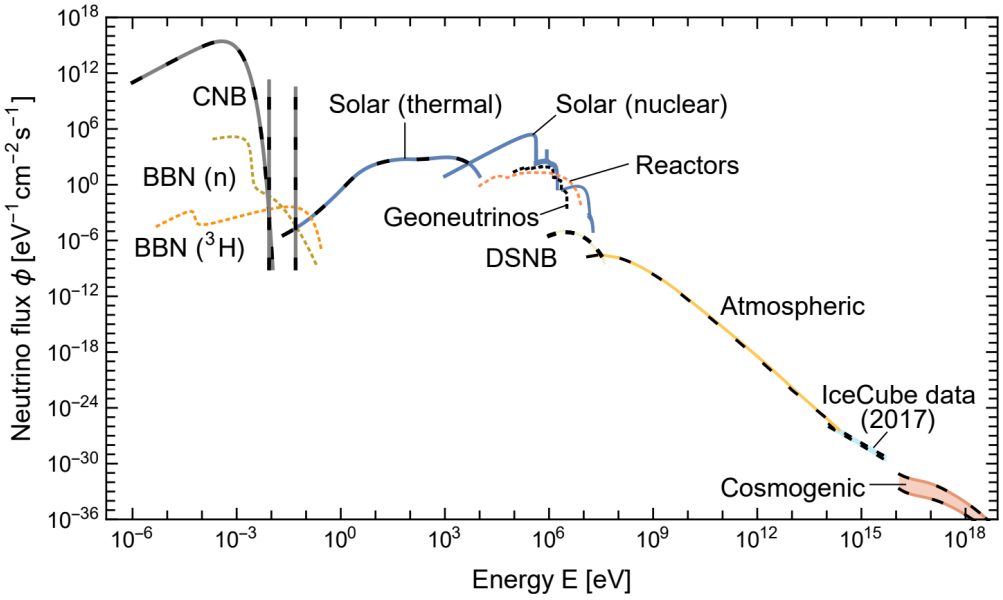


**Figure 1.4:** Direction and flavour-integrated neutrino flux spectrum at Earth [22]. The solid lines represent neutrinos, while the dotted or dashed lines depict antineutrinos, and the overlaying solid and dashed lines are sources of both.

integral to the dark matter composition, could illuminate neutrino physics, particularly their fundamental nature as either Dirac or Majorana particles (determining whether neutrinos are their own anti-particles). Similarly, neutrinos from BBN, created through processes such as neutron decay ($n \rightarrow p + e^- + \bar{\nu}_e$) and tritium decay ($^3\mathrm{H} \rightarrow {}^3\mathrm{He} + e^- + \bar{\nu}_e$), played a pivotal role in the early universe's nuclear reactions, influencing the abundance of primordial elements.

### Supernovae and Diffuse Supernova Neutrino Background

Supernova (SN) neutrinos are produced in the explosions of massive stars, generally around 1.5 - 2 times the solar mass. They carry away information about the core-collapse process and the physics of dense nuclear matter in the core of the dying stars. As they rarely interact, they are considered better candidates to study the SN creation process in comparison to the photons released, which could be absorbed or scattered while transversing through space. The neutrinos emitted from all the past SN in the universe form a low-energy background and are termed the diffuse supernova neutrino background. While the neutrinos from SN bursts are transient signals and thus not included in Figure 1.4, the DSNB dominates the flux spectrum at 10-25 MeV. Studying

these neutrinos provides important insights into the supernova collapsing mechanism and the properties of massive stars across spacetime.

### 1.4.2 Solar and Terrestrial Sources

#### Solar

Thermal and nuclear processes within the Sun produce a significant flux of neutrinos, which is key to understanding solar energy generation mechanisms. In the keV range, neutrinos of all flavours are generated through thermal activities, such as plasmon decay and electron bremsstrahlung. Though not detectable at present, it is thought to dominate the neutrino flux on Earth for energies below 4 keV. Additionally, about 2.3% of the Sun's nuclear energy is emitted as MeV-range electron neutrinos, stemming from fusion reactions [22]. As illustrated in Figure 1.5 [23], there are two known fusion reaction chains occurring in the Sun: the proton-proton (pp) chain and the carbon-nitrogen-oxygen (CNO) cycle.

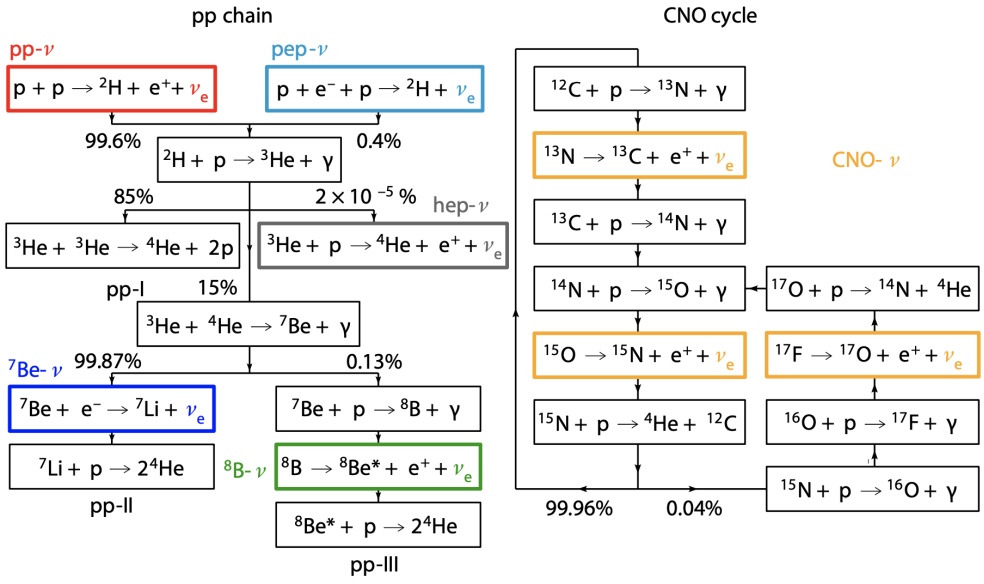


**Figure 1.5:** The pp chain and the CNO cycle in the Sun [23].

The pp chain predominantly starts with the fusion of three protons to form a helium-3 nucleus, $3p + e^- \rightarrow {}^3\mathrm{He} + \nu_e + \gamma$ , then the helium-3 is either stabilised into a helium-4 or goes through further interactions to create heavier particles in the periodic table.

The carbon in the CNO cycle of the Sun is not originally produced within the Sun. It is a remnant from previous generations of stars, and the carbon elements within the Sun are essentially inherited from the cosmic environment.

The study of these solar neutrinos has been crucial in uncovering neutrino flavour conversion and the matter effect, and in the concise measurements of $\sin^2\theta_{12}$ and $^2_{21}$. Moreover, solar neutrinos are increasingly relevant in dark matter research.

### The Reactors

Nuclear reactors are significant sources of antineutrinos, produced during the fission processes of nuclear fuel, mostly comprising of $^{235}$U (56%), $^{239}$Pu (30%), $^{238}$U (8%) and $^{241}$Pu (6%) [22]. Their energy is typically in the MeV range.

One of the outstanding mysteries in neutrino physics is the reactor neutrino anomaly, which concerns the mismatch between observed and predicted reactor antineutrino fluxes. Recent analyses, particularly from 2023, suggest that this anomaly may not be a sign of new physics, such as the sterile neutrino, but rather a result of experimental errors in electron data analysis [24]. These electrons, produced in the same beta decay as antineutrinos, are used to predict antineutrino spectra. The recalculated spectra, incorporating the fundamental theory of beta decay and a phenomenological model, have shown discrepancies with earlier electron measurements, indicating possible biases in these experiments. This revelation has shifted the focus from searching for new physics to seeking precision in existing measurement techniques.

### Geoneutrinos

Geoneutrinos, antineutrinos emanating from the decay of long-lived radioactive isotopes within Earth, such as $^{238}$U, $^{232}$Th, and $^{40}$K, are of significant interest in both particle physics and geology. These isotopes contribute to a substantial MeV-range antineutrino flux, exceeding $10^{25}$ antineutrinos per second coming out of the Earth's surface [25]. Although, in regions where nuclear reactors are located, their flux surpasses that of geoneutrinos. This flux offers a unique method for investigating Earth's internal mechanisms, particularly radiogenic heat production, which plays a crucial role in driving geological phenomena like plate tectonics and vulcanism.

### Atmospheric

Atmospheric neutrinos are vital to neutrino research and were the first 'natural' neutrinos to be observed [26, 27]. They are created when cosmic rays (CRs), primarily protons and atomic nuclei from outer space, collide with the Earth's atmosphere. These collisions result in a cascade of secondary particles, including pions, which subsequently decay into neutrinos. The processes can be written as

$$\pi^+ \to \mu^+ + \nu_\mu,\ \mu^+ \to e^+ + \nu_e + \bar{\nu}_\mu \tag{1.13}$$

and

$$\pi^- \to \mu^- + \bar{\nu}_\mu,\ \mu^- \to e^- + \bar{\nu}_e + \nu_\mu. \tag{1.14}$$

Atmospheric neutrinos come in all three flavours and have a wide range of energies, from a few MeV to several TeV. Due to their origin and interactions, they play a crucial role in understanding neutrino oscillations and are instrumental in studies searching for new physics beyond the Standard Model.

### The Accelerators

Accelerator neutrinos are a key component in the exploration of neutrino oscillations. Figure 1.6 is a schematic diagram illustrating the neutrino production pipeline in the Tokai to Kamioka (T2K) experiment [28], an example of long-baseline (LBL) neutrino oscillation experiments designed to study the oscillation behaviours of muon neutrinos and antineutrinos. Mirroring the production mechanisms of atmospheric neutrinos, accelerator neutrinos are generated by bombarding a fixed target with protons accelerated by a synchrotron, yielding both $\pi^+$ and $\pi^-$ mesons. The use of electro-magnets, known as horns, selectively focuses the charged pions. Subsequently, as described in Equation 1.13 and 1.14, the decay of the pions and the daughter muons produces a (anti)neutrino beam, typically with on-axis energy centred around 1 GeV. Crucial to T2K are the near and far detectors: the near detectors ND280 and INGRID, monitors the initial, unoscillated beam and measures neutrino-nucleon cross-sections, while the far detector Super-K, 295 km away, observes the oscillated neutrinos. This near-far

detector setup allows for a comprehensive analysis of muon neutrino disappearance and significantly reduces systematic uncertainties.

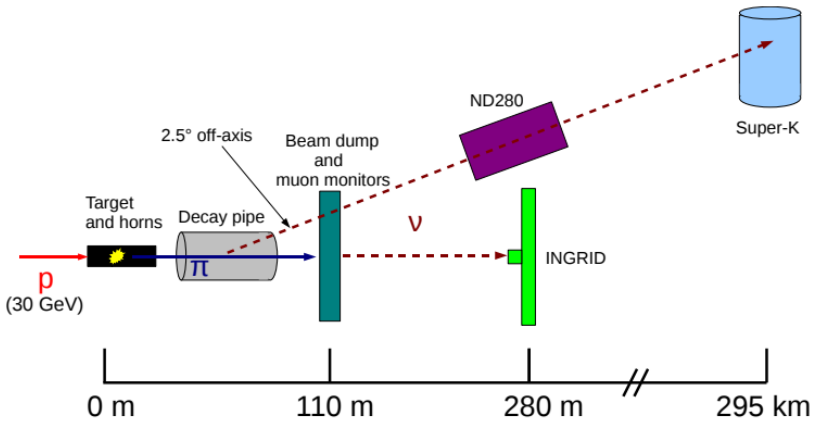


**Figure 1.6:** Schematics of the neutrino beam production pipeline in T2K [29].

## 1.5 The Determination of Neutrino Mass Ordering and the Measurement of $\delta_{CP}$

Three main routes can lead to the grand reveal of the neutrino mass hierarchy, through direct mass measurements, by observing the different rates of (anti-)neutrino oscillation caused by the matter effect, or by examining reactor anti-neutrino flux at the Jiangmen Underground Neutrino Observatory (JUNO) [30].

One of the direct measurement methods that has been providing promising results concerns the study of the kinematics of $\beta$ decays or electron capture processes. This method has the advantage of being independent of the neutrino mass origin theories and any cosmological models. The KArlsruhe TRItium Neutrino (KATRIN) experiment [31], which analyses the endpoint of the Tritium single-$\beta$ decay kinematic spectrum, has set the current best limit on the upper bound of neutrino mass - 0.8 eV (90% CL) [32]. Other constraints and measurements of the neutrino masses can come from cosmology, neutrino-less double beta decay processes and SN neutrino energy spectra.

It can be shown that the oscillation probability of $\nu_\mu \to \nu_e$ ($\bar{\nu}_\mu \to \bar{\nu}_e$) is enhanced

in the NO (IO) regime at the MSW resonance [33]. Therefore, the anomaly in rates in the $\nu_e/\bar{\nu}_e$ appearance channels at various LBL experiments, such as T2K, NOvA [34] and DUNE [35], or excess upward-going $\nu_e$ from atmospheric $\nu_\mu$ at stand-alone neutrino observatories could also help to discern neutrino mass ordering.

Lastly, JUNO is yet another experiment poised to resolve the mass ordering problem with its high-precision detection capabilities. With a baseline of 52.5 km, it is designed to study the fine interference pattern caused by $\Delta m^2_{32}$ and $\Delta m^2_{31}$ in the oscillated reactor antineutrino spectrum, without the influence of $\delta_{CP}$ and $\theta_{23}$.

The measurement of the CP-violating phase, $\delta_{CP}$, in neutrino oscillations primarily involves comparing the oscillation probabilities of neutrinos and antineutrinos in appearance channels, such as $\nu_\mu \to \nu_e$ and $\overline{\nu}_\mu \to \overline{\nu}_e$. LBL experiments are designed with specific baselines and neutrino energy to maximise oscillation and sensitivity to $\delta_{CP}$. Differences in the transition probabilities between neutrinos and antineutrinos, adjusted for matter effects from Earth's crust, indicate the presence of CP violation. The exact measurement of $\delta_{CP}$ requires precise detection capabilities and extensive data to overcome statistical and systematic uncertainties and other influencing factors.

## 1.6 Present Status of Oscillation Parameter Measurements

The latest best-fit ($\pm 1\sigma$) results for neutrino oscillation parameters under both Normal Ordering and Inverted Ordering hypotheses are as detailed in Table 1.1, reported in NuFIT5.1 [36]. Some questions remain to be answered, including determining the neutrino mass hierarchy, the extent of CP violation in the neutrino sector, and resolving the octant of the mixing angle $\theta_{32}$. The 'octant' of $\theta_{32}$ refers to whether this angle is smaller than 45 degrees (lower octant) or greater than 45 degrees (upper octant). This distinction is critical because it affects the interpretation of neutrino oscillation data and has implications for neutrino mass and mixing theories.

**Table 1.1:** The latest best fits ($\pm 1\sigma$) of the three flavour neutrino oscillation parameters as presented in NuFIT5.1 [36]. The results below include Super-K atmospheric data in the analysis. The variable $\Delta m^2_{3\ell} \equiv \Delta m^2_{31} > 0$ for NO and $\Delta m^2_{3\ell} \equiv \Delta m^2_{32} < 0$ for IO.

| **Oscillation Parameters** | **Normal Ordering** | **Inverted Ordering** |
|---|---|---|
| $\sin^2\theta_{12}$ | $0.304^{+0.012}_{-0.012}$ | $0.304^{+0.013}_{-0.012}$ |
| $\theta_{12}/^\circ$ | $33.45^{+0.77}_{-0.75}$ | $33.45^{+0.78}_{-0.75}$ |
| $\sin^2\theta_{23}$ | $0.450^{+0.019}_{-0.016}$ | $0.570^{+0.016}_{-0.022}$ |
| $\theta_{23}/^\circ$ | $42.1^{+1.1}_{-0.9}$ | $49^{+0.9}_{-1.3}$ |
| $\sin^2\theta_{13}$ | $0.02246^{+0.00062}_{-0.00062}$ | $0.02241^{+0.00074}_{-0.00062}$ |
| $\theta_{13}/^\circ$ | $8.62^{+0.12}_{-0.12}$ | $8.61^{+0.14}_{-0.12}$ |
| $\delta_{\rm CP}/^\circ$ | $230^{+36}_{-25}$ | $278^{+22}_{-30}$ |
| $\Delta m^2_{21}/(10^{-5}{\rm eV}^2)$ | $7.42^{+0.21}_{-0.20}$ | $7.42^{+0.21}_{-0.20}$ |
| $\Delta m^2_{3\ell}/(10^{-3}{\rm eV}^2)$ | $+2.510^{+0.027}_{-0.027}$ | $-2.490^{+0.026}_{-0.028}$ |

## 1.7 Summary

The study of neutrinos started at the beginning of the 1900s with the 'missing' energy in the $\beta$ decays. It gradually developed into a fully-fledged field in the 20th century with the measurement of neutrinos from various sources, and the observation of three generations of them, corresponding to the three charged leptons. Interesting problems arose along the way, including the solar neutrino deficit and the reactor neutrino anomaly. At the tail end of the century, Super-K announced the groundbreaking results of the observation of atmospheric neutrino oscillations, which consolidated that neutrinos have non-zero mass. A few years later, SNO confirmed the neutrino oscillation phenomenon within the solar sector due to its capability of being able to detect neutrinos of all flavours, settling the solar neutrino problem once and for all. This result has also revealed that $m_2 > m_1$ with the consideration of the matter effect in the Sun. Since then, the parameters of the PMNS matrix have been increasingly accurately measured by a range of past and current experiments, and more detectors are being constructed to further the precision.

# Chapter 2

# Two Generations of Kamiokande Detectors

## 2.1 A Brief History of Water Cherenkov Experiments in Japan

The evolution of water Cherenkov experiments in Japan represents a significant chapter in the history of particle physics, characterised by a series of advanced detectors designed to probe the fundamental aspects of neutrino interactions. These sophisticated experiments have substantially contributed to the broader scientific community's understanding of particle physics and astronomical phenomena. The journey began in the early 1980s with the establishment of the Kamioka Nucleon Decay Experiment (Kamiokande), a pioneering venture that set the foundation for subsequent advancements in the field.

Kamiokande, located in the Kamioka Mine in Gifu Prefecture, was designed to detect proton decay, a key prediction of Grand Unification Theories. It comprised a large cylindrical tank 16 m in height and 15.6 m in width, filled with 3000 t of pure water and surrounded by 1000 Photomultiplier Tubes (PMTs) to detect Cherenkov light from particle interactions [37]. Figure 2.1 shows a schematic drawing of the Kamiokande detector.

After two years of operation, Kamiokande became Kamiokande-II in 1986 following

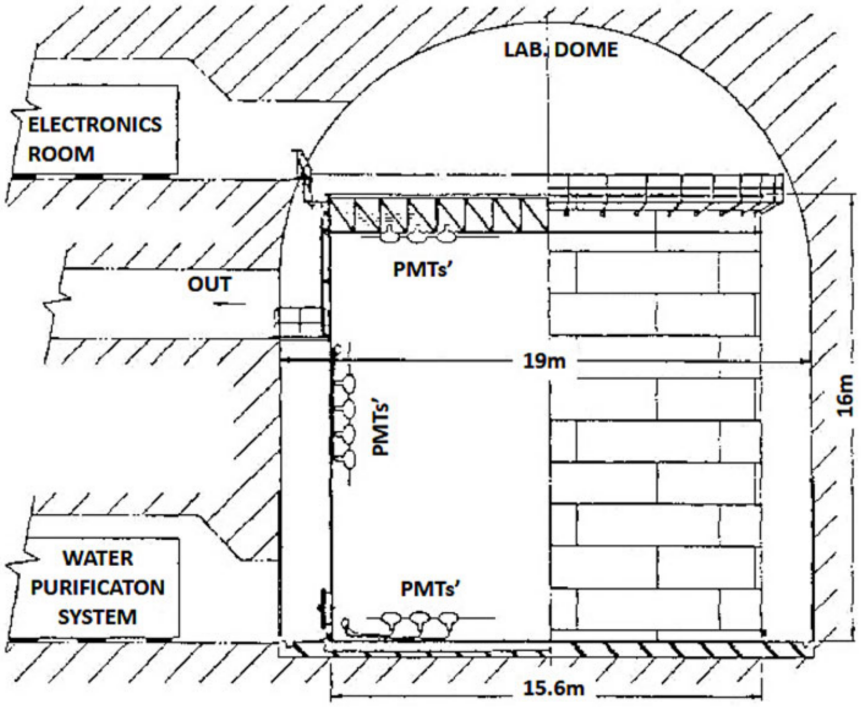


**Figure 2.1:** A schematic drawing of the Kamiokande [37].

an upgrade to the electronics and water purification systems and the addition of an outer veto region, which enabled an energy resolution of as low as 10 MeV. Though the experiment intended to study proton decay, signals generated by secondary interaction products of atmospheric neutrinos were also studied extensively. These interactions were important as they made up the majority of the background to the proton decay signals [38]. Therefore, despite the fact that Kamiokande did not observe any proton decays, it was able to confirm the observed solar neutrino deficit problem that first arose in the Homestake Experiment [39]; in addition, together with another water Cherenkov detector known as the Irvine-Michigan-Brookhaven (IMB) experiment, Kamiokande-II had reported that the fraction of muon decays originating from atmospheric neutrinos was smaller than expected [40, 41]. These landmark discoveries contributed to the Nobel Prize in Physics for Masatoshi Koshiba in 2002. Furthermore, both the Kamiokande-II and the IMB experiments reported the observation of neutrinos originating from Supernova (SN) 1987a [42, 43], granting the first-ever test on the theory of core-collapse SN's neutrino production.

Following the decommissioning of the Kamiokande experiment, a new detector was constructed to take advantage of the Kamiokande detector cavity. The KamLAND experiment [44], short for Kamioka Liquid-scintillator Anti-Neutrino Detector, represents a significant shift in focus and technology compared to its predecessors. Operational between 2002 and 2009, KamLAND was filled with a liquid scintillator designed to study anti-neutrinos irradiated from various rectors in Japan as well as geoneutrinos.

Building on Kamiokande's legacy, the Super-Kamiokande (Super-K) detector [16] was proposed to further investigate the solar and atmospheric neutrino problems, together with the continued search for proton decays. Situated 1 km underneath Mt. Ikeno (rock burden equivalent to 2700 m of water), the Super-K detector shares the same ground-level access tunnel system as the Kamiokande/KamLAND experiment. Members of the IMB experiment, who joined the Kamiokande experiment earlier, along with the Kamioka collaborators, shared the design and construction responsibilities. As shown in Figure 2.2, the resulting Super-K tank design is a cylinder with a height of 41.1 m and a diameter of 39.3 m, capable of holding 50 kt of ultra-pure water, which is roughly 17 times the volume of the Kamiokande detector. The experiment area also consists of a hall above the water tank to house front-end electronics and calibration equipment, an access tunnel, and a series of control rooms whereby the collaborators monitor the experimental operation status.

The cavern excavation operation spanned from 1991 to 1994, followed by the detector construction, which commenced between 1994 to 1996. Data taking with the Super-K detector started on April 1, 1996. With a significantly larger scale and more PMTs, it offered enhanced sensitivity and precision. Super-K's major achievement was the confirmation of neutrino oscillations through atmospheric neutrinos, a discovery honoured with half of the Nobel Prize in Physics in 2015. Super-K has also made significant contributions to the study of solar neutrinos, supernova neutrinos, and the ongoing search for proton decay. Section 2.3 provides an in-depth discussion of the important components that make up the Super-K detector.

The Hyper-Kamiokande (Hyper-K) project [46] represents the latest advancement

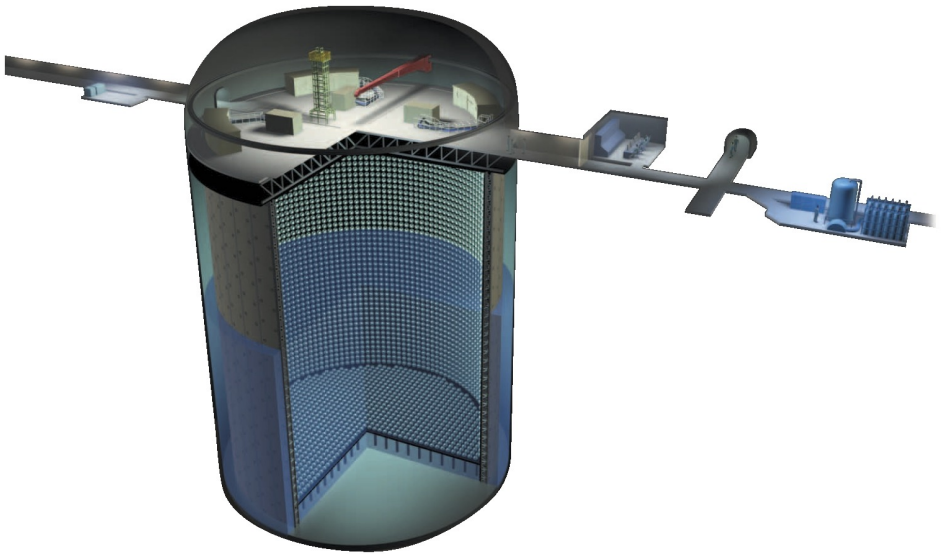

**Figure 2.2:** A rendition of the Super-K tank from an artist [45], illustrating the inner and outer detector regions, as well as the control room and the access tunnel. The dome above the detector houses all the front-end electronics and hardware calibration devices.

in this series, the size comparison of the three generations can be found in Figure 2.3. As a large-scale detector, Hyper-K aims to delve deeper into CP violation in the neutrino sector, explore nucleon decay, and advance neutrino astrophysics. This ambitious project underscores Japan's commitment to maintaining a leading position in neutrino research. A comprehensive examination of the various aspects of Hyper-K is presented in Section 2.4.

## 2.2 Charged Particle Detection in Water Cherenkov Detectors

This section focuses on the key principles involved in detecting charged particles in Water Cherenkov Detectors. A detailed exploration will be presented on the phenomenon of Cherenkov radiation and the fundamental workings of PMTs, both of which are integral to the detector designs.


**Figure 2.3:** The size comparison of three generations of Japanese neutrino detectors [47]. The fiducial mass refers to the region in the inner detector where the neutrino interactions are analysed. This volume is placed to avoid regions near detector walls where background events due to cosmic rays or radioactivity can mimic or obscure genuine neutrino interactions.

### 2.2.1 Cherenkov Radiation

Water Cherenkov detectors, exemplified by Super-K and Hyper-K, are able to detect charged particles through medium-emitted Cherenkov light. First reported by P. A. Čerenkov in 1934, pure liquids or solids were observed to emit weakly visible radiations when fast electrons pass through [48]; here, fast electrons refer to Compton electrons knocked off by $\gamma$-rays, or $\beta$ particles from radioactive decays. Following this discovery, I. M. Frank and I. E. Tamm furthered the exploration of such radiation by formulating a quantitative theory of the phenomenon [49]. They proposed that in a medium characterised by its refractive index $n$, an electron moving at a velocity, $v$, faster than the speed of light in the medium, i.e. $\beta \equiv \frac{v}{c} > 1/n$, must emit radiation propagating at an angle $\theta_C$ from the electron travel direction. Generalising the theorem to all charged particles, the Cherenkov angle of a particle is given by

$$\cos\theta_C = 1/\beta n. \tag{2.1}$$

For ultra-relativistic charged particles, one can approximate their $\beta$ to 1; in a water Cherenkov detector with $n = 1.33$, the maximum achievable Cherenkov angle is thus around 42°.

Due to the constraint on particle velocity in the medium, the principles of special relativity impose a minimum energy requirement for such Cherenkov-light-generating particles, which is as follows

$$E_{th} = m\sqrt{1 + \frac{1}{n^2 - 1}}, \tag{2.2}$$

where $m$ is the mass of the given particle. According to this equation, one can deduce the Cherenkov energy threshold for a few commonly observed particles in the Super-K detector, as listed in Table 2.1. Although $n$ is typically wavelength-dependent, for light that falls within the visible wavelength spectrum, its value only fluctuates within a few percent. Note that the refractive index $n$ for Super-K is taken as 1.34. It is also worth mentioning that even though $\pi^0$s and $\gamma$s are not charged particles themselves, they all eventually decay into electromagnetic showers and become significant background events for electrons from neutrino interactions. The effective Cherenkov energy threshold for $\pi^0$s and $\gamma$s are respectively four times and twice as large as the electron thresholds since $\pi^0$ decays into two $\gamma$s, which in turn go through pair production and end up as two electron-positron pairs.

**Table 2.1:** Cherenkov Energy threshold for a few commonly observed particles in Super-K. †Effective Cherenkov threshold for a neutral particle to see Cherenkov light. The value for $\pi^0$ and $\gamma$ are four times and twice as large as the electron threshold, according to the decay chain where $\pi^0$ decays to two $\gamma$'s and a $\gamma$ pair produces an electron-positron pair.

| Particle | Cherenkov Energy Threshold (MeV) |
|---|---|
| $e^{\pm}$ | 0.775 |
| $\mu^{\pm}$ | 160 |
| $\pi^{0\dagger}$ | 3.07 |
| $\gamma^{\dagger}$ | 1.53 |

The number of Cherenkov photons produced by a charged particle per unit length

travelled, $x$, per wavelength, $\lambda$, is given by the Frank-Tamm formula [49]

$$\frac{\partial N}{\partial x \partial \lambda} = \frac{2\pi\alpha Z^2}{\lambda^2}\Big(1 - \frac{1}{\beta^2 n(\lambda)^2}\Big), \tag{2.3}$$

where $\alpha$ is the fine structure constant, and $Z$ is the charge of the particle. In water, a charged particle generates approximately 3000 photons per centimetre within the wavelength range of 300 nm to 550 nm.

In a water Cherenkov detector, the charged particles will initially move faster than the speed of light in a given medium, but as they traverse through the detector volume, they will gradually lose their kinetic energy to ionisation. A portion of these charged particles will lose so much energy that they fall below the Cherenkov threshold. As the energy requirement no longer holds, the particles stop generating light, and when the previously generated Cherenkov photons project onto a surface, they form iconic ring shapes. Figure 2.4 are two example event displays of Cherenkov rings generated by an electron and a muon neutrino event in the Super-K, respectively.

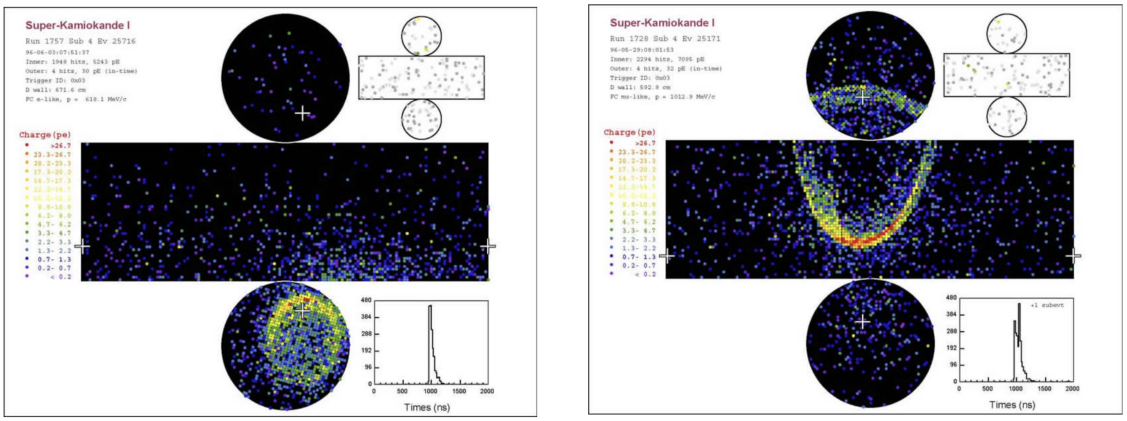


**(a)** An electron neutrino event

**(b)** A muon neutrino event

**Figure 2.4:** Two types of neutrino events observed in Super-K [50], displayed in a 'flattened' detector, where the two circles correspond to the top and bottom of the detector. Both events are fully contained in the inner detector of the Super-K, which means that the neutrinos interact in the inner detector volume (black background), and the daughter particles are stopped before entering the outer detector (white background). The lack of excess hits shown in the outer detector region signifies these are fully contained events. The electron neutrino event on the left shows a fuzzier ring than the muon neutrino event, as electrons are much lighter and thus much easier to deflect by the atomic structures than muons. The white crosses are reconstructed vertex positions.

### 2.2.2 Photo-Multiplier Tubes

Water Cherenkov experiments rely on the PMTs installed on all surfaces of the detector volume to convert Cherenkov radiation into electric pulses for further signal processing. Despite having 'tube' in its name, PMTs found in the Super-K, Hyper-K and a myriad of other Cherenkov detectors are bulb-shaped, each comprised of a spherical head and a torus body with a circular cross section; an example can be found in Figure 2.5a. Nonetheless, the photon-to-electric-signal-conversion principle that applies to the tube-shaped PMTs (Figure 2.5b) holds true for the bulb-shaped ones as well.

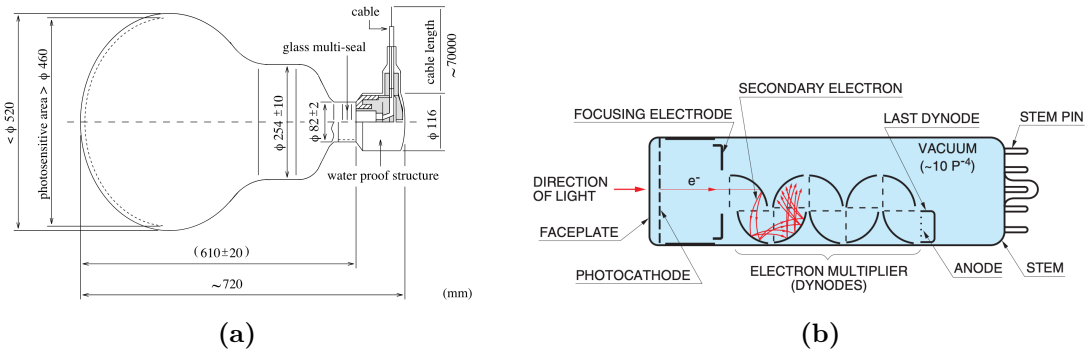


**Figure 2.5:** (a) Cross-section of a Super-K inner-detector PMT [16], which is made up of a sphere connected to a circular torus, and connected to the electronics; (b) A tube-shaped PMT example, labelled with all the essential components of a PMT [51].

The photon-to-current conversion process starts with a Cherenkov photon incident on the front of a PMT, going through the glass, and the subsequent photocathode layer (commonly made from Bialkali, suitable for detecting visible light [51]) converts it into a photoelectron (p.e.) through the photoelectric effect, provided that the photon possesses enough energy. Then, the photoelectron is accelerated and honed in by the focusing electrode and strikes the first electron multiplier (dynode) of the series.

Following its incidents onto the first dynode, the original electron induces secondary electron emissions in the dynode sequence, resulting in $10^6$ or $10^7$ electrons emitted from the last dynode. There are a few well-utilised dynode configurations, including the venetian blind, box-and-line, and linear-focused [51, p. 46]. The dynode structures for the original Hamamatsu PMTs that were installed in the Super-K back in 1995, R3600 for the inner detector and R1408 for the outer detector, are both of the venetian blind types [52, 53]. However, at least all the newly installed Super-K outer detector

PMTs follow the box-and-line dynode configuration [54]. Lastly, the electron cascade is collected by an anode and becomes an electric pulse. The inside of the PMT is kept as a vacuum to reduce the obstruction on electron trajectories caused by collisions with air molecules. Thus, an implosion would occur when the outer glass housing is breached, foreshadowing the catastrophic incident that happened in the Super-K in 2001, where half of the PMTs were lost to a chain-implosion event.

The operation of a PMT requires a high voltage supply, ranging between 500 and 2000 V at positive or negative potentials. Employing an array of resistors in series, the voltage is distributed unevenly between the photocathode, dynodes and anode to drive the electron progressions.

### Quantum Efficiency

The quantum efficiency (QE) of a PMT refers to the ratio of photoelectrons released from the photocathode to the incoming photon count, commonly expressed in a percentage. When used in the context of this thesis, it also encompasses the collection efficiency, which is the probability of a photocathode-emitted p.e. reaching the first dynode.

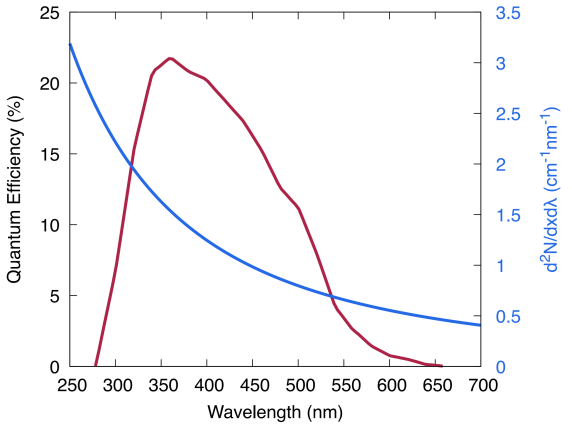


**Figure 2.6:** An overlay of the quantum efficiency curve of a Hamamatsu R3600 used in Super-K (left axis) and the Cherenkov photon spectrum described by Equation 2.3 (right axis) [55]. The Super-K PMT is at the highest photon-to-signal conversion efficiency at the UV/blue visible light range, but the number density of Cherenkov photons is the highest at the shortest wavelength detectable by the PMT.

Figure 2.6 displays the all-encompassing QE of a PMT used in the Super-K and the Cherenkov radiation spectrum predicted by Equation 2.3 [55]. As illustrated by the plot, the PMT QE commonly peaks at the UV/blue visible light wavelength range, with a drop in both wavelength directions. The QE of a PMT is influenced by the angles at which photons strike the photocathode. This relationship is determined through various calibration activities in every experiment involving PMTs.

### Gain

Nominally, the gain of a PMT measures how many secondary emission electrons are collected at the anode, given that one photoelectron has impinged on the first dynode of the series. Nevertheless, in water Cherenkov detector applications, the gain generally refers to how much output current results from one impinging Cherenkov photon.

Several factors can affect the gain of a PMT; one of the most significant ones is the operating voltage. The gain as a function of supplied voltage for a Super-K PMT can be found in Figure 2.7. Note that the relationship is not linear. Other gain-affecting factors include voltage stability, temperature, geomagnetic field, photocathode condition, and electrical interference.

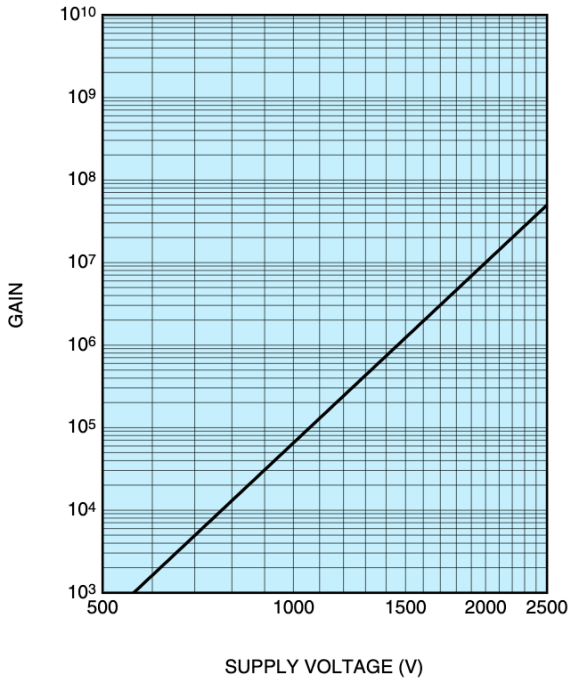


**Figure 2.7:** Gain as a function of voltage for a Super-K PMT [52]. The higher the voltage, the larger the gain; however, the relationship is not linear.

### Dark Currents or Dark Rates

Dark currents, or dark rates, in a PMT, refer to the electrical current that is generated in the absence of light or photon input. The phenomenon is an inherent characteristic of PMTs and is caused primarily by thermal electrons emitted from the photocathode or dynode surfaces. Other factors include current leakage between the anode and

other electrodes, scintillation of the glass or other components, radiations from the radio-isotopes in the glass housing, etc [51]. It is also an important factor in PMTs as it contributes to the noise level of the device, potentially impacting its sensitivity and accuracy in low-light detection scenarios. The magnitude of dark current typically increases with temperature and supplied voltage, although the increment rate is not linear with the increasing voltage. On the other hand, storing the PMT in a dark place for a few hours is effective in suppressing the dark current generation as it helps the materials within the PMT that can become 'excited' or ionised by light or environmental changes to return to a ground state, minimising unwanted electrical activity and noise.

Figure 2.8 is an example histogram displaying the dark current, as well as hits recorded by a single PMT from a laser signal in Super-K's outer-detector calibration data. The peak at approximately 1500 ns contains photons from the laser, while the scattered hits of the rest of the histogram are the PMT dark currents.

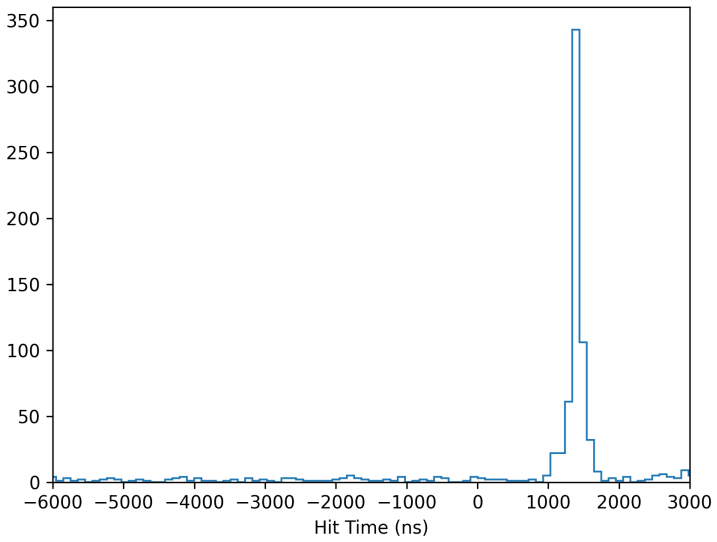


**Figure 2.8:** Hit time distribution of a Super-K outer-detector PMT plotted from the Super-K laser calibration data. The hits recorded from a laser signal accumulate to a peak centred around 1500 ns, whereas the rest of the hits are all caused by the dark currents.

### Pedestal and Single-Photon Peak

In low light conditions, defined by the emission of no more than two photoelectrons (p.e.s) within a PMT's time resolution, the average amount of output current from one p.e. for the given PMT can be deduced. The time resolution of a PMT is the measure of a PMT's ability to distinguish between separate photon-induced events. The accumulated PMT pulse height over a period of time would typically take the shape shown in Figure 2.9. Note that in this specific example, the pulse height is quantified in Analogue-to-Digital Converter (ADC) units, where its correlation to the actual output current is established through a Heaviside step function. In the subsequent chapters, the pulse height can also be found to be in units of p.e.s.

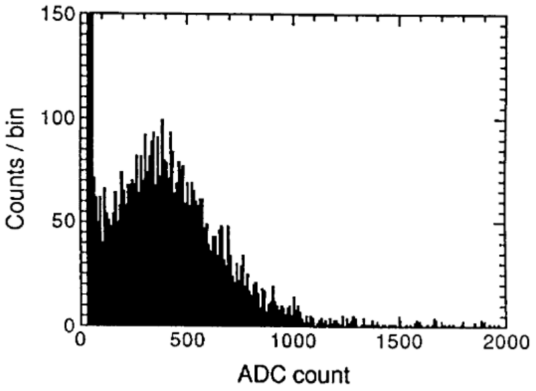


**Figure 2.9:** A distribution of single photoelectron pulse heights for a typical Hamamatsu R3600 PMT [16]. The x value is measured in Analogue-to-Digital Converter (ADC) counts, which are correlated with the actual output current through a Heaviside step function. The peak close to zero ADC counts is caused by the dark currents.

In Figure 2.9, the peak close to the zero ADC count, canonically termed the pedestal, is caused by the dark currents. The other peak is commonly known as the single-photoelectron (s.p.e.) peak, where the gain or the ratio of 1 p.e. to the output current (usually measured in pC) can be extracted using a Gaussian fit function.

### PMT Input-Output Linearity and Saturation

PMTs generally exhibit a linear relationship between the incident light intensity and the output current to some extent. Saturation, on the other hand, refers to the phenomenon of the output current losing linearity with increasing light intensity. For a given Super-K outer detector PMT, the ratio of detected to expected photons against the true photons supplied is shown in Figure 2.10. The black horizontal line represents an

ideal, non-saturating scenario, whereas the red line, follows the function [56]

$$f(k) = \frac{1}{k + 1/\mathrm{Q}_{\mathrm{true}}}, \tag{2.4}$$

where $k$ is the saturation parameter [56] and $\mathrm{Q}_{\mathrm{true}}$ is the true charge that the PMT would record at high light levels, assuming that the linear relationship between the inbound photon number and output charge value at low light conditions holds true and that the PMT can never be saturated.

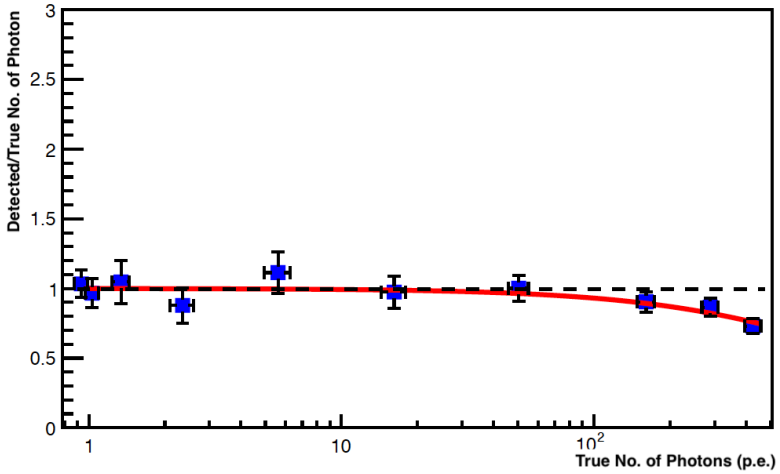


**Figure 2.10:** The detected to true photon ratio as a function of true photons supplied for a Super-K OD PMT. The black line illustrates a scenario when the PMT is never saturated; the red line is a function, $f(k) = 1/(k + 1/\mathrm{Q}_{\mathrm{true}})$, fitted to the data points, where $k$ is known as the saturation parameter of that PMT and $\mathrm{Q}_{\mathrm{true}}$ is the true charge value the PMT should report provided the saturation effect does not occur. It is clear that the ratio between the number of observed and true photons begins to deviate from one before 100 photons were impeding the PMT.

Notably, in the figure, the discrepancy between observed and true photon counts begins before the 100-photon mark, signalling an early departure from ideal detection. The criteria for a PMT being 'saturated' can vary by experiment, and even by detector segment; for example, Super-K considers an OD PMT that reports an observed charge exceeding 200 p.e. as saturated, corresponding to roughly 15% deviation from linearity. This saturation threshold is critical in Super-K's data analysis, as it defines the upper bound of the OD PMTs' reliable operational range. When a PMT saturates, reconstruction algorithms may need to account for the non-linearity by applying corrections. Therefore, understanding and compensating for OD PMT saturation is crucial in

maintaining the accuracy of CR muon vetoing and high-energy event reconstructions.

Several factors can cause PMT saturation: photocathode saturation, dynode saturation, space charge effects, anode current limit, etc. [51].

## 2.3 Super-Kamiokande

As mentioned previously, neutrino detection is challenging due to their small interaction cross-sections, especially for solar and accelerator neutrinos. Accelerator neutrinos, with energies around 1 GeV/c, have cross-sections near $10^{-38}\text{cm}^2$ [57], while solar neutrinos, under 10 MeV/c, have even lower cross-sections [58]. Large detectors are used in neutrino experiments to capture enough interactions for statistical significance. These detectors must analyse the final-state particles to determine neutrino properties but face background interference from cosmic rays and natural radioactivity, requiring mitigation techniques.

Super-K has been a key experiment in the field of neutrino research, utilising large water tanks surrounded by PMTs to detect Cherenkov radiation from charged leptons in neutrino interactions. Although the rock overburden above the detector tank can remove some neutrino-signal-mimicking backgrounds, such as CR muons, challenges persist with atmospheric neutrinos and beta decays from nuclear spallation products, which are isotopes created by CR muon interacting with oxygen nuclei in the water. Precision in distinguishing signal from background is crucial, techniques such as adding Gadolinium (Gd) to the detector's medium to improve neutron detection efficiency and improving the accuracy of event reconstruction algorithms are employed to address the issue.

### 2.3.1 The Detector Specifications

The Super-K structure features a stainless steel framework lined with the dark side of Tyvek® material that segregates the detector into two optically independent sections. Positioned approximately 2.6 m from the tank walls, this framework delineates an inner volume known as the inner-detector (ID) and an outer volume referred to as the outer-detector (OD), as depicted in Figure 2.11a. The steel structure is attached to the tank

walls through the top and bottom support structures.

The detector is constructed from 'super-module' units, each supporting a $3 \times 4$ array of ID PMTs on one side and two OD PMTs on the other. Examples of such units for the top, barrel and bottom regions can be found in Figure 2.11b. The super-modules have a dimension of $2.1 \times 2.8 \times 0.55$ m and are interconnected with each other in both vertical and horizontal directions.

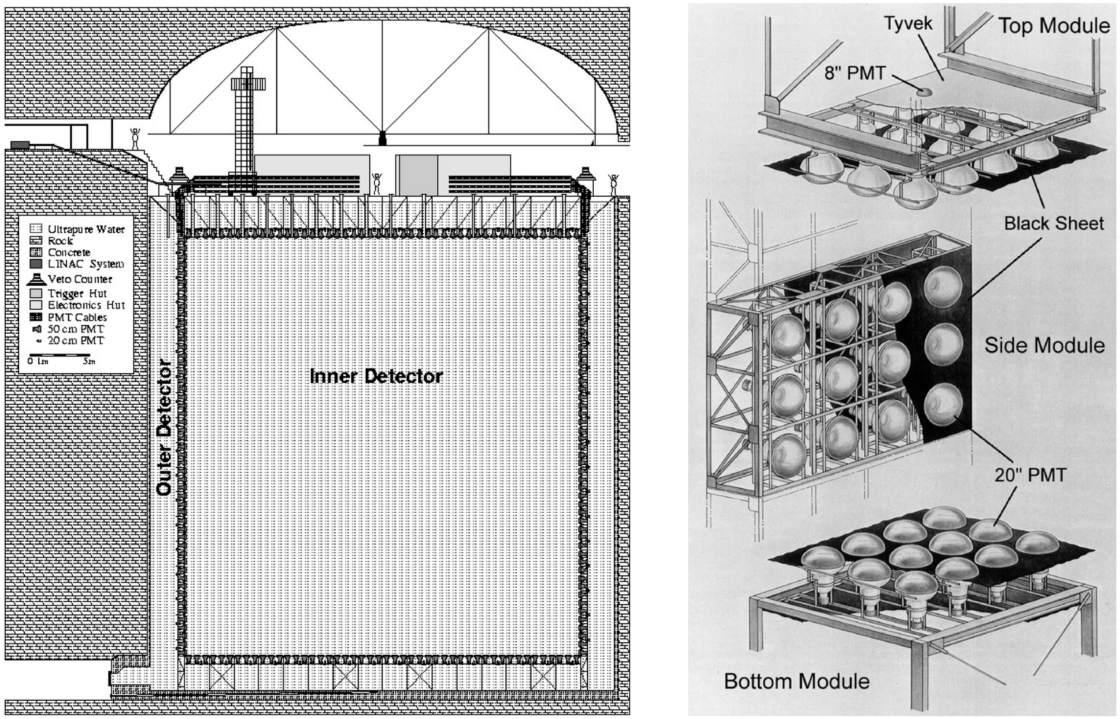


**(a)** **(b)**

**Figure 2.11:** (a) The cross-section view of the Super-Kamiokande detector [16]; (b) The super-module units used inside Super-K, each module supports 12 ID PMTs and 2 OD PMTs [16].

### The Inner-Detector

The ID, capable of holding 32 kt of water, houses 11,146 inward-facing 20-inch (50 cm) Hamamatsu R3600 PMTs [52]. A schematic diagram of the R3600 PMT cross-section can be found in Figure 2.5a in Section 2.2.2. The number of installed ID PMTs aims to guarantee a photocoverage of approximately 40%. After the implosion incident in 2001, acrylic covers were designed and installed on all the remaining ID PMTs and on

any newly introduced PMTs in 2006 to prevent any further chain implosions.

### The Outer-Detector

In the 18 kt volume of the OD, there are 1885 8-inch (20 cm) PMTs. Before 2006, most of them were Hamamatsu R1408 type PMTs, recycled from the IMB experiment; during the 2006 and 2018 open-tank restoration campaigns, many of the IMB PMTs were replaced by new Hamamatsu R5912 models, which are designated as the successors to the R1408s since their discontinuation. After the 2018 tank-open work, only about 20% of the OD PMTs are from IMB [55]. The IMB PMTs were originally placed uniformly throughout the OD region. However, during maintenance in 2018, they were relocated to the upper sections, including the top of the barrel and the top cap areas. This strategy was adopted because the IMB PMTs, being older, were deemed at risk of not handling the increased water pressure at greater depths effectively. Even so, the rapid failure of these PMTs in recent years has gradually weakened the OD's capability to veto CR muons. For example, since the start of December 2023, tens of these units have failed to meet operational standards (dark rate $< 167$ Hz) within just four weeks [59], indicating a pressing need for reassessment of the background reduction for Super-K data processing.

Two diagrams in Figure 2.12 show the cross-sections of R1408 and R5912, respectively; Figure 2.13 illustrates the QE of two models, where the datasets are derived from plots in Ref. [60] and [54].

Since the OD PMTs are positioned fairly sparsely on the steel structures, Wavelength-Shifting (WLS) plates were installed with the OD PMTs to increase the light collection efficiency in the OD since the beginning. These WLS plates are square-shaped, with a length of 0.6 m and a thickness of 0.013 m, and each has a machined hole in the centre for PMT mounting [16]. To further improve light detection, all walls of the OD are lined with the white side of the Tyvek® sheets to facilitate multiple reflections of the Cherenkov photons in the region. This design choice resulted in a lowered resolution for Cherenkov ring patterns but an increased light collection efficiency.

Though it originally existed as a whole volume, the OD was eventually segmented into three optically isolated sections (top, barrel and bottom) using Tyvek® in 2006

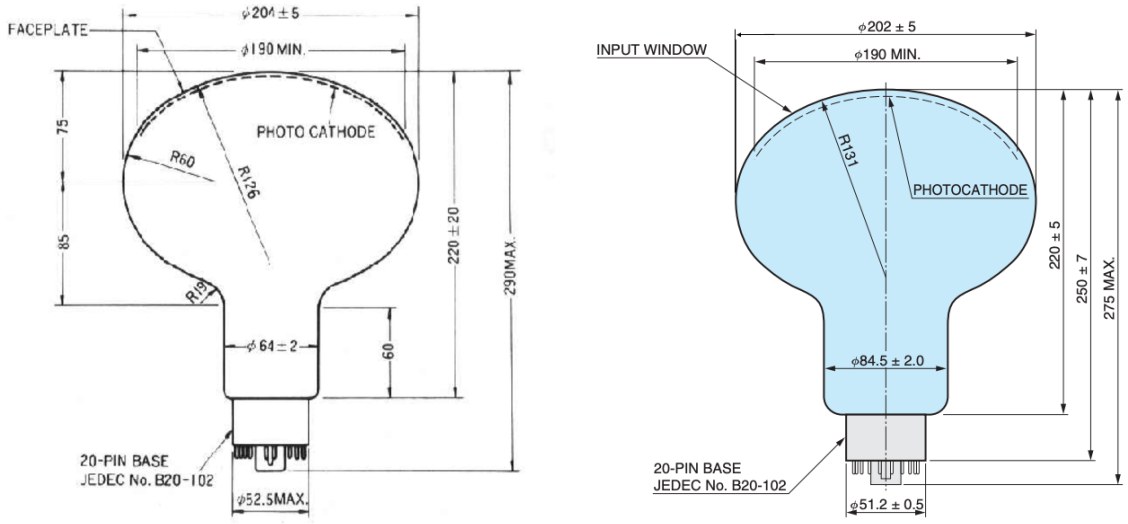


**(a)** Hamamatsu R1408 **(b)** Hamamatsu R5912

**Figure 2.12:** Cross-sections of two types of OD PMTs [54, 61].

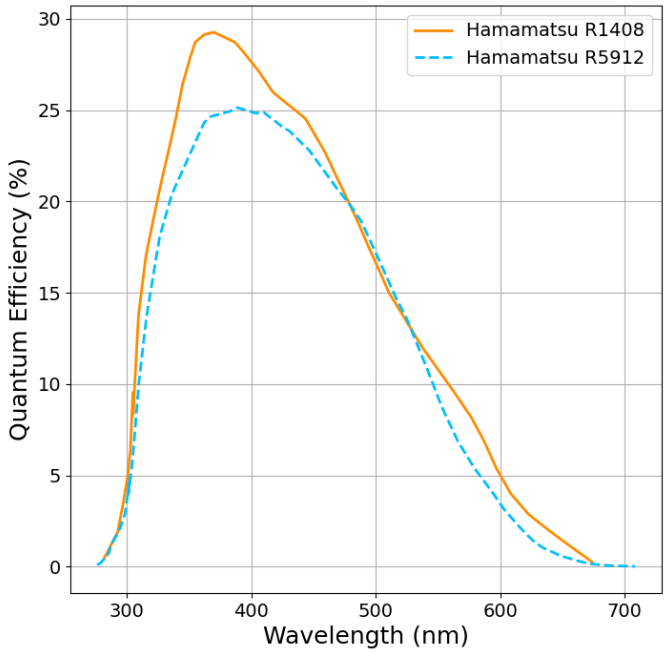


**Figure 2.13:** Quantum efficiencies of Hamamatsu PMT model R1408 (IMB PMTs in the OD) and its successor R5912 (newer PMTs in the OD), used in Super-K OD. The QE datasets are sampled from Ref. [60] and [54]. The new version of the OD PMT appears to have slightly lower QE in general.

[56]. This segmentation was introduced to enhance the veto ability of the 'corner-clipping' CR muons from the escaping leptons originating from atmospheric neutrino

interactions inside the ID.

### 2.3.2 Geomagnetic Field at Super-Kamiokande

As mentioned in Section 2.2.2, the geomagnetic field present at the PMT operation site is one of the significant factors affecting the gain and timing of a PMT. Essentially, the geomagnetic field affects the trajectories of the electrons within the PMT and could delay their travel times and/or deviate them from the expected path.

At Super-K, the average geomagnetic field is measured to be around 450 mG and intercepts the horizon at a 45° angle [16, 56]. To counteract the field, 26 Helmholtz coils were installed along the inner surface of the tank, and their locations are illustrated in Figure 2.14.

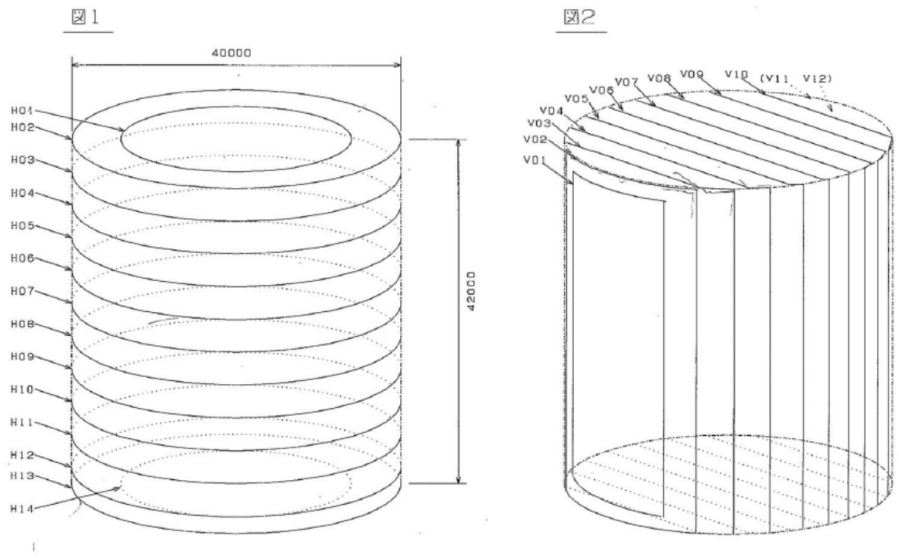


**Figure 2.14:** Locations of the Super-K geomagnetic compensation coils [62]. In general, every four loops in the horizontal and vertical directions are grouped together and share the same power supply. Note that group 7 only includes coils H01 and H14. There are three and four groups for vertical and horizontal coils, respectively.

Every four vertical or horizontal coils are grouped into one set and share a power supply, apart from group 7, which only consists of two horizontal coils. The grouping arrangement and the current going through each group are detailed in Table 2.2. Pictures in Figure 2.15 display one of the junctions where the compensation coils in group one are joined together.

After the coil compensation, the magnetic field is reduced to approximately 50 mG on average.

**Table 2.2:** Grouping of the Super-K geomagnetic compensation coils and the amount of current flowing through during normal operations [62].

| Coil Group | Coil Numbers | Current (A) |
|---|---|---|
| 1 | V01 - V04 | 30.10 |
| 2 | V05 - V08 | 28.60 |
| 3 | V09 - V12 | 30.10 |
| 4 | H01, H03 - H05 | 31.35 |
| 5 | H06 - H09 | 31.35 |
| 6 | H10 - H12, H14 | 31.35 |
| 7 | H01, H13 | 28.20 |

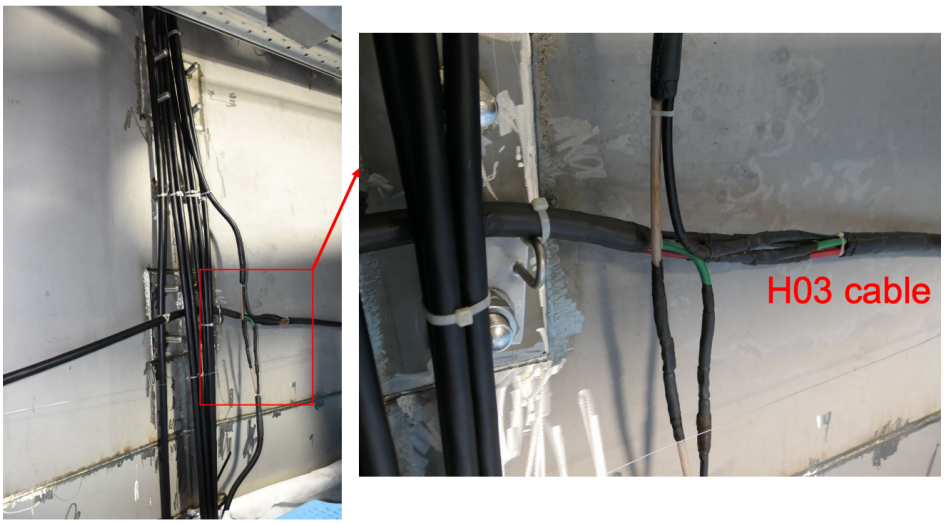


**Figure 2.15:** Picture of a junction where group 1 coils are joined together [62].

### 2.3.3 Data-Taking Periods of Super-Kamiokande

The data obtained from the Super-K detector is sorted into eight phases, with the start of each phase signifying the completion of work performed on the detector hardware. Table 2.3 displays the periods of the phases, their corresponding operating conditions and the reason for switching to a new run period.

In July 2020, the doping of gadolinium compound ($Gd_3(SO_4)_3 \cdot 8H_2O$) into the detector water marked a new era for Super-K. The addition of Gd improves thermal neutron detection from IBD interactions by reducing neutron capture time (from 200 µs to less than 30 µs) and tripling the energy released (from 2.2 MeV to over 8 MeV). The gamma-ray cascade from neutron capture on Gd coincides with the prompt Cherenkov light produced by the positron, enhancing detection efficiency [63]. With 0.03% Gd in the tank, neutron tagging efficiency rises to 75%, up from less than 20% before doping. This boosts sensitivity to IBD interactions, aiding the search for DSNB and SN neutrino bursts, as well as improving T2K results and proton decay sensitivity.

**Table 2.3:** Definition of Super-K data periods and the corresponding operating conditions. The drop in the ID photocoverage seen in SK-II is caused by PMT implosions that happened at the end of SK-I. The broken PMTs were replaced, and acrylic anti-implosion covers were installed on all ID PMTs before SK-III.

| **Phase** | **Dates** | **ID Photocoverage** | **Target** | **Reason for Ending the Current Run** |
|---|---|---|---|---|
| SK-I | 1996 - 2001 | 40% | $H_2O$ | Maintenance |
| SK-II | 2002 - 2005 | 19% | $H_2O$ | Full Tank Refurbishment |
| SK-III | 2006 - 2008 | 40% | $H_2O$ | Electronics Upgrade |
| SK-IV | 2008 - 2018 | 40% | $H_2O$ | Full Tank Refurbishment |
| SK-V | 2019 - 2020 | 40% | $H_2O$ | First Gd Doping |
| SK-VI | 2020 - 2022 | 40% | $H_2O + 0.011\%$Gd [63] | Second Gd Doping |
| SK-VII | 2022 - 2023 | 40% | $H_2O + 0.03\%$Gd | Two Geomagnetic Field Correction Coils Broke |
| SK-VIII | 2023 - Present | 40% | $H_2O + 0.03\%$Gd | - |

### 2.3.4 The Electronics and Data Acquisition System

The Super-K detector employs specialised electronics for reading precise charge and timing data from its PMTs. These electronics are crucial for triggering the detector to

record data during particle interactions based on the number and temporal distribution of PMT hits. The ID and OD PMTs have their high voltage and signal transmissions facilitated through cables that connect the PMTs inside the tank to the equipment on the top of the detector. These cables lead to four electronics huts, each responsible for a quadrant of the detector, housing high voltage supplies and readout electronics for the PMTs. Notably, each ID PMT is supplied with individually adjustable high voltage through CAEN SY527 mainframes, while every 12 OD PMTs receive one high voltage value provided to them via custom 'paddle cards'. Additionally, the OD PMTs utilise combination cables that carry both high voltage and light detection signals.

The Super-K detector has seen two sets of readout electronics in its history, the first set was used during the SK I-III phases and it was later replaced in 2008 before SK-IV started, with a new software trigger implemented. The update aimed for an easier digitisation of the ID and OD PMT recorded charge and signal arrival times, and the new electronics compresses of Charge-to-Time Converter (QTC) Based Electronics with Ethernet (QBEE) modules, where a QTC is a chip that converts the signal into a fixed-width pulse. These QBEEs encode time and total charge in a single pulse, and they offer multiple PMT gain settings and can process signals with varied gains simultaneously, improving the dynamic range and charge resolution compared to the old system.

In every phase of Super-K, computers located within the mine compile digitised charge and time data pairs (hits) into 'events' based on the number of hits within sliding time windows, where the window widths are defined by the triggers. From 2008 onwards, there are six triggers used in the Super-K, namely Super Low Energy (SLE), Low Energy (low-E), High Energy (HE), Super High Energy (SHE), OD and after (AFT) [55]. After being grouped into events, the data is then periodically transmitted from the detector area to off-site computers through optical fibre for further processing and storage. The data is saved in both ZEBRA format [64] and as ROOT [65] files.

### 2.3.5 Detector Calibrations

The following section only mentions the important ID calibrations, while others can be found in Ref. [56]. The details of the OD calibrations are discussed in Chapter 3

and 4.

### Water Parameters

The water parameters are measurements of light absorption and scattering in the Super-K water and are used in the Super-K event simulations. A laser system with five available wavelengths [56] injects light into the ID to provide analysis data. The observed light intensity, $I(\lambda)$, at distance $l$ from the source follows an exponential decay [56]

$$I(\lambda) = I_0 \; e^{-l/L(\lambda)}, \tag{2.5}$$

where $I_0(\lambda)$ is the source intensity and $L(\lambda)$ is the combined attenuation length from scattering and absorption effects, as defined in the Super-K simulation as

$$L(\lambda) = \frac{1}{\alpha_{abs}(\lambda) + \alpha_{sym}(\lambda) + \alpha_{asy}(\lambda)} \tag{2.6}$$

where $\alpha_{abs}(\lambda)$ is the absorption amplitude, $\alpha_{sym}(\lambda)$ and $\alpha_{asy}(\lambda)$ are the symmetric and asymmetric components of the angular distribution of the scattered light. Rayleigh scattering, which occurs when the wavelength of light is much larger than the target particle sizes, and the symmetric element of Mie scattering, which happens when the wavelength and particle size are similar, make up $\alpha_{sym}(\lambda)$; while the forward peak in Mie scattering is accounted for by $\alpha_{asy}(\lambda)$. Figure 2.16 shows the data obtained in SK-IV and overlays the fitted water parameter functions.

### The Calibration of ID PMTs

The calibration of the ID PMTs is approached from two aspects: charge output and response time, with the objective of synchronising the signals captured by all PMTs. This process unfolds in three stages. Initially, the high-voltage supply is fine-tuned via a scintillator ball linked to a xenon lamp. This is followed by the determination of each PMT's relative gain, employing sources of both high and low light intensity. The final step involves computing an average gain value across the entire ID volume, utilising a nickel source. A detailed account of these calibration activities can be found in Ref.

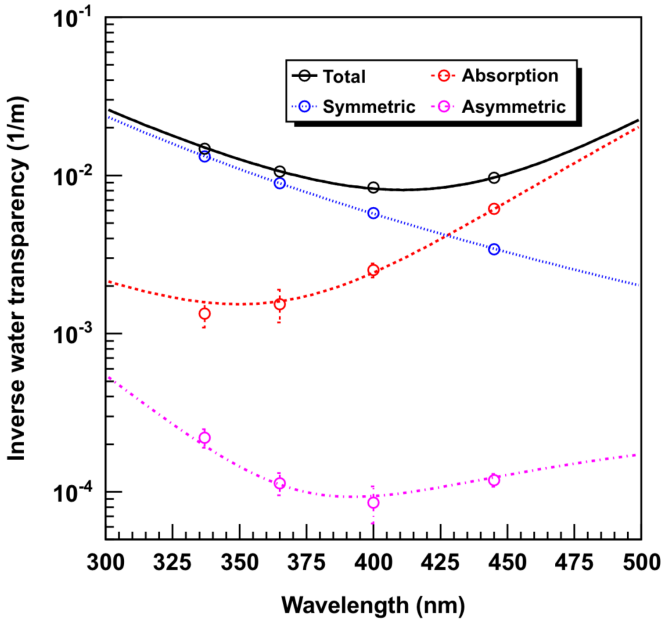


**Figure 2.16:** Water coefficient functions fitted on data obtained in April 2009 [56].

[56].

The timing signal of ID PMTs is influenced by the overall processing time, encompassing the photoelectrons' transit time within each PMT, plus the variations in the length of PMT cables, and the time-walk effect, which refers to the phenomenon where signals of higher charges arrive earlier than those with lower charges. For timing calibration across ID PMTs, a nitrogen laser is linked to a wavelength-shifting dye laser and a light intensity-varying system, which is then connected to a scintillator bulb to provide the necessary light. (This laser setup is also utilised for OD calibration, with its application in the OD detailed in Section 4.4.) By adjusting the laser light intensity, a T-Q distribution, which plots the time-of-flight(ToF)-corrected laser photon signal timing against the recorded charge, is generated for each ID PMT. Figure 2.17 depicts a T-Q distribution for a given PMT. In this plot, higher time values represent earlier reported detections, while lower values indicate later ones. The observed trend, where hits with greater charges are recorded more quickly than those with lesser charges, is known as the 'time-walk' effect. This phenomenon is caused by the property of a PMT, where the rise time of a larger pulse is quicker than that of a smaller one [56].

The timing calibration constant, 'T-Q map', which is unique to each PMT, is derived by fitting a polynomial to this T-Q distribution. More explicitly, a timing

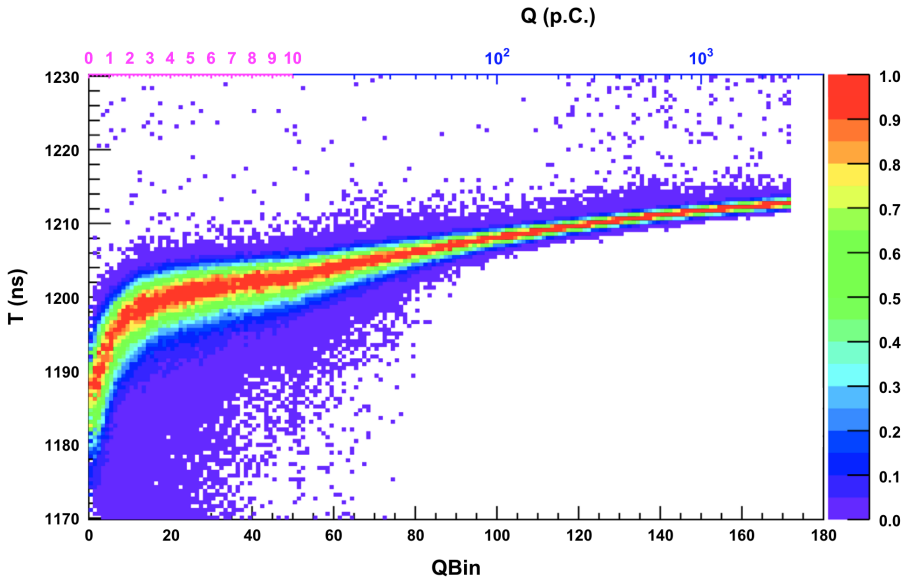


**Figure 2.17:** A typical T-Q distribution for an ID PMT, where the laser-photon-ToF corrected hit times are plotted against the charge of each hit. In this distribution, larger time values correspond to earlier hits and vice versa. The phenomenon of a hit with a large charge being registered faster than a smaller-charged hit, which is observed in the plot, is known as the 'time-walk' effect and is an intrinsic property of a PMT [56].

offset is generated for each given measured charge per PMT.

### 2.3.6 The Super-K Detector Simulation

#### SKDetSim

The detector simulation software for Super-K, SKDetSim, operates on a GEANT3 framework [66] and incorporates the NEUT neutrino interaction model [67]. This software is instrumental in generating official Monte Carlo (MC) simulated datasets used for both physics research and calibration purposes. (Note that the simulated data is sometimes referred to as MC data hereafter.) Additionally, it offers the flexibility to create custom Monte Carlo simulations tailored to specific user needs. SKDetSim is capable of simulating a wide range of scenarios, including neutrino interactions and background events, thereby facilitating comparisons between observed data and theoretical predictions.

The simulation pipeline is structured as follows: depending on the neutrino source of

interest, a flux model is selected. For the atmospheric neutrinos at Super-K, the Honda 3D model [68], which was designed specifically for the site, is predominantly used. while other models such as Honda 1D [69, 70], FLUKA 3D [71] and Gaisser 1D [72] are also consulted. The chosen neutrino flux then feeds into the NEUT event generator, which simulates neutrino interactions within the Super-K tank and outputs information about daughter particles. This output is input into SKDetSim, which simulates particle behaviour within the detector. SKDetSim accommodates simulations for various phases of the detector, from SK-I to SK-V, by incorporating specific simulation libraries and calibration coefficients from diverse calibration sources into the simulation framework.

#### SKG4

The new simulation software SKG4 [73], built upon the latest toolkits for particle trajectory simulations (GEANT4 [74]), was developed specifically for the new Gd-loaded phase of the Super-K experiment, enhancing the geometry reproduction capabilities of its predecessor, SKDetSim. In comparison with SKDetSim, SKG4 sees a 2.6% variance in the number of emitted Cherenkov photons by a 10 MeV/c electron and a 0.2% difference in the reduction ratio due to absorption effects [75]. The implementation of a new model for gamma rays from the Gd(n,$\gamma$) reaction has also been an advancement from the old simulation software, showing results aligning with the theory prediction, which states that neutron capture time and distance from the capture location are shorter in the Gd-enhanced water compared to pure water. Throughout its operation, SKG4 has been fine-tuned using real SK calibration data. With gadolinium now dissolved in the SK water, SKG4 continues to be instrumental in various analyses within the SK-Gd framework.

## 2.4 Hyper-Kamiokande

As one of the most ambitious upcoming projects in particle physics, Hyper-K aims to push the boundaries of precision in measuring neutrino parameters, advancing the frontier of knowledge in this field of research. Situated approximately 8 km south of the existing Super-K detector, it is being constructed near the town of Kamioka,

and 650 m under the peak of Mt. Nijugo (1750 m water equivalent of rock burden). Building upon the legacy of Super-K, it uses the same Cherenkov-ring idea for neutrino physics analyses, and it also takes the shape of a cylinder, but with a diameter of 64.8 m and height of 65.8 m, resulting in four times the total volume of Super-K. The commencement of construction was marked in 2020, and the facility is expected to begin data collection in 2027. All the key milestones of the detector construction are marked in the Gantt chart in Figure 2.18 [76].

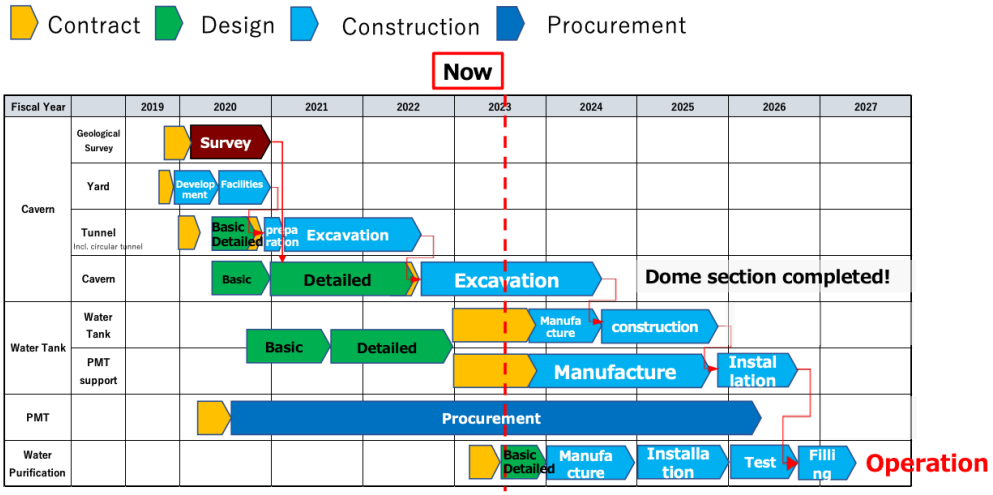


**Figure 2.18:** The construction timeline of Hyper-K [76].

Similar to Super-K, Hyper-K features a principal structure composed of a substantial tank volume, which will be filled with ultra-pure water, situated below, and a dome above, designated for housing experimental equipment. As of 3 October 2023, the excavation work for the dome has been completed (see Figure 2.19), establishing it as one of the largest man-made underground cavities in existence.

### 2.4.1 The Detector Specifications

Using the same method as Super-K (with stainless steel structures and Tyvek sheets), Hyper-K segregates its total detector volume into two optically independent regions, the ID and OD. The gaps between the steel structure and the tank wall on the top and bottom sides are a constant 2 m apart, whereas the gap in the vertical barrel region is merely 1 m, which resulted in an ID volume of 191 kt and OD volume of 26 kt.

**Figure 2.19:** Photo of the completed Hyper-K dome [77].

### The Inner-Detector

The ID of Hyper-K has a baseline design which uses 40% photocoverage with a new model of 20-in (50 cm) PMTs; however, current conservative estimates are set at 20%. These new 20-in PMTs, specifically manufactured for Hyper-K, exhibit significant enhancements over their predecessors used in Super-K. They possess double the sensitivity, improved charge resolution, and enhanced pressure tolerance [47]. A key consideration in the detector design involves the prevention of chain implosions. Each 20-inch ID PMT is fitted with a protective cover during installation to mitigate this.

The mass manufacturing of the 20-in PMTs commenced in December 2020. In April 2022, production was temporarily halted to investigate the defect rate of the delivered PMTs. Following improvements and thorough screening by the manufacturer, production resumed in May 2023. Despite this pause, the schedule for delivery completion remains on track as initially planned. To ensure the highest standards of quality, ongoing inspections of the 20-in PMTs are being conducted regularly at Kamioka. These stringent quality checks are vital for maintaining the integrity and reliability of the experiment.

Additionally, the Hyper-K ID will be equipped with multi-PMT (mPMT) modules, comprising a cluster of 19 3-inch PMTs and the necessary electronics, all housed within a pressure-resistant vessel, as shown by the Computer-Aided Design (CAD) drawing and the photo in Figure 2.20. The inclusion of mPMT modules is poised to enhance the accuracy of Cherenkov ring reconstruction and provide a reliable reference for detector calibration. As of now, the exact number of mPMTs to be installed has not been finalised.

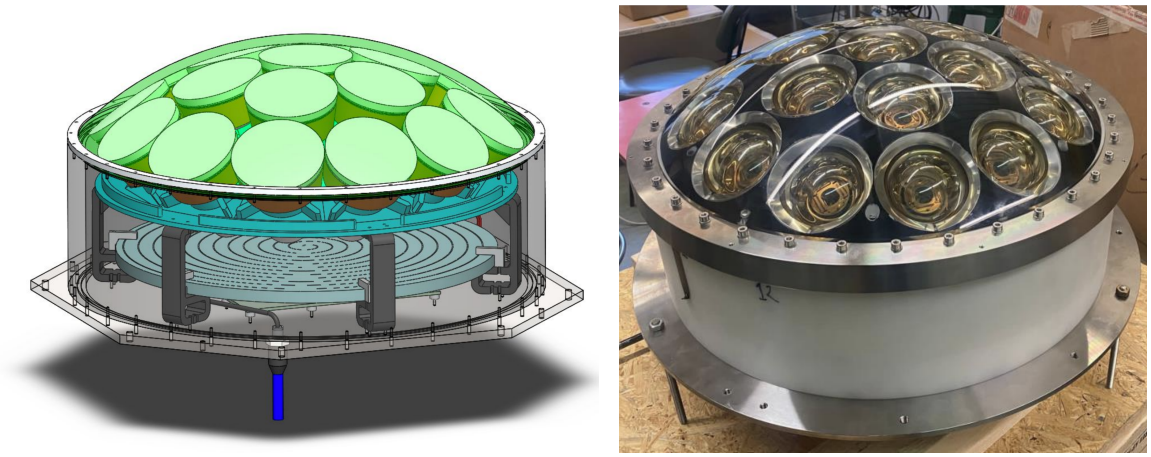

**(a)** **(b)**

**Figure 2.20:** (a) A CAD drawing and (b) a photo of the mPMT module in the Hyper-K ID [47]. Each mPMT module has a diameter of 20 inches and comprises of 19 3-in PMTs.

The detector geometry comprising both 20-in PMTs and mPMTs is known as HybridHK in the following text. The number of each type of PMT used in the analysis presented in the thesis is discussed in Chapter 6.

### The Outer-Detector

In the design of the Hyper-K, OD plays a crucial role in ensuring the background events caused by CR muons and particles of other origins are vetoed effectively. The tried-and-tested method from the construction of Super-K, which combines a small PMT with a WLS plate and lining the walls with highly-reflective Tyvek® to increase the photon-collection efficiency, is also applied to the Hyper-K OD, which uses 3-in (8 cm) PMTs instead of 8-in PMTs in the Super-K OD. The final number of OD PMTs has not yet been decided.

### The Front End Electronic System

In Super-K, each PMT sends its signal through a cable extending at least 70 m to the front-end electronics outside the tank to be processed. This arrangement inherently introduces a time delay in the transmission of the PMT signal and poses an inconvenience in accurately synchronising the reported hit times from PMTs across both the ID and OD. To mitigate this issue, the Hyper-K front-end electronics are designed to be housed in water-tight vessels placed right next to the PMTs whose signals they are assigned to process. Two types of electronic vessels exist: the ID-only type and the hybrid type. As the name suggests, the ID-only vessel connects with ID PMTs only; it has 24 channels, and the signal is read out by two Printed Circuit Boards (PCBs). On the other hand, the hybrid vessels process signals from 20 ID PMTs and 12 OD PMTs together.

The integration of 20-inch PMTs and multi-PMT (mPMT) modules in the ID, in conjunction with the front-end electronics and OD PMTs, is depicted in Figure 2.21 [47].

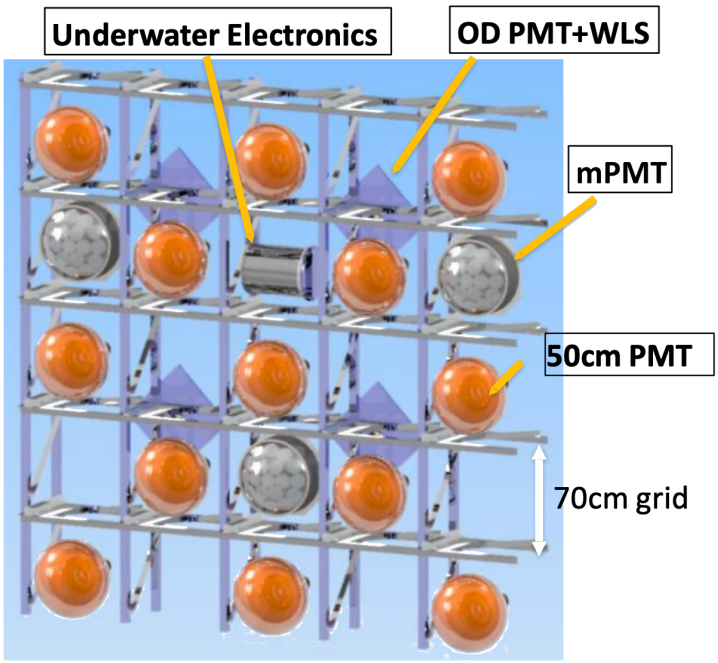


**Figure 2.21:** The installation design for the ID PMTs, front-end electronics and OD PMTs on the steel structure separating the ID and OD [47].

### 2.4.2 The Intermediate Water Cherenkov Detector

As mentioned in Chapter 1, the T2K experiment stands as a beacon of advancement in the field of neutrino physics. Looking forward, there are ambitious plans to integrate Hyper-K as the far detector for a new iteration of the experiment, colloquially known as T2HK. This evolution of T2K aims to leverage Hyper-K's advanced detection capabilities to gain deeper insights into neutrino properties and behaviours.

Complementing the far detector setup, the T2HK project also includes plans for a near detector, similar to the ND280 in T2K, this near detector, named the Intermediate Water Cherenkov Detector (IWCD) [78], will play a pivotal role in monitoring the flux components of the neutrino beam. Unlike ND280, which is located 280 meters from the source, the IWCD is planned to be positioned at a distance of 1-2 km from the neutrino source. The IWCD will have a cylindrical design, relatively small in size, measuring less than 10 meters in both diameter and height.

The choice to use water as the target medium in IWCD is strategic. This decision is driven by the desire to minimise the complication in dealing with systematic errors when fitting oscillation parameters. A water-based detector offers a more straightforward approach to understanding and managing these errors compared to the more complex ND280. By closely mirroring the target material of the far detector, Hyper-K, the IWCD ensures a more consistent and reliable analysis across the experiment. The implementation of IWCD will thus be a significant step in enhancing the precision and effectiveness of the T2HK experiment.

### 2.4.3 Physics Goals

Hyper-K's physics program primarily focuses on two goals: elucidating the nature of neutrino oscillations and searching for rare processes like proton decay.

Through its enhanced detection capabilities, Hyper-K aims to deliver unprecedented statistics across a broad energy spectrum. It is designed to detect solar neutrinos with energies as low as 3.5 MeV and is expected to capture thousands of atmospheric neutrinos in the TeV range [46, 79]. The Hyper-K as a stand-alone water Cherenkov observatory aims to solve the neutrino mass ordering problem with only atmospheric

neutrino data at a significance between 2.2-$\sigma$ and 4.9-$\sigma$ after a ten-year exposure. As a far detector for the next-generation LBL neutrino oscillation experiment in Japan, Hyper-K is designed to achieve 5-$\sigma$ significance at probing $> 55\%$ of the $\delta_{CP}$ phase-space and determine the octant of $\sin^2\theta_{23}$ outside $(0.44, 0.58)$ with 10-year exposure to beam neutrino only [80]. A combined analysis of atmospheric and beam neutrino data can reject the false mass ordering from 3.8-$\sigma$ to 6.2-$\sigma$, with the significance increasing as the true $\sin^2\theta_{23}$ value increases.

Additionally, other ambitions of the Hyper-K include more detailed studies on the solar neutrinos, the observation of SN neutrinos from sources at different distances from the Earth, and the detection of proton decay through its decay channels including $p \to \pi^0 + e^+$. All the goals mentioned above are central to the broader scientific mission of Hyper-K and represent key contributions to our understanding of the fundamental constituents of matter.

## 2.5 Summary

Using ultra-pure water and photomultiplier tubes, a family of water Cherenkov detectors based in the deep mountains of Japan have contributed to a deepened understanding of neutrino properties, from confirming the solar neutrino deficit problem with Kamiokande, observing neutrinos originating from a supernova in Kamiokande-II, to providing proof for neutrino oscillation through the measurement of atmospheric neutrinos using Super-K. These observations were only made possible with sophisticated detector setups and extensive calibration programs, some of which were discussed in this chapter. With the addition of 0.03% Gadolinium in the water, the neutron tagging ability in Super-K has improved drastically, thus increasing the sensitivity to IBD events and furthering the studies of DSNB and SN neutrino burst as well as improving T2K results and the sensitivity to proton decay.

The construction of the next-generation Japanese water Cherenkov detector, Hyper-K, has been underway since the start of the 2020s. A new type of PMT module, multiPMT, has been developed to increase the granularity of the detected signal. The much larger volume compared to Super-K will provide much higher statistics, aiding

the determination of the mass hierarchy and the value of $\delta_{CP}$ within the first decade of Hyper-K's operation among other physics goals.

# Chapter 3

# Outer-Detector PMT Monitoring at Super-Kamiokande

The constant calibrations of the detector are instrumental in ensuring the quality of the raw data. There are two aspects to the calibration activities: one is to understand the detector properties, which include PMT characteristics and light attenuation in the water; the other is to refine fundamental physics properties, such as maintaining high-quality vertex reconstructions and accurate estimates of energy resolution. This Chapter will document two of the essential Outer Detector (OD) property calibrations, namely the PMT charge and timing calibrations, and present the latest monitoring results.

The OD is equipped with six types of PMTs, specifically IMB, IPMU, UCI, KEK, recovery (also known as REC), and *Upgrade* PMTs. The names of the first four PMT types originate from their previous installation sites. Recovery PMTs include all units installed in 2002 and 2006, which replaced those destroyed during the 2001 PMT implosion incident. Note that the KEK PMTs are excluded from the following discussions on PMT constant calibration, as only one remains operational in the tank. The *Upgrade* PMTs, installed during the 2018 Super-K tank-open work, are collectively referred to under the 'All' category in subsequent discussions and are not separately analysed.

## 3.1 OD PMT Charge/Gain Monitoring

As mentioned in Section 2.2.2, a PMT converts the incoming photons into current outputs through layers of dynodes. It is important to have a precise understanding of the relationship between a single photo-electron (s.p.e.) and the PMT current output (typically measured in photo-electrons, hence in units of pCs) since they are essential to the veto power of the Super-K OD. Hereafter, this s.p.e. to current output concept will be referred to as the 'pC2pe ratio', also known as a PMT's gain (though the gain is expressed as the number of electrons). There are two approaches to obtaining the ratios for each OD PMT, either through the 'dark rate method', which exerts minimum disruption to the normal Super-K data-taking, or through analysing laser data, which requires a dedicated one-day data-acquisition campaign. The details of the first aforementioned method will be documented in this section, while the laser-utilising technique will be detailed in the next Chapter. It is reported that the results from the two methods agree within 10% [56]. The pC2pe ratios used in the official data-analysis pipeline are not frequently updated. However, they are monitored daily to ensure their deviations from the current values are within tolerance; see Section 3.1.1 for details. The pC2pe values used for data analysis currently are based on the May 2021 calculations and were updated to the shared server in January 2022 using a version control software, Apache Subversion (SVN) [81].

The dark rate method for calculating the pC2pe ratios relies on the hits recorded by PMTs in a specific time window preceding the event trigger at 0 ns; Figure 2.8 from Section 2.2.2 is an example hit histogram generated from SK-V laser data. The dark hits are mainly due to single-photon detections [56]; thus, by accumulating the dark hits in a histogram for each PMT, an s.p.e. peak can be observed. The pC2pe ratio of each PMT can subsequently be extracted by taking the mean value. Currently, dark hits within 5 µs before the event trigger from 300 subruns are used in the daily pC2pe constant monitoring program.

For all but one type of PMTs in the OD, the s.p.e. peak follows a roughly Gaussian shape (see Figure 3.1a), whereas the dark rates of the IMB PMTs seemingly accumulate to an exponential decay shape (Figure 3.1b). As a result, a Gaussian fit is used to

extract the mean of the s.p.e. histogram for all other types of OD PMTs (the red line in Figure 3.1a), while the arithmetic mean is taken for the IMB's histograms.

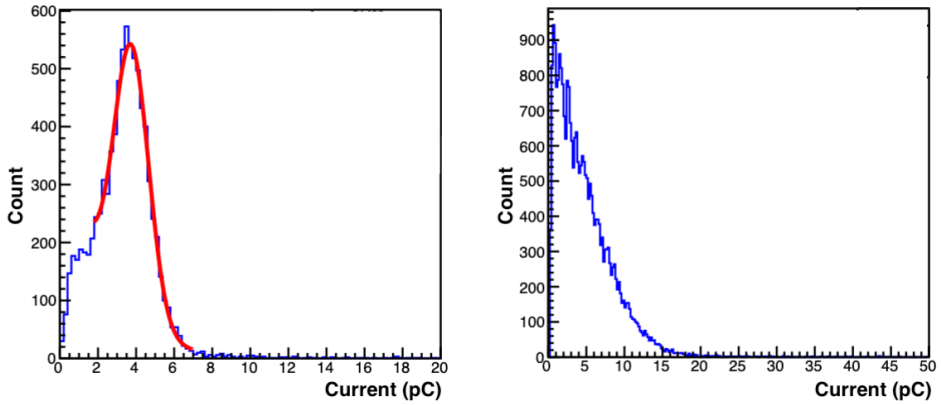


**(a)** IPMU PMT **(b)** IMB PMT

**Figure 3.1:** Typical dark hits accumulated SPE histogram for (a) IPMU PMTs, and (b) IMB PMTs. Most histograms for IMB PMTs do not exhibit a peak structure due to either its intrinsic dynode arrangement or old age. In contrast, all other types of PMTs generally have histograms shaped similar to that shown in (a).

### 3.1.1 Recent Monitoring Results

Figure 3.2 presents three plots that illustrate the evolution of the latest pC2pe ratios compared to those employed in official data analyses. The updates are conducted daily for a duration of 30 days, weekly over a span of 6 months, and monthly from the commencement of SK-V, offering both a detailed perspective and an overview of the overall trend. The error on each data point is the standard error ($\sigma/\sqrt{n}$), but it is too small to be observed. The pC2pe values have been relatively stable, within 3% at most for a given type of PMT, in relation to the official constants. An upward-drifting trend can be observed for IPMU PMTs in particular, which is a known phenomenon, as reported in [82].

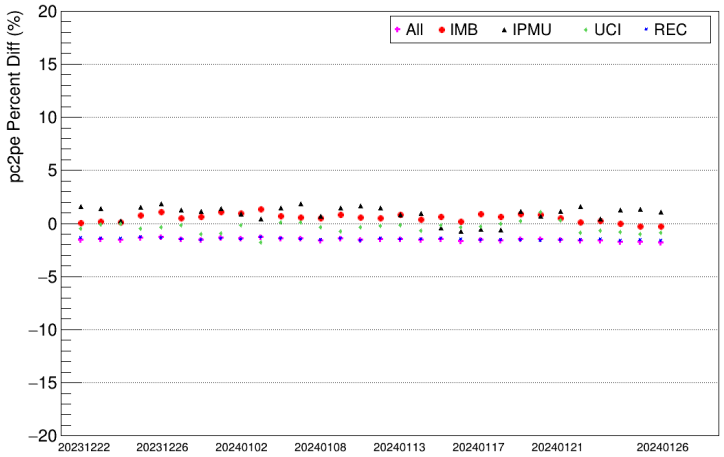


**(a)** Daily

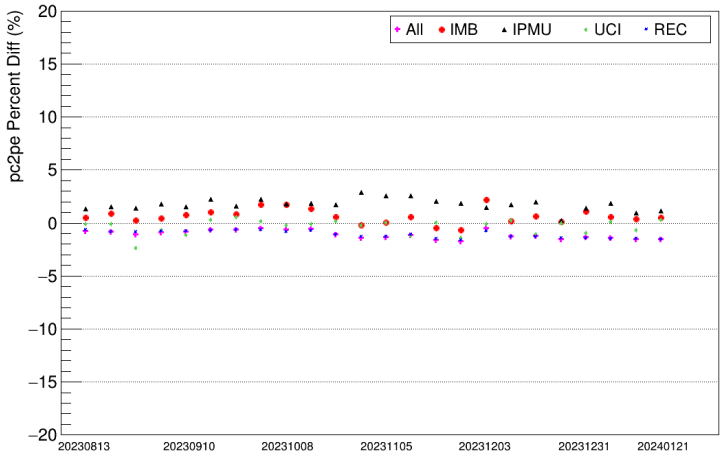


**(b)** Weekly

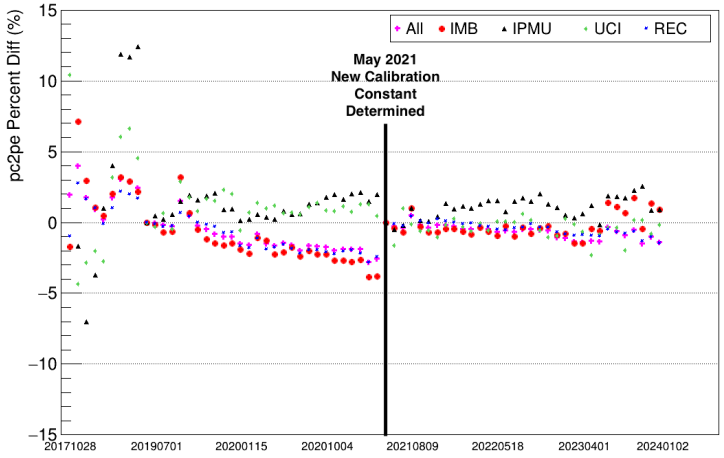


**(c)** Monthly

**Figure 3.2:** Average percentage difference in pc2pe ratio per PMT type between the latest value and the officialised constants used in the reconstruction. The plots are updated (a) daily, (b) weekly on Sundays, and (c) monthly using the first normal run of the month. The standard error on each point is too small to show.

## 3.2 OD PMT Timing Monitoring

In addition to monitoring the gain of each OD PMT, the timing offsets between the OD and ID PMTs are also closely surveilled with the help of cosmic-ray muons. Selection criteria are devised such that only the muons that pass through both the OD and the ID remain after the screening. Then, the muon trajectories (ID entry points and travel directions) are reconstructed using ID PMT hits, providing information to extrapolate the muon tracks back into the OD region, as depicted in Figure 3.3. The OD PMT with the highest charge recorded, closest to the extrapolated muon track, is used in the time offset calculation, where the correction aims to ensure the equation (OD time - ID time - OD timing offset - muon time of flight) remains zero. In applications, the correction is incorporated into the reported OD PMT time. The muon time of flight (ToF) in the above formula is calculated assuming it travels at the speed of light.

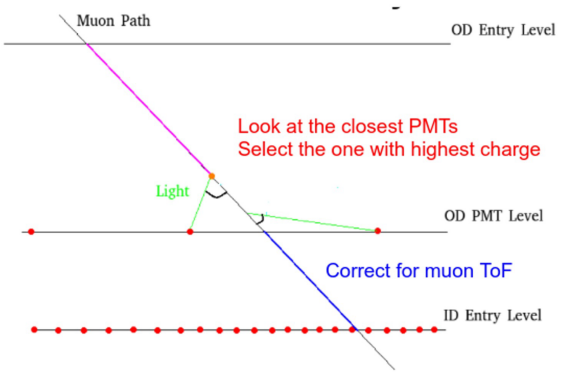


**Figure 3.3:** Example diagram of cosmic-ray muon trajectory through the OD into the ID.

It is also possible to obtain these timing corrections with the OD laser light injection system [56]; however, as mentioned, the laser data taking interrupts normal runs and thus has not been performed since the early 2010s. The latest officially used offset constants use values that were determined in November 2022 and were updated to the SVN main branch in July 2023.

As well as the OD-ID timing corrections, relative timing offsets between OD PMTs also exist due to the difference in cable length. According to [56], 87% of the cables are 70 m long, and the rest are between 71 and 78 m. The size of the OD-ID offsets, usually within 1 ns, are dwarfed in comparison to the time differences introduced by different cable lengths, which are in the order of tens of ns.

### 3.2.1 Recent Monitoring Results

Figure 3.4 shows the timing offset values calculated once per month before May 2023 and once every 6-20 days thereafter. The error bars show the standard error of the mean ($\sigma/\sqrt{n}$) and have only been calculated since May 2023 after the author took over the OD constant monitoring.

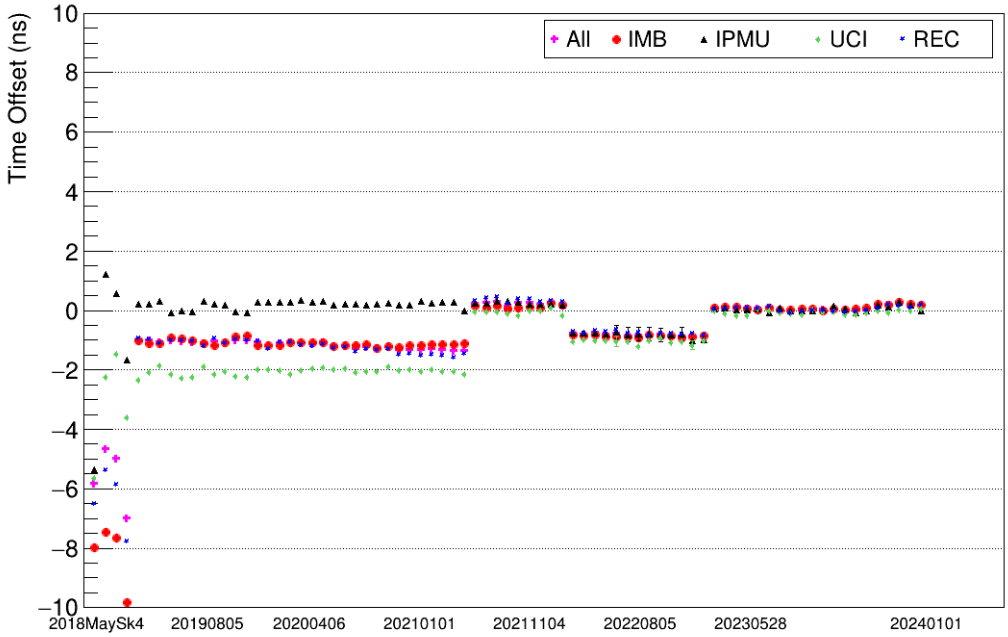


**Figure 3.4:** The second-order PMT relative timing values are monitored monthly before May 2023 and once every 6 to 20 days thereafter. The errors displayed are the standard error ($\sigma/\sqrt{n}$).

Since the adjustment to the timing constant in May 2021, the timing offsets between the ID and OD PMTs have consistently been around 0 ns. This consistency was disrupted in March 2022 due to the ID team implementing a hardware change [83] and updating the ID T-Q map [84] to correct a relative timing issue observed among ID PMTs connected to electronic hut no. 3, subsequently referred to as Hut 3. This Hut 3 issue also impacted a subset of OD PMTs that transmit signals to Hut 3. However, this impact was not detected during standard OD constant monitoring because the OD timing calibration focuses solely on the relative timing offsets between ID and OD

PMTs, thereby negating the Hut 3 effect, i.e.

$$\begin{aligned}\text{OD Timing Constant} = (\text{OD time} + \cancel{\textbf{Hut 3 Effect}}) \\ - (\text{ID time} + \cancel{\textbf{Hut 3 Effect}}) \\ - \text{CR Muon ToF.}\end{aligned} \tag{3.1}$$

However, following the updates committed by the ID team, the timing effect now only exists among Hut 3 OD PMTs, changing the above equation to

$$\text{OD Timing Constant} = (\text{OD time} + \textbf{Hut 3 Effect}) - \text{ID time} - \text{CR Muon ToF}, \tag{3.2}$$

and the effect has manifested as a $-1$ ns shift in Figure 3.4. This shift, although not large enough to significantly affect data analysis, was still addressed in the subsequent timing constant update in November 2022, and the shift has subsequently disappeared.

## 3.3 Impact of the Failed Geomagnetic Coil 1 and 2

On 24 October and 15 November 2023, the geomagnetic compensation coils 2 and 1 failed. The breakdown is anticipated to negatively impact the collection efficiency and the gain of the PMTs. This effect is confirmed with the ID PMTs (shown in Figure 3.5), which reported a 20% drop in average charge collection compared to before the incident.

At the same time, investigations were carried out to explore the impact of the coil failure on the OD PMT gain and timing offset constants. Figure 3.6 shows three ratio plots examining the change in OD PMT gains after the coil failures; they display the ratios of pC2pe values calculated on (dd-mm-yyyy) 26-10-2023 (after Coils 2&1 were both broken), 18-11-2023 compared to 8-8-2023 (only Coil 2 was broken), and 18-11-2023 compared to 12-11-2023 (Coil 1 had just broken after Coil 2), respectively. The plots aim to demonstrate the effect on the PMT gain from the breakdown of Coils 2 and 1. The motivation for using gains obtained on 8-8-2023 as the benchmark is that according to Figure 3.7, the current through Coil 2, monitored through the Slow Control System, has been in steady decline since the end of August. Thus, the unaffected gain calculations have to be sought before then. To supplement the plots,

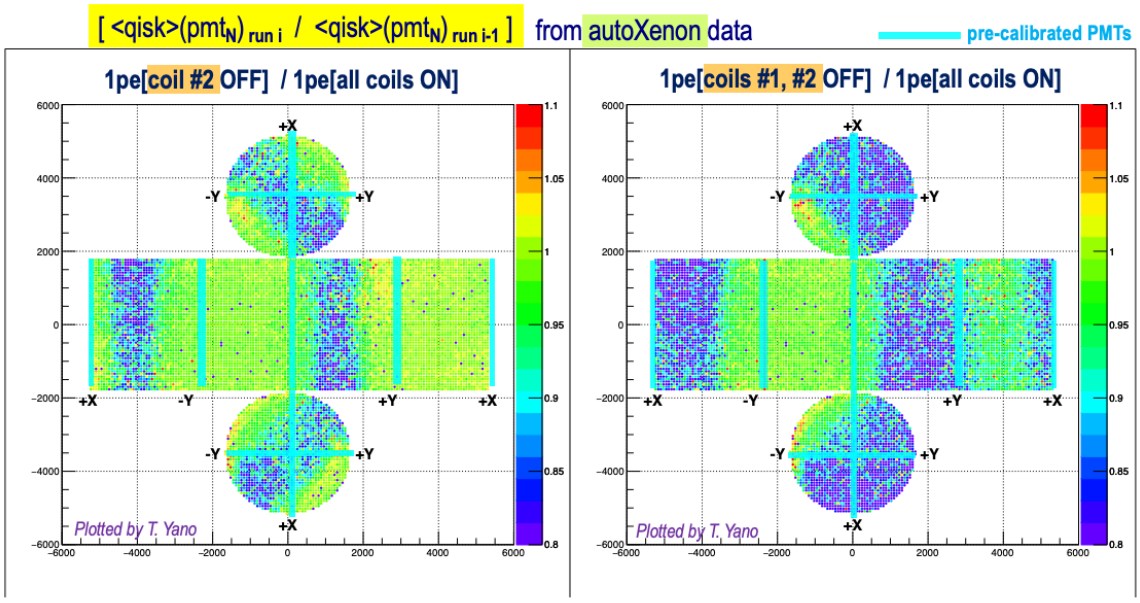


**Figure 3.5:** Ratio of charge collected per ID PMT before and after geomagnetic compensation coil 1&2 failure [85]. A xenon lamp and a scintillator bulb were employed for this calibration. The ID PMTs positioned along the failed coil had recorded observably less charge than before.

Table 3.1 details the average gain for each type of OD PMT before and after Coil 2 and 1 failed and the percentage difference between the values in the three periods.

However, as one can see in the figures and the table, the deficiency of Coil 1 and 2 does not seem to have a sizeable impact on the OD PMT gains. Two of the most affected OD PMT types are IMB and IPMU PMTs. However, the percentage deviation is within the error allowance, and IMB PMTs are at least 30 years old and are known to have large gain fluctuations. The clear pattern seen in the ID PMT charge collection ratio in Figure 3.5 cannot be observed in the same type of plots for the OD. On the other hand, the OD PMTs are much smaller than the ID ones (8-inch compared to 20-inch in diameter). Hence, the photo-electron path deviations caused by the geomagnetic pull inside the OD PMTs may be insignificant in affecting the collection efficiency.

Regarding the timing offset constants of the OD PMTs, the percentage change before and after the failure of Coils 2&1 is significant, as illustrated in Table 3.2. This significance is attributed to the timing offsets' relatively small values ($\mathcal{O}(0.1)$ ns), making any deviation in their values result in a substantial percentage difference. Despite these large percentage changes, the absolute values of the timing offsets still

align within error margins. Additionally, considering that the timing offset attributed to cable length differences is $\mathcal{O}(10)$ ns, the minor relative timing differences between the ID and OD PMTs are deemed negligible.

In conclusion, the breakage of Coil 1&2 does not have a significant effect on the PMT gain and timing in the OD region, compared to that observed in the ID PMTs. This is possibly due to the OD PMTs having smaller volumes, thus being less affected by the Earth's magnetic field. On the other hand, the geomagnetic compensation coil failures had caused considerable havoc in the reported charge and timing of the ID PMTs. If left unaddressed, these effects could manifest bigger issues in low-energy particle reconstructions.

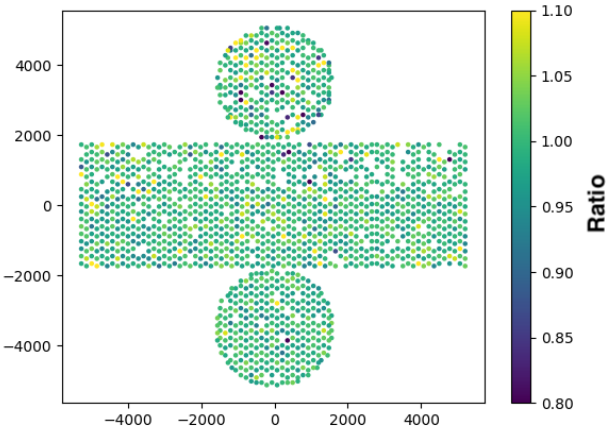


**(a)** 26-10-2023 compared to 8-8-2023 (impact of Coil 2)

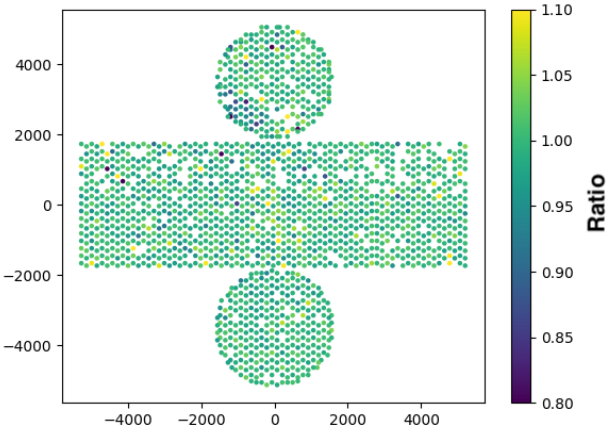


**(b)** 18-11-2023 compared to 12-11-2023 (impact of Coil 1)

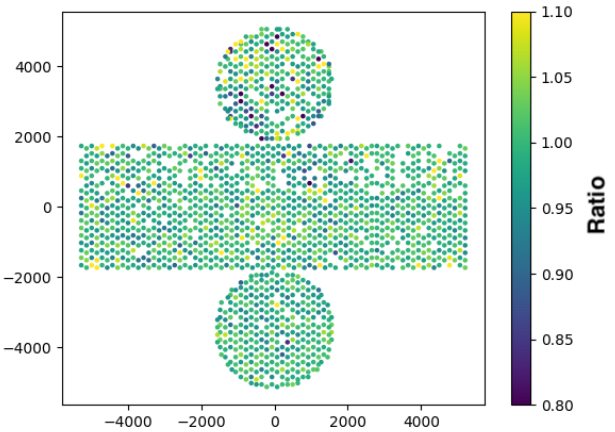


**(c)** 18-11-2023 compared to 8-8-2023 (impact of Coil 1&2)

**Figure 3.6:** Ratios of pC2pe value per OD PMT calculated over three periods (dates shown in dd-mm-yyyy), to assess the significance of the coil failures on the OD PMT charge collection. The plots are outlier-adjusted, where ratios outside the [0.8, 1.1] boundary are assigned the minimum or maximum values.

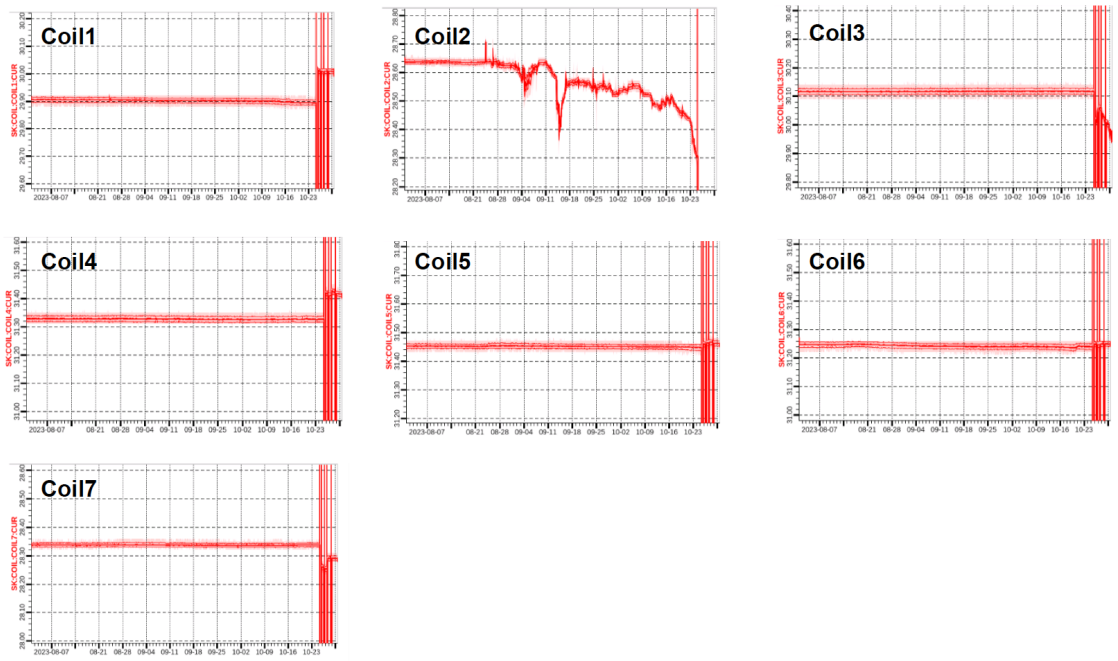


**Figure 3.7:** Current in each geomagnetic-field-correction coil group from 7 August 2023 to 30 October 2023 [86], the graphs were obtained through the Slow Control Monitoring System. The current passing through Coil 2 deviated from a constant value a few months before its eventual failure, indicating a gradual decline in health.

**Table 3.1:** Average pC2pe ratios across OD PMT types and their variance over three periods, with coil health deteriorating in Periods 2 and 3. The errors on the average are standard deviations, while the uncertainties on the percentage differences are standard errors propagated from those on the means. *Since there is only one working KEK PMT in the OD, there is no standard deviation. The data point for the KEK PMT is also omitted in the previous plots.

| | Period 1<br>Before Coil 2 Broke<br>(2-7-2023 - 23-10-2023) | | Period 2<br>After Coil 2 Broke<br>(26-10-2023 - 14-11-2023) | | Percentage Difference (%)<br>(Period 2 to Period 1) |
|---|---|---|---|---|---|
| | Average pC2pe | Good PMT No. | Average pC2pe | Good PMT No. | |
| IMB | $4.82 \pm 0.11$ | $363 \rightarrow 359$ | $4.77 \pm 0.08$ | 359 | $-0.982 \pm 0.005$ |
| KEK* | 0.49 | 1 | 0.53 | 1 | $7.788 \pm 0.184$ |
| IPMU | $2.15 \pm 0.06$ | 94 | $2.17 \pm 0.05$ | 94 | $0.632 \pm 0.004$ |
| UCI | $3.14 \pm 0.08$ | $60 \rightarrow 59$ | $3.14 \pm 0.07$ | 59 | $-0.130 \pm 0.008$ |
| *Upgrade* | $3.19 \pm 0.07$ | 133 | $3.17 \pm 0.06$ | 133 | $-0.831 \pm 0.004$ |
| Recovery | $2.66 \pm 0.04$ | 1208 | $2.65 \pm 0.03$ | 1207 | $-0.469 \pm 0.002$ |

| | Period 3<br>After Coil 2&1 Broke<br>(16-10-2023 - 25-11-2023) | | Percentage Difference (%)<br>(Period 3 to Period 2) | Percentage Difference (%)<br>(Period 3 to Period 1) |
|---|---|---|---|---|
| | Average pC2pe | Good PMT No. | | |
| IMB | $4.75 \pm 0.06$ | 359 | $-0.321 \pm 0.002$ | $-1.302 \pm 0.007$ |
| KEK* | 0.53 | 1 | $-0.413 \pm 0.034$ | $7.351 \pm 0.493$ |
| IPMU | $2.15 \pm 0.06$ | 94 | $-0.886 \pm 0.012$ | $-0.261 \pm 0.003$ |
| UCI | $3.12 \pm 0.07$ | 59 | $-0.525 \pm 0.005$ | $-0.663 \pm 0.006$ |
| *Upgrade* | $3.14 \pm 0.06$ | 133 | $-0.734 \pm 0.006$ | $-1.548 \pm 0.012$ |
| Recovery | $2.64 \pm 0.03$ | 1207 | $-0.331 \pm 0.002$ | $-0.799 \pm 0.004$ |

**Table 3.2:** Average timing offsets across OD PMT types and their variance over three periods, with coil health deteriorating in Periods 2 and 3. The errors on the average are standard deviations, while the uncertainties on the percentage differences are standard errors propagated from those on the means. The incredibly large percentage differences are due to having fewer available timing offset constants as it requires roughly 6-8 days of data to calculate one data point, which resulted in Periods 2 and 3 only containing two data points each. *No data is available for KEK PMTs.

| | Period 1<br>Before Coil 2 Broke<br>(2 Jul - 23 Oct) | | Period 2<br>After Coil 2 Broke<br>(26 Oct - 14 Nov) | | Percentage Difference (%)<br>(Period 2 to Period 1) |
|---|---|---|---|---|---|
| | Average Timing Offset (ns) | Good PMT No. | Average Timing Offset | Good PMT No. | |
| IMB | $0.01 \pm 0.36$ | $363 \rightarrow 359$ | $0.21 \pm 0.27$ | 359 | $1328.29 \pm 9583.08$ |
| KEK* | Nan | 1 | Nan | 1 | N/A |
| IPMU | $0.01 \pm 0.28$ | 94 | $0.12 \pm 0.18$ | 94 | $804.47 \pm 5221.28$ |
| UCI | $-0.07 \pm 0.38$ | $60 \rightarrow 59$ | $-0.03 \pm 0.30$ | 59 | $-56.31 \pm 412.32$ |
| *Upgrade* | $0.08 \pm 0.66$ | 133 | $0.15 \pm 0.57$ | 133 | $80.80 \pm 278.36$ |
| Recovery | $-0.02 \pm 1.17$ | 1208 | $0.11 \pm 0.73$ | 1207 | $-560.07 \pm 8476.58$ |

| | Period 3<br>After Coil 2&1 Broke<br>(16 Oct - 25 Nov) | | Percentage Difference (%)<br>(Period 3 to Period 2) | Percentage Difference (%)<br>(Period 3 to Period 1) |
|---|---|---|---|---|
| | Average Timing Offset (ns) | Good PMT No. | | |
| IMB | $0.23 \pm 0.24$ | 359 | $9.86 \pm 11.62$ | $1469.11 \pm 10569.24$ |
| KEK* | Nan | 1 | N/A | N/A |
| IPMU | $0.23 \pm 0.19$ | 94 | $95.02 \pm 116.32$ | $1663.94 \pm 10697.23$ |
| UCI | $0.004 \pm 0.28$ | 59 | $-113.09 \pm 5742.49$ | $-105.72 \pm 5317.44$ |
| *Upgrade* | $0.29 \pm 0.45$ | 133 | $91.33 \pm 257.95$ | $245.91 \pm 614.40$ |
| Recovery | $0.13 \pm 0.68$ | 1207 | $18.43 \pm 111.73$ | $-644.86 \pm -9578.99$ |

# Chapter 4

# Laser Calibration System for the Super-Kamiokande Outer-Detector

## 4.1 Introduction

The current laser hardware equipped for Super-K ID and OD calibration has over 20 years of history, dating back to before 2000.

At the earlier times of the Super-K experiment (around 2000), this laser system had two purposes, both relating to the calibration of timing information of the OD PMTs [87]:

- To ensure all PMTs are synchronised, a list of relative timing corrections is measured using the laser system. The light output from the laser shines into the OD through 52 fibre ends situated evenly on the tank walls (see discussion later in this chapter). The timing offset for each PMT is determined according to the calculated photon travel time and the PMT's response time to that calibration pulse; and
- To generate a 'T-Q map' for each OD PMT, using the same methodology as ID PMT 'T-Q maps'.

However, the usage of the laser has since evolved. The OD PMT timing calibration function of the laser system mentioned above has since been replaced by using CR muons, and the timings are calculated in relation to ID PMT timing. The 'T-Q map' is no longer generated for OD PMTs. Currently, the laser system is employed in the following two ways:

- To generate the new saturation parameters of each OD PMT for simulation purposes. The saturation parameter is checked once every data period. The SKDetSim is updated with the latest saturation parameters each time the hardware has been altered in the Super-K tank. The last update was implemented after the 2018 tank-open work, although there have been two Gadolinium loading campaigns since. However, as the laser intensity declined dramatically from 2020 onwards (see Section 4.5), the saturation parameters have not been updated for SK-VII.
- To aid the health check for OD calibration fibres without requiring tank-open work.

This chapter will start by introducing some essential concepts of lasers, which will be helpful in later discussions. Then, the rest of the sections aim to summarise the current laser system, preserve the knowledge shared by previous collaborators, and document the latest status of the laser system as of October 2023.

## 4.2 Laser Basics

Since their creation, lasers — short for Light Amplification by Stimulated Emission of Radiation — have evolved with diverse physical properties and operational parameters to address various needs across multiple fields. At the core of laser light production is the process of stimulated emission. This process occurs when an excited electron or molecule releases energy as it transitions to a lower energy state upon interacting with an incoming photon of a specific frequency. The energy emitted is in the form of an electromagnetic wave, which mirrors the incoming photon in frequency, polarisation, and direction of travel.

Lasers can be categorised in terms of the light-emitting materials employed, i.e. there are gas, liquid or solid-state lasers; alternatively, they can be characterised by the wavelength of the photons produced, visible lasers (380-700 nm) and UV lasers (100-400 nm) for instance [88]. In addition, the output light beam properties, such as continuous wave (CW), pulsed, or modulated, can also be used to categorise lasers [89]. Since the application in the Super-K OD only involves a pulsed Nitrogen ($N_2$) laser and a dye laser, only the aforementioned concepts will be discussed in detail.

### 4.2.1 Lasers

A laser generates light through stimulated emission. It generally consists of three components: a gain/active medium, a mechanism to energise the medium and an optical feedback system, as indicated in Figure 4.1. An active medium is defined by its ability to achieve population inversion while not in thermal equilibrium, where population inversion refers to the scenario when the number of electrons in an excited state is greater than that in the ground state.

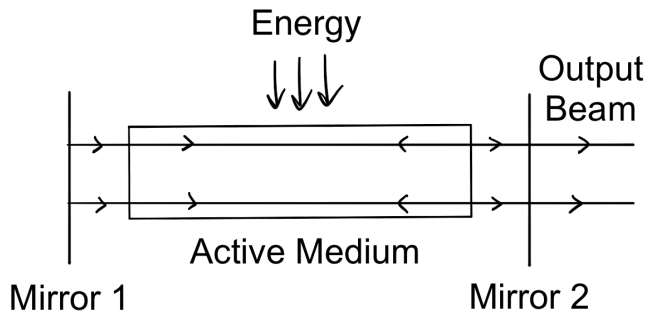


**Figure 4.1:** An example of a lasing unit consisting of two mirrors and an active medium sandwiched in between. The energy is supplied to the active medium first to create a population inversion, and then the de-excitations of electrons within the material release monochromatic light. The mirrors then reflect the plane electromagnetic wave, which is amplified each time it passes through the active medium. One of the mirrors is chosen to be partially transparent, allowing an output laser beam to be extracted.

The technique employed to excite an active medium from its ground state to achieve population inversion is known as pumping. The pumping process can be accomplished through optical or electrical means. More specifically, optical pumping involves the usage of a powerful, incoherent lamp or a laser beam, while electrical pumping exploits the current that flows through the gain medium [90]. Due to the narrow absorption bands of gaseous active media, the optical pumping method is usually avoided because of the inefficiency of converting the input light to an excited gain medium [91]. Therefore, gas lasers are normally pumped electrically by passing a large current through the gaseous media. The current can be continuous, at radio frequency, or pulsed, where the first two correspond to DC and AC currents at radio frequency, respectively.

The optical feedback system typically consists of two mirrors: one with high re-

flectivity and the other partially reflective, enabling a portion of the light to exit as the laser's output. This arrangement sustains the light's intensity by establishing a continuous oscillation of emitted light between the mirrors. This oscillation facilitates the constant excitation of the active medium, ensuring a stable and consistent light intensity.

### 4.2.2 Nitrogen Lasers

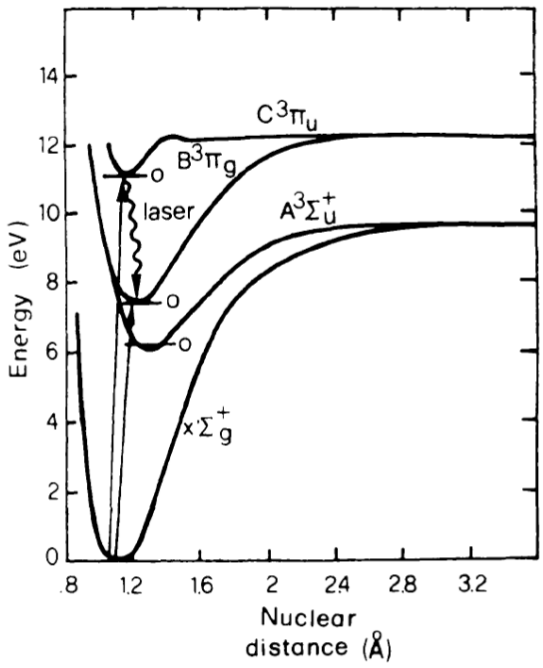


**Figure 4.2:** The relevant energy levels of an $N_2$ molecule; only the lowest vibrational state for each level is shown for simplicity [92]. It illustrates the ground state $x'\Sigma_g^+$, and the excited states $A^3\Sigma_u^+$, $B^3\Pi_g$, and $C^3\Pi_u$. The letters denote the electronic states in order of increasing energy, the Greek letters describe the symmetry properties of the molecular orbitals, the super-/subscripts indicate symmetry upon inversion, and the numbers before the states indicate spin multiplicity.

$N_2$ lasers are a subset of molecular gas lasers that achieve monochromatic light emission by transitioning between molecular energy levels. Moreover, $N_2$ lasers are an example of vibronic lasers, which utilise the vibration levels within different excitation states of gas molecules [93]. Most lasers with this light-emitting mechanism have radiation in the UV region. For an $N_2$ laser, its most prominent emission is at $\lambda = 337.1$ nm.

Figure 4.2 displays the relevant $N_2$ molecule excitation states and the lowest vibrational energy level within. The ground state of the $N_2$ molecule $x'\Sigma_g^+$ is excited to the $C^3\Pi_u$ state ($C$ state) through collision with an electron from the pumping current. The transition from $C$ state to $B^3\Pi_g$ state ($B$ state) results in the 337.1 nm radiation emission (marked by 'laser' in Figure 4.2). Here, the letters (x, A, B, C) correspond to electronic states in ascending energy order, the Greek letters indicate the symmetry properties of molecular orbitals, the super-/subscripts signal symmetry upon inversion of the wave

function, and the numbers preceding the states specify spin multiplicity.

Interestingly, $N_2$ lasers can only be driven by a pulsed current as the lifetime of the two transition states, 40 ns for $C$ state and 10 µs for $B$ state, do not satisfy the inequality [94]

$$\tau_1 < \tau_{21} \tag{4.1}$$

where $\tau_1$ and $\tau_{21}$ are the lifetimes of the lower laser level and the higher to lower level transition, respectively. The inequality ensures that the lower laser level depopulates quickly relative to the rate at which the upper level feeds it, maintaining a population inversion.

Due to the pressure of the gaseous active medium (on the order of one bar) and the presence of a strong electric field (tens of $\mathrm{kV\,cm^{-1}}$), $N_2$ lasers commonly employ a setup called Transversely Excited at Atmospheric pressure (TEA). This configuration, illustrated in Figure 4.3 below, was originally designed for $CO_2$ lasers but can also be used for Nitrogen laser constructions.

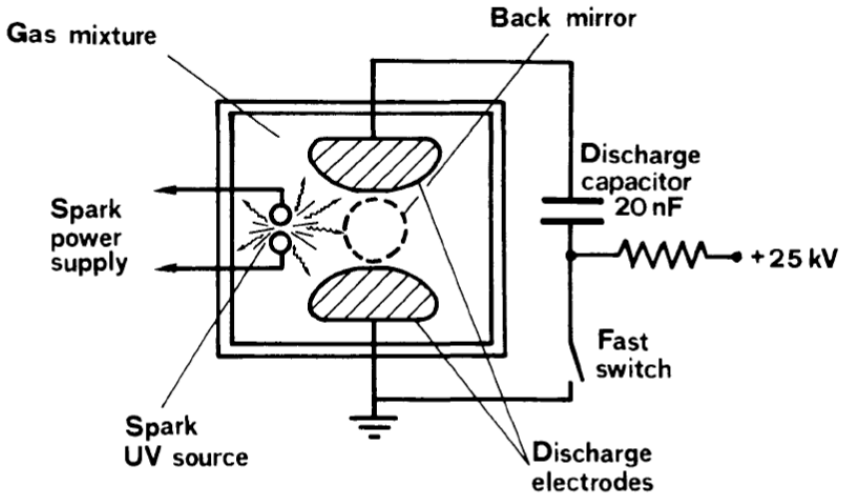


**Figure 4.3:** The schematic diagram showing the setup of a $CO_2$ TEA laser. Nitrogen lasers usually exploit the same configuration [91].

### 4.2.3 Dye Lasers

Dye lasers utilise different solutions as the gain medium, with each solution comprising an organic dye dissolved in a liquid solvent. The liquid solvent can include water,

alcohol (such as the methyl or ethyl groups), and others [95]. There are three classes of dye solutions, classified according to their emission wavelengths. The one employed in the Super-K OD belongs to the Coumarin class, with the wavelength in the blue-green region, i.e. 400-500 nm.

Many dyes that emit visible light are sensitive to light in the UV range, which makes the Nitrogen laser a good candidate for pumping dye lasers. This falls under the category of optical pumping with pulsed lasers. One drawback of utilising UV light for driving the dye lasers is the lower conversion efficiency ($\sim$10%) compared to visible pump lasers, which can achieve an efficiency of 30-40%.

### 4.2.4 Pulsed Lasers

Lasers that emit light in periodic pulses (pulse trains) are known as pulsed lasers. As mentioned above, there are various ways to achieve optical pulses. Nonetheless, the notations used to describe the properties of the pulsed lasers remain the same.

The shape of laser pulses comes in a spectrum between rounded peaks (as shown in Figure 4.4), and rectangular peaks, although in reality, perfect Heaviside square waves can never be achieved. For a typical laser pulse, its power increases slowly at the beginning before quickly climbing to the peak, then drops off in such a manner that leaves the pulse shape roughly symmetric [96]. A pulse can also take a more nuanced form, with the addition of a short pre-pulse and/or a long tail trailing after the main peak. The two features are both illustrated by dashed lines in Figure 4.4.

Two characteristic parameters of a laser pulse, the *rise* and *fall* times, are determined by the time it takes for the pulse to rise or fall between 10% to 90% of the peak power. Another well-used parameter for pulsed lasers, *pulse width*, which measures the duration of the pulse, is defined as Full Width at Half Maximum (FWHM). It is the period when the pulse power is above 50% of the peak power, which is generally on the order of ns to ps for pulsed lasers. Although for most lasers, the maximum power is only reached briefly per pulsing period, for the vast majority of the applications, it is safe to assume that a laser transmits at peak power for the duration of FWHM. As a result, the calculation of the pulse energy/peak energy is markedly simplified. With the above assumption, one can avoid the need for calculus and simply write the *pulse*

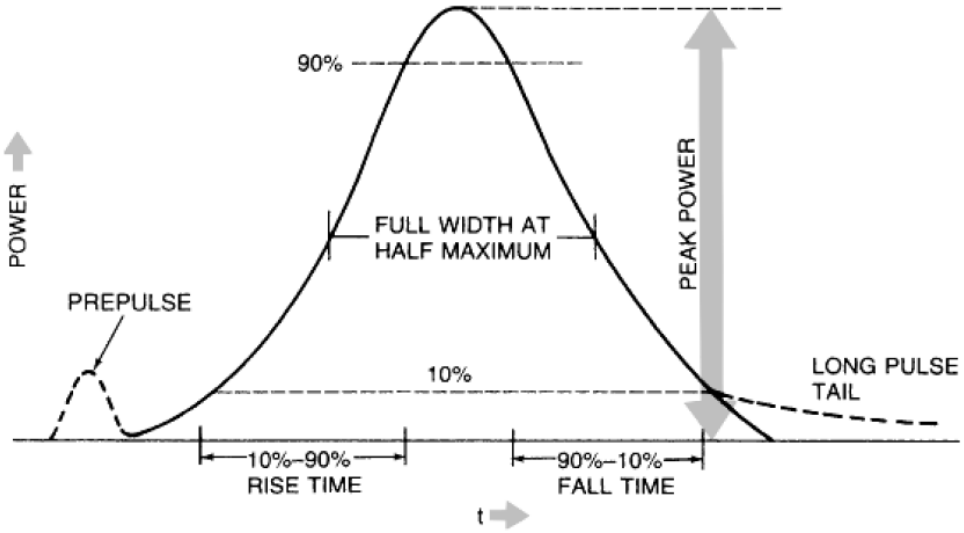


**Figure 4.4:** A typical laser pulse with a pre-pulse and a pulse tail. The pulse power rises and falls as a function of time [96].

*energy*, $E$, as

$$E = P \times \tau_{\text{FWHM}} \tag{4.2}$$

where $P$ is peak power and $\tau_{\text{FWHM}}$ is pulse width. Equation 4.2 can also be rearranged to obtain the peak power of a laser provided that pulse energy is known.

One other useful quantity is the *repetition rate*, which represents the number of pulses per second and is measured in hertz. Figure 4.5 is a diagram of a generic pulse train with pulse width $\tau_{\text{FWHM}}$ and pulsing period $\tau_0$, which is the reciprocal of the repetition rate. Knowing the period of a laser allows the computation of another quantity, the average power, $P_{\text{ave}}$; in contrast to the peak power, it measures the amount of energy discharged during a pulse cycle. One can calculate the average power with

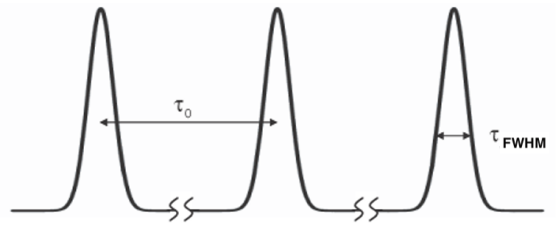


**Figure 4.5:** A diagram displaying pulse period, $\tau_0$ and pulse width, $\tau_{\text{FWHM}}$ in a pulse train [89].

$$P_{ave} = \frac{E}{\tau_0}, \tag{4.3}$$

in case the pulses are uniformly spaced and with the same energy, it can also be

expressed as

$$P_{ave} = E \times \text{repetition rate.} \tag{4.4}$$

### 4.2.5 External Trigger Signal

In the realm of laser physics, a trigger is essentially a signal or event that initiates the laser's light-emission process. Lasers can be activated either internally, through built-in control circuits, or externally, via sources like TTL (Transistor-Transistor Logic) pulse generators and microcontrollers. External triggering offers the advantage of synchronising the laser with other instruments for precise, timed measurements and experiments.

Among various logic families used in electronics, TTL stands out for its historical significance and widespread adoption in academic research since the 1960s. TTL circuits, known for their use of transistors as electronic switches, facilitate the construction of logic gates like NAND, NOR, and NOT. Operating typically at 5V, TTL divides its voltage into LOW (close to 0V, or logic 0) and HIGH (2-5V, or logic 1) signal outputs. In laser applications, TTL signals often regulate the laser's modulation or intensity, highlighting its versatility and importance in precise experimental setups.

### 4.2.6 Signal Loss/Gain Representation

In the field of microwave engineering, the ratio of two power levels, $P_1$ and $P_2$, before and after a signal attenuator or amplifier is commonly represented in the unit of decibel (dB) [97]

$$10 \log \frac{P_2}{P_1} \text{ dB}, \tag{4.5}$$

where a positive value indicates power gained, and vice versa. For instance, a power loss of 10-fold, i.e. a ratio of 0.1, is equivalent to $-10$ dB; whereas a power gain of two folds can be written as roughly $+3$ dB. This greatly simplifies the expression of the effective loss/gain especially after the signal travels through a series of equipment designed to suppress or boost its power. A signal passing through a system with a 5 dB attenuator followed by a piece of equipment that causes 3 dB of loss will thus have a compounded loss of $|-5-3| = 8$ dB.

In the last section of this chapter, the loss of photons incurred by the inefficiency

of various pieces of equipment transmitting the laser light is also quantified in units of dB, since the number of photons per pulse is correlated with output power. More explicitly, the number of photons after going through an experimental apparatus, $N_2$, is related to the number before, $N_1$, through

$$N_2 = N_1 \times 10^{-\text{loss}/10}, \tag{4.6}$$

where loss has units of dB.

## 4.3 OD Light Injector Hardware

### 4.3.1 The OD Lasers

The laser system used in the OD consists of a $N_2$ pulsed laser and a dye laser, both produced by Laser Science, Inc. (LSI) in the late 1990s.

The $N_2$ laser, VSL-337ND-S, emits pulses with a wavelength of 337 nm, it has a pulse width of 4 ns and peak energy of 300 µJ. The laser can pulse at a frequency between 1 to 30 Hz; at 20 Hz, the peak power is 75 kW, and the average power is 6 mW, as quoted on the manufacturer specification table below (Table 4.1). The $N_2$ laser can both accept and export TTL signals for triggering or syncing with external instruments. Figure 4.6 displays the internal structure of a VSL-337ND laser. It is important to note that while this model number differs from the one described above, both versions possess very similar internal configurations.

The collimated beam produced by the $N_2$ laser is fed into a dye laser, DLM-220. Although no description of the DLM series could be found anywhere, the second column of Table 4.1 contains the specifications of LSI dye laser models that are thought to have similar characteristics to DLM-220.

The dye loaded in the LSI DLM-220 dye laser is known as the Exalite 384 [87], which shifts the $N_2$ laser output from 337 nm to around 384 nm.

The organic compound named Exalite 384 dye has 38 carbon and 42 hydrogen molecules, more details can be found in Ref. [99]. The compound appears as a white crystalline solid on its own[99].

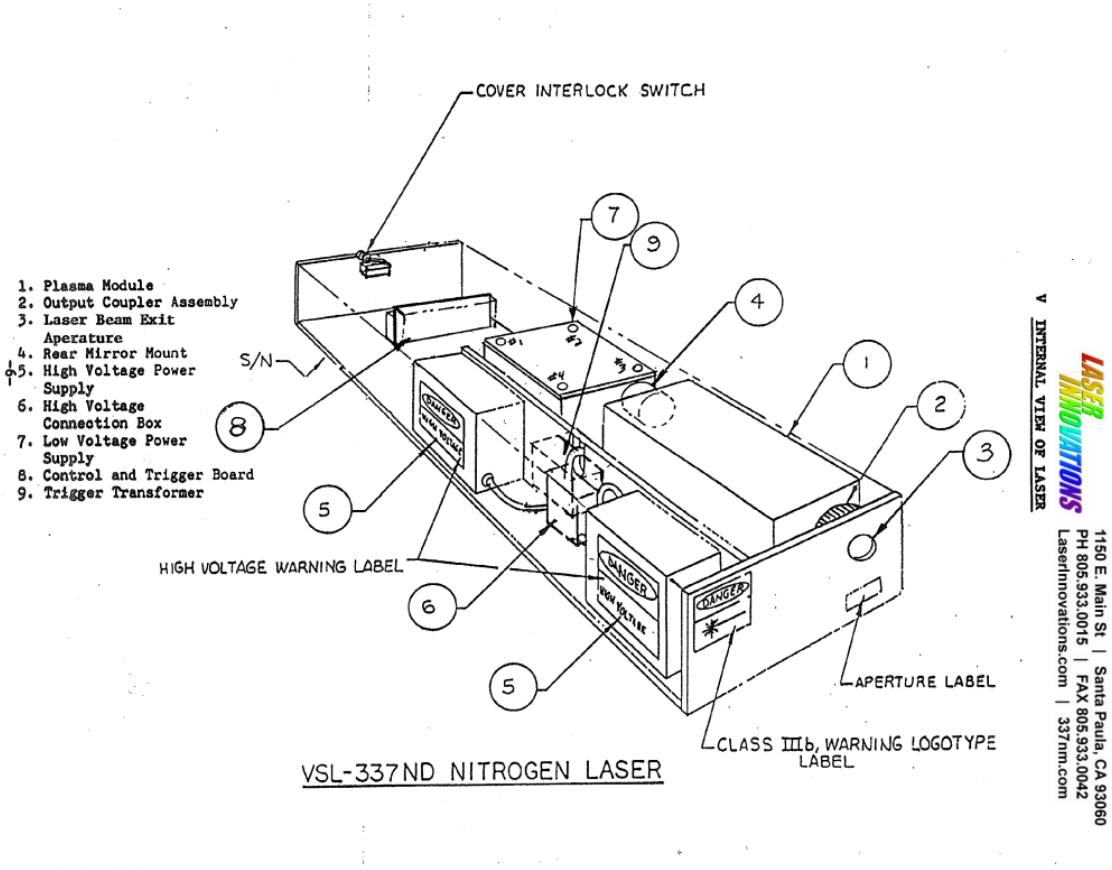


**Figure 4.6:** The internal structure of a LSI VSL-337ND $N_2$ laser [98].

**Table 4.1:** Specifications of the VSL-337ND-S $N_2$ laser and DUO-220 dye laser by LSI [98].

| Specifications | VSL-337ND-S | DUO-220 |
|---|---|---|
| Type | $N_2$ Laser | Dye Laser |
| Wavelength (nm) | 337.1 | Variable between 360 - 700 |
| Spectral Bandwidth (nm) | 0.1 | 0.3 |
| Repetition Rate (Hz) | 1 - 30 | 1- 30 |
| Pulse Width FWHM (ns) | 4 | 3 |
| Pulse Energy (µJ) | 300 | Depending on the Dye Used |
| Peak Power (kW) | 75 | Depending on the Dye Used |
| Beam Area ($mm^2$) | 35 | $2 \times 3$ |
| Beam Divergence (mrad) | 0.3 | 4 |

To pump the dye with a Nitrogen laser, the manufacturer suggests using p-dioxane as the solvent. The light emitted from a dye laser equipped with Exalite 384 dissolved in p-dioxane is reported to have peak output intensity at 382 nm, and bandwidth (FWHM) of 6 nm (1.6%) [100]. A distributor website claims that the efficiencies of the dye, dissolved in p-dioxane, pumped by high-energy or high-repetition-rate pulsed laser at 355 nm are 15% and 14% respectively [101].

Figure 4.7 displays the absorption and emission curves of the dye in various alcohol solvents [102]. No accurate plots of the absorption and emission spectra of the Exalite 384 suspended in p-dioxane can be found online. Since there is no documentation of the solvent used for the dye currently sitting in the Super-K DLM-220 module, it is difficult to conclude if the curves depicted in Figure 4.7 are close to the actual spectra.

As part of the measurement campaign conducted in July 2023 (more details in Section 4.7), the output wavelength of the dye laser is evaluated with a Panasonic computer that runs Windows 98, and an Ocean Optics USB2000 spectrometer. The spectrometer measures light intensity as a function of wavelength, with data-taking intervals spaced evenly between 340 nm and 800 nm. The measurement was repeated 41 times with varying laser repetition rates controlled by the LSI $N_2$ laser's internal triggering system. In addition, one extra set of data was taken to record the background intensity level without any laser light. Figure 4.8 is an overlay of the 41 measurement results

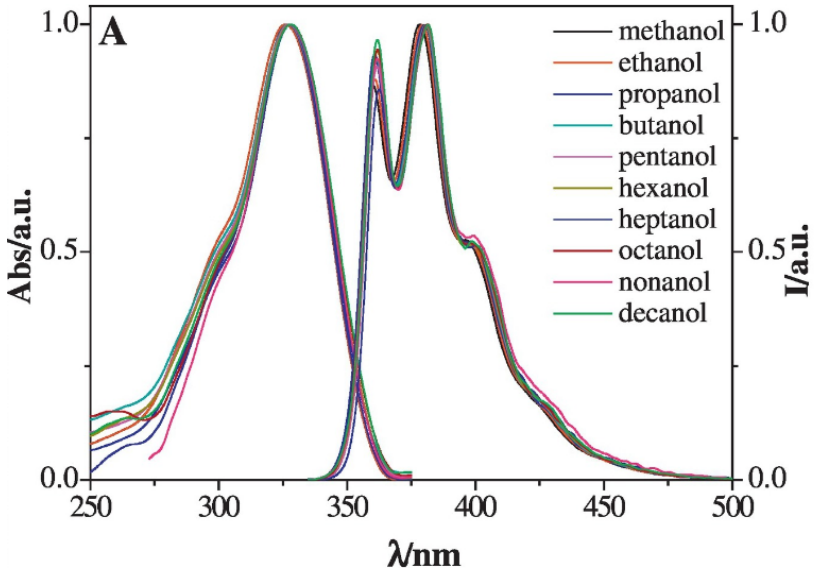


**Figure 4.7:** The absorption and emission spectra of Exalite 384 in different solvents [102].

each with background-level intensity subtracted. The average wavelength outputted from the LSI dye laser is calculated to be $394.04 \pm 0.14$ nm.

One should note that due to the age of the spectrometer (∼25 years), a few nanometers of intrinsic error should be expected. Unfortunately, it is difficult to calibrate the spectrometer, hence the exact wavelength of the measured light source is difficult to estimate. Additionally, one may notice that previous literature from the early 2000s mentioned that the dye laser output was set to 384 nm, which is inconsistent with the current measurement result. No records have been found for the dye laser wavelength readjustment.

### 4.3.2 The System Between the Laser and the Tank

The components, which the laser light goes through before being injected into the Super-K ID and OD, are arranged in the following manner, as indicated in Figure 4.9a. Figure 4.9b is a photo of the inside of the cabinet which houses the OD lasers and the rest of the light injection system. The front side of the LSI laser unit used in the OD and the controls of the LSI $N_2$ laser can be seen in Figure 4.10. Additionally, Figure 4.11 contains a panel of four photos of the system viewed from different angles, two of which were taken during the September 2022 SK-IV OD laser calibration campaign,

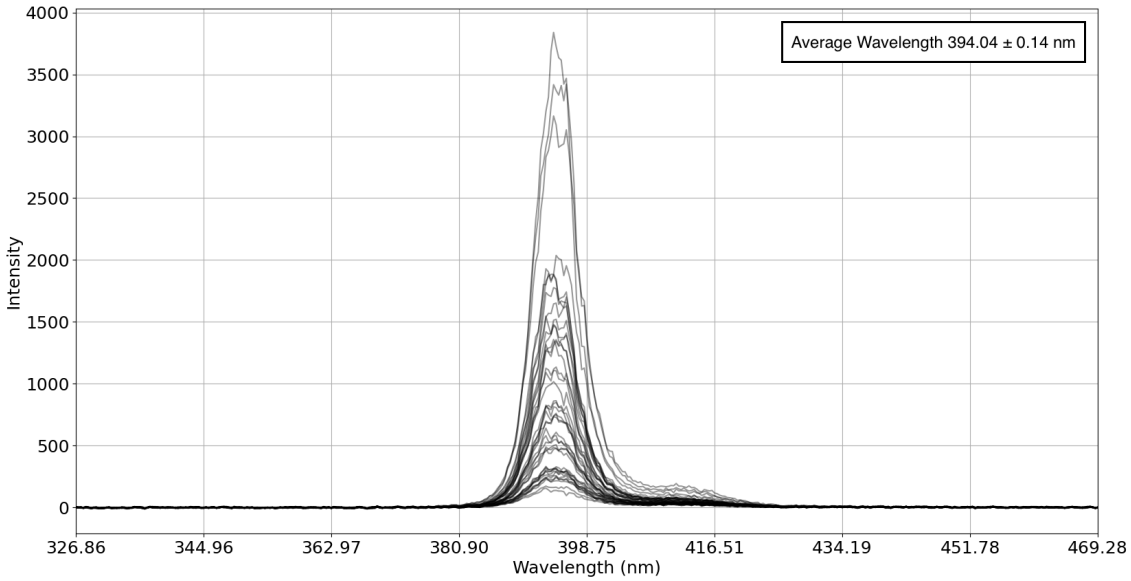


**Figure 4.8:** Background-subtracted LSI dye laser output wavelength measurement results. Each line represents a set of data taken with a specific repetition rate, and there are 41 sets of measurements shown in this plot.

one from Thorlabs website, and one taken in 1999 [87, 103].

The OD laser cabinet is positioned in front of the Central Hut, to the right of its door. The LSI $N_2$ laser and dye laser appear as one unit, positioned in the middle of the second shelf from the top, as one can see in Figure 4.9b; Figure 4.10a is a closeup shot, while Figure 4.10b shows the controls of the laser [104]. The red cable coming out from the dye laser is an optical fibre fitted with a SubMiniature version A (SMA) connector on one end; it guides the light emitted from the dye laser to a filter wheel.

Located on the top shelf of the laser rack (Figure 4.11a) is the logarithmically graded filter wheel, which enables users to attenuate the output light from the dye laser by selecting a step number. The step number is said to have a range of $[300, \sim 1800]$ in the last published literature mentioning this equipment in 1997 [105, p. 35], where step 300 denotes the least amount of attenuation. The slope of the filter wheel, as measured in the same source, is approximately 270 steps per decade, representing how much the filter wheel setting, $f$, changes with every tenfold decrease in light intensity. For the last three laser calibration campaigns during the SK-V, SK-VI and SK-VII periods, ten fixed step numbers were used, which are 50, 150, 300, 600, 900, 1200, 1500, 1800, 2100 and 2400. It is not known why the current highest filter wheel setting exceeds the

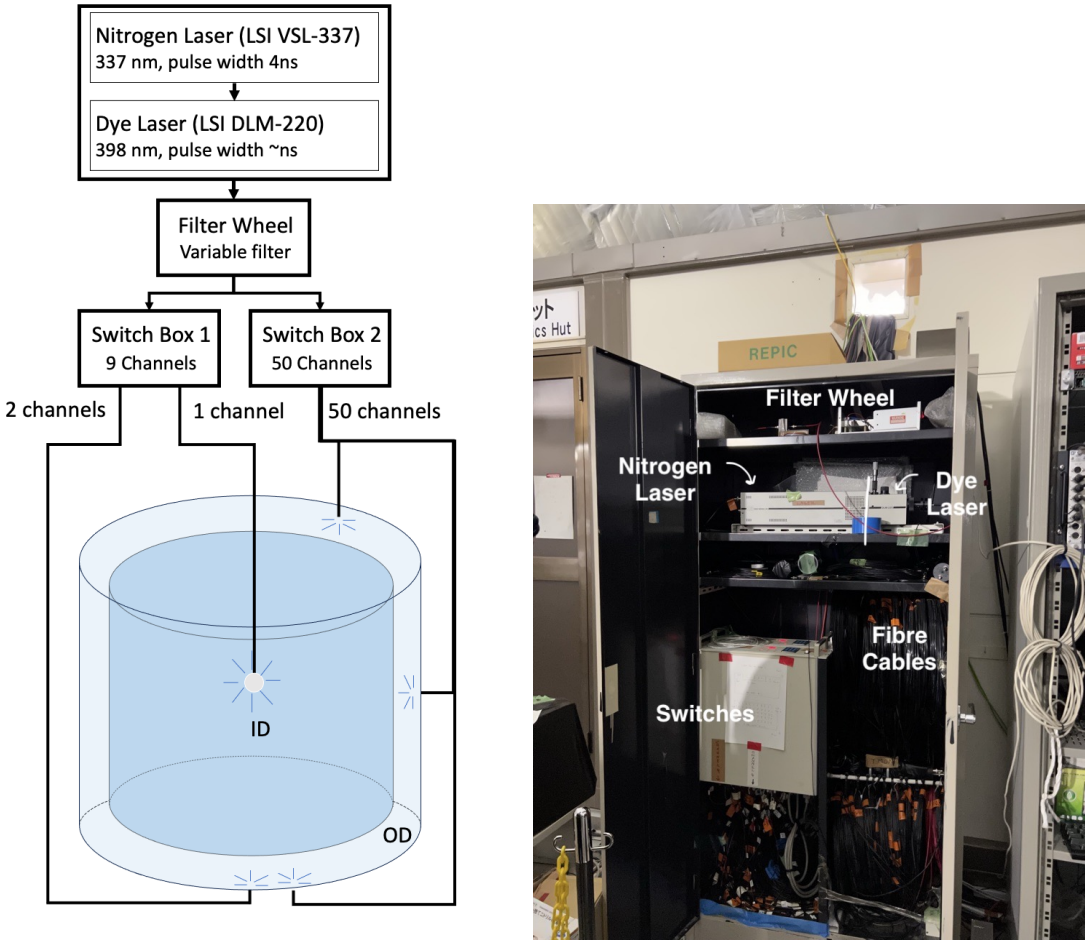


**(a)** **(b)**

**Figure 4.9:** (a) A schematic diagram indicating the OD laser system setup. The locations of the fibres in the OD tank are detailed in Section 4.3.3; (b) The rack housing the OD laser system on top of the Super-K tank (photo taken 21 September 2022).

(a) (b)

**Figure 4.10:** The front and side view of the current LSI lasers. (a) The LSI Laser and dye laser unit viewed from the front on the Super-K equipment rack; (b) An image of the LSI $N_2$ laser found on a UK resale website UniGreenScheme [104].

previously defined boundaries; however, the above settings do produce sensible data.

In the right half of Figure 4.11a is the stepper-motor controller for the filter wheel, cased in a CAMAC crate.

Figure 4.11b is an example of a filter wheel manufactured by Thorlabs [103]; note that the filter wheel for OD lasers probably has more filter capacities than this product, which only has six channels. The operation instructions of the filter were documented in the OD laser manual [87], one can also find the control commands from scripts used in previous OD laser data-taking campaigns.

The output of the filter wheel (left side in Figure 4.11a) is fed into one of the two Dicon optical switch boxes, labelled Switch 1 and Switch 2. The switches are normally controlled by a GPIB controller [105, p. 35]. A close-up photo of the face of the switches can be seen in Figure 4.11c. Switch 1 and 2 have nine and 50 output channels available, respectively. The downstream to the switch boxes are 52 + 1 (OD and ID) optical fibres which direct the laser light into different sections of the Super-K tank for calibration activities. The first two channels on Switch 1 are assigned to fibre 51 and 52 of the OD fibres located at the bottom section of the OD, while the third channel is connected to a fibre then a diffuser bulb that is placed permanently in the ID for daily ID PMT timing calibration. The use case of the remaining six channels on Switch 1 is unknown. On the other hand, all 50 channels of Switch 2 are connected with the optical fibres going into the OD.

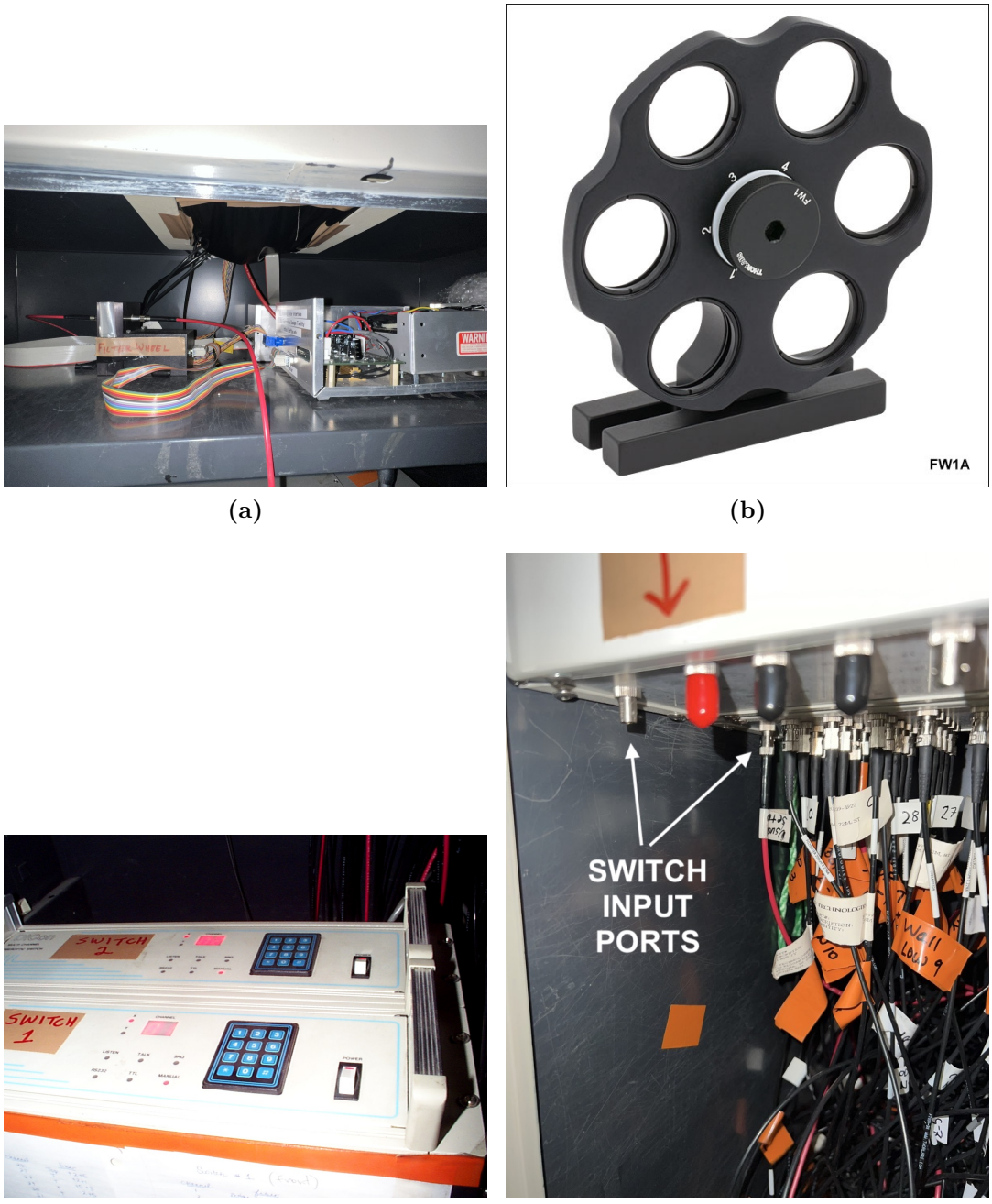


**(a)** **(b)** **(c)** **(d)**

**Figure 4.11:** Photos from 21 September 2022, online, and the internal manual for the laser. (a) Picture of the filter wheel. The distorted text reads 'Stepping Motor Interface; BU Electronic Design Facility; https://edf.bu.edu'; (b) An example of a filter wheel sold by Thorlabs [103]; (c) The front of the Switch boxes. Photo taken from Ref. [87]; (d) Picture of the input ports of the switches.

The optical cable coming out from the filter wheel can only be connected to one of the switches at a time, to switch between the two, one has to manually unplug the SMA connector from one input port and plug into the other. The input ports of the two switch boxes are indicated in Figure 4.11d. In addition, the laser light can only go through one fibre at a time, hence performing a full OD laser data-taking campaign utilising all 52 fibres, and repeating the light injection 400 times at each fibre opening takes more than eight hours to complete.

### 4.3.3 Light Injection System Inside the OD Tank

All the openings of the fibres are mounted to the outer walls of the OD, facing towards the OD PMTs. Of the 52 fibres, 14 are installed at the top region; 24 are installed at the barrel region, split evenly between $z = 980$ and $z = -1017$ cm; and 14 are installed at the bottom region. The optical fibres feeding to the top and barrel regions have a length of 70 m, while the ones feeding to the bottom are 110 m long. One can find the locations where the fibre ends are positioned in the OD in Figure 4.12. During the 2018 tank-open work, 18 optical fibres were replaced, in addition, four diffuser tips of the remaining fibres were repaired. Results of the health checkup, once done before 2018 and once done after, are also shown in the figure.

Figure 4.13a indicates how the new diffuser tips were made, while Figure 4.13b illustrates how the fibre tips were fixed to the walls of the three sections of the OD [106]. Figure 4.14 is a photo of the OD in which one can see the protruding fibre ends in the barrel region [107].

### 4.3.4 Light Injection System Inside the ID Tank

The basic design of the ID diffuser bulb, still being used today, was detailed in Ref. [87]. The Super-K calibration paper [56] has included a schematic drawing of the diffuser bulb's cross-section (Figure 4.15a). Used as part of the ID PMT timing calibration, the bulb was placed at the centre of the ID through the 'centre hole', which sits at $x = +35.3$ cm and $y = -70.7$ cm from the centre of the circle; the bulb is dropped by 2145 cm from the top of the tank to reach $z = 0$ position. The attenuated laser

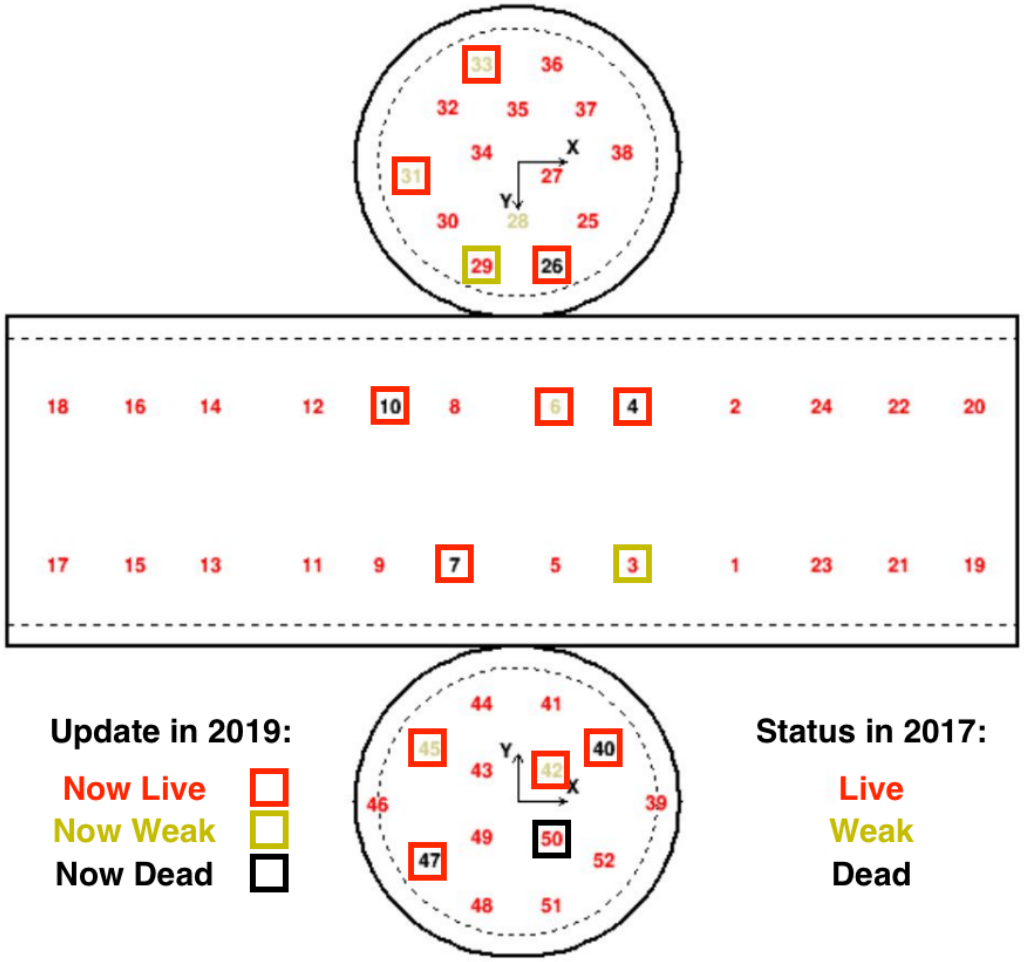


**Figure 4.12:** The locations of the 52 fibre entrances into the OD, are indicated on a cylinder net diagram of the OD. Note that this position map illustrates the newest locations of fibres since the 2018 tank-open work. Please refer to Fig. 35 in [56] for previous locations.

light is fed into the diffuser bulb from Channel #4 on Switch 1 through a 50-m-long optical fibre with a 400 µm diameter core. Since this fibre is equipped with a Japanese standard Fibre Connector (FC), but the switch box output ports are of the American standard, Straight Tip (ST), an FC/ST adaptor was utilised for the conversion at the switch box. The laser light is diffused fairly evenly by the bulb, with a less than 0.2 ns variation in photon emission time in $4\pi$ directions [56, p. 264].

An important point to note is that all the substances making up the current diffuser bulb are of solid acrylic material, which is thought to have more longevity than the previous liquid design. Before 1999, the diffuser bulb had an entirely different construction, as mentioned in the Super-K detector paper [16, p. 424]. Designed by

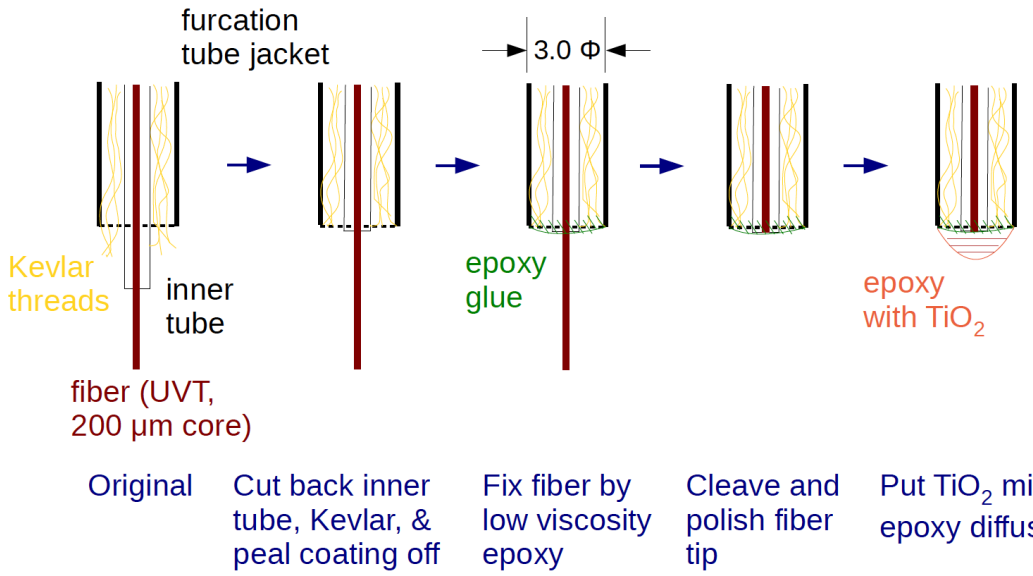


(a)

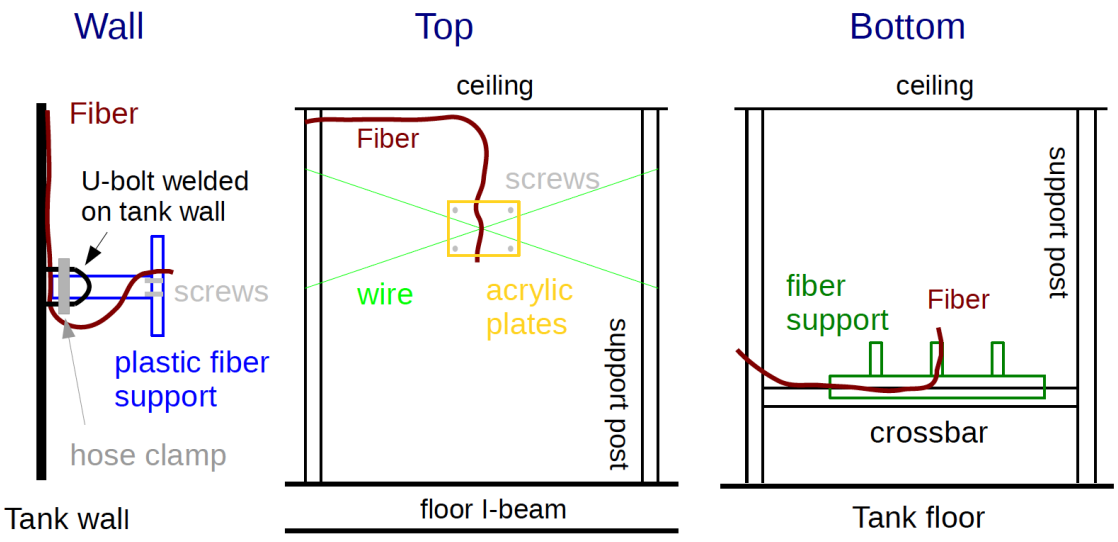


(b)

**Figure 4.13:** Figures taken from slides presented in two Calibration Meetings in 2016 [106]. (a) Diagrams comparing the OD fibre opening designs used before and after the 2018 tank opening work. The diameter of the entire enclosure, Φ, is 3.0 cm; (b) Diagrams indicating how the optical fibres are attached to the barrel, top and bottom sections of the OD during the 2018 tank-open work.


**Figure 4.14:** Photo taken in the OD barrel region showing a few protruding fibre tips (circled in pink) [107]. Visible at the bottom of the image is the steel structure that supports the OD PMTs on one side, as seen in the photo, and the ID PMTs on the opposite side, which are not visible. The ID volume is located behind this wall.

the University of Hawaii, it consisted of a shell made from glass with a diameter of approximately 8 cm; a diffuser tip in the centre of the ball, made of $TiO_2$; and the rest of the cavity was filled with LUDOX®, a DuPont product that is made of 20 nm glass fragments suspended in liquid. A photo can be found in Figure 4.15b.

## 4.4 The Application of the OD Laser

As mentioned in Section 4.3.2, the LSI laser units are employed to calibrate both the OD and ID PMTs; though the calibrated parameters and frequencies are different for each volume.

For the OD, the laser is employed to provide different light levels in the OD for the calculation of saturation parameters for each OD PMT. Subsequently, the parameters are used in SKDetSim.

As mentioned in Section 2.2.2, saturation in the context of Super-K OD PMTs is defined as having recorded 200 or more p.e.s. The saturation parameter, $k$, for a

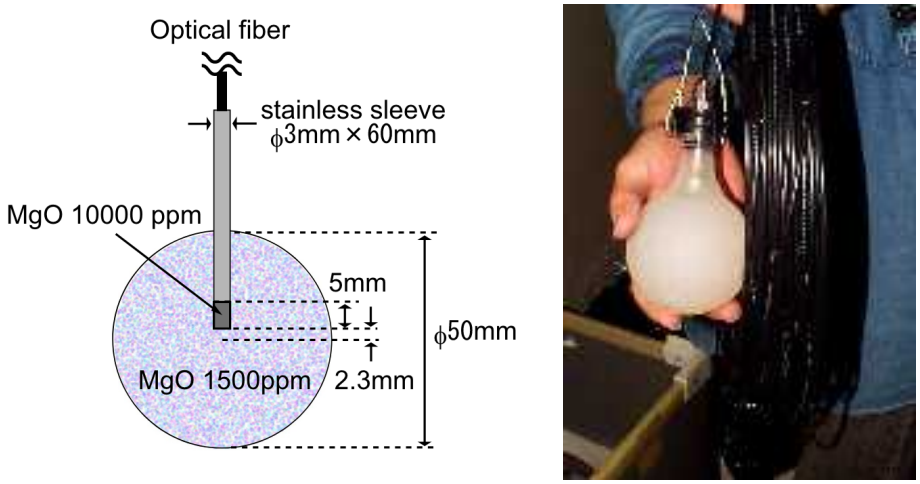


(a) (b)

**Figure 4.15:** (a) A schematic drawing of the ID diffuser bulb cross-section [56]. The laser light emitted from the OD laser is transmitted to the bulb through an optical fibre with a stainless steel sleeve. The tip of the fibre within the MgO-filled bulb is also made of MgO of different densities, where the use of MgO, a solid at room temperature, is to disperse the laser light isotropically; (b) A picture of the old diffuser ball used for ID calibrations before 1999, photo taken from Ref. [87].

given PMT, characterises the non-linearity of its response to increasing light intensity and is inversely proportional to the saturation point. Hence, the larger the saturation parameter, the quicker a PMT saturates [108]. Values calculated using SK-IV data suggest that $k$ normally ranges between $0.001 - 0.003$ p.e.$^{-1}$ [56].

Ideally, the saturation parameters used in SKDetSim are updated once every Super-K data period. However, because the maximum intensity of the OD lasers has declined drastically since the end of the tank-open work in 2018, the only successful laser calibration campaign, which resulted in an update to the SKDetSim, happened at the end of 2019 during the SK-V period. Nonetheless, the laser data-taking campaign commenced on 28 January 2021 and 21 September 2022, respectively, for the SK-VI and VII periods. The manual for conducting a laser data-taking campaign is attached in Appendix A.

On the other hand, the OD laser is fired continuously throughout the year for the ID PMT timing calibration. The lasers are integrated into the `autocalib` scheduler program, which runs in conjunction with normal run data acquisition. The `autocalib` program has a period of 3.6 seconds, and the different calibration sources included in

the scheduler can be found in Figure 4.16.

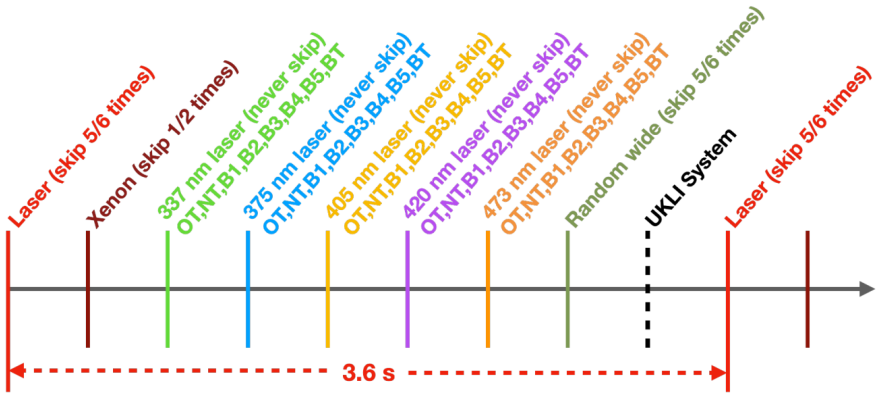


**Figure 4.16:** Light injection order in the `autocalib` scheduler [109]. The term 'Laser' (in red text) refers to the OD laser, which emits light into the Super-K ID every 21.6 seconds. The `autocalib` program also integrates various other calibration sources that operate at different intervals. These include the Xenon lamp (in brown text), used for calibrating the ID PMTs; ID lasers that emit light at wavelengths ranging from 337 to 473 nanometers, and the UK light injectors (UKLI), which are utilised for monitoring the optical properties of water.

## 4.5 The Decrease in Intensity of the OD Laser

The gradual drop in intensity of the LSI $N_2$ and dye laser units is a well-known problem. Specifically, the content of the plasma cartridge in the $N_2$ laser is known to leak into the atmosphere slowly. According to the Super-K calibration group convener, in 2011, a new plasma cartridge was purchased to replace the (by then) more than 10-year-old component. In 2018, an investment in a new laser for the OD was proposed to restore the maximum available intensity. However, the proposal did not go through, leaving the original LSI lasers working to the current day.

The OD lasers have been included in the `autocalib` program for ID PMT timing monitoring since the end of tank-open work in 2018. In addition, at the beginning of 2020, two of the fibres in the bottom region of the OD, 51 and 52 (F51/F52), were also included in the `autocalib` program to monitor the water quality before, during and after the first Gd loading [63], which happened in July and August of 2020. Three plots, two from the OD and one from the ID [110], all show the daily average of total charge collected from the OD laser against the time follows a steady downward trend,

as one can see in Figure 4.17 and 4.18. The filter wheel settings used for each time period marked in the figures are listed in Table 4.2.

**Table 4.2:** Time periods, as marked on Figure 4.17 and 4.18, and their corresponding filter wheel settings. †Light injection into the OD was off during this period but continued for the ID. Between 2022-02-14 and 2022-03-12 $f = 1000$, and on 2022-03-13 $f$ was set to 100.

| Data Period | Number on Figure | Start Date | End Date | Filter Wheel Setting $f$ |
|---|---|---|---|---|
| SK-VI | (1) | 2020-03-13 | 2021-01-27 | 1000 |
| | (2) | 2021-01-28 | 2021-01-29 | 50 |
| | (3) | 2021-01-30 | 2022-02-13 | 1000 |
| | (4) | 2022-02-14 | 2022-05-23 | 100† |
| SK-VII | (5) | 2022-05-24 | 2022-09-21 | 100 |
| | (6) | 2022-09-22 | 2022-10-01 | 50 |
| | (7) | 2022-10-02 | 2022-10-12 | 1000 |
| | (8) | 2022-10-13 | 2022-11-16 | 50 |

Two things to note, one is that the total charge collected from Fibre 51 through the bottom PMTs is always one order of magnitude larger than that from Fibre 52. The other is that whenever the optical fibre is disconnected and reconnected to Switch Box 1, the laser light intensity (correlated with the total charge collected in the ID) always temporarily recovers and then degrades with time, as illustrated by the jump from the end of (1) to (3) (both with $f = 1000$) in three figures. It is postulated that the drop in laser intensity could be caused both by the decay of the laser, and the increasing misalignment between some components in the light injection system. The two factors are difficult to consider independently.

In July 2023, the pulse energy of the LSI dye laser was evaluated using a Thorlabs power meter and a photodiode sensor, with the specific equipment and measurement methods detailed in Section 4.7. The findings indicated that the dye laser output was $0.270 \pm 0.249$ nJ at 30.87 Hz. Taking into account the dye efficiency of $14-15\%$ outlined in Section 4.3.1, the estimated pulse energy of a new LSI dye laser using Exalite 384 approximates 45 µJ at 20 Hz. While these results are not directly comparable due to variations in measurement repetition rates, a significant reduction in laser intensity —

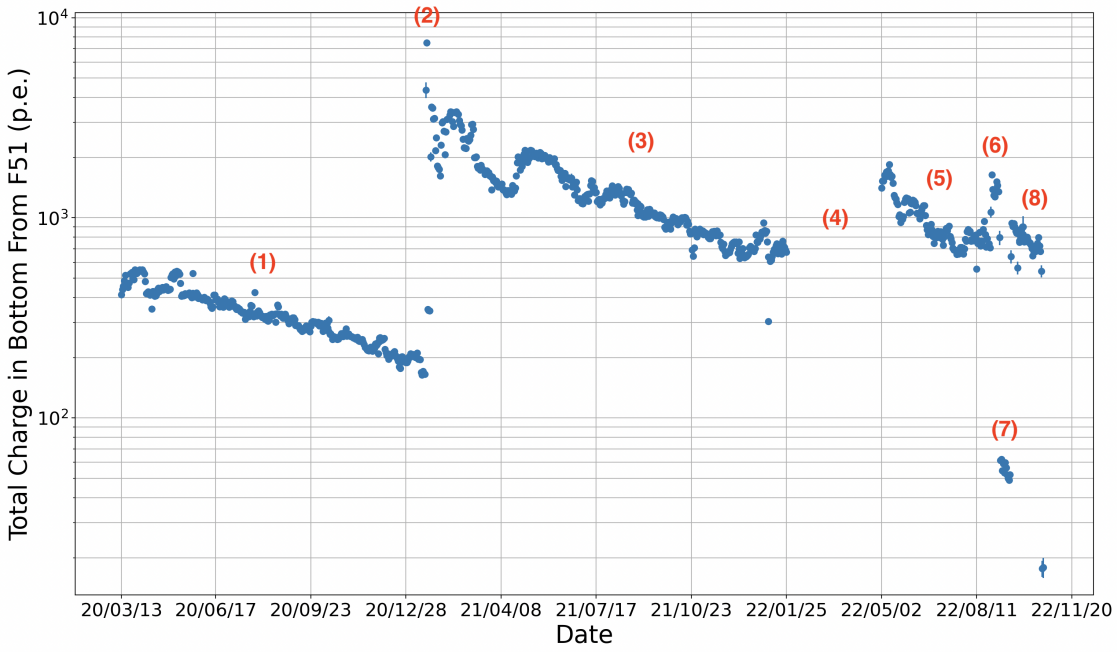


**(a)**

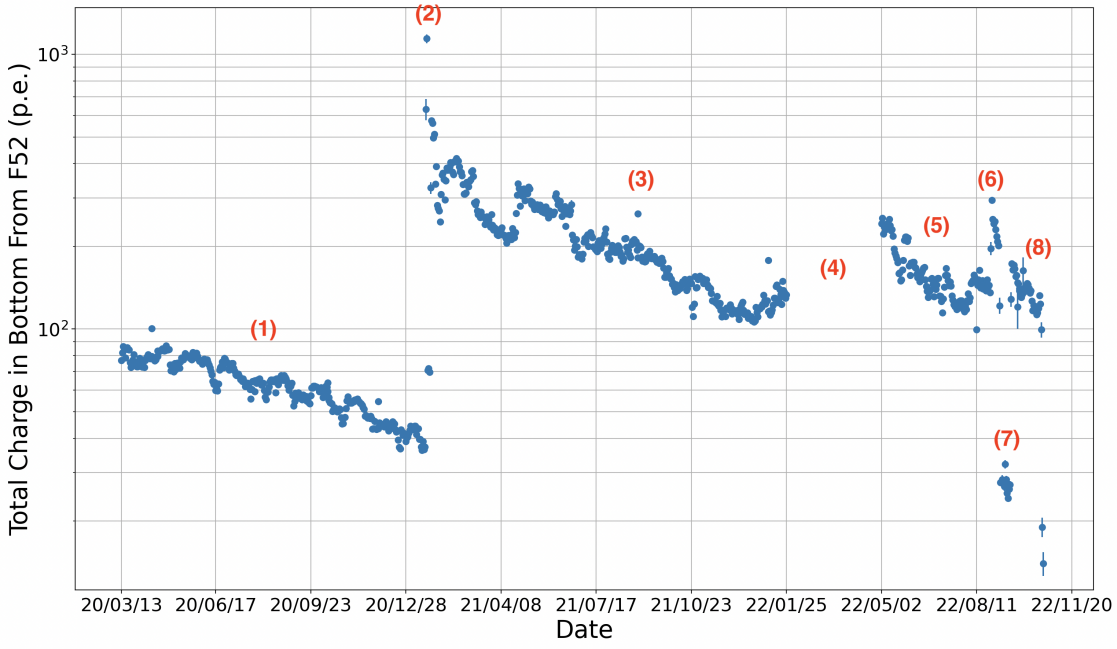


**(b)**

**Figure 4.17:** Daily average of the total charge (in p.e.) collected from the OD bottom region, between March 2020 and November 2022, as part of the `autocalib` program. Light was emitted from (a) Fibre 51, and (b) Fibre 52. Eight time periods are indicated on the plots, each has a different filter wheel setting ($f$) as indicated in Table 4.2.

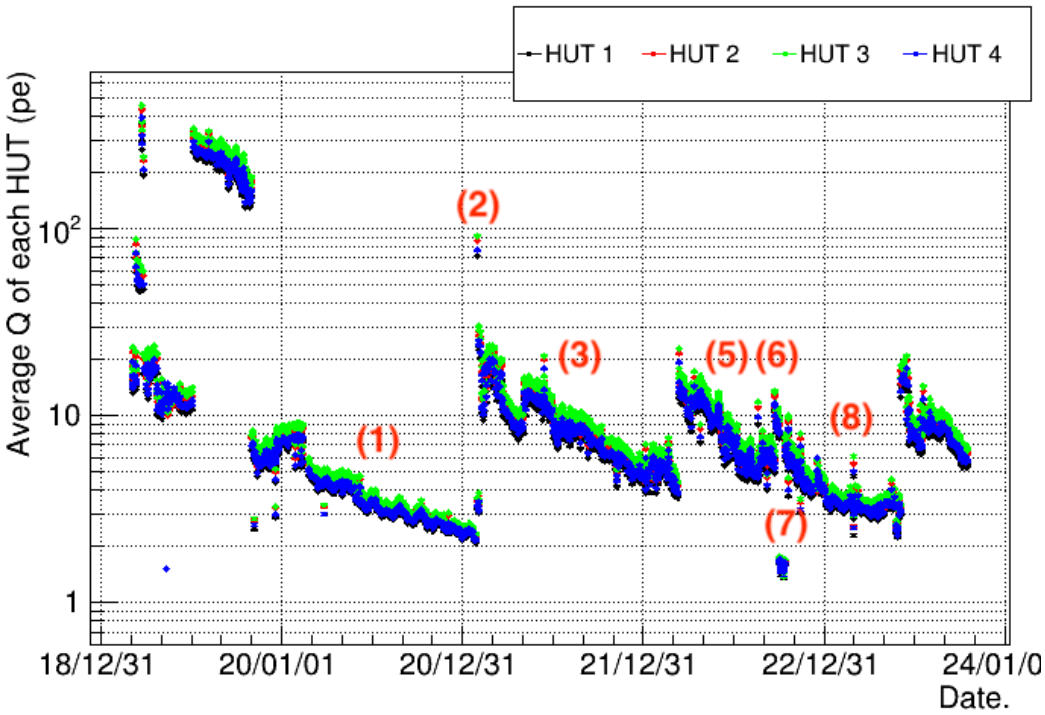


**Figure 4.18:** Daily average charge per hut as a function of time, published on the internal Auto T-Q Monitoring website maintained by the Korean group [110]. The filter wheel settings during the marked periods are the same as Figure 4.17, listed in Table 4.2. The settings before (1) are unknown; the setting after November 2022 has remained at 50 as of 18 October 2023.

by at least five orders of magnitude from its original state — is evident.

For context, the manufacturer estimates that the plasma cartridge within the $N_2$ laser can still emit at least 70% of its original energy after 20 million pulses or two years, whichever occurs first [98]. The cartridge in the current $N_2$ laser was last replaced around 2012. Assuming it was not in constant use, after ten years in service, the reduction in output energy from the $N_2$ laser alone should not exceed more than one order of magnitude.

The five orders of magnitude reduction in total output power from the dye laser suggests additional hardware issues. Possible causes include the expiration of the dye solution, misalignment between the $N_2$ laser and dye laser, or dust accumulation within the apparatus which prevents light propagation.

## 4.6 SK-VII OD Laser Data-Acquisition Campaign

The SK-VII laser data-taking campaign commenced on 21 September 2022. Laser light was sent through all 52 OD fibres one by one; for each of the ten filter wheel settings mentioned in Section 4.3.2, the fibre flashed 400 times at a frequency of 20 Hz. The data is recorded in the GPS bank.

Since SK-V laser data was the last eligible result used to calculate and update OD PMT saturation parameters, all the subsequent analyses of SK-VII laser results in this Section will be benchmarked against that of the SK-V.

### 4.6.1 Data Reduction

Two cuts are applied before the data is analysed. One cut is on the timing of the recorded hits. The OD trigger window is large, ranging between $[-5, 35]$ µs. However, it is known that the PMT hits caused by laser photons centre at approximately 1500 ns after the trigger signal. Thus, a timing cut is applied to only retain hits between $[-500, 5000]$ ns.

The second cut is on the distance between the hit PMT and the fibre which emitted the photons, only hits recorded by the PMTs closest to the active fibre remain after the cut. This cut is devised to reduce miscounting dark hits of far away PMTs as signals caused by the laser photons. The average number of PMTs per fibre, the average distance between a PMT and a fibre, and the spread of the statistics for each section of the OD tank are listed in Table 4.3 below. Figure 4.19 illustrates the distribution of the distance between PMT to its nearest fibre in cm.

**Table 4.3:** Statistics of PMTs per Fibre, PMT-Fibre Distances, and Spread by OD Tank Section. The errors quoted on the values are the calculated standard deviations.

| Fibre Location | Ave. PMTs per Fibre | Ave. Distance to PMT (cm) |
|---|---|---|
| Top | $21.6 \pm 3.06$ | $354.7 \pm 101.9$ |
| Barrel | $53.1 \pm 6.15$ | $590.4 \pm 220.5$ |
| Bottom | $22.0 \pm 3.18$ | $350.2 \pm 112.3$ |
| Total | $36.3 \pm 16.33$ | $513.4 \pm 221.36$ |

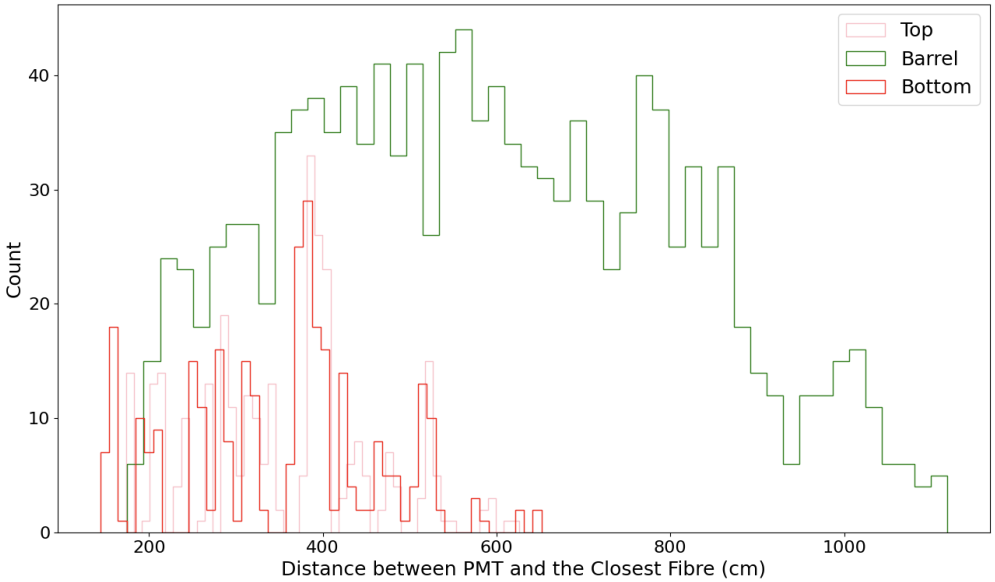


**Figure 4.19:** Distance between PMT and its nearest fibre for three OD regions.

### 4.6.2 Results

#### PMT Saturation

The SK-VII campaign was designated as a health checkup for the OD fibres, as it was already estimated beforehand that the OD laser would not be able to saturate most PMTs with even the least amount of attenuation at the filter wheel. Nevertheless, the number of saturated PMTs in the SK-VII campaign was counted and it was surprising to find that none of the PMTs were saturated. Figure 4.20a and 4.20b displays the charge recorded at maximum luminosity averaged over the number of events per OD PMT (represented by its electrical cable number) for SK-V and SK-VII periods, respectively. The plot legends specify the types of PMT used in the OD, a detailed discussion of each type can be found at the beginning of Chapter 3. Note that both REC02 and 06 PMTs are subsets of the recovery PMTs.

#### Hit Time and Charge Distributions

Two plots in Figure 4.21 compare the hit time and charge distributions of fibre 1 and 3 for the two data periods. The histograms are normalised with respect to the total number of events. Additional plots for fibres 2 and 4-52 can be found in Appendix B.

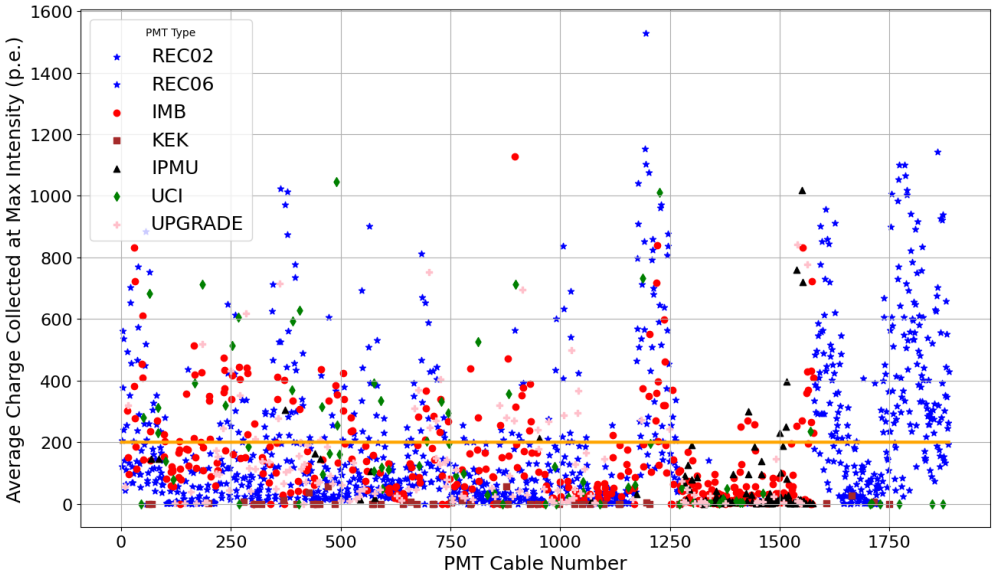


**(a)** SK-V

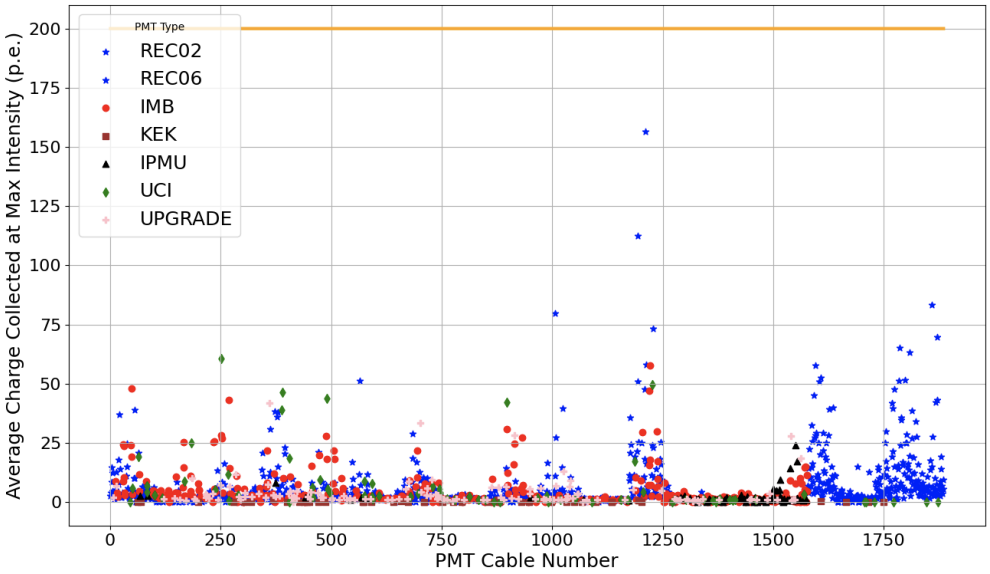


**(b)** SK-VII

**Figure 4.20:** Average charge per event collected by each OD PMT, identified by its electric cable number, using the maximum OD laser intensity during (a) SK-V, and (b) SK-VII periods. Note that the two plots have different scales on the y-axis. In the SK-V result, 599 OD PMTs were saturated (registered more than 200 p.e.s) with the maximum laser intensity, whereas the laser was not able to saturate any of the PMTs in SK-VII.

The time distribution of fibre 1 for SK-V in Figure 4.21a displays a distinct secondary peak. In contrast, such a feature is not seen in the SK-VII line in the same plot, nor observed in the time histograms for Fibre 3 during both periods, shown in Figure 4.21b. Incidentally, the charge recorded in the three graphs without the second peak is significantly lower than that from Fibre 1 in SK-V. A similar observation can be made in other plots attached in the appendix, where the larger the total charge recorded from one fibre, the more prominent the second peak in the hit time distribution. Thus, it is suspected the second peak is caused by the data acquisition electronics dead time. More study is needed to unveil the exact reason behind it.

### Fibre Health Assessment

Figure 4.22a illustrates the absolute charge comparison between SK-VII and SK-V, with each data point in the figure representing an average derived from approximately 400 events. Additionally, Figure 4.22b presents the normalised charge ratio of SK-V to SK-VII concerning the ratio of Fibre 1 for the two data periods. This choice of using Fibre 1 as the normalisation reference is attributed to its known healthy status.

It was found that the charge generated per fibre with maximum laser intensity was $57.8 \pm 7.4$ times less in SK-VII (Sep 2022) compared to that of SK-V (late 2019). Evidently, according to Figure 4.22b, the majority of fibres remained in good health, with only three exceptions: Fibre 3, 16, and 22.

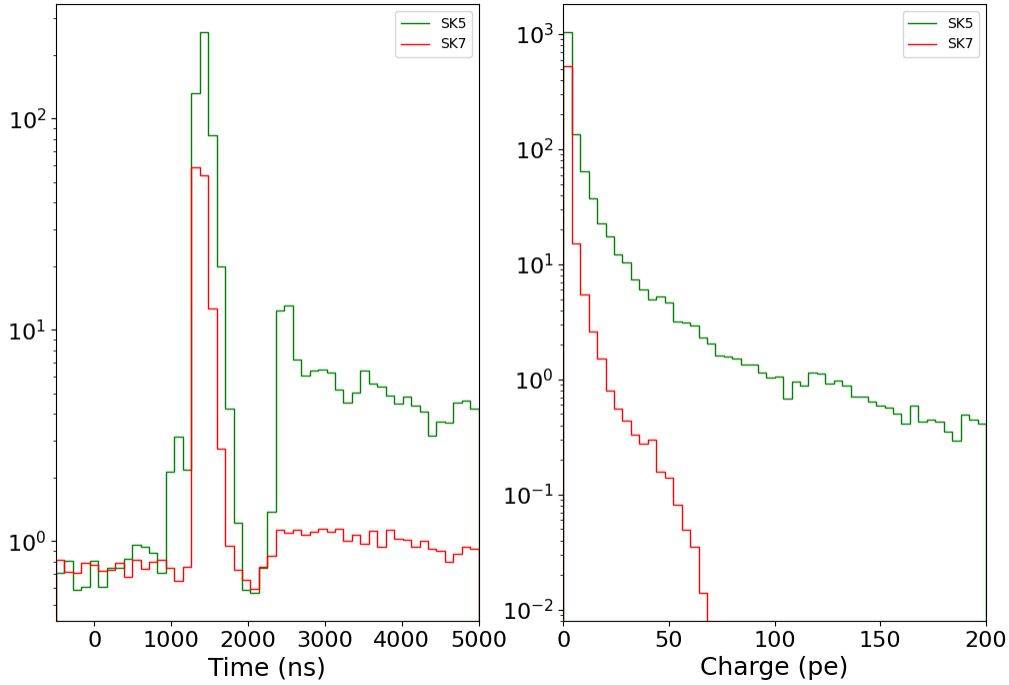


**(a)** Fibre 1

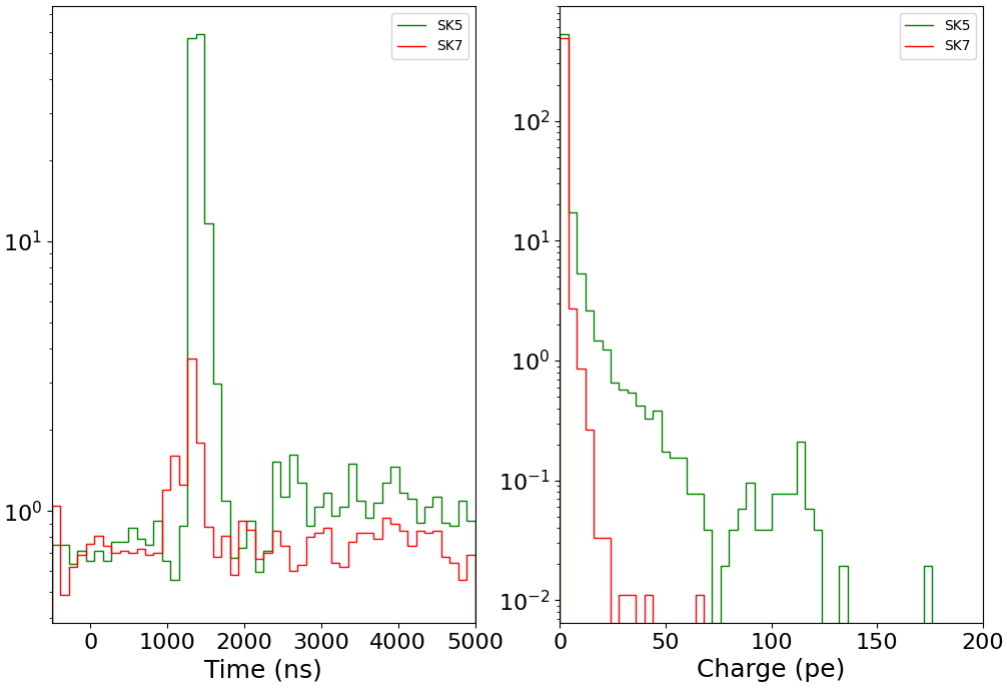


**(b)** Fibre 3

**Figure 4.21:** Comparison of hit time and charge distributions between SK-V and SK-VII data periods for two fibres.

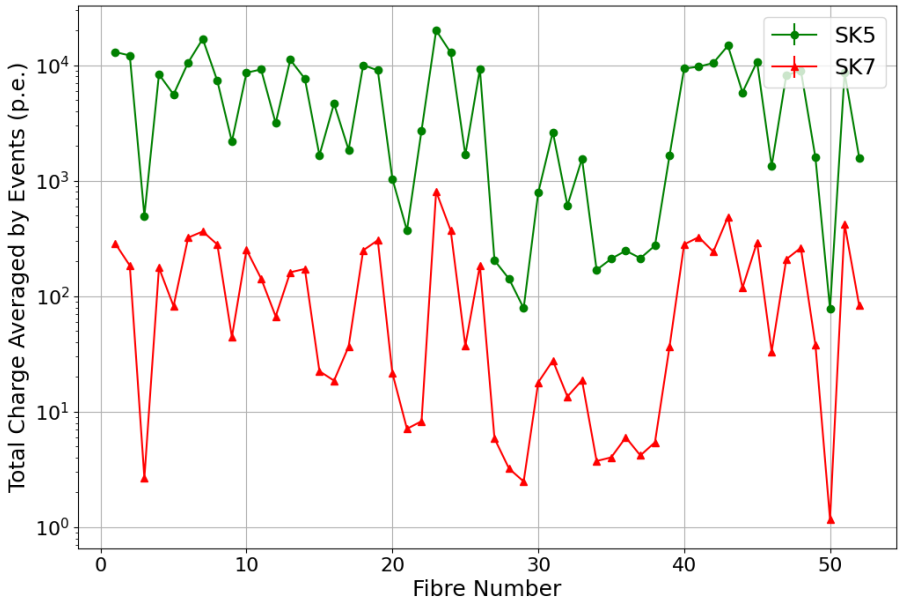


**(a)**

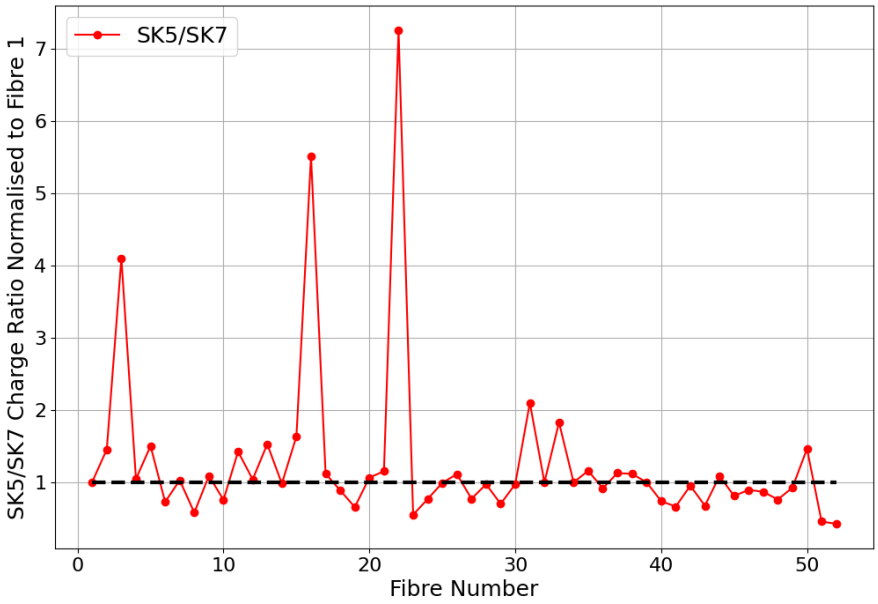


**(b)**

**Figure 4.22:** (a) The comparison of total charges induced by each fibre between SK-V and SK-VII, with each data point in the figure representing an average derived from approximately 400 events; (b) Charge ratio between SK-V and SK-VII, normalised with respect to ratio for Fibre 1.

## 4.7 Potential Replacement Light Source Testing

In July 2023, four alternative light sources were investigated as potential temporary or permanent replacements for the LSI lasers, seeing that the intensity of the LSI lasers is incapable of supporting a much-needed full ID OD PMT calibration campaign. All of the light sources tested have a picosecond pulse width (FWHM), which is one of the selection criteria for a replacement.

Two of the tested light sources belong to the Hamamatsu PLP-10 laser diode head series [111], with wavelengths of 375 nm and 405 nm (Figure 4.23a and 4.23b). They were driven by dedicated Hamamatsu controllers C10196 (Figure 4.23c). A collaborator from ICRR, University of Tokyo, provided both the laser heads and controllers. The 405 nm laser head is used constantly in calibration activities for Supernovae events [112], while the other is a spare.

The two other light sources supplied by a collaborator from Keio University are LED pulsers produced by Mrongen [113], with wavelengths of 375 nm and 385 nm (Figure 4.23d). For the sake of simplicity, henceforth, the light sources shall be denoted as Hamamatsu Laser Head 1, 2, and Mrongen LED Pulser 1, 2, following the order of wavelengths mentioned above.

Additionally, the output power of the current OD dye laser was measured to serve as a magnitude benchmark for the pulse energy of the four light sources. The operational parameters of the light sources are detailed in Table 4.4.

Laser searches conducted prior to July 2023 revealed the unavailability of a 400 nm laser within the allocated budget. The lasers within budget and specification constraints emit at significantly shorter wavelengths (around 350 nm). Thus it was hoped that at least one of the aforementioned light sources would have higher pulse energy than the current OD laser such that it could be connected to the OD light injection system and help to explore the effect of a shorter wavelength on the PMT saturation parameter measurements.

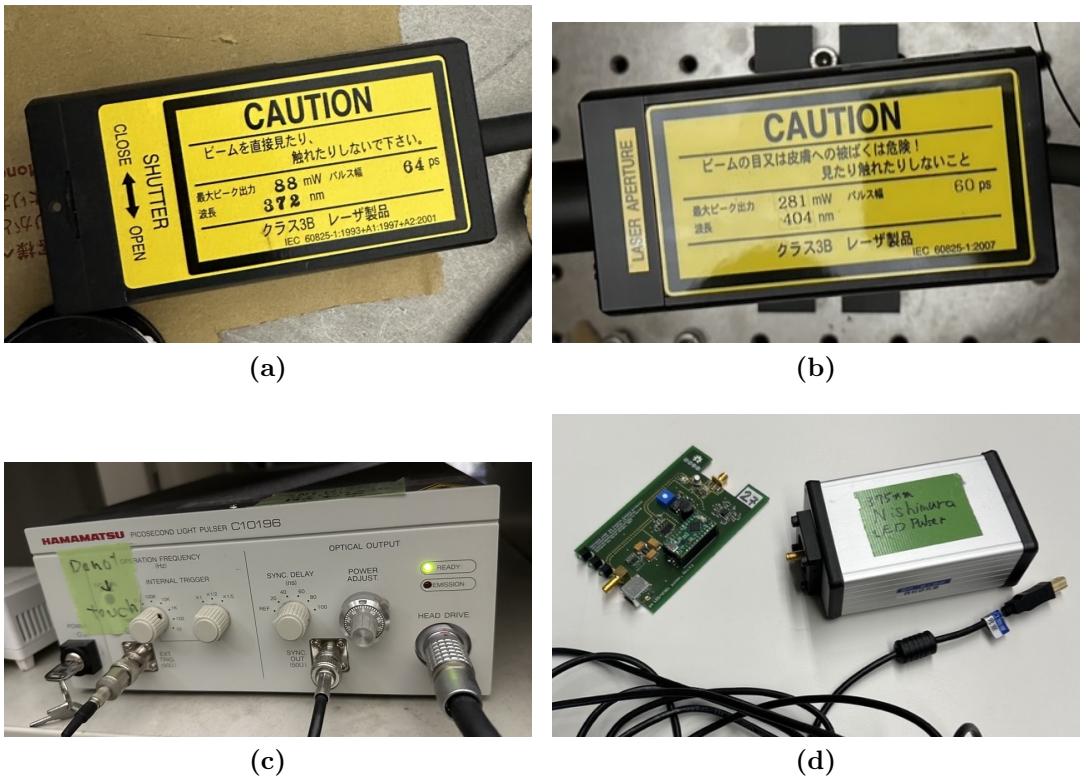


**(a)** **(b)**

**(c)** **(d)**

**Figure 4.23:** (a) Hamamatsu Laser Head 1; (b) Hamamatsu Laser Head 2; (c) the controller for Hamamatsu Laser Head 2, controller for Hamamatsu Laser Head 1 is exactly the same but not pictured; (d) Mrongen LED Pulser 2 (electronic board on the left) and 1 (in the box on the right).

**Table 4.4:** Parameters of the tested light sources, as stated in the manufacturer datasheets. †The pulse widths quoted on the datasheet are the shortest possible values.

| Light Source | Wavelength (nm) | Pulse Width (FWHM) (ns) | Repetition Rate Range (Hz) |
|---|---|---|---|
| LSI Dye Laser | 384 | 3.0 | 1 - 30 |
| Hamamatsu Laser Head 1 | 372 | 0.064 | 1 - 100M |
| Hamamatsu Laser Head 2 | 404 | 0.060 | 1 - 100M |
| Mrongen LED Pulser 1 | 375 | 0.57† | 1 - 25k |
| Mrongen LED Pulser 2 | 385 | 0.28† | 1 - 25k |

### 4.7.1 Measurement Equipment and Methods

A Thorlabs power meter, PM100USB, along with its corresponding photodiode power sensor, S150C, (as shown in Figure 4.24 [114]) were enlisted for power output measurements over 60 s periods. It is important to note that the power meter's manual cautions about reduced accuracy when the wavelength of the light source being measured falls below 390 nm. This uncertainty could have a significant effect on the pulse energy results reported in the next section since the majority of the light sources tested in July 2023 have shorter than 390 nm wavelengths.


**(a)** **(b)**

**Figure 4.24:** (a) Thorlabs power meter, PM100USB; (b) Thorlabs photodiode sensor S150C [114].

The pulse energy of a pulsed light source, $E_{pulse}$, can be found by

$$E_{pulse} = \frac{P_{ave}}{f} \tag{4.7}$$

where $P_{ave}$ is the average power determined by the Thorlabs measurement software and $f$ is the repetition rate of the light source. The repetition rate for each of the four light sources was kept at tens of Hz, in order to compare their pulse energy results with that of the OD dye laser, which only has a range between one and 30 Hz.

Three of the four light sources are already fibre-coupled, which can be easily attached to Thorlabs' photo-sensor using either the SMA or the FC connector provided.

A photo of the measurement setup for the Mrongen LED pulsers can be found in Figure 4.25a.

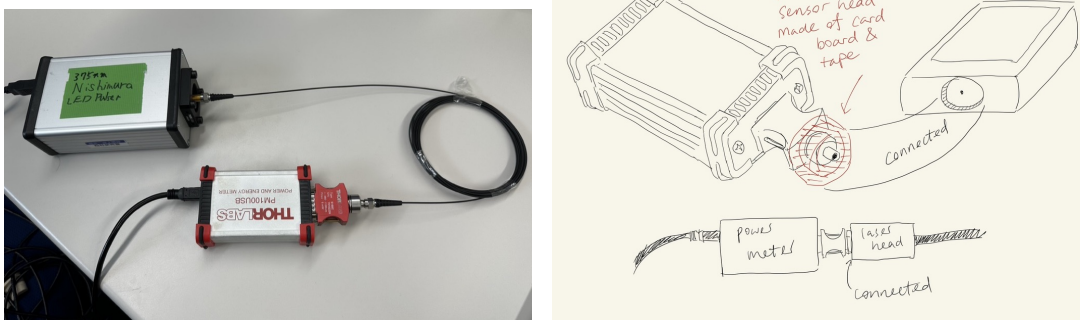


**(a)** **(b)**

**Figure 4.25:** The measurement setup for (a) Mrongen LED Pulser 1 and 2; and (b) Hamamatsu Laser Head 1.

On the other hand, Hamamatsu Laser Head 1 lacked fibre coupling. In addition, it has a wide indentation around the light output, making it impossible to connect to the photo-sensor without causing a light leak. An ad-hoc solution was devised by crafting an adapter for the photo-sensor using cardboard strips and electrical tape, and then fitting the assembly into the laser head's indentation. Drawings indicating the setup can be found in Figure 4.25b.

### 4.7.2 Results

Five plots in Figure 4.26 display the rolling average of measured power over time; the rolling window is chosen to be 1000 data points. Due to the calculation method used for the rolling average, the presented results do not start from 0 ms. As one can see in Figure 4.26a, the output power of the current OD dye laser is fairly unstable, which is to be expected for a laser with an extended service life of more than 25 years.

Although none of the manufacturers specified that the tested light sources require a certain warm-up period after switching on, it is suspected that at least the Mrongen LED pulsers need some time to stabilise since both Figure 4.26d and 4.26e exhibit slight downward trends.

The parameters of each light source, the measured power output and standard

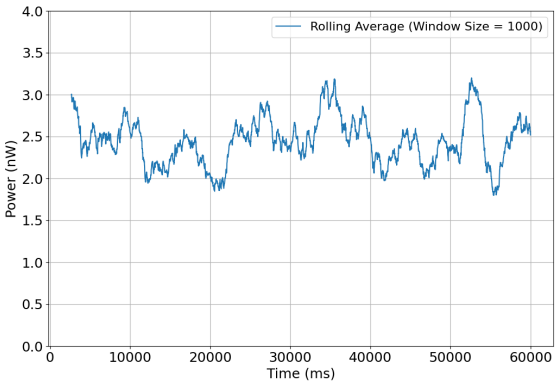


**(a)** OD dye laser

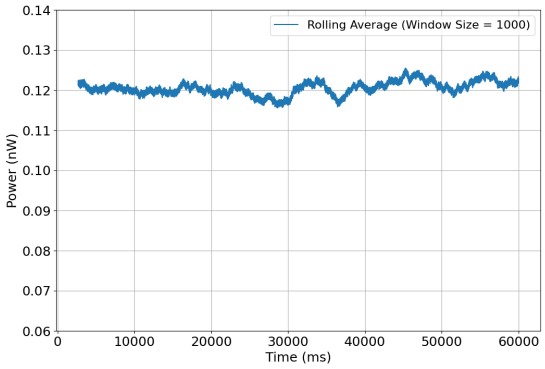


**(b)** Hamamatsu Laser Head 1

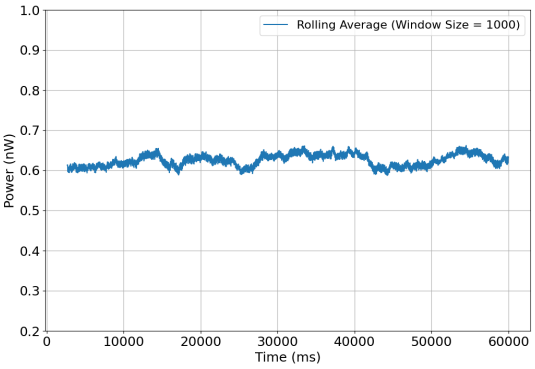


**(c)** Hamamatsu Laser Head 2

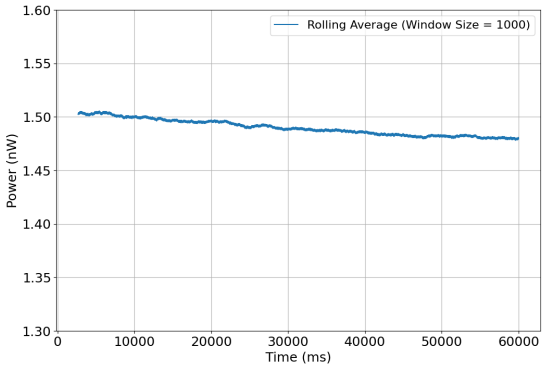


**(d)** Mrongen LED Pulser 1

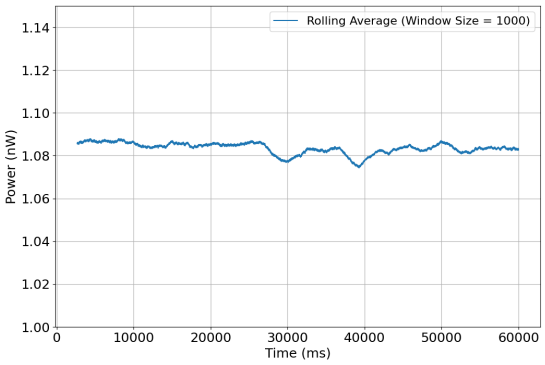


**(e)** Mrongen LED Pulser 2

**Figure 4.26:** The rolling average of measured output power for five light sources. Each rolling window contains 1000 data points.

deviation over 60 s, as well as the calculated pulse energy and its uncertainty are detailed in Table 4.5. Each repetition rate quoted in the table was cross-checked with a Python peak finding algorithm and additional calculations. The standard deviations on the power outputs were automatically calculated by the user interface software provided by Thorlabs.

**Table 4.5:** Parameters and results of the light sources tested using Thorlabs power meter and photo-sensor. The errors on the average power and pulse energy are the standard deviations.

| Light Source | Wavelength (nm) | Repetition Rate (Hz) | Ave. Power (nW) | Pulse Energy (nJ) | Expected Pulse Energy (nJ) |
|---|---|---|---|---|---|
| LSI Dye Laser | 402 | 30.9 | $8.32 \pm 7.96$ | $0.269 \pm 0.258$ | $4.50 \times 10^4$ |
| Hamamatsu Laser Head 1 | 372 | 20.0 | $0.121 \pm 0.120$ | $0.0065 \pm 0.006$ | 0.0300 |
| Hamamatsu Laser Head 2 | 404 | 10.0 | $0.627 \pm 0.899$ | $0.0627 \pm 0.0899$ | 0.0150 |
| Mrongen LED Pulser 1 | 375 | 10.0 | $1.64 \pm 0.0616$ | $0.164 \pm 0.00616$ | 0.0106 |
| Mrongen LED Pulser 2 | 385 | 10.0 | $1.08 \pm 0.0513$ | $0.108 \pm 0.00513$ | $2.58 \times 10^{-5}$ |

As revealed by the table, none of the near light sources possesses a greater pulse energy than the LSI lasers, signifying a lower photon emission per pulse when compared to the functioning LSI laser. This observation aligns with expectations, considering that the manufacturers have already specified low pulse energy levels for these sources.

In conclusion, these four light sources are not powerful enough to saturate any OD PMTs and thus are not further considered as replacement laser candidates.

## 4.8 Replacement Laser Specification Requirements

As highlighted in Section 4.6, the barrel region sees some of the longest distances between fibres and PMTs, with a handful reaching beyond 10 m. Thus, the eligibility of a new light source to replace the old is determined by whether a PMT 10 m away from its nearest fibre can receive more than 200 photons from the said fibre.

This section consists of two sub-sections, first the loss of photons between the light source and the end of the fibre in the tank is estimated. The next sub-section reports photon losses in water estimated by two methods; one relied on back-of-the-envolope calculations, utilising the water transparency parameters reported in the Super-K calibration paper [56] and QE reported by Hamamatsu of its R5912 8-inch PMTs [54]; the other method uses the calibration mode of the latest SKG4 simulation software.

### 4.8.1 Photon Losses Before the Tank

Per Section 4.3.2, photons emitted from the $N_2$ laser pass through five optical components before reaching the OD water. Table 4.6 presents the starting photon populations, losses caused by each component, and the resultant populations for three lasers in two scenarios. The table examines LSI $N_2$ laser in factory condition with the LSI dye laser, a 349 nm laser from Spectra-Physics [115] without dye laser and a 337 nm $N_2$ laser from LaserTechnik Berlin (LTB) [116] without/with the LSI dye laser. The latter two lasers were two potential replacement candidates considered during mid-to-late 2023. All losses marked with asterisks are informed approximations, while the ones without are calculated from available data.

**Table 4.6:** Laser parameters, starting photon populations, component-related losses, and final populations for three lasers in two different scenarios (with or without dye laser). Notably, losses marked with asterisks are informed estimations, while others are calculated from available data.

| | Cause of Loss | LSI Laser w/ Dye Laser | Spectra-Physics Laser [115] | LTB Laser [116] | |
|---|---|---|---|---|---|
| | | | | w/o Dye Laser | w/ Dye Laser |
| Primary Laser Wavelength (nm) | | 337.1 | 349 | 337.1 | 337.1 |
| Pulse Energy (µJ) | | 300 | 120 | 130 | 130 |
| Starting Population | | $5.10 \times 10^{14}$ | $2.11 \times 10^{14}$ | $2.21 \times 10^{14}$ | $2.21 \times 10^{14}$ |
| ① Loss (dB) | Laser Over Spec | 3* | 3* | 3* | 3* |
| ② Loss (dB) | Dye Efficiency | 9 | - | - | 9 |
| | Dye Laser Equipment | 3* | - | - | 3* |
| ③ Loss (dB) | Coupling to Wire | 22.8 | 1.05 | 25.8 | 25.8 |
| ④ Loss (dB) | Filter Wheel | 5* | 5* | 5* | 5* |
| ⑤ Loss (dB) | Switch Box | 3* | 3* | 3* | 3* |
| ⑥ Loss (dB) | Cable | 4.4 | 9.5 | 11 | 4.4 |
| ⑦ Loss (dB) | Epoxy Diffuser | 3* | 3* | 3* | 3* |
| Total Loss (dB) | | 53.2 | 24.6 | 50.8 | 56.2 |
| Population after Losses | | $2.44 \times 10^{9}$ | $7.32 \times 10^{11}$ | $1.84 \times 10^{9}$ | $5.30 \times 10^{8}$ |

A few comments on the losses listed in the table:

① Laser over spec refers to the discrepancy between the pulse energy quoted by the manufacturers and that measured in a university laboratory after the purchase. A 3 dB loss (50% drop) is possibly an overestimation for any new lasers as their pulse energy over time is generally fairly stable.

② The loss caused by the dye efficiency is calculated according to the data quoted

for Exalite 384, which sits at 15%. The optical alignment between the $N_2$ laser and the dye laser, and other losses due to the design of the dye laser are broadly included in the dye laser equipment loss.

(3) Photon losses at the coupling location between different lasers and wires depend on the laser beam dimensions, as the diameter of the wire core is assumed to be 200 µm for all lasers considered. Both $N_2$ lasers by LSI and LTB have $mm^2$ beams, roughly two orders of magnitude larger than the cross-section of the wire; whereas the Spectra Physics laser outputs a sub-$mm^2$ beam, with comparable area to the wire.

(6) The length of the cable is taken as 110 m for every laser. For LSI and LTB $N_2$ laser with dye laser, the loss is approximately 0.04 dB per meter, while the loss is roughly 0.077 dB per meter for LTB laser without dye laser. On the other hand, the Spectra Physics laser light sees a light loss of 0.069 dB per meter.

As one can see from the table, the number of photons drops between three to six orders of magnitude travelling through various OD light injector components. The cables that come between the switch boxes and the OD water are the most efficient at transmitting wavelengths close to 400 nm; however, this advantage is offset by the losses caused by the wavelength-shifting dye laser.

### 4.8.2 Photon Losses in OD Water

#### Estimation Using Water Parameter and Quantum Efficiency from Graphs

The number of photo-electrons, $N$, counted by a PMT at a distance $l$ away from an epoxy diffuser fixed on the outer wall of the OD can be found by

$$N(\lambda) = I_0(\lambda) \underbrace{\frac{\pi r^2}{2\pi l^2}}_{(1)} \underbrace{e^{-l/L(\lambda)}}_{(2)} \underbrace{\frac{2}{l}}_{(3)} \underbrace{\mathrm{QE}(\lambda)}_{(4)}, \tag{4.8}$$

where $I_0(\lambda)$ is the photon population at the diffuser, $r$ is the radius of the PMT, $L(\lambda)$ is the attenuation length in pure water, and $\mathrm{QE}(\lambda)$ is the quantum efficiency of the PMT. As indicated by the braces under Equation 4.8, four main effects dictate the resultant photo-electron number that an OD PMT would see:

(1) accounts for the geometrical spreading of light by considering the effective detection

area of a PMT compared to the total surface area of a hemisphere centred at the light source;

(2) takes into account the attenuation of light due to the scattering and absorption effects caused by the water; and finally,

(3) further reflects the fact that as the distance $l$ from the source increases, the light is distributed over a larger area;

(4) is the probability of the PMT detecting a photon.

Other factors in the OD, such as the reflectivity of the Tyvek® lining and the absorption and emission spectra of the wavelength-shifting (WLS) plates surrounding each OD PMT, can have a significant influence on the final photo-electron count. According to Ref. [56, p. 429], the presence of a WLS plate enhances light collection efficiency by 1.5 times compared to setups without one. However, the literature lacks data on the efficiency increase attributable to reflections from Tyvek®.

All but two quantities in Equation 4.8 are known, namely the water attenuation length $L(\lambda)$ and quantum efficiency $\mathrm{QE}(\lambda)$, which can be read from Figure 2.16 and 2.13 discussed in Chapter 2. Note that Figure 2.16 presents the inverse attenuation length, $1/L$, as a function of wavelength.

Table 4.7 presents the numbers of photo-electrons a Hamamatsu R5912 PMT would see at 2, 5, and 10 m away from the epoxy diffuser, with light generated by each of the three laser sources, with or without utilising the LSI dye laser. The initial photon population $I_0$ is carried forward from the results found in Table 4.6.

Assuming the starting populations at the epoxy diffuser are the same for every laser light, with differences only arising from the water transparency and quantum efficiency parameters, the percentage differences of p.e. recorded from a 400 nm light source compared to a 337 nm one are 18.32%, 16.53%, and 17.43% for distances of 2, 5, 10 m respectively.

In conclusion, preliminary photon-loss calculations indicate that the laser from Spectra-Physics is the top replacement candidate, potentially delivering $\mathcal{O}(3)$ more detectable photons to the OD PMTs than the other two options. However, it is important to note that the Spectra-Physics model is a Class 4 laser — the most hazardous type — which would require significant modifications to the current light injection setup.

**Table 4.7:** Number of photo-electrons seen by a PMT at three distances away from the emission location in Super-K OD, with regard to water transparency and quantum efficiency of the PMT, for three light sources with or without using a dye laser.

| | | LSI Laser w/ Dye Laser | Spectra-Physics Laser [115] | LTB Laser [116] | |
|---|---|---|---|---|---|
| | | | | w/o Dye Laser | w/ Dye Laser |
| Wavelength (nm) | | 400 | 349 | 337.1 | 400 |
| Population at Wall $I_0$ | | $2.44 \times 10^9$ | $7.32 \times 10^{11}$ | $1.84 \times 10^9$ | $5.30 \times 10^8$ |
| Water Coefficient $1/L$ (1/m) | | $8.26 \times 10^{-3}$ | $1.27 \times 10^{-2}$ | $1.49 \times 10^{-2}$ | $8.26 \times 10^{-3}$ |
| PMT Diameter $r$ (m) | | | 0.2 | | |
| Quantum Efficiency (%) | | 25.2 | 23.0 | 20.7 | 25.2 |
| Photo-Electron Count at Distance $l$ | 2 m | $7.56 \times 10^5$ | $2.05 \times 10^8$ | $4.62 \times 10^5$ | $1.64 \times 10^5$ |
| | 5 m | $4.72 \times 10^4$ | $1.26 \times 10^7$ | $2.82 \times 10^4$ | $1.03 \times 10^4$ |
| | 10 m | $5.66 \times 10^3$ | $1.48 \times 10^6$ | $3.28 \times 10^3$ | $1.23 \times 10^3$ |

Consequently, the laser from LTB, which falls under Class 3b, may be a safer and more practical alternative.

### SKG4 Simulation Study

This simulation study aims to confirm the reported result in the previous paragraph that the observed photo-electron number declines as the wavelength shortens from 400 to 337 nm and all the other variables kept the same. SKG4 trunk version published in September 2023 was used to simulate laser calibration events in the Super-K tank. SKDetSim was also explored as an option, however, the laser simulation module was designed for Korean lasers in the ID only and was difficult to modify.

Table 4.8 lays out the various parameter values used in simulations in the ID and OD. The macro files are a version of the example laser macro. The beam parameter $\sigma$ mentioned in the table controls the spread of photon beam, which has a quadratic relationship with the opening angle of the beam in degrees, where $[0, 45°]$ in angle corresponds to $[0, 8000]$ in $\sigma$. In addition, in Figure 4.27 are two event displays of the simulated events in ID (left) and OD (right).

To investigate the difference in observed photo-electron number caused by the two wavelengths, an average p.e. count per event is computed for each tank region, and presented in Table 4.9 below. From the listed results, the ID simulation only sees a 5.11% decrease in p.e. recorded as wavelength shortens from 400 to 337 nm, whereas

**Table 4.8:** Parameters used in the SKG4 simulation of laser calibration events that are different to the default values already set in the `Calib_Laser.mac` macro.

| | ID | OD |
|---|---|---|
| No. of Events | 1000 | 1000 |
| Photons per Event | 10,000 | 10,000 |
| Photon Wavelength (nm) | 400 and 337 | 400 and 337 |
| Location (cm) | $x = +35.3$, $y = -70.7$, $z = 0$ (Same as ID Diffuser Ball) | $x = 1893.8$, $y = 305$, $z = 1020$ (Same as Fibre 1) |
| Mean Direction of the Photon Beam | $\hat{x} = -0.917$, $\hat{y} = -0.148$, $\hat{z} = 0$ ($-x$ Direction) | $\hat{x} = -0.917$, $\hat{y} = -0.148$, $\hat{z} = 0$ ($-x$ Direction) |
| Beam Parameter $\sigma$ | 6000 | 6000 |

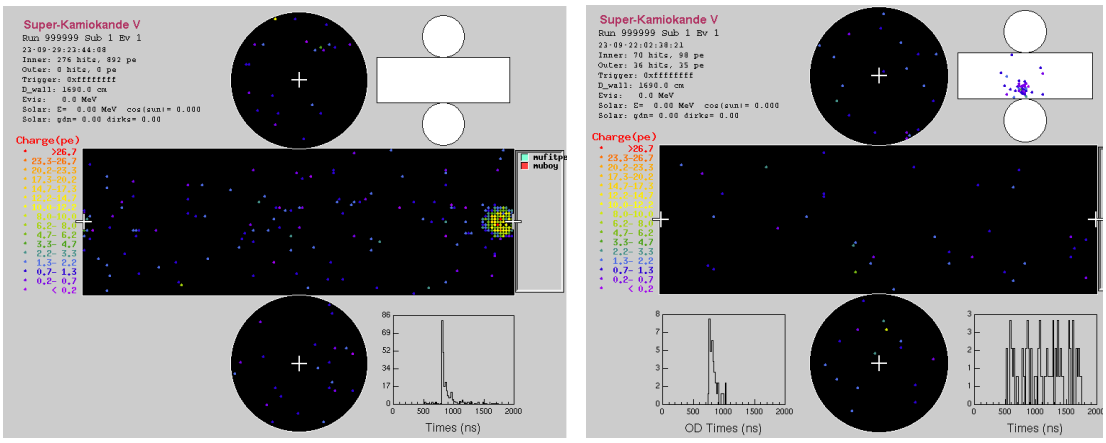


**(a)** **(b)**

**Figure 4.27:** Event displays of simulated events in (a) the ID, and in (b) the OD. One event contains 10,000 photons. The starting position in the ID is at $x = +35.3$cm, $y = -70.7$cm, and $z = 0$, while that of the OD is at the location of Fibre 1. Both photon beams point towards the $-x$ direction, with a beam opening parameter, $\sigma$, of 6000.

the OD simulation result displays an unexpected increase in p.e. count while it is expected to decline due to the wavelength-dependent water parameter.

However, it is important to note that the percentage changes reported in the last paragraph of the previous subsection are not directly comparable to the simulation results here, as the previous calculations were based on discrete distances between the PMT and the source, insomuch as the numbers here are the sum of all charges in either the ID or the OD. Despite this, they do provide some references for the drop in p.e. count that one should expect. In addition, it is still suspicious that the average p.e.

**Table 4.9:** SKG4 simulation result using the laser calibration mode for two wavelengths in the ID and the OD.

| Wavelength (nm) | Ave. p.e. per Event | |
|---|---|---|
| | ID | OD |
| 400 | $4455 \pm 16.67$ | $46.3 \pm 0.23$ |
| 337 | $4227 \pm 16.48$ | $48.2 \pm 0.21$ |

collected in the OD simulation feels no effect from the change in wavelength.

### 4.8.3 Discussions

The findings from the simulation were communicated to the Okayama group, which is responsible for developing and maintaining SKG4. It was discovered that the results, as described above, incorporated the OD PMT dark rate simulation, significantly inflating the recorded hit count. Upon removing the dark rate, the Okayama group confirmed that the hit numbers aligned with theoretical predictions.

Due to funding constraints and laser safety concerns, it was eventually decided that a new $N_2$ laser from LTB alone would be enough to replace the LSI laser, providing photons for the calculation of the OD PMT saturation parameters. However, with the new knowledge coming to light from a 1997 thesis [105], it was found that the cables used inside the switch boxes in the OD light injection system are doped with Germanium, which fluoresces when transmitting $N_2$ laser output as the chemical has an absorption line at around 330 nm. The thesis had warned against supplying 337 nm light directly into the switch box and suggested disconnecting the switches from the system if one insists on employing a $N_2$ laser. No meaningful conclusion has been drawn at the time of writing this thesis.

# Chapter 5

# Machine Learning, Deep Learning and PointNet

Machine Learning (ML) and Deep Learning have increasingly become pivotal in a wide array of disciplines, reshaping the way data is analysed and interpreted. Their applications extend far beyond traditional boundaries, significantly impacting fields such as physics. In particle physics, particularly, ML has revolutionised the approach to data analysis, allowing for a more precise and comprehensive understanding of complex phenomena. The ability of these techniques to efficiently process and extract meaningful insights from vast datasets has proven invaluable, marking a significant evolution in scientific methodologies and research capabilities.

This chapter aims to offer a comprehensive exploration of common ML algorithms, in addition to an in-depth discussion focusing on the model employed in the analysis discussed in the subsequent chapter. It begins by introducing fundamental ML concepts before delving into the intricacies of Deep Learning, emphasising the PointNet architecture. The discussion will demystify complex elements such as Artificial Neural Networks, Multi-Layer Perceptrons, and Convolutional Neural Networks, highlighting their pivotal roles in advancing data analysis within neutrino physics. In the latter half, the chapter provides a thorough examination of PointNet, setting the stage for its application in the analyses detailed in Chapter 6.

## 5.1 Machine Learning Concepts and Formalisms

Machine Learning is a branch of Artificial Intelligence (AI) that involves the development and application of statistical algorithms to data to generalise trends and perform inferences. An ML problem typically involves finding a function (model), $f : \boldsymbol{X} \to \boldsymbol{Y}$, that optimises a given metric known as the loss function or cost function, $\mathcal{L}(\boldsymbol{y}, f(\boldsymbol{x}))$. This operation is commonly referred to as learning or training. Here, $\boldsymbol{X}$ represents the space of observable data (input) and the function maps to a target space $\boldsymbol{Y}$ (outputs or predictions) [117].

In most ML applications in particle physics, the model undergoes supervised learning, where the supplied datasets are annotated with known desired outputs, known as the labels, targets or truth information. The data employed to train the ML model is typically segmented into three distinct collections: the training set, the validation set, and the test set. The process begins with the model 'learning' from the training set. Following this, if the model demonstrates reasonable performance, it is then applied to make predictions on the validation set. Lastly, the test set, comprising exclusively of data not previously used in training, is utilised to offer an unbiased assessment of the model's effectiveness.

### 5.1.1 Artificial Neural Networks

In a problem where a function is sought to map human-readable sensory input data, such as a collection of pixels that make up an image, to object identity, it is extraordinarily difficult if one were to seek such a mapping directly. Instead, the problem can be immensely simplified by splitting one convoluted mapping function into nested layers of mappings. The input and output layers are known as visible layers, as their values are human-observables. In contrast, the layers sandwiched in between are known as the hidden layers, since they contain increasingly abstract features determined by the model.

For a more concrete example, consider an Artificial Neural Network (ANN). Taking inspiration from the neural network in a biological brain, an ANN consists of a collection of nodes known as neurons, and they are interconnected through a web of

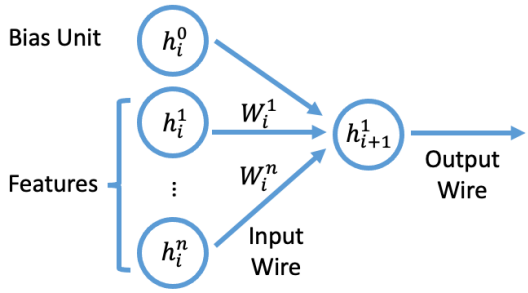


**Figure 5.1:** The architecture around one neuron in the artificial neural network. Every neuron in the network, between the input and the output layers, is derived from a transformation operation using some activation function to act on the weighted neuron values from the previous layer plus a bias term.

transformations. Figure 5.1 illustrates how one neuron, $h_{i+1}^1$, in layer $i+1$ is derived from a weighted combination of neurons, $\boldsymbol{h}_i$, in the previous layer; mathematically, one can express the transformations from neurons in one layer to the next as [117]

$$\boldsymbol{h}_{i+1} = g_i(W_i \boldsymbol{h}_i + h_i^0), \tag{5.1}$$

where $g_i$ is known as the activation function, $W_i$ are the elements of the weight matrix for layer $i$, and $h_i^0$ is known as a bias unit. A frequently used activation function used in neural networks is the Sigmoid/logistic function,

$$g(h) = \frac{1}{1+e^{-h}}. \tag{5.2}$$

where $h$ represents a non-specific neuron.

The transition from the input visible layer to the first hidden layer is achieved through $\boldsymbol{h}_0 \equiv \boldsymbol{x}$, and the model prediction $\boldsymbol{y}$ is obtained with $\boldsymbol{y} \equiv \boldsymbol{h}_{i+1}$ from the last hidden layer.

A common loss function utilised in ANN training is the mean squared error (MSE) function, which takes the form of

$$\mathcal{L} = \frac{1}{N}\sum_{i=0}^{N}(y_i - \hat{y}_i)^2 \tag{5.3}$$

where $N$ is the total number of samples in the dataset, while $y_i$ and $\hat{y}_i$ are the $i$th entry

in the predicted output vector $\boldsymbol{y}$ and the ground truth vector $\hat{\boldsymbol{y}}$ respectively. At the beginning of the network training stage, the weight matrix and the bias unit of each layer are initialised to random numbers; then, as the model calibrates its output with the given target and tries to minimise the MSE, the weights and biases are adjusted accordingly. This is typically done using optimisation algorithms like gradient descent, where the gradient of the loss function with respect to each parameter (weight and bias) in the network is computed. The parameters are then updated in a direction opposite to the gradient, aiming to find the parameter values that result in the minimum possible loss.

### 5.1.2 Multi-Layer Perceptrons

Multi-layer Perceptrons (MLPs) are a type of artificial neural network that is able to differentiate data which is not linearly separable [118]. Constructed with at least one hidden layer of neurons, it is always fully connected, which means each neuron in a layer is connected to every neuron in the subsequent layer, as seen in Figure 5.2. MLPs belong to the family of feedforward networks, which use the output of the previous layer of neurons as the new input into the activation function.

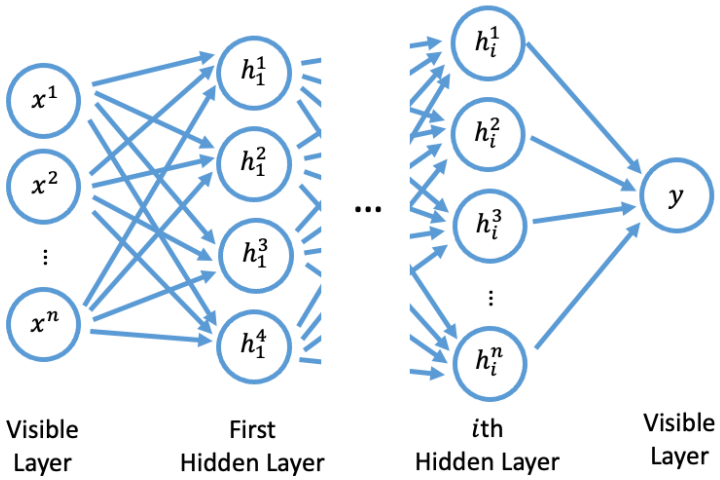


**Figure 5.2:** An example structure of a multi-layer perception with $n$ input features, $i$ hidden layers and a single output neuron.

### 5.1.3 Deep Learning and Convolutional Neural Networks

Historically, deep neural networks or deep learning algorithms are defined as models with multiple hidden layers, in contrast to shallow neural networks, which only have one hidden layer. For a long time, it was believed that a shallow network is able to achieve the same level of sophistication in finding the appropriate mapping function as the deep networks [119]. Nevertheless, a practical implementation of an effective shallow network might demand a significantly large number of nodes in its hidden layer. Moreover, in real-world applications, shallow neural networks frequently struggle to extract meaningful functions from datasets with many features.

In a broader sense, deep learning encompasses a wide array of machine learning techniques that focus on hierarchical data representations and modular, differentiable components. These deep networks are known not just for their enhanced expressive capacity, which refers to their ability to capture a broad range of complex patterns and functions, but also for the way their layers incrementally construct a hierarchical representation of the data. Due to their ability to approximate high-complexity mapping functions and a leap in hardware performance in recent decades, deep neural nets have been increasingly adopted in the computer vision field for pattern recognition [120].

First created in 1998 by Le Cun *et al.* for document recognition [121], Convolutional Neural Networks (CNNs) have since become some of the most prominent models in facial recognition, object identification and document classification applications. Figure 5.3 illustrates the pipeline of a CNN architecture designed for particle track classification [122].

#### Convolutional Layers

As shown in Figure 5.4 [120], a convolutional layer involves the addition of neighbouring pixels or features weighted by a kernel to generate a new feature map. The number of elements involved in the addition is determined by the dimension of the chosen kernel, which is normally $3 \times 3$.

The convolution operation offers three primary benefits [123]:

1) The weight-sharing mechanism within the same feature map decreases the overall number of parameters required;

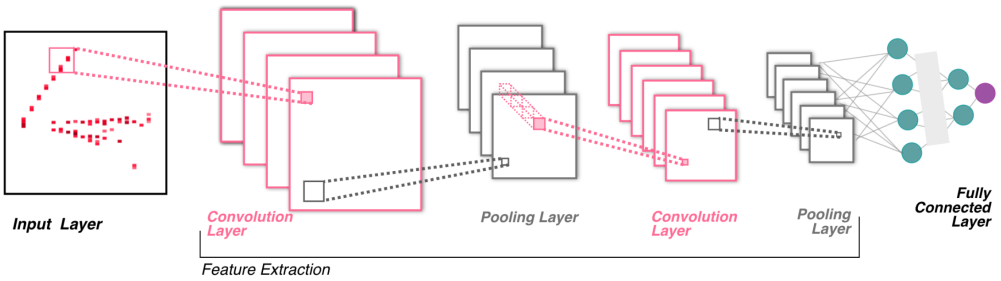


**Figure 5.3:** An example structure of a convolutional neural network used for particle track classification in a liquid Argon detector [122]. The model first extracts the features of the input data using two sets of convolution plus pooling layers in succession. The extracted features are then fed into a fully connected ANN to reduce the information to simple number(s) representing the particle's type (known as a class in ML application) in the event display.

2) It facilitates local connectivity, enabling the learning of correlations among adjacent pixels; and
3) It provides invariance to the positioning of these pixels within the input [124].

To accelerate the learning speed, several notable studies [125, 126] have adopted a convolutional layer in place of fully connected layers. In particular, a technique known as the Network in Network [127] proposed the substitution of the standard convolutional layer with a small MLP. This approach replaced the linear kernel solution with a nonlinear activation function and has yielded impressive outcomes in the field of image classification.

### Pooling Layers

In a CNN architecture, a layer produced from convolution is typically followed by a layer of pooling operation, which serves to reduce the dimension of the feature map and the number of overall network parameters. An example structure can be found in Figure 5.5. Comparable to the convolutional layers, the pooling layers also maintain translation invariance, since their activation functions apply small spacial regions recursively, thus aggregating information from the neighbouring pixels. The most prevalent technique used in pooling is max pooling [128, 129] since it negates the cancellation between elements and has the tendency to select superior invariant features and lead

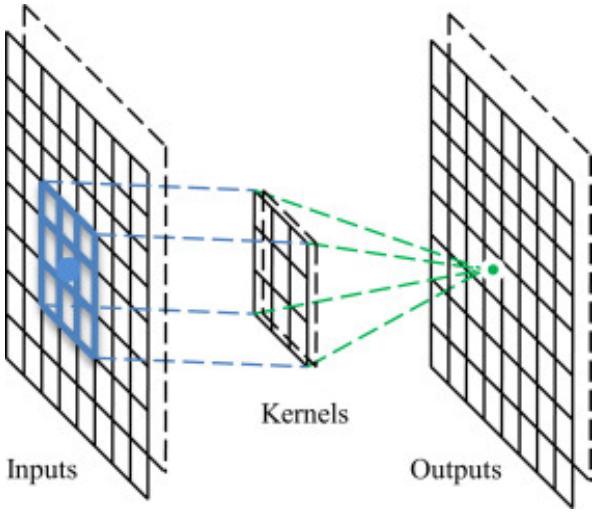


**Figure 5.4:** A convolutional layer in a CNN [120]. A kernel, essentially a weight matrix, is used to aggregate data in the $3 \times 3$ grid of the matrix in the previous layer to obtain each value of the output matrix.

to more generalised results; however, mean pooling is also a common choice.

#### Fully Connected Layers

A CNN typically has one or more fully connected ANN layers that come between the convolution-pooling layers and the final classifier. These intermediate layers aim to reduce a 2D feature map into a 1D feature vector with a pre-determined length. This output can then be processed to present a final score, which corresponds to a category in image classification, or to be fed into procedures for further processing.

### 5.1.4 Hyperparameters

There exist other variables that can control the performance of a model, which are generally termed 'hyperparameters'. These are the settings or configurations external to the model itself that govern the training process. Unlike model parameters, such as the weight matrix mentioned above, which are learned directly from the data during training, hyperparameters are usually set manually before the training step. Examples of hyperparameters include the learning rate, which determines the step size at each iteration while moving toward a minimum of the loss function, the number of epochs, which specifies the total number of training cycles, and the size of the mini-batch,

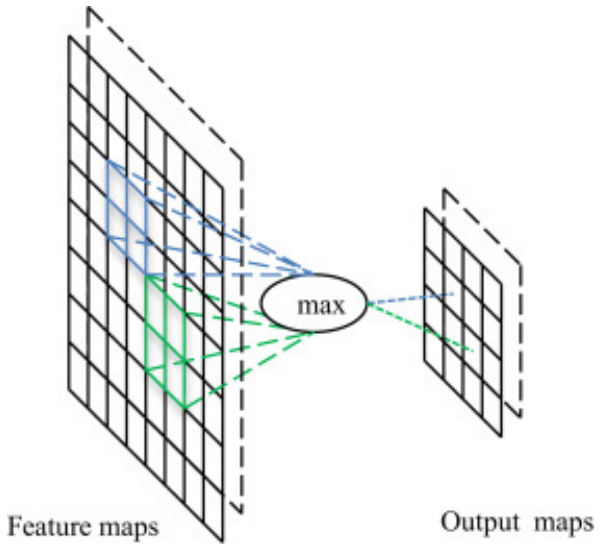


**Figure 5.5:** A pooling layer in a CNN [120].

affecting the convergence speed and stability of the learning process. Adjusting these hyperparameters can significantly influence the model's ability to learn and generalise from the training data, thereby affecting its overall performance on unseen data. Tuning hyperparameters is thus a critical step in the development of a robust ML model, requiring careful experimentation and validation.

## 5.2 Examples of Machine Learning Application in Neutrino Physics

Investigating neutrino signals in detection devices often encounters numerous obstacles, including dominant background interference, elusive signal detection, and limited statistics. The separation of signals from the backgrounds and the reconstruction of physical parameters are crucial stages in the data analysis algorithms. Traditionally, event classification and reconstruction depend on statistical techniques. Nevertheless, since the last decade of the $20^{\text{th}}$ century, machine learning approaches have been increasingly incorporated into neutrino physics analyses. For instance, ANNs were utilised for event categorisation at the Sudbury Neutrino Observatory (SNO) before 1998 [130].

The application of machine learning in data analysis has seen significant growth

recently, revolutionising data interpretation in neutrino experiments. This evolution has introduced various challenges, including the adaptation of standard image recognition algorithms to the unique demands of specific experiments, the quantification of biases and uncertainties, and the interpretation of the physical significance of the processes and outcomes. Despite these hurdles, the integration of machine learning has brought about potential benefits, such as the advancement of algorithms tailored to the complexities of neutrino physics and other innovations spurred by its application in the field.

Neutrino detectors vary in their signal characteristics, necessitating tailored machine-learning algorithms for signal/background differentiation and momentum reconstruction. For example, deep neural networks were selected for electromagnetic particle identification in the MicroBooNE experiment since this experiment uses a Liquid Argon Time Projection Chamber (LArTPC), which generates detailed images of particle paths [131].

At the forefront of these advances, the NOvA experiment became the first high-energy particle physics experiment to publish results analysed using a CNN. By employing an advanced type of CNN, known as a convolutional visual network, the classification efficiency of $\nu_e$ CC events was significantly improved, leading to a 30% gain in sensitivity compared to the results reported previously, which utilised more traditional methods [132].

Research into the use of machine learning techniques for lepton energy reconstruction in a proposed intermediate detector for the Hyper-Kamiokande experiment reveals that certain machine learning tools can enhance energy resolution by over 50% compared to traditional methods, such as lookup tables [133].

## 5.3 PointNet

Most CNNs such as ResNet [134], which was implemented for IWCD event classification and kinematics reconstruction [135], require the input data to be highly standardised. For instance, if one wants to apply the traditional models to 3D datasets, the raw data is typically processed as 3D pixels or flattened into 2D projections. In the case

of the ResNet application on IWCD data, the hit PMT data in the cylindrical shape has to be flattened before being used by the model, as illustrated by the example Hyper-K event display in Figure 5.6b. Although reporting preliminary results improves upon the statistical reconstruction tool FiTQun [136], the disadvantage of unwrapping the cylindrical geometry lies in that the topological relationships between PMTs on different surfaces of the volume are not preserved. This could hinder the ability of the model to generalise and optimise event reconstructions.

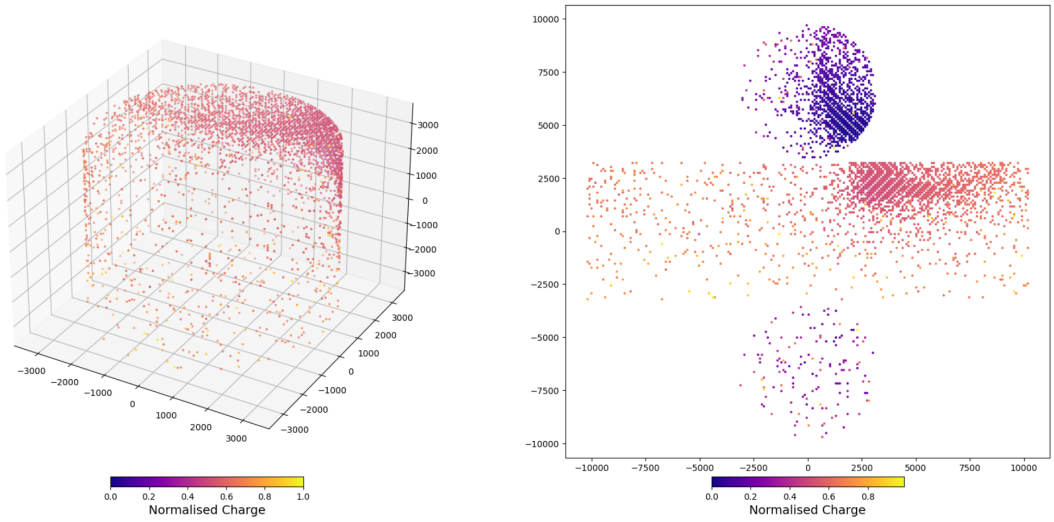


**(a)** **(b)**

**Figure 5.6:** (a) A 3-dimensional display of a simulated electron event in the Hyper-K; (b) The 2D version of the same event display.

On the other hand, with PointNet, a deep learning model capable of performing classification, part segmentation and semantic segmentation tasks (as demonstrated in Figure 5.7), one can input 3D data directly into the model in the form of point clouds [137]. A point cloud is a set of unordered points, where each point is designed to be a 3-vector of Cartesian coordinates, sampled from a shape. The point cloud datasets are required to have three properties:

- Firstly, the points must be unordered, i.e. they have to be invariant to $N!$ permutations, where $N$ is the number of points in one set;
- Following from the previous property, the points are also required to be invariant under transformation; and
- Lastly, the neighbouring points need to be meaningfully correlated. In other words,

the local structures are an important aspect of the point cloud; each point cannot exist in isolation.

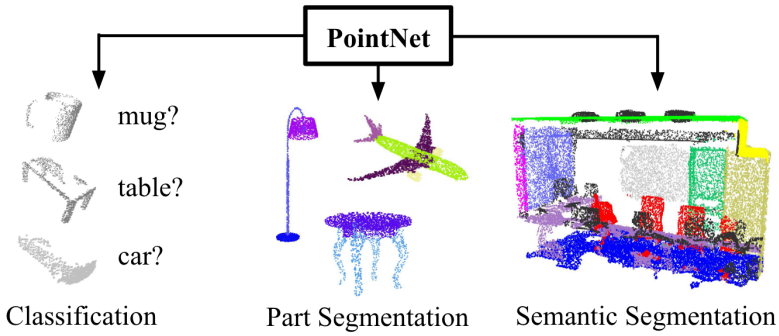


**Figure 5.7:** PointNet is able to handle three types of tasks: classification, part segmentation, and semantic segmentation [137]. Classification sorts point sets into distinct shape classes, part segmentation isolates individual object components, and semantic segmentation labels each point to provide detailed insights into object and scene compositions.

PointNet is an impressively robust model that retains high efficiency even with 50% of the input data missing; it was reported to have dropped merely 3.8% in classification efficiency compared to training with 100% of data [137]. Figure 5.8 displays the lower and upper bound of an input point cloud that would result in the same model-determined informative points.

For the application to Hyper-K events, each point cloud in the dataset represents an event, while each point within the cloud represents a PMT that has recorded Cherenkov photon(s); in addition to the $(x, y, z)$ information of a hit PMT (Figure 5.6a for example), a point usually has three other features, which are the charge it has recorded, the hit time from the event trigger and a PMT-type flag indicating whether the point is a 20-in or 3-in PMT. Additionally, there is an option to include the PMT orientation represented by the point.

In this thesis, the capability of PointNet to perform particle classifications and physics kinematics reconstruction is explored. The results of these studies discussed in the Section 6.4 and 6.5 are produced with a PointNet model modified for Hyper-K geometry under the WatChMaL framework [138].

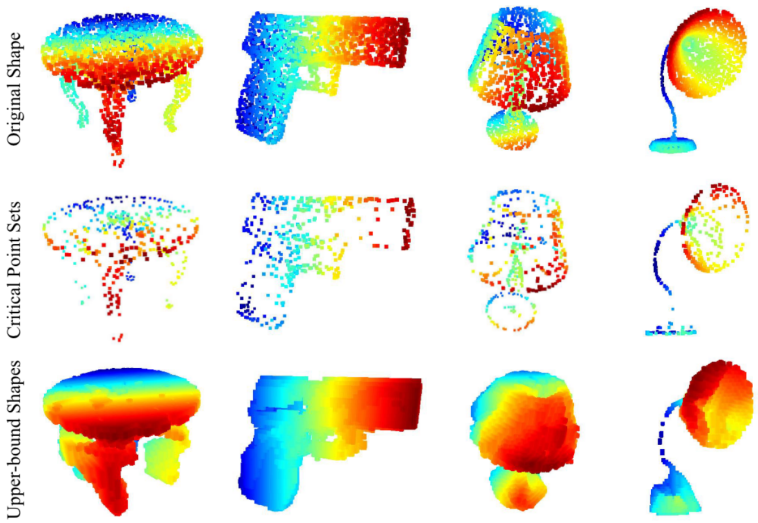


**Figure 5.8:** The maximum (upper-bound) and minimum (critical) number of points in shapes within which PointNet retains its ability to classify effectively [137]. The colour coding on the plot indicates the 3D depth of each data point, with redder points being closer to the camera and bluer points further away.

### 5.3.1 PointNet Architecture

Figure 5.9 illustrates the architectural design of PointNet[137] for an input point cloud of population $n$, where each point has three features, namely the Cartesian coordinates. Since only the classification model was adopted in the Hyper-K application, the segmentation network is thereby not discussed in detail.

The classification section of the network is constructed such that it learns to identify the most informative points out of the whole dataset and preserves the reason for their selection. Then, a global descriptor for the event is distilled from these selected points. Three main components have been constructed to achieve the classification objective, which are two feature transformations, three MLPs, and a down-sampling step in the form of max pooling.

#### Feature Transformations

The feature transformation steps, details shown in the dotted boxes in Figure 5.9, involve the data undergoing affine geometric transformations so as to align every event to a 3D canonical space. Essentially, events are spatially transformed such that they are presented at the ideal angle according to the model. These manipulations only translate

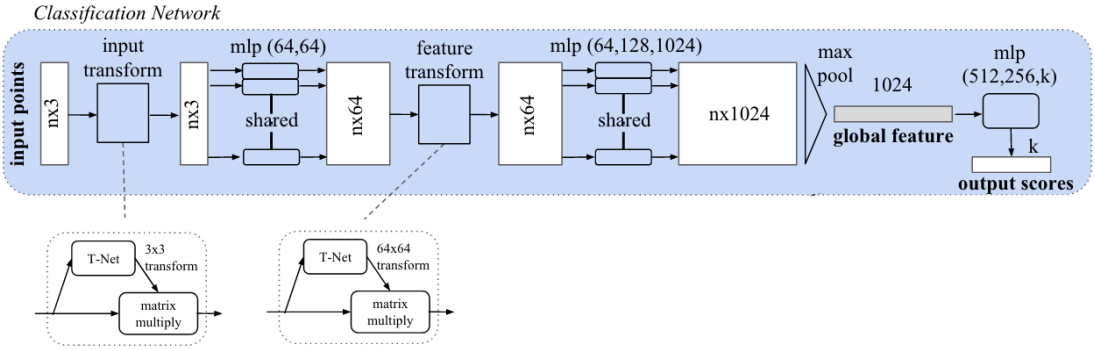


**Figure 5.9:** The architecture of PointNet for classification tasks [137]. For a typical PointNet structure used in the paper, the input $n$ data points, each with three features ($x$, $y$ and $z$), of every object to be classified, are first transformed/rotated to align with the canonical space. This transformation does not allow information communication between data points. Then the rotated points are fed into a three-layer MLP to aggregate local information, where each output point now contains 64 features. This is followed by another rotation transformation and MLP combination to allow further mixing of local knowledge, and the number of features per point comes to 1024. Through the max-pooling operation, which feeds the $x \times 1024$ matrix into a function that finds the maximum of the data points, the matrix is distilled into a single vector known as the global feature. Lastly, this vector is fed to a four-layer MLP that reduces the number of neurons from 1024 to k, where k has the dimension of the number of classes of the object to be classified.

the data points linearly. Thus, the relative positions of the points are preserved, and the number of features of the output data matches that of the input.

An example of such transformation in 2D can be found in Figure 5.10 [139], where the original input $U$ is translated into $V$ using an affine transformation matrix $\tau_\theta(G)$. Mathematically, the relationship between the output/target coordinates, $(x_i^t, y_i^t)$, and the input/source coordinates, $(x_i^s, y_i^s)$, can be expressed as [139]

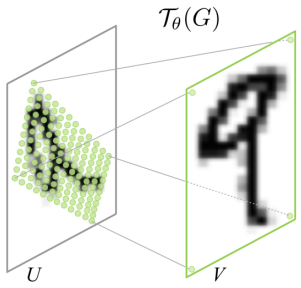


**Figure 5.10:** Before and after the affine transformation matrix $\tau_\theta(G)$ [139].

$$\begin{pmatrix} x_i^s \\ y_i^s \end{pmatrix} = \tau_\theta(G_i) = \boldsymbol{A}_\theta \begin{pmatrix} x_i^t \\ y_i^t \\ 1 \end{pmatrix} = \begin{bmatrix} \theta_{11} & \theta_{12} & \theta_{13} \\ \theta_{21} & \theta_{22} & \theta_{23} \end{bmatrix} \begin{pmatrix} x_i^t \\ y_i^t \\ 1 \end{pmatrix}. \tag{5.4}$$

Note that the aforementioned 2D spatial transformation example differs from PointNet in the spatial transformation matrix; however, the underlying translation principle remains the same.

### Multi-Layer Perceptrons in PointNet

In the PointNet application, MLPs are employed to aggregate local information by first increasing the features of each point in the set from 5 to 64 through a hidden layer of 64 neurons, then from 64 to 1024 using an MLP with two hidden layers of 64 and 128 neurons each. In addition, a third MLP is implemented to aggregate the model-selected unphysical features down to a global descriptor, e.g. class scores, of a given event.

The activation functions used in these MLPs are rectified linear units (ReLU) [140]. Taking the form of

$$f(x) = \max(0, x), \tag{5.5}$$

it returns $x$ when $x$ is positive and returns 0 otherwise. This simplicity allows for faster computation and helps mitigate issues like the vanishing gradient problem in deep neural networks, where the vanishing gradient problem occurs during the training of deep neural networks as gradients of the loss function become exponentially smaller as they are propagated back through each layer. This diminishing gradient results in very small updates to the weights of the earlier layers, severely slowing down the learning process or causing it to stall completely.

### Down Sampling

Downsampling, or max pool operation according to Figure 5.9, is the act of distilling to find the most interesting point and a crucial step in the PointNet structure. Since the input point cloud is resilient to permutations, a symmetric function can be employed to reduce the number of neurons, which are the outputs of the second MLP, from 1024 in the above example down to one. Symmetric functions are functions that are blind to the order in the set, operations such as finding the maximum, minimum, sum, or mean of a number set are all valid symmetric functions.

### 5.3.2 PointNet for Hyper-K

The PointNet application to the Hyper-K data is made through the WatChMaL framework [138], managed by the WatChMaL organisation, which oversees the application of machine learning techniques on particle identification (PID) and kinematic variable reconstructions for water Cherenkov detectors. Current members are involved in applying a variety of 2D and 3D CNNs to the Hyper-K, IWCD and Super-K's low-energy MC data.

#### PointNet for Classification

The signal/background classification segment of the PointNet model is trained to separate $e^-$ events (signal class) from three classes of background events, $\gamma$, $\mu^-$ and $\pi^0$, with each class assigned a unique class value: 0 for $\gamma$, 1 for $e^-$, 2 for $\mu^-$ and 3 for $\pi^0$.

The model provides softmax scores for each input class, where softmax scores are the values that translate the raw outputs of the neural network into a probability distribution over the class values. The softmax function ensures that these scores fall within a range of 0 to 1, summing to 1 across all potential classes, thus offering a probabilistic interpretation of each event's class membership. As an example, in the binary classification scenario of $e^-$ versus $\mu^-$ events, the softmax scores are outputted as a NumPy array [141] with two columns, where the first column represents the electron class and the second is the muon class. For a true electron event, if the model is working properly, it should assign a number close to 1 to the first entry and a value close to 0 to the second; the two values would sum up to 1.

While PointNet is capable of multi-class discrimination, e.g. performing classification between $e^-$, $\mu^-$ and $\pi^0$ together, through trial, it is found that it achieves optimal performance in a binary or two-class setting.

#### PointNet for Kinematics Reconstruction

The kinematics reconstruction tasks using PointNet focus either on momentum reconstruction or position reconstruction and are approached one particle at a time to ensure precision and accuracy.

As discussed in the previous section, PointNet first extracts a global feature vector from the input data, a condensed representation encapsulating the essential information required for later. Then, a regression network is employed to process the global feature vector. The architecture of this network is tailored to gradually refine the broad array of features into specific, targeted predictions; in other words, it is designed to map the extracted global features to the desired kinematic outputs, such as the energy level or the spatial position of a particle. This network transforms the high-level features into precise kinematic properties, thereby translating complex input data into meaningful physical information.

## 5.4 PointNet Result Interpretation

### 5.4.1 Classification

In the context of machine learning, a Receiver Operating Characteristic (ROC) curve is a plot that illustrates the capability of a binary classifier system as its discrimination threshold is varied. It is created by plotting the True Positive Rate (TPR) against the False Positive Rate (FPR) at various threshold settings. The TPR is defined as the ratio of correctly identified signal events, True Positives (TP), to all events classified as signal:

$$\mathrm{TPR} = \frac{\mathrm{TP}}{\mathrm{TP} + \mathrm{FN}}, \tag{5.6}$$

where FN means False Negative. Similarly, FPR is defined as the ratio of incorrectly identified background events, False Positives (FP), to all events classified as backgrounds:

$$\mathrm{FPR} = \frac{\mathrm{FP}}{\mathrm{FP} + \mathrm{TN}}, \tag{5.7}$$

where TN represents True Negatives.

The softmax scores derived from the PointNet model serve as a basis for ranking event predictions. A threshold value is chosen for the binary classification task. Events that yield a signal class softmax score above this threshold are classified as signals, while those below are designated as background. Adjusting this threshold enables a controlled manipulation of the True Positive Rate (TPR) and False Positive Rate

(FPR). This variation in the threshold produces a spectrum of TPR and FPR pairs, which, when plotted, form the ROC curve; an example can be seen in Figure 5.11a, graphically representing the model's classification performance. When the classification performance is close to perfect, the details of the ROC curve are more difficult to inspect. In this case, the TPR and inverse FPR, commonly known as the signal efficiency and background rejection in particle physics, are used as $x$ and $y$ in the ROC curve plotting, an example can be found in Figure 5.11b.

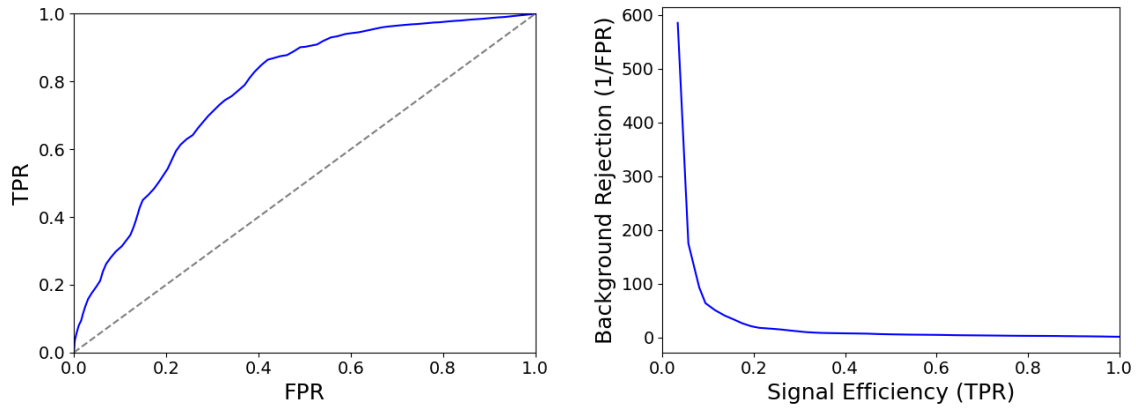


**(a)** **(b)**

**Figure 5.11:** (a) An example of a conventional ROC curve is shown in blue [142]. The dotted line represents a model with no discrimination ability (equivalent to random guessing), i.e. its AUC is 0.5; (b) Inverse FPR (background rejection) plotted against TPR (signal efficiency) of (a) to increase ROC curve detail visibility when the classification is close to perfect.

The Area Under the Curve (AUC) of the ROC curve is generally used as the figure of merit when discussing binary classification outcomes. It quantifies the overall ability of the model to discriminate between the positive and negative classes irrespective of the threshold chosen. The AUC ranges from 0.5 to 1, with a value of 0.5 representing a model with no discrimination ability (equivalent to random guessing) and 1 representing a perfect model that achieves 100% sensitivity across all thresholds.

In addition to the investigation of the overall performance, the classification performance as a function of the true kinematics parameters of the track, e.g. momentum, vertex positions, etc., are also explored, providing a more detailed analysis of the results. Theoretically, this performance analysis can be applied to every point on the ROC curve; however, it would be very time-consuming, and a large portion of the

obtained plots bear minimal meaning. Thus, it is decided that the performance would only be analysed at a certain high TPR value, as suggested by the intersection between the red line and blue curve in Figure 5.12. The selected values will be stated before presenting the signal efficiency against true kinematics plots in the next chapter. The plotting method of the figures is described in the following section.

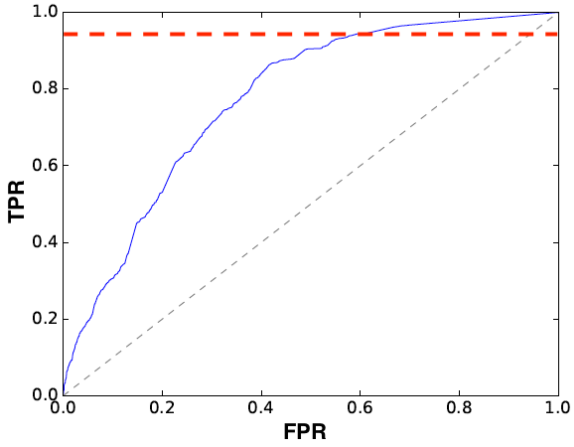


**Figure 5.12:** A ROC curve (blue) with a line (red) indicating where the event discrimination performance is evaluated.

### 5.4.2 Kinematics Reconstruction

Unlike the classification task, the reconstruction task does not have a straightforward number to summarise the overall performance. A comparison is made between true values and predictions from a model like PointNet to evaluate the resolution of energy and position estimations as functions of kinematics variables. For this analysis, events are first binned according to a true kinematic variable, such as momentum or position. The resolution in each bin is quantified by the 68th percentile of the absolute residuals, where the residual of an event is the difference between predicted and true values, normalised only for the energy predictions. These measures of resolution are then plotted against the centre values of the kinematic variable bins. Figure 5.13 is an illustration of the method described above for plotting against true electron momentum.

The graphical representation of reconstruction resolution allows one to discern how the model's prediction accuracy varies with different true kinematic conditions. The process is repeated for multiple sets of predictions from PointNet and FiTQun (dis-

cussed in the next chapter) to compare their performance. This methodical approach to assessing the model's predictions provides a detailed understanding of its accuracy in reconstructing various physical parameters across the range of true values.

## 5.5 Summary

This chapter has covered various structures used in the machine learning field, including ANNs, Deep Learning, and MLPs. Among these models, PointNet stands out as an excellent candidate for Hyper-K data analysis.

PointNet offers a significant advantage in its ability to process unordered point clouds, considerably reducing the pre-processing typically necessary for 2D CNNs. This capability is especially beneficial for handling Hyper-K data, where PointNet is tasked with crucial functions such as particle classification and kinematics reconstruction. Notably, compared to traditional statistical reconstruction tools, PointNet is anticipated to increase the efficiency of processing each Hyper-K event. This improvement in processing time, along with a detailed examination of the inner workings of the statistical tool and a performance comparison between it and PointNet, will be thoroughly discussed in Chapter 6.

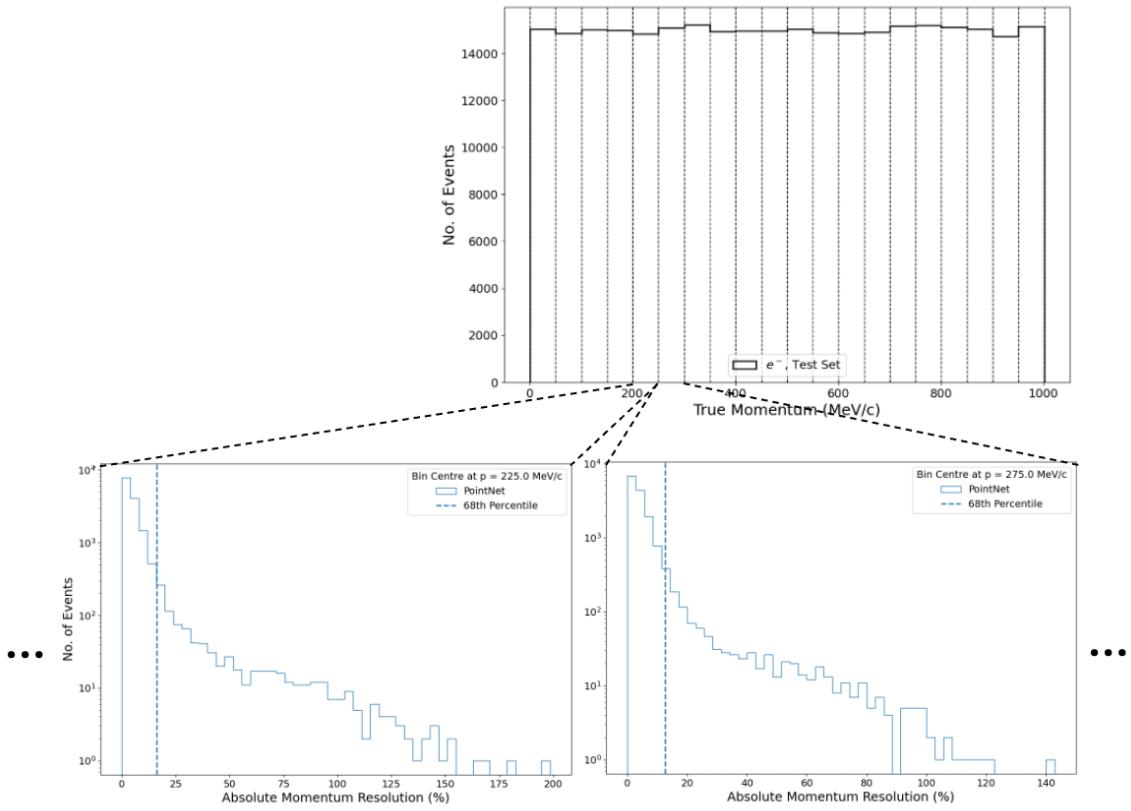


**Figure 5.13:** A diagram showcasing the plotting of resolution against true kinematics for reconstruction results. The events are first sorted into bins based on their true kinematic variable value, momentum in this case. The reconstruction resolution for each bin is then chosen to be the value at the 68th percentile of the resolution distribution.

# Chapter 6

# Physics Reconstruction at Hyper-Kamiokande

In the context of the Hyper-K experiment, precise particle classification and kinematic reconstruction are essential. These processes are key to interpreting the neutrino interactions captured by Hyper-K's advanced detector system, thereby ensuring the accuracy and reliability of the experimental findings. There is an ongoing effort to migrate FiTQun, which is a statistics-based physics reconstruction tool in the Super-K, to the Hyper-K geometry. While FiTQun has been an effective and precise tool for reconstruction, its main limitations are computational expense and slow processing time. On the other hand, PointNet, as discussed in Section 5.3, represents the emerging trend of applying Convolutional Neural Networks (CNNs), a branch of machine learning, in neutrino physics, offering a much quicker reconstruction process once trained.

This chapter presents a detailed efficacy analysis comparing the use of PointNet with FiTQun in signal-background discrimination and kinematics reconstruction within the framework of the Hyper-K experiment against the backdrop of simulated data. The discussion begins with an overview of the theoretical foundations of FiTQun and then delves into a brief discussion on WCSim, the Hyper-K detector simulation software, followed by a detailed account of the kinematic distributions of the simulated particles. This sets the stage for a practical evaluation, where the focus will be on their performance in specific tasks crucial to Hyper-K, such as signal-background separation and the accuracy of kinematic reconstructions. The comparative analysis aims to quantify

the improvements offered by machine learning over traditional methods and to identify scenarios where conventional techniques may still be advantageous.

## 6.1 Hyper-Kamiokande Analysis Framework

In Super-K and Hyper-K, neutrino events are captured through the charge and timing data from each PMT hit. Before this raw data can be used in physics analyses, it must undergo a process of reconstruction. The reconstruction algorithms are essential for discerning both the type and kinematics of the particles resulting from the neutrino interactions. Figure 6.1 outlines the structure of the overall analysis framework for Hyper-K. The reconstruction algorithm in this pipeline can either be a machine learning algorithm like PointNet, or a traditional statistical model such as FiTQun.

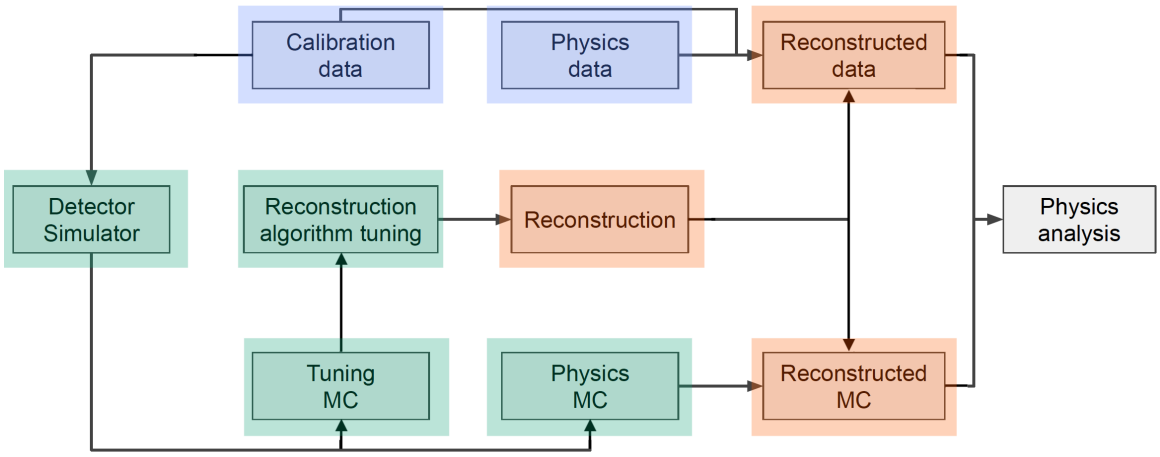


**Figure 6.1:** Current design for the data analysis framework at Hyper-K [143], where MC represents Monte Carlo, or simulated data. The framework starts with various data-taking activities (blue boxes), generating both physics and calibration data. Subsequently, the calibration data is utilised to tune various software (green boxes), meanwhile, the MC data is generated during this step. Finally, both real and simulated data undergo reconstruction with the selected algorithm, before being fed into the downstream analysis process (orange boxes).

The processes that precede physics reconstruction can be broadly divided into three categories, following the sequence of the pipeline:

1. Obtaining data (both data used in physics analysis and various calibrations) (marked blue).

   Physics data collection is a continuous operation, which runs without break through-

out the years, while the calibration activities can range from low-impact — conducted alongside the regular physics data acquisition or utilising selected physics data for calibration purposes, such as OD PMT constants monitoring and T-Q map monitoring in the ID using the OD laser — to more disruptive calibration campaigns like OD PMT saturation parameter calibrations;

2. Parameter Tuning and Physics MC Generation (marked green).
   For the analysis detailed in this chapter, WCSim is the default detector simulation software. The tuning of WCSim involves a rigorous process of comparing simulated outcomes with actual data. Additionally, the reconstruction algorithms, such as FiTQun and machine learning algorithms, are adjusted to align the reconstructed results with the initial conditions of the particles introduced into WCSim. This stage also encompasses the generation of simulated data;
3. Particle Information Reconstruction (marked orange).
   In the final phase, the reconstruction process takes place, during which both real and MC data are processed to retrieve particle information from simple PMT signals.

## 6.2 FiTQun for Physics Reconstruction

At Super-K, FiTQun plays a pivotal role in the reconstruction of high-energy events. Its maximum-likelihood approach was first developed by the MiniBooNE experiment [144], then adapted for the Super-K geometry in 2016 [136]. There has been an ongoing effort to modify FiTQun for Hyper-K reconstruction, and the latest update can be found in Ref. [145]. The following section discusses FiTQun in the Super-K geometry and event information context. However, the foundational premise also holds true for the application to Hyper-K event reconstruction.

At the core of the FiTQun algorithm is a likelihood function that encompasses all PMT information in the Super-K for any event. For a given particle hypothesis, $\boldsymbol{x}$, defined with seven variables (track parameters), including particle type, vertex, direction and momentum[1], the function is constructed with the unhit and hit PMT

[1]There can be more than one type of particles included in the hypothesis.

probabilities,

$$\mathcal{L}(\boldsymbol{x}) = \prod_{j}^{\text{unhit}} P_j(\text{unhit}|\boldsymbol{x}) \prod_{i}^{\text{hit}} \{1 - P_i(\text{unhit}|\boldsymbol{x})\} f_q(q_i|\boldsymbol{x}) f_t(t_i|\boldsymbol{x}) \tag{6.1}$$

where $P_j(\text{unhit}|\boldsymbol{x})$ and $\{1 - P_i(\text{unhit}|\boldsymbol{x})\}$ are the probabilities that the $j$-th/$i$-th PMT do not/do record a hit given hypothesis $\boldsymbol{x}$, and the $f_q(q_i|\boldsymbol{x}) f_t(t_i|\boldsymbol{x})$ term represents the probabilities of the $i$-th PMT registering $q_i$ amount of charge at time $t_i$. The hypothesis $\boldsymbol{x}$ contains seven parameters to be fitted, namely the particle vertex position ($x$, $y$ and $z$), the time of interaction ($t$), its scalar momentum ($p$) and its travel direction ($\theta$, $\phi$). The most optimal reconstructed variables are the ones that maximise the likelihood function; however, in practice, it is much more computationally viable to minimise the log-likelihood function, $\ln \mathcal{L}$, for reconstruction.

A twist on the original likelihood function is that the charge collected by a PMT and the output of the subsequent electronic response is not directly correlated with the track parameters of a particle. Hence, the Poisson mean of charge (in p.e.) expected to be detected at $i$-th PMT, $\mu_i(\boldsymbol{x})$, is introduced as a replacement for $\boldsymbol{x}$, and Equation 6.1 becomes

$$\mathcal{L}(\boldsymbol{x}) = \prod_{j}^{\text{unhit}} P_j(\text{unhit}|\mu_j) \prod_{i}^{\text{hit}} \{1 - P_i(\text{unhit}|\mu_i)\} f_q(q_i|\mu_i) f_t(t_i|\boldsymbol{x}) \tag{6.2}$$

where the $\mu_i$ value is comprised of two components, one direct component from the Cherenkov radiation and an indirect component from other processes that happen in water, such as scattering and reflections. The two elements are individually found by integrating over the Cherenkov emission profile at the PMT with other factors. A detailed description of the derivation for all the components mentioned above can be found in Ref. [136, pp. 56-96].

The reconstruction of the electron, muon and $\pi^{\pm}$ track information falls under FiTQun single-ring hypotheses. For each type of particle, the reconstructed parameters include a Negative Log-Likelihood (NLL) score $-\ln \mathcal{L}$ (note that in the following text the '-' is always dropped), vertex position in Cartesian coordinates, momentum at the vertex, direction of travel, etc., a comprehensive list can be found in Ref. [146].

The NLL score for each hypothesis of a different particle type is compared to perform particle identifications (PID). For instance, for a given track, if the NLL score of the electron hypothesis is greater than that of the muon hypothesis, i.e. $(\ln \mathcal{L}_e) > (\ln \mathcal{L}_\mu) \rightarrow (\ln(\mathcal{L}_e/\mathcal{L}_\mu)) > 0$, then the track is more likely to be an electron.

In the T2K experiment, which is a long-baseline neutrino oscillation experiment designed to measure oscillation parameters and CP-violating phase, Neutral Current $\pi^0$ (NC$\pi^0$) events in the Super-K tank are one of the two dominant backgrounds to the $\nu_e$ appearance signals. The $\pi^0$ from these events are caused by neutrinos interacting with an oxygen nucleus, and once created, the $\pi^0$ mostly decay immediately into two photons, which in turn produces two $e^-e^+$ pair travelling along the photon paths. Under certain circumstances, one photon can carry away most of the energy of the $\pi^0$ in the lab frame and create a Cherenkov ring pattern mimicking one created by an electron from a $\nu_e$ CC interaction in Super-K. Therefore, FiTQun is also designed to reconstruct $\pi^0$ events using a multi-ring fitting hypothesis. This hypothesis is an extension of the single-ring electron hypothesis, where two $\gamma$'s with a shared vertex is introduced into the formulation. There are 12 track parameters outputted from the FiTQun $\pi^0$ reconstruction, which are the usual ones for the $\pi^0$ (including an NLL score, momentum, position, direction, etc.) as well as additional parameters for fitting the secondary $\gamma$ particles.

## 6.3 Data Production to Analysis Pipeline

The results discussed later in this chapter emerge from a comprehensive pipeline that spans from specifying the requirements for simulated events to analysing the reconstruction outcomes using PointNet and FiTQun. Figure 6.2 outlines this entire process from beginning to end. Subsequent subsections will delve into the setups related to detector simulation (Section 6.3.1), followed by an exploration of data generation, partitioning, and processing through PointNet and FiTQun in Section 6.3.2.

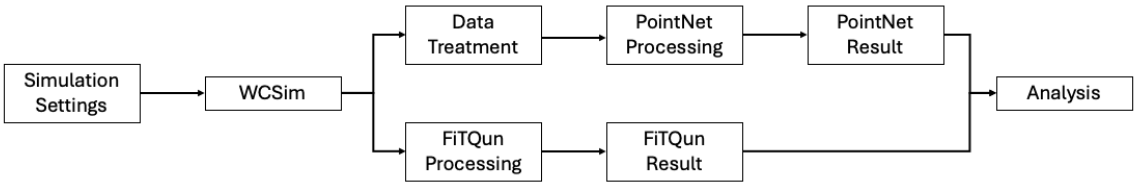


**Figure 6.2:** Data production to analysis pipeline employed to produce results presented in this thesis.

### 6.3.1 Hyper-Kamiokande Detector Simulation

Water Cherenkov Simulator (WCSim) [147] is a sophisticated and adaptable event simulator primarily designed for use in water Cherenkov detectors. As an open-source tool, it is developed within the GEANT4 framework [74] and adopts ROOT [148, 65] as the default data analysis toolkit. With a core functionality of simulating the passage and interactions of particles in water, including the generation of Cherenkov radiation, WCSim has found significant application in large-scale neutrino observatories such as Hyper-K and its near detector IWCD.

As mentioned in Section 2.4, the Hyper-K detector is planned to house both 20-in PMTs and mPMT modules (HybridHK geometry), and this combination of PMTs of different sizes was first reflected in the detector simulation developed on a forked WCSim repository known as nuPRISM [149]. Note that the nuPRISM simulation does not contain Hyper-K OD. The development of the HybridHK geometry in nuPRISM was completed in May 2021, and all the results presented in the following sections are generated with this branched-off WCSim repository; the simulation was compiled on Compute Canada's (CC) Cedar Cluster on 21 October 2021. Before 2 June 2023, the simulated Hyper-K ID contained only 20-in PMTs; release v1.11.0 [150] published on that day has successfully merged nuPRISM into the main production branch of WCSim, and since then the HybridHK simulation includes both 20-in PMTs and mPMTs in the ID and an OD section.

Figure 6.3 illustrates the PMT layout in the barrel region of the simulated ID, where cyan dots indicate 20-in PMTs and purple clusters represent mPMTs. This version of the simulation contains 18952 20-in PMTs and 4715 mPMTs, thus a total of 89604 3-in PMTs from all the mPMT modules. The geometry is designed such that the mPMTs

would occupy the diagonals of a $5 \times 5$ PMT grid.

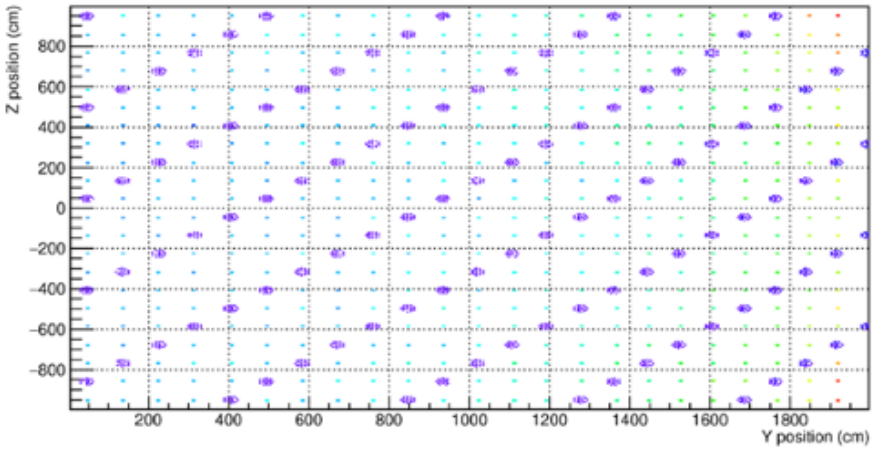


**Figure 6.3:** The barrel layout of the Hybrid Hyper-K geometry. There are a total of 18952 20-in PMTs (cyan) and 4715 mPMTs (purple) in this version of the Hyper-K ID.

### 6.3.2 Data Generation, Partition and Processing

For this analysis, three million events of each particle type concerned ($e^-$, $\mu^-$, $\pi^0$ and $\gamma$) are generated, and for the ease of partial data regeneration, these events are simulated in a batch of 3000 events; hence, WCSim would output 1000 files for each particle. The particles' kinematics follow the parameters outlined below, all generated using the nuPRISM WCSim on the CC Cedar cluster:

- Energies: uniformly distributed between $[0, 1000]$ MeV plus the respective Cherenkov energy threshold as stated in Table 2.1. This range is specifically selected as it encloses the lower end of the Hyper-K detectable energy spectrum, and it aligns with the peak region of the neutrino beam energy distribution in the T2K experiment;
- Positions: uniformly distributed within the Hyper-K ID volume; and,
- Directions: isotropically distributed across $4\pi$.

Note that due to human error, the effective Cherenkov threshold of $\pi^0$ (3.07 MeV) was mistakenly set to the same as $\mu^-$'s (160 MeV) in the simulation. This error resulted in an increased amount of training data for $\pi^0$ in the higher energy region under study, potentially enhancing the ability of PointNet to distinguish $\pi^0$ from $e^-$ above 1000 MeV. Further studies are required to understand the impact of this discrepancy

fully.

The dataset division for Training, Validating, and Testing (TVT) PointNet adheres to the following ratios: for classification tasks, it is split into 1.5 million (5 parts), 0.3 million (1 part), and 1.2 million (4 parts) events, respectively. For kinematics reconstruction tasks, the ratio is 7:2:1, corresponding to 2.1 million, 0.6 million, and 0.3 million events. Additionally, the 1.2 million test events from the classification tasks were processed using FiTQun for comprehensive reconstruction. The reasoning behind the above partitions is discussed in Section 6.5.2.

Once the partition index files for each particle type are created using the specified ratios, the kinematics distribution within each set for each particle is examined. This is done to confirm that the distribution in the divided datasets accurately reflects the overall distribution present in the entire dataset. Figure 6.4 presents normalised event counts for particles ($\gamma,\ e^-,\ \mu^-,\ \pi^0$) across datasets (top) and their distribution ratios relative to the training set for model consistency (bottom) for TVT $= 7:2:1$. Similarly, Figure 6.5 shows the Cherenkov-energy-threshold-subtracted versions of the distributions presented in Figure 6.4. The momenta for each simulated particle across all datasets are uniformly distributed as expected.

The accompanying series of normalised 2D histograms in Figure 6.6 provides a visual representation of the spatial distribution for the four types of particles within the detector volume. These plots are categorised across training, validation, and test datasets and demonstrate the uniformity in spatial coverage achieved in the simulations. Additionally, two plots in Figure 6.7 confirm that the particle directions are isotropically distributed over the entire $4\pi$ solid angle, which aligns with expectations.

The output of the HybridHK WCSim, in ROOT file format, consists of various information about each simulated event, including,

- The ground truths about the primary particle, such as its type, initial momentum, event vertex position, etc;
- The true hits, i.e. the raw hits before being processed by the simulated front-end electronics; and

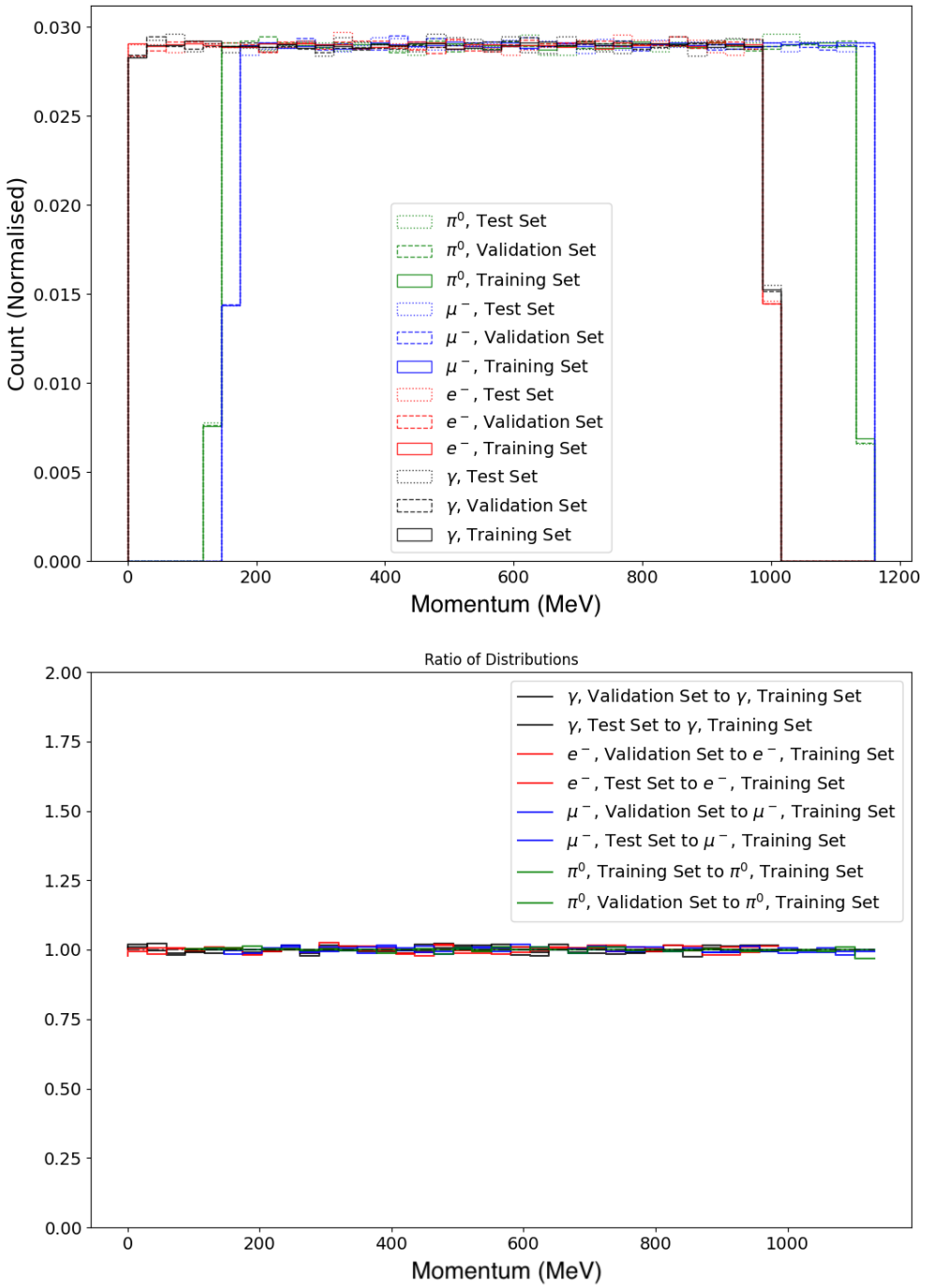


**Figure 6.4:** Comparative analysis of particle momentum distributions: normalised counts of particle events ($\gamma$, $e^-$, $\mu^-$, $\pi^0$) across different datasets (test, validation, training) (Top). The ratio of distributions, comparing each subset (test and validation) to the training set for consistency across particle types, ensuring model robustness in classification and kinematic reconstruction tasks (bottom).

- The digitised hits (PMT numbers, recorded charges in p.e. and hit times), which have been parsed through the simulated DAQ system within WCSim.

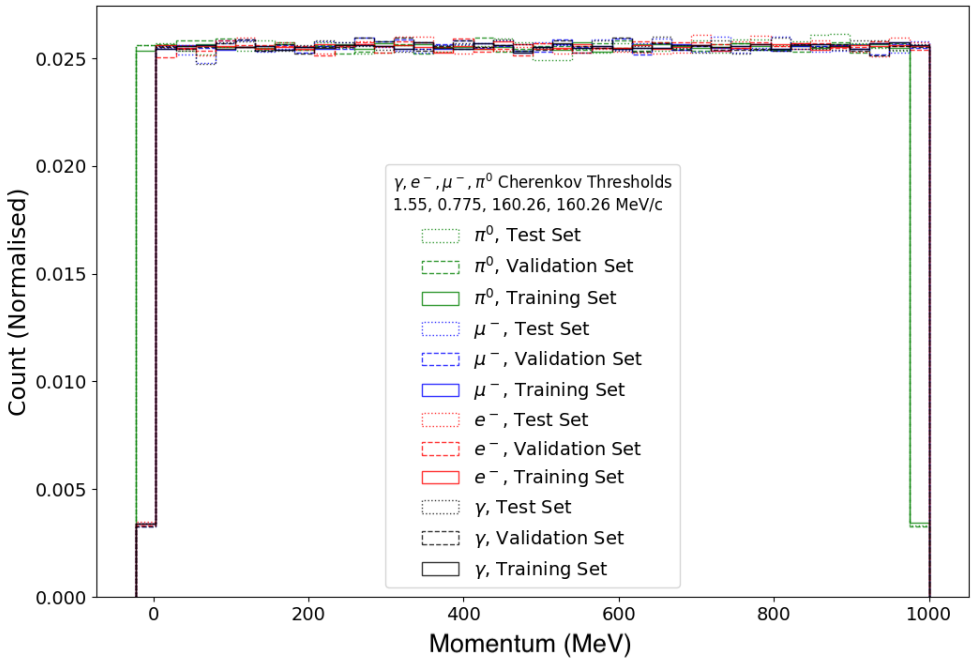


**Figure 6.5:** Normalised Cherenkov-energy-threshold-subtracted momentum distribution of $\gamma$, $e^-$, $\mu^-$, $\pi^0$ events in test, validation, and training sets. Note that the effective Cherenkov threshold for $\pi^0$ (3.07 MeV) was incorrectly set to that of $\mu^-$ (160 MeV) due to an error, potentially affecting the ability to distinguish $\pi^0$ from $e^-$ in an energy region under study and requiring further investigation to understand the impact.

The ROOT files outputted from the WCSim simulation are ready for direct use with the FiTQun framework to begin the reconstruction processes. Nevertheless, these ROOT files must undergo a two-step conversion to merge into one data file prior to being input into the WatChMaL pipeline for the training phase. The two-stage approach is designed to address the otherwise vast amount of computational resources required to process and store the intermediate data. The 4000 ROOT files for all four particles are first converted into 4000 numpy files (npz) [141], each containing all the information stripped from the corresponding ROOT file. Note that the hits recorded by the 20-in PMTs and 3-in PMTs are stored separately in all the data used by PointNet, as in this version of nuPRISM WCSim, the two types of PMTs are triggered separately (which is not realistic). Then, the various files are combined into one single data file.

In addition, the WatChMaL framework also requires the user to input a separate file describing the detector geometry, specifically, the positions and orientations of the 20-in and 3-in PMTs within the mPMT modules at Hyper-K. This detector information

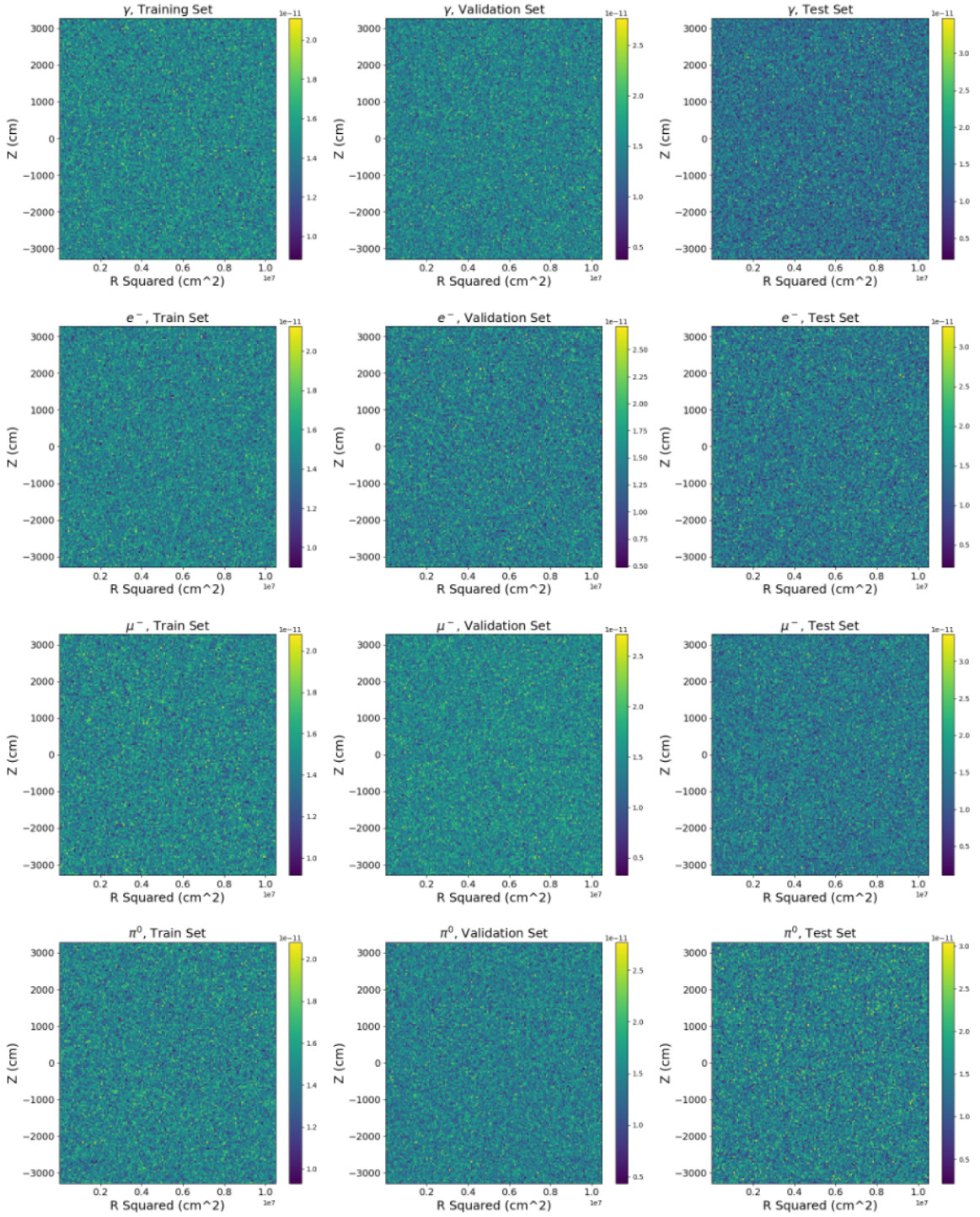


**Figure 6.6:** Heatmaps of $z$ vs. $r^2$ for particle types: the series of 2D histograms display the vertex position distribution for $\gamma$, $e^-$, $\mu^-$, $\pi^0$ particles (rows) within the detector volume, across training, validation, and test datasets (columns), illustrating uniformity in spatial coverage.

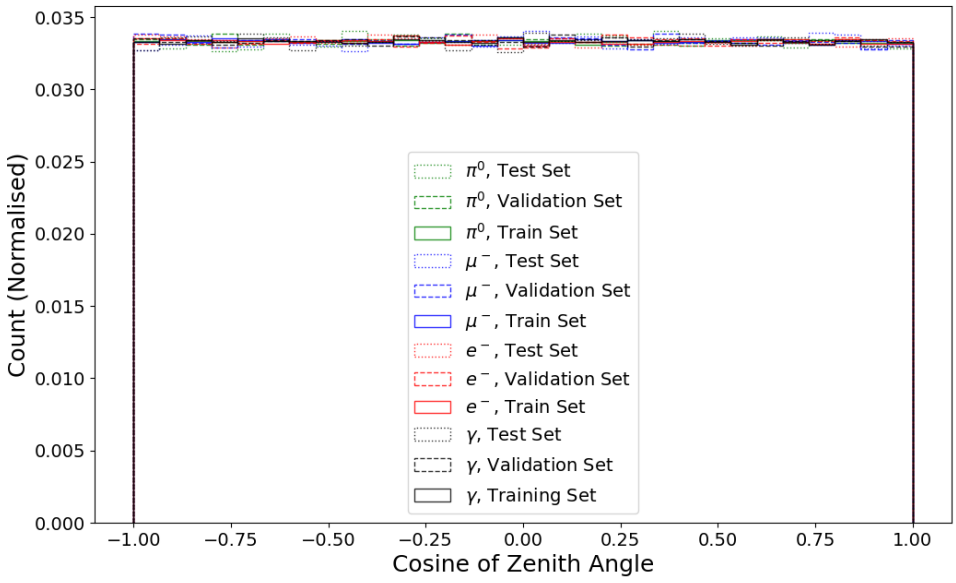


**(a)**

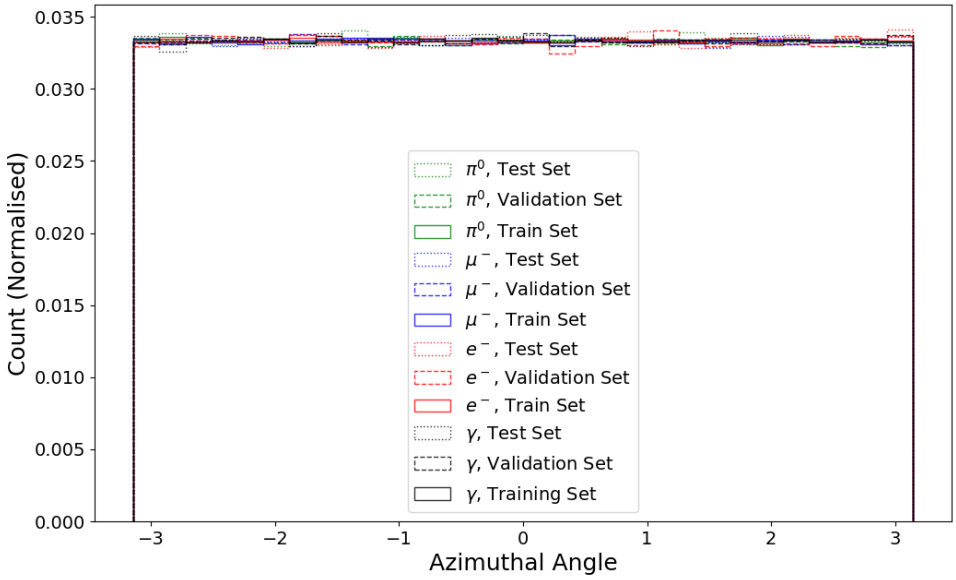


**(b)**

**Figure 6.7:** (a) The normalised distribution of $\gamma$, $e^-$, $\mu^-$, $\pi^0$ events by cosine of zenith angle across test, validation, and training datasets; (b) the corresponding distributions by the azimuth angle, also normalised and segmented by dataset type.

can be extracted from any of the aforementioned ROOT files.

## 6.4 Particle Classifications

As mentioned previously, the performance of PID is quantified by converting softmax scores from PointNet and negative log-likelihood values from FiTQun into ROC curves. The Area Under the Curve (AUC) serves as a standard metric to evaluate the overall classification effectiveness. This section will delve into the effectiveness of PointNet and FiTQun in distinguishing electron events (signals) from backgrounds, including muon, neutral pion, and photon events. The presented results will explore two data configurations: those incorporating both the 20-inch PMTs and mPMT hits and those exclusively using 20-inch PMT hits. These configurations are denoted as with mPMT (w/ mPMT) and without mPMT (w/o mPMT), respectively. The colour blue is chosen to represent PointNet outputs, while red is for FiTQun results.

### 6.4.1 $e^-/\mu^-$ Separation

Figure 6.8 displays a set of four histograms showcasing the distributions of PointNet softmax scores alongside FiTQun Negative Log-Likelihood (NLL) differences for electron and muon particle tracks, derived from the raw data with mPMT hits.

The bottom x-axis in the figure illustrates the PointNet softmax score, which ranges from 0 to 1, indicating the likelihood of the event containing a muon track (score of 0) or an electron track (score of 1). Solid and dashed blue lines represent the softmax score distributions for true electron and muon events. The majority of events are well-classified, aligning with the performance indicated by the ROC curves discussed in the subsequent figure. Notably, both the electron and muon distributions exhibit a minor peak at a softmax score of about 0.2. It was suspected that these peaks might consist of 'empty' events where no hits were recorded by either 20-inch or 3-inch PMTs despite the event kinematics being conducive to PMT hit registration. Efforts to exclude these events have been challenging, and as such, they are included in the ROC analyses that follow. Nonetheless, these 'empty' events constitute a near negligible fraction — roughly 0.1% - of the total 1.2 million test events, thereby exerting an inconsequential influence on the overarching classification outcomes.

The upper x-axis in the figure represents the FiTQun NLL Difference, which ex-

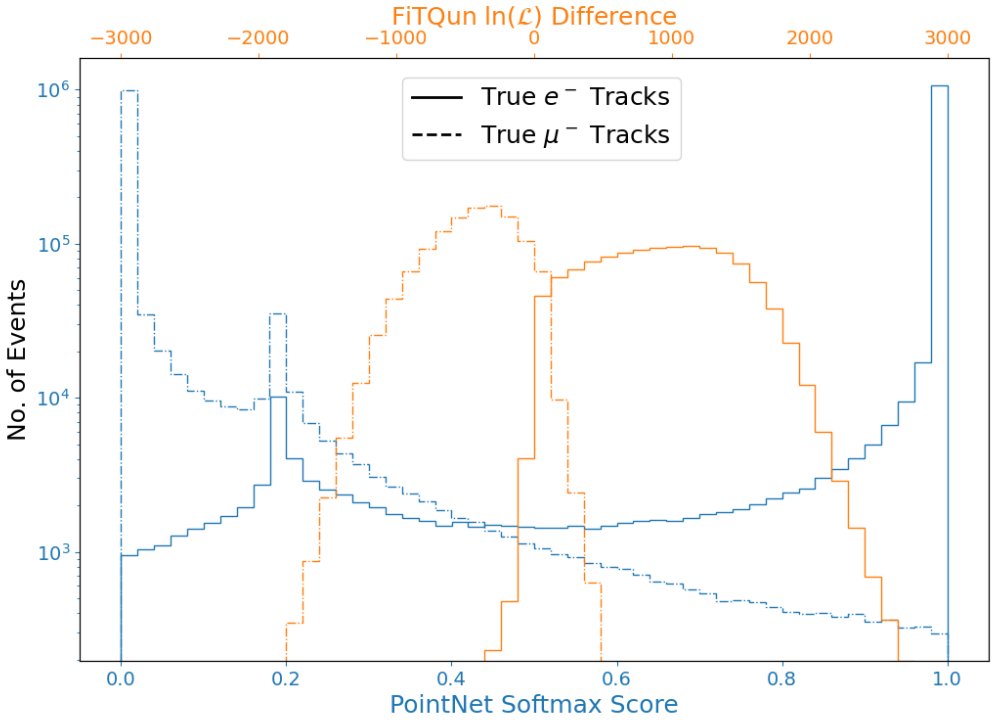


**Figure 6.8:** Histograms comparing PointNet Softmax Scores and FiTQun NLL Differences for $e^-/\mu^-$ event classification. The solid lines represent true $e^-$ events, while the dashed lines indicate true $\mu^-$ events. The peaks around the softmax score at approximately 0.2 in the PointNet classification distributions are thought to be caused by empty events with no hits recorded. However, due to data treatment difficulties, these events remained in the result analyses. The number of the empty events is in the order of thousands nevertheless, and makeup about 0.1% of the total test events, thus not hugely influential to the final PointNet classification results.

hibits a broader range due to the magnitude of NLL values. The NLL difference is calculated by subtracting the NLL of the muon hypothesis from that of the electron hypothesis, a process thoroughly described at the end of Section 6.2. An event is considered an electron event if the resulting NLL difference is positive; conversely, a negative value indicates a muon event. The distributions for true $e^-$ events are depicted with solid lines, while those for true $\mu^-$ events are shown with dashed lines. Both distributions are colour-coded in red to denote the FiTQun results. The FiTQun outcomes generally show good separation between two types of particle events.

### The ROC Curves

Figure 6.9 presents ROC curves that show the trade-off between true positive rates (TPR) and false positive rates (FPR) for the separation of electron and muon events. As a reminder, TPR represents the percentage of correctly identified signal events, while FPR portrays the rate of misidentifying background events. The ROC curves are from PointNet and FiTQun outputs, with (solid line) and without (dashed line) the use of multi-PMT signal in the processing. The uniformity of high AUC scores across the curves signifies a strong discriminative capacity of these classification models; though for data that contains mPMT signals, the AUC of FiTQun is slightly higher than that of PointNet, indicating a tiny advantage in the classification task.

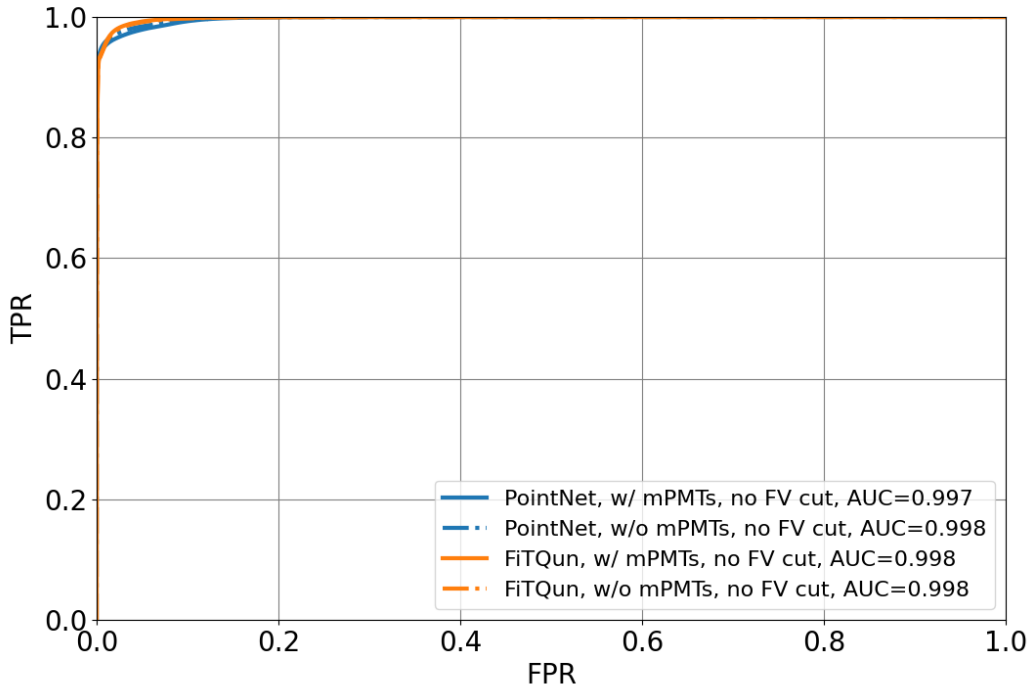


**Figure 6.9:** ROC curves illustrating the trade-off between true positive rates (TPR) and false positive rates (FPR) for $e^-/\mu^-$ event separation using PointNet and FiTQun, both with and without multi-PMT hits. The consistently high AUC scores reflect the models' discriminative power.

Further refining the plot, Figure 6.10a transforms the TPR and FPR data from the previous figure, where 1/FPR (illustrating muon background rejection) is plotted against TPR (indicating electron signal efficiency), ensuring better clarity and exposing

details that are less discernible in the standard ROC format. Since muon background rejection is the inverse of FPRs, the larger the value of background rejection, the worse the classification outcome. Hence, though not by much, the overall performance of FiTQun in $e^-/\mu^-$ Separation exceeds that of PointNet regardless of the mPMT signals. However, PointNet out-performs FiTQun in the extremely high signal efficiency region, as shown in Figure 6.10b. This phenomenon is further explored in the next section where $e^-$ signal efficiency v.s. true $e^-$ kinematics are examined.

**Signal Efficiency Against True Electron Kinematic Variables**

As mentioned in Section 5.4, the performance v.s. true kinematics analyses focus on one representative TPR/signal efficiency value. For $e^-/\mu^-$ event discriminations, the performance at FPR = 0.5% is studied, i.e. when 0.5% of $\mu^-$ events are incorrectly identified as $e^-$'s. The following figures illustrate the efficiency of electron identification as a function of various electron parameters compared between PointNet and FiTQun w/ mPMT data.

Figure 6.11 evaluates the electron event identification efficiency in relation to the true electron momentum, illustrating a rapid increase to peak efficiency from both models as momentum grows, though FiTQun overshadows PointNet's performance slightly, followed by consistent performance across the higher momentum spectrum. This is likely the cause of the slight performance boost by PointNet seen in Figure 6.10b. The drop off of efficiency when electron momentum tends towards 1000 MeV is strange; currently, there is no hypothesis to explain it.

Figure 6.12a and 6.12b depict the classification efficiency as a function of dwall — the shortest distance from the event vertex to the nearest detector wall — and towall — the distance from the event vertex to the wall along the particle's trajectory. Both metrics reveal a decline in PointNet's and FiTQun's ability to accurately classify particle tracks as the event vertices approach the detector walls. This confirms the anticipated challenge of event reconstruction in proximity to wall boundaries. In a cylindrical detector with a height of 6574 cm and a radius of 3240 cm, the maximum possible distance between two points (the tank's diagonal) is approximately 9230 cm. Events with large towall values are typically closer to the detector's corners, where

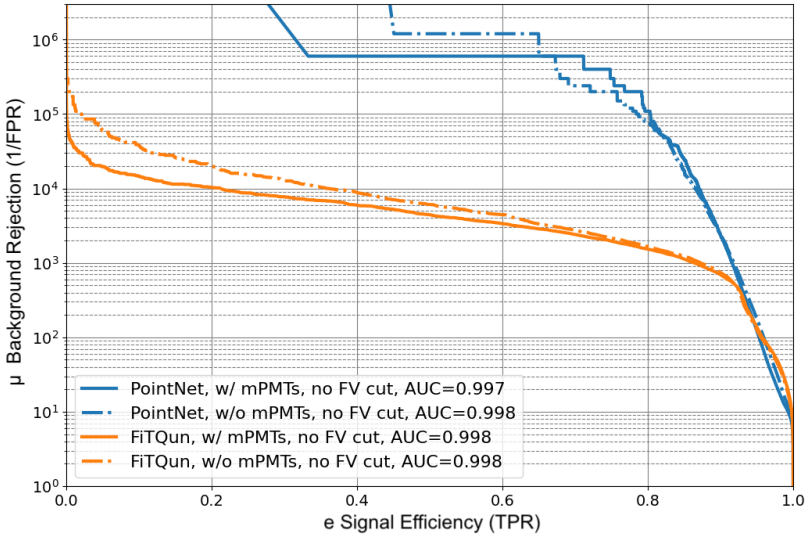


**(a)**

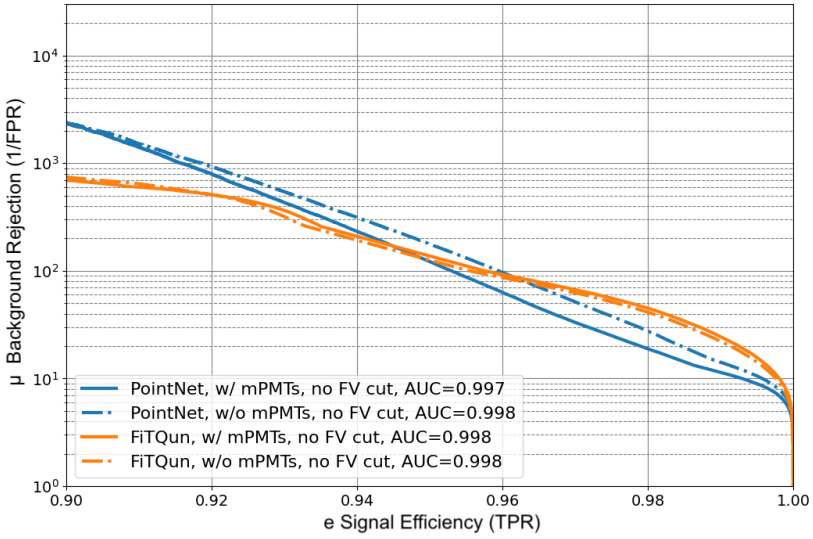


**(b)**

**Figure 6.10:** (a) The inverse of FPR ($\mu^-$ background rejection) against TPR ($e^-$ signal efficiency) is plotted to improve clarity and highlight details not visible in FPR v.s. TPR; (b) High signal efficiency region ($[0.9, 1]$) of (a).

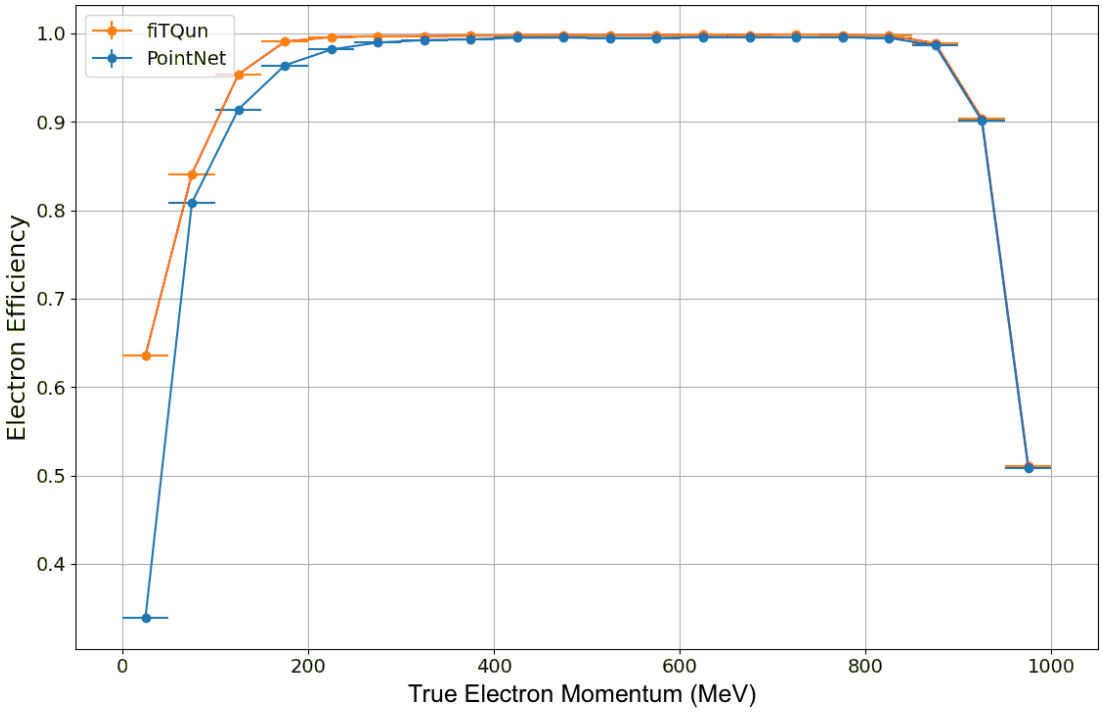


**Figure 6.11:** Electron efficiency v.s. true electron momentum for $e^-/\mu^-$ separation at 0.5% $\mu^-$ event mis-ID rate. The performance of both models is significantly worse at low energy ($[0, 200]$ MeV) and high energy ($[900, 1000]$ MeV) regions. As there are not many PMT hits in low-energy events, the lack of discrimination efficacy is understandable. However, the same cannot be said for the high-energy region.

Cherenkov ring patterns recorded by the PMTs may become significantly distorted, contributing to the reduced efficiency observed as the towall value increases.

Moving beyond spatial parameters, Figure 6.13a investigates the impact of the cosine of the zenith angle on detection efficiency, showing remarkable stability across the range, suggesting minimal influence from this angular variable. Figure 6.13b explores efficiency against azimuth angles, reinforcing the model's consistent performance irrespective of rotational positioning around the detector.

Overall, the performance of $e^-/\mu^-$ classification relative to $e^-$ kinematics generally aligns with expectations, with FiTQun demonstrating a slightly superior performance compared to PointNet.

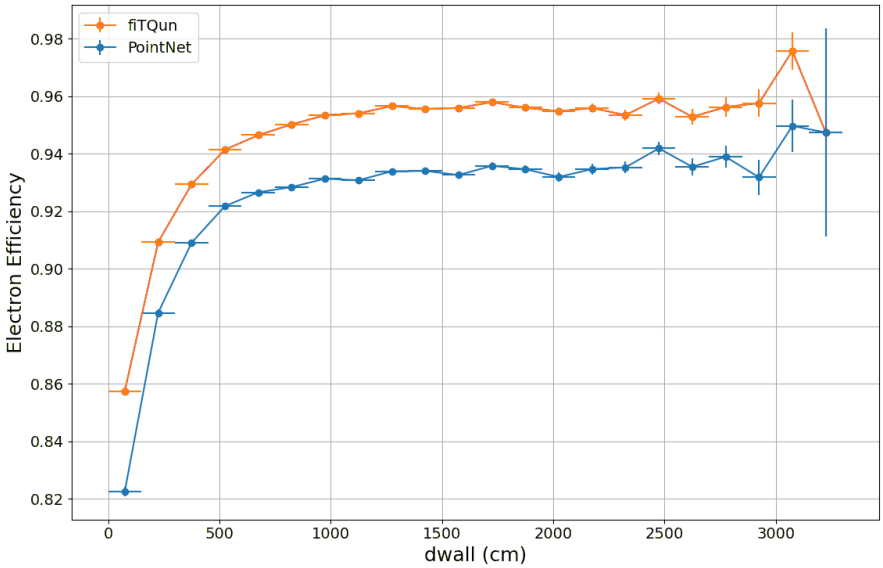


**(a)**

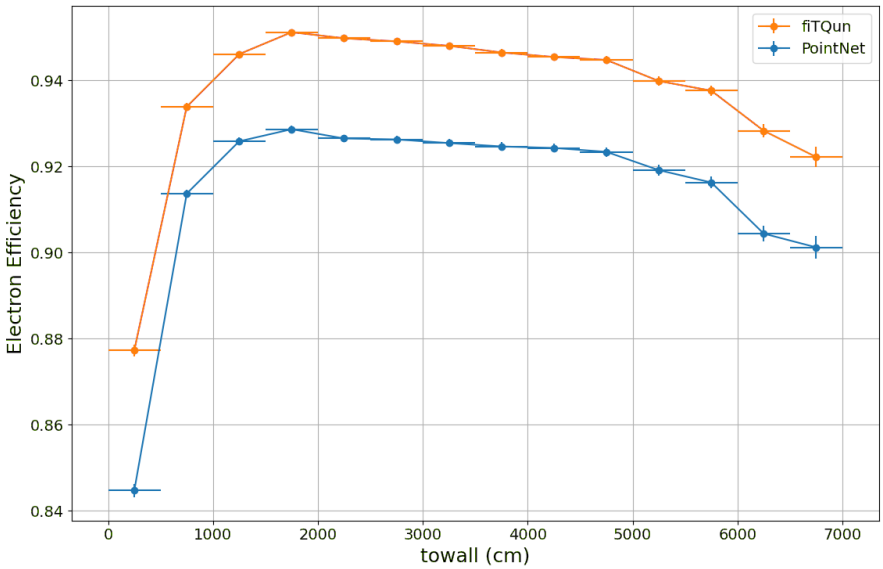


**(b)**

**Figure 6.12:** Electron efficiency against spatial kinematics for $e^-/\mu^-$ separation tasks performed by PointNet and FiTQun. Specifically, the kinematics variables examined here are (a) distance from vertex position to the nearest detector wall (dwall), and (b) distance from vertex position to a detector wall in the particle direction (towall) (only $[0, 7000]$ cm is shown). Both figures show an increase in classification efficacy as the event vertex veers clear from the tank walls.

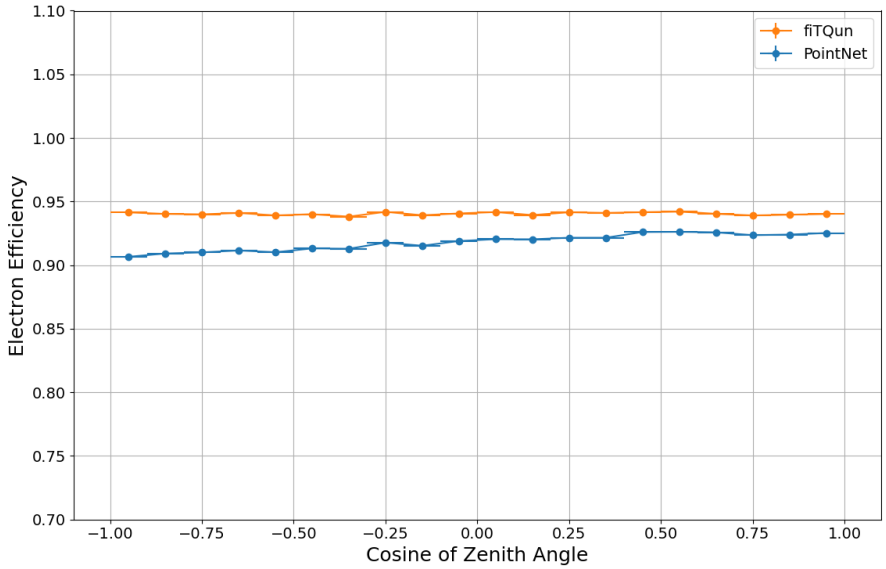


**(a)**

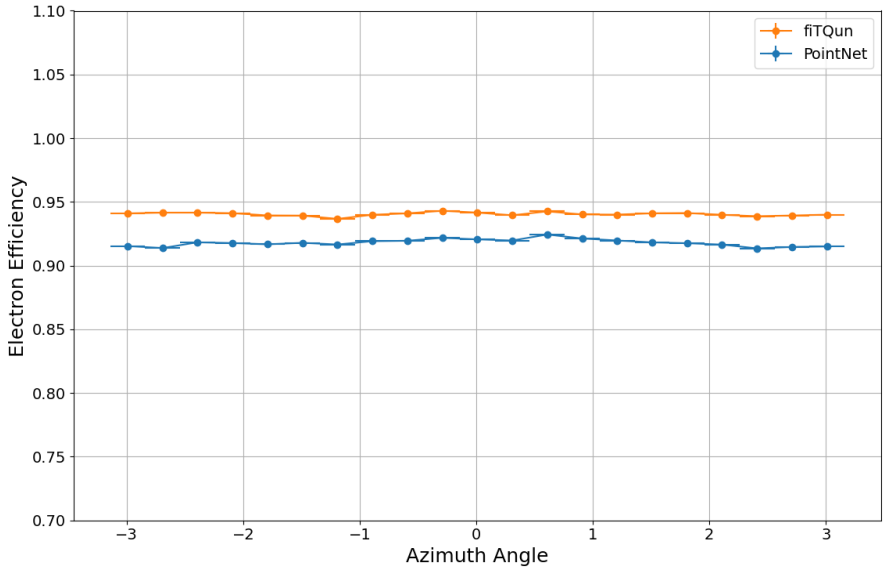


**(b)**

**Figure 6.13:** Electron efficiency against true directional kinematics for $e^-/\mu^-$ separation tasks performed by PointNet and FiTQun. The kinematics variables examined are (a) cosine of zenith angle of the particle direction, and (b) the azimuth angle of the particle direction. The figures indicate there are no directional dependencies during the particle classification process.

### 6.4.2 $e^-/\pi^0$ Separation

The plot in Figure 6.14 details the PointNet softmax scores and FiTQun NLL Differences for distinguishing between $e^-$ and $\pi^0$ events. True $e^-$ events are indicated by solid lines, and true $\pi^0$ events by dashed lines. Peaks observed around the midpoint of the softmax score within the PointNet model suggest the presence of 'empty' events, similar to the $e^-/\mu^-$ classification case, that have not generated any hits. Furthermore, the increased overlap between the two distributions for each model suggests a less distinct separation, hinting at a less optimal classification capability in differentiating $e^-$ from $\pi^0$ events, as opposed to the clearer distinction achieved in $e^-/\mu^-$ classification.

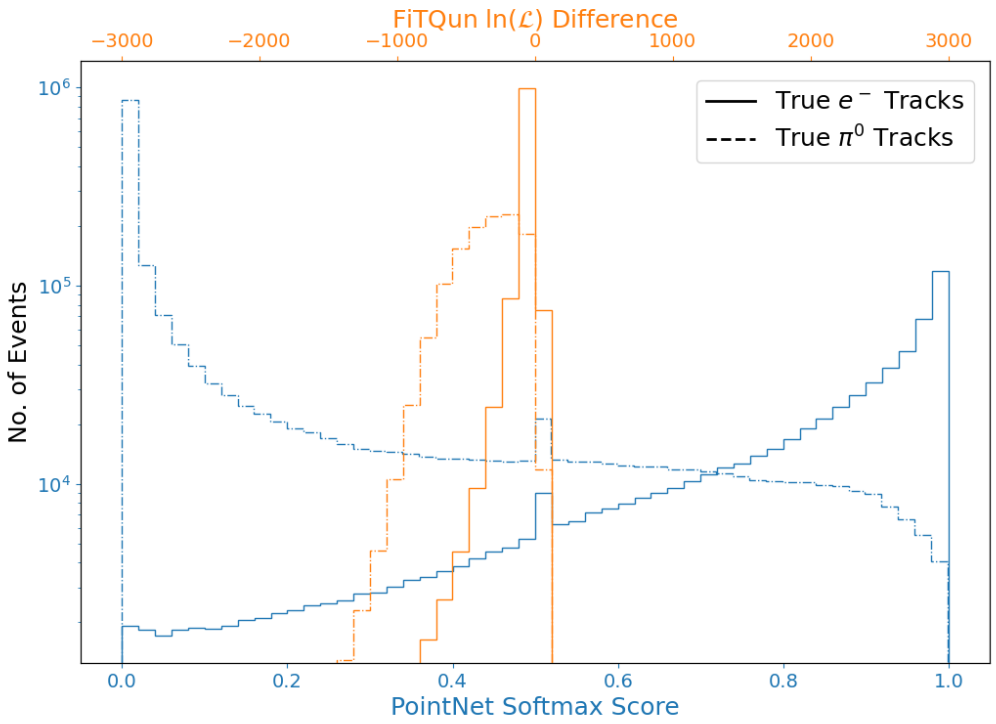


**Figure 6.14:** The distribution of PointNet softmax scores and FiTQun NLL Differences in the classification of $e^-$ and $\pi^0$ events. In these distributions, solid lines delineate the presence of true $e^-$ events, whereas dashed lines correspond to true $\pi^0$ events. Notably, the peaks at a softmax score near 0.5 within the PointNet classification are, again, believed to originate from 'empty' events that failed to trigger any hits. The separation between the two distributions for each model is less prominent, indicating a less perfect classification performance compared to that of $e^-/\mu^-$ separation.

### The ROC Curves

Figure 6.15 displays ROC curves that map out the change in TPR and FPR values as the chosen threshold varies in the context of $e^-/\pi^0$ event classification, employing both PointNet and FiTQun. The curves include scenarios with and without the integration of multi-PMT data. While not matching the exceptional scores seen in the electron versus muon differentiation, the AUC values still stand out, showcasing the substantial classification capabilities of the models in question. In the same manner where Figure 6.10a is calculated from Figure 6.9, Figure 6.16a is derived from reformatting the data shown in the previous plot, i.e. by converting the FPR into $\pi^0$ background rejection rates and plotted against electron signal efficiency rates, which serves to sharpen the visual discernment of the classifiers' nuances. Furthermore, Figure 6.16b hones in on higher signal efficiency region, specifically between $[0.9, 1]$, showing that PointNet performs better than FiTQun in this region.

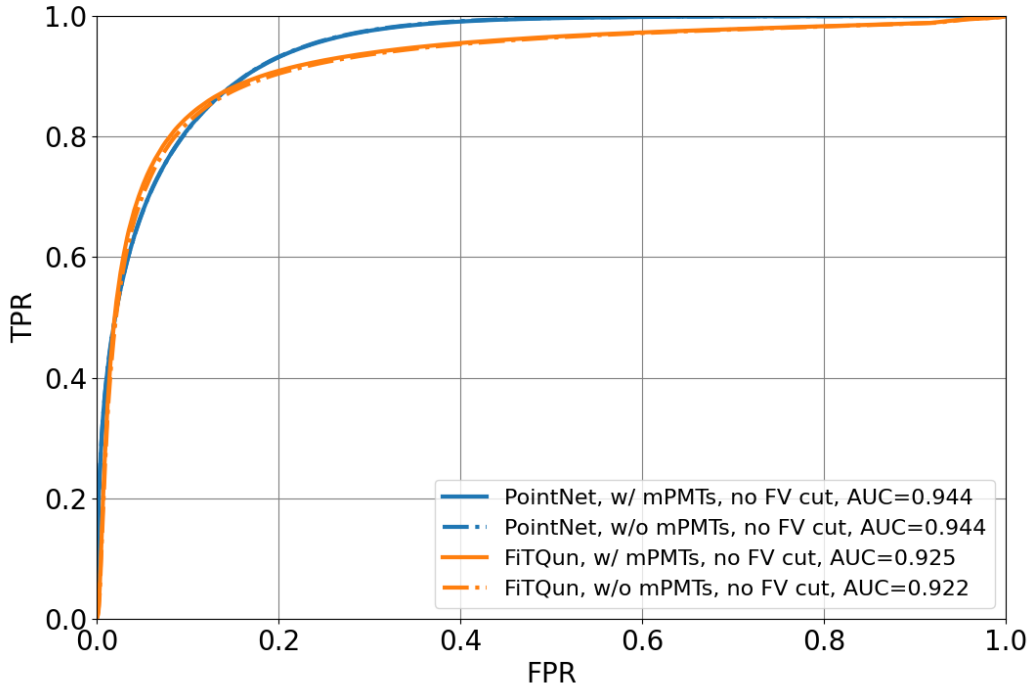


**Figure 6.15:** ROC curves illustrating the trade-off between TPR and FPR for $e^-/\pi^0$ event separation using PointNet and FiTQun, both with and without multi-PMT hits. Although the AUCs are not as high as the $e^-/\mu^-$ case, they remain high relatively speaking, reflecting the models' discriminative power.

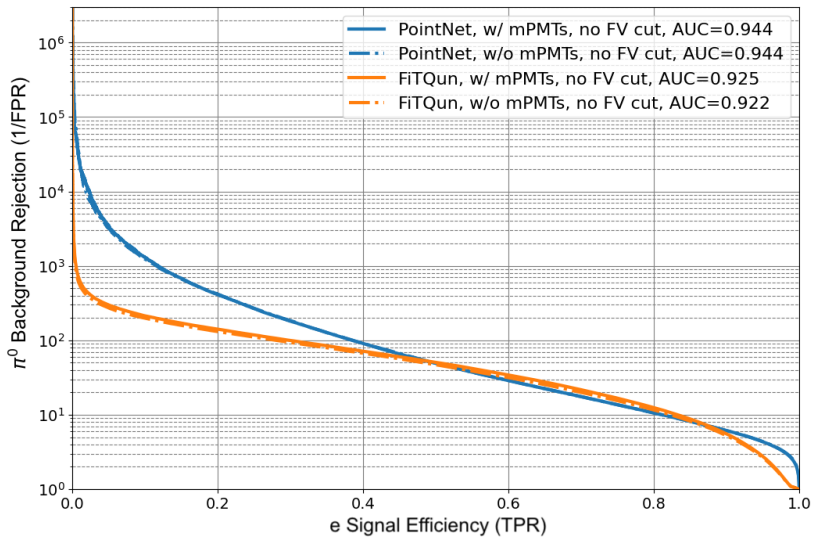


**(a)**

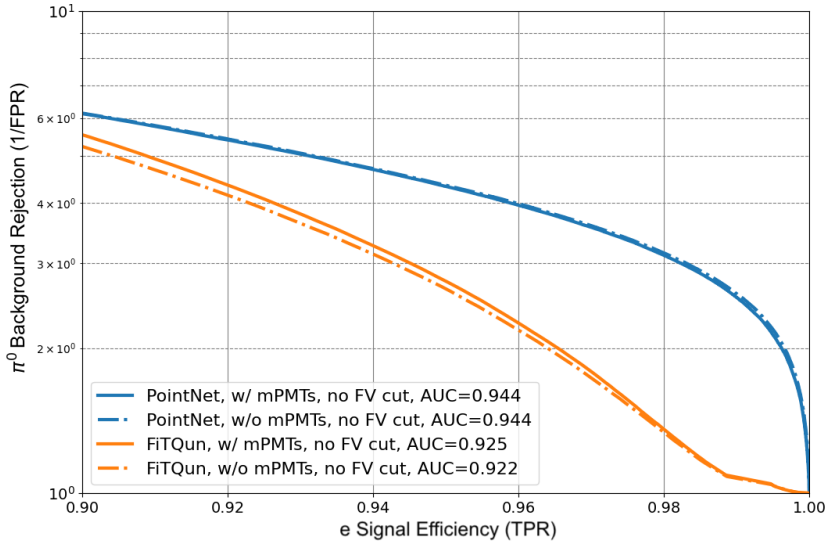


**(b)**

**Figure 6.16:** (a) The TPR and FPR are re-plotted as $\pi^0$ background (1/FPR) rejection against $e^-$ signal efficiency (TPR) to highlight details not visible in the original representation; (b) is the high signal efficiency region ($[0.9, 1]$) of (a).

### Signal Efficiency Against True Electron Kinematic Variables

For $e^-/\pi^0$ classification, the performance of the PointNet and FiTQun models are evaluated at 10% $\pi^0$ mis-ID rate against every kinematic variable. The efficiency of electron identification as a function of various electron parameters compared between PointNet and FiTQun for w/ mPMT data is depicted in the figures below.

In Figure 6.17, the efficiency trends related to true electron momentum demonstrate a slight incline at lower momentum values for PointNet, which is not seen for FiTQun, and reaching a plateau as momentum increases. While both models showcase a high efficiency for the majority of the momentum spectrum, FiTQun maintains a slight edge over PointNet. Notably, both models experience a precipitous drop in efficiency as the momentum approaches 1000 MeV/c, signifying a potential area for model improvement or a peculiarity in the dataset at high momentum values.

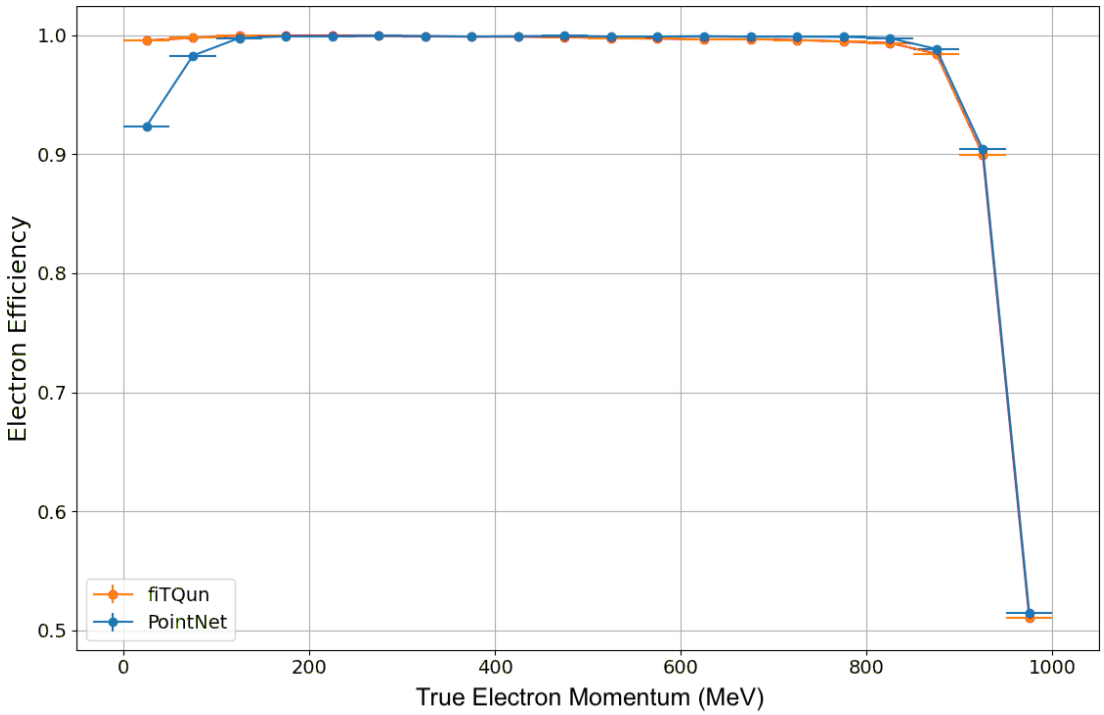


**Figure 6.17:** Electron efficiency v.s. true electron momentum for $e^-/\pi^0$ separation at 10% $\pi^0$ event mis-ID rate. The performance of both models is significantly worse in high energy ($[900, 1000]$ MeV) regions, the reason for such a drop in efficacy is unknown.

As shown in Figure 6.18a, both models display a robust efficiency for events occurring away from the detector walls but show a marked decrease in performance as

events draw nearer. This decline suggests difficulties in distinguishing particle tracks close to the walls, likely due to complex Cherenkov ring patterns in these regions.

Efficiency remains consistent for a tiny range of towall values, as one can see in Figure 6.18b, with FiTQun outperforming PointNet as usual. However, as the distance increases towards the maximum possible value within the detector's dimensions, a slight downturn in efficiency is observed for both models. It is worth noting that the plot is zoomed in on the y-axis, resulting in a seemingly more prominent downward trend. This tendency highlights challenges in event classification as vertices approach the detector corners, where distorted Cherenkov rings can obscure the decisions made by the discrimination models.

The efficiency across the cosine of the zenith angle and the azimuth angle (Figure 6.19a, and 6.19b) showcase a stable performance for both models over the entire range. This suggests that the orientation of the particle track relative to the detector's vertical or horizontal axis has a minimal impact on the models' classification abilities.

### 6.4.3 $e^-/\gamma$ Separation

As one can see from Figure 6.20, the distributions of $e^-$ and $\gamma$ event softmax scores from PointNet mostly overlap; thus no threshold value exists such that the distributions of the two types of events can be separated. More explicitly, the PointNet model possesses no ability to tell the $e^-$ and $\gamma$ events apart in Hyper-K. Similar arguments can be made for the FiTQun $e^-/\gamma$ classification results. A further examination of the ROC curve (shown in Figure 6.21) leads to the same conclusion.

The lack of distinction between the two particle types is expected, as neither FiTQun nor PointNet were specifically tuned to differentiate the subtleties of these events. This represents a potential area for future improvement.

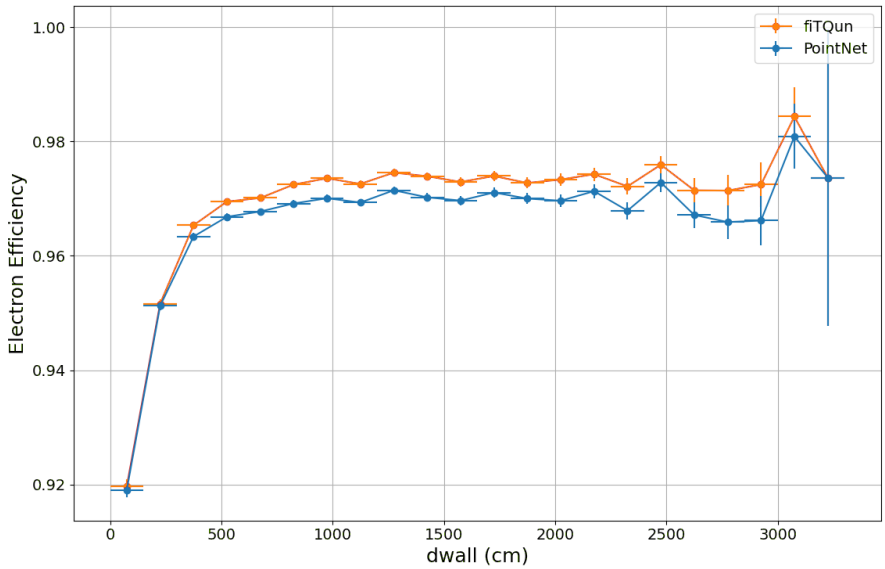


**(a)**

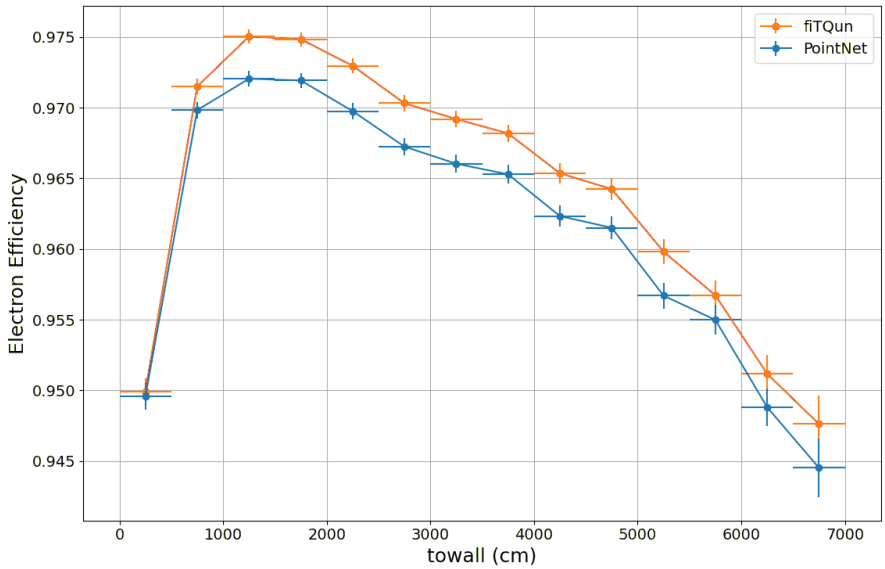


**(b)**

**Figure 6.18:** Electron efficiency against spatial kinematics for $e^-/\pi^0$ separation tasks performed by PointNet and FiTQun. The kinematics variables examined are (a) distance from vertex position to the nearest detector wall (dwall), and (b) distance from vertex position to a detector wall in the particle direction (towall) (only $[0, 7000]$ cm is shown). Both plots show worsened PID performance towards the ID walls, with the performance against the towall variable remaining mostly constant at larger distances while the classification efficacy against towall drops slightly from the peak. This drop could be due to the Cherenkov rings being obscured closer to the tank corners.

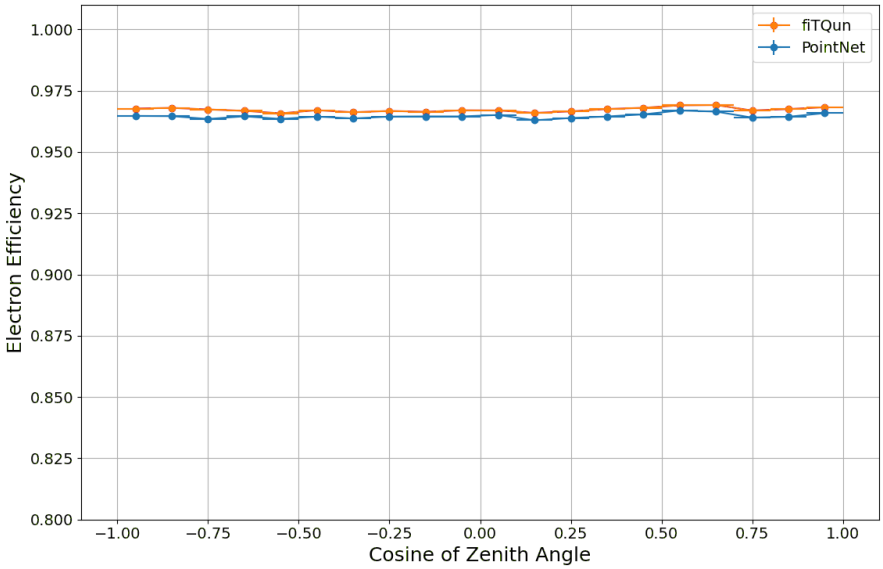


**(a)**

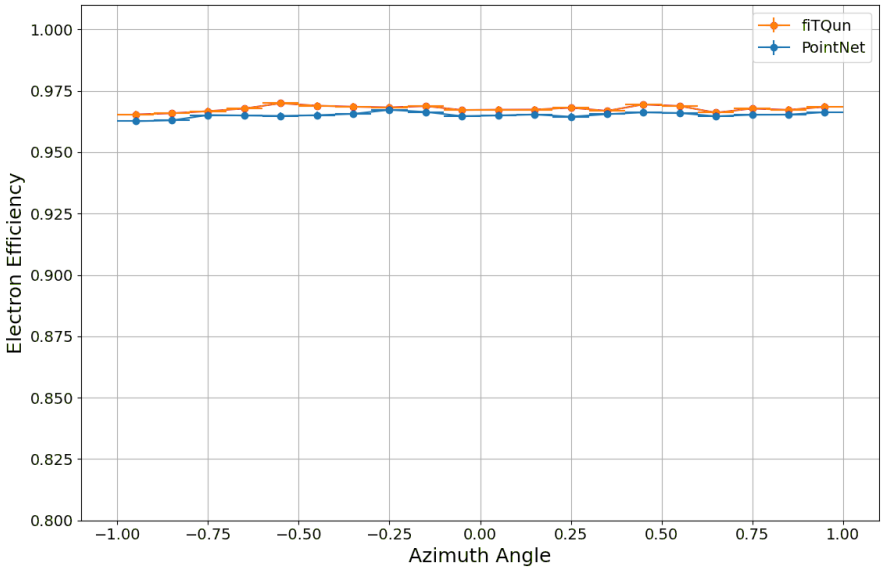


**(b)**

**Figure 6.19:** Electron efficiency against directional kinematics for $e^-/\pi^0$ separation tasks performed by PointNet and FiTQun. The kinematics variables examined here are (a) cosine of zenith angle of the particle direction, and (b) the azimuth angle of the particle direction. The PID efficacies of both models are independent of the particle directions.

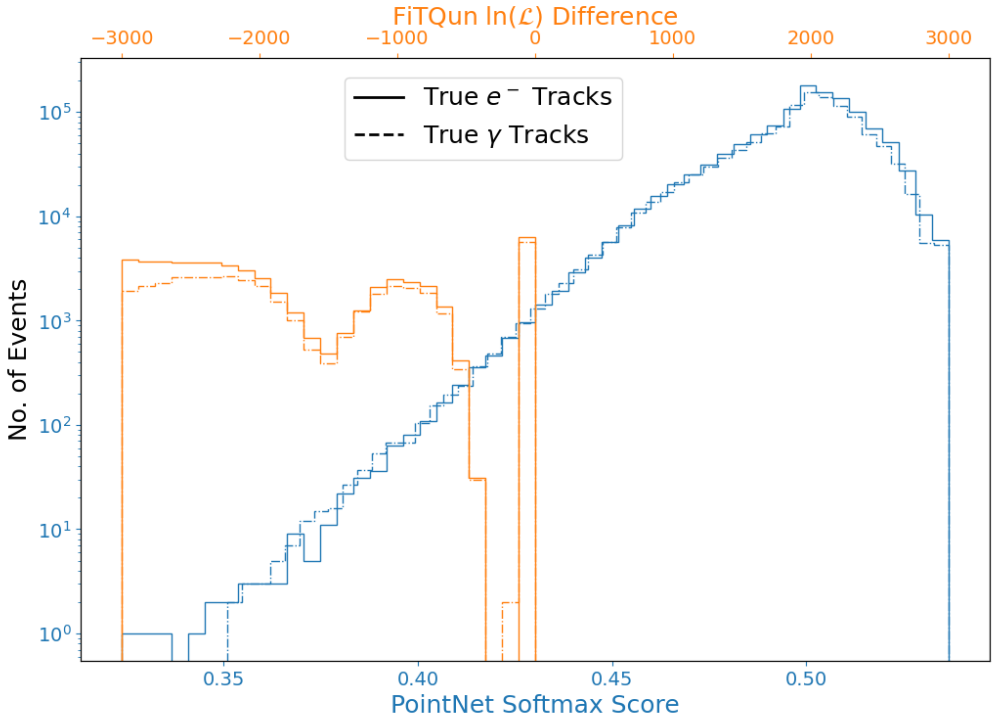


**Figure 6.20:** The distribution of PointNet softmax scores and FiTQun NLL Differences in the classification of $e^-$ and $\gamma$ events. In these distributions, solid lines delineate the presence of true $e^-$ events, whereas dashed lines correspond to true $\gamma$ events. The separation between the two distributions for each model is not possible, indicating that both PointNet and FiTQun can not discriminate $e^-/\gamma$ events.

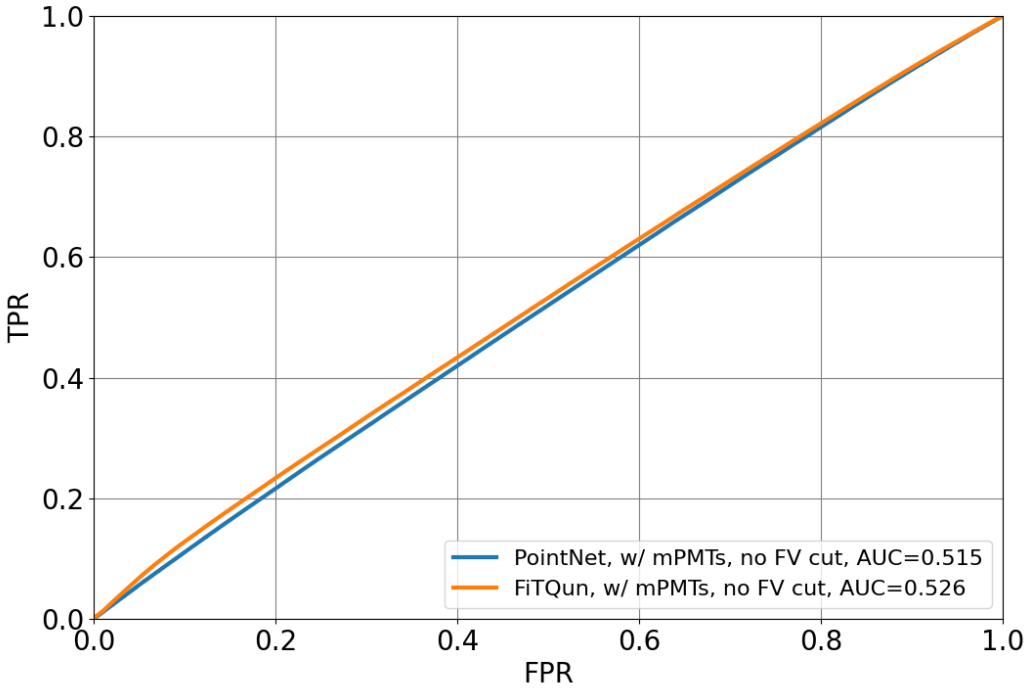


**Figure 6.21:** ROC curves illustrating the trade-off between TPR and FPR for $e^-/\gamma$ event separation using PointNet and FiTQun, both with and without multi-PMT hits. The softmax scores for $e^-$ and $\gamma$ events largely overlap for both tools, indicating that there is no specific threshold value at which the two event types can be distinctly separated by neither PointNet nor FiTQun.

## 6.5 Kinematics Reconstructions

The kinematics variable reconstructions, which include energy and vertex position, were only performed on the $e^-$ and $\mu^-$ MC samples. As mentioned in Section 6.3.2, the partition of data for reconstruction is set to Training : Validation : Test = 7 : 2 : 1. The reason for this ratio selection is discussed in Section 6.5.2. The data processed by the models for reconstruction have excluded mPMT hits, as it was found after the classification task was performed that the mPMT from the simulation-outputted root files have peculiar looks, which indicates the detector simulation most likely contains a bug. Due to time constraints, retraining for classification was not feasible, marking a potential area for future improvement.

Similar to the classification result analysis against true kinematics, the kinematics reconstruction examines the resolution across eight track variables: true momentum, x, y, z, dwall, towall, cosine of zenith angle, and the azimuth angle. The output from PointNet's momentum reconstruction actually represents energy, matching the dimension of the supplied ground truth (i.e. energies). Conversely, FiTQun directly outputs momentum. Before comparison with FiTQun, PointNet's results are converted to momentum values.

### 6.5.1 Cuts Applied

In the analysis of momentum reconstruction results, three cuts are applied to the reconstructed events. These cuts are crucial for ensuring data quality and enhancing the accuracy of the computed resolution. Out of the three cuts, two are for data quality improvement. They are applied to the dataset in all kinematic variable analyses. On the other hand, the last cut is implemented to the dataset used in all kinematic parameter plots except the true momentum one.

The first cut is implemented to address a peculiar feature observed in the PointNet momentum reconstruction test dataset. In Figure 6.22a, the plots compare the reconstructed to true momenta of electron events with PointNet (left) and FiTQun (right). It is clear that some events in the PointNet result have formed a horizontal line at a non-zero reconstructed momentum value. (Although the visual example is

given using electron events, a horizontal line could also be found in the muon reconstruction results.) Upon closer examination, the event displays of these events revealed no PMT hits, which is unexpected as they are generated with sensible energies and vertex positions and are, thus, supposed to have some recorded hits. The exact cause of the 'empty' events remains unidentified, though it is suspected to be related to the simulation software version. Nonetheless, the 'empty' events, 1599 of $e^-$ and 5956 of $\mu^-$, are removed from the respective datasets to avoid skewing the analysis.

The second cut is designed to filter out events with unrealistic vertex positions reconstructed by FiTQun. As shown in Figure 6.23a, for some events, the FiTQun reconstructed vertex positions are well beyond the physical dimensions of the detector, which are 3240, 3240 and 3287 cm for maximum $x$, $y$ and $z$ respectively). The event displays of these mis-reconstructed electron events were investigated, however, it does not reveal any intrinsic abnormality of the event. This performance issue has been reported to the Hyper-K FiTQun migration group, and in the meantime, these inaccurately reconstructed events, 19 for $e^-$ and 69 for $\mu^-$, are also excluded from the analysis dataset.

The distribution of reconstructed v.s. true momentum after the first two cuts mentioned above can be found in Figure 6.22b.

Lastly, the third cut targets the lower energy events, particularly those with 100 MeV or less energy above Cherenkov thresholds, i.e. the cut is set at 100 MeV for electron events and 261 MeV for muons. This cut is not applied when plotting against true momentum but is used for other kinematic variables. For all other kinematic parameters, the inclusion of these low-energy events in every bin led to a poorer resolution in the analysis. Moreover, these events would typically be processed by a specialised low-energy reconstruction tool (e.g. BONSAI [151] for Super-K) in the actual analysis pipeline. Therefore, to achieve a more realistic understanding of the momentum resolution capability of the detector system, these events are removed during resolution computation. The removal of the low-energy events sees a reduction in the uncertainty of the momentum resolution in true $x$ vertex position bin in PointNet (blue) and FiTQun (orange) reconstructions, as illustrated by Figure 6.24a (before the cut) and 6.24b (after the cut). The contents in each bin of both figures were studied to

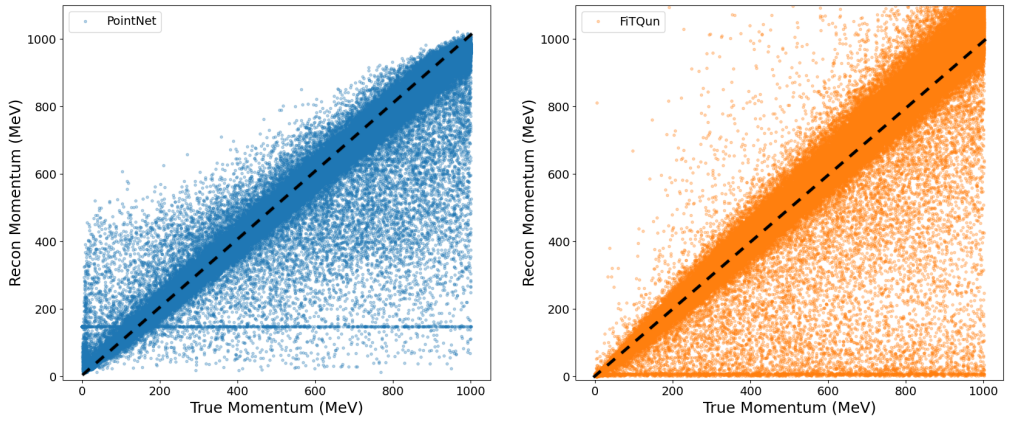


**(a)** Before cuts

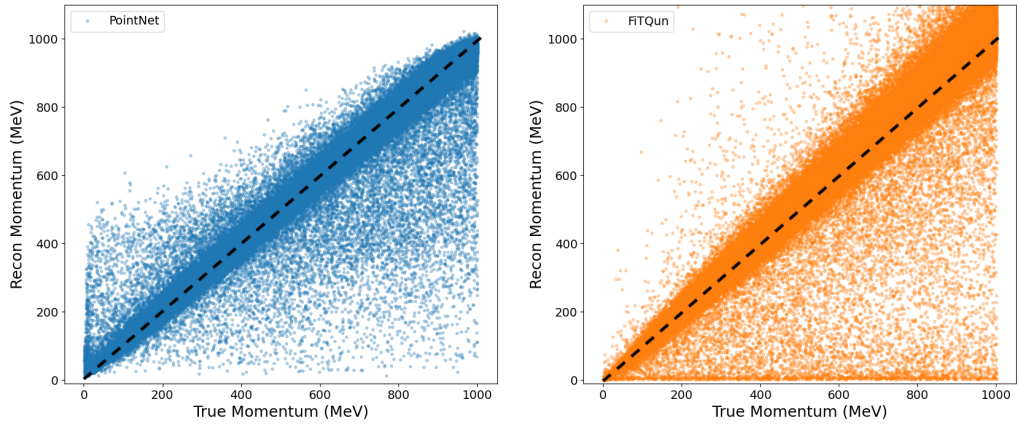


**(b)** After the empty event and bad FiTQun position reconstruction cuts

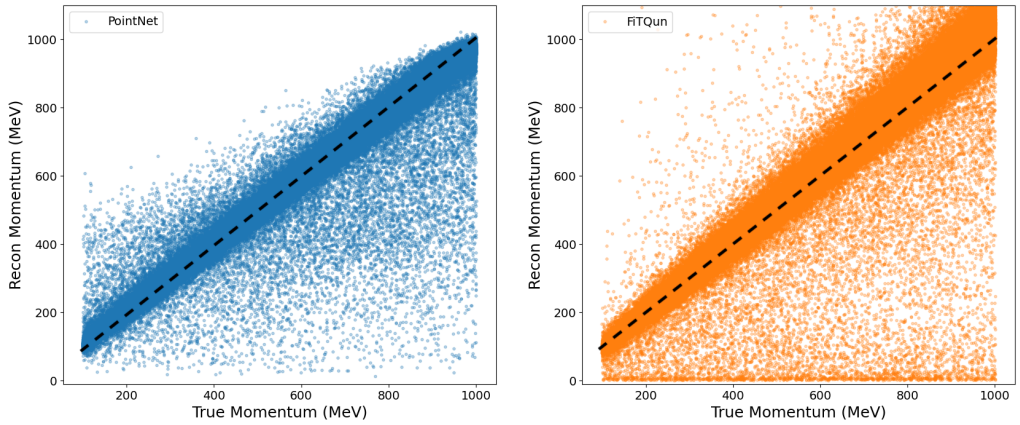


**(c)** After the empty event, bad FiTQun position reconstruction and low-energy event cuts

**Figure 6.22:** The reconstructed v.s. true momentum distributions of the PointNet (left) and FiTQun (right) electron results before and after the empty event and bad FiTQun position reconstruction cuts, in addition to the low-energy event cuts. The black dotted lines indicate where the reconstructed values are equal to true. The horizontal line of events consists of 'empty', i.e. no hits, events seen in the PointNet result in (a) has disappeared after cut application.

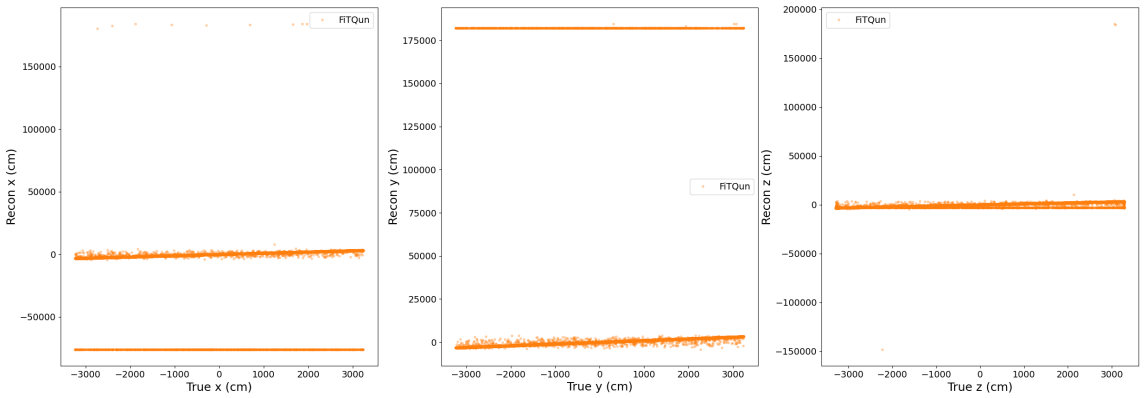


**(a)** Before cut

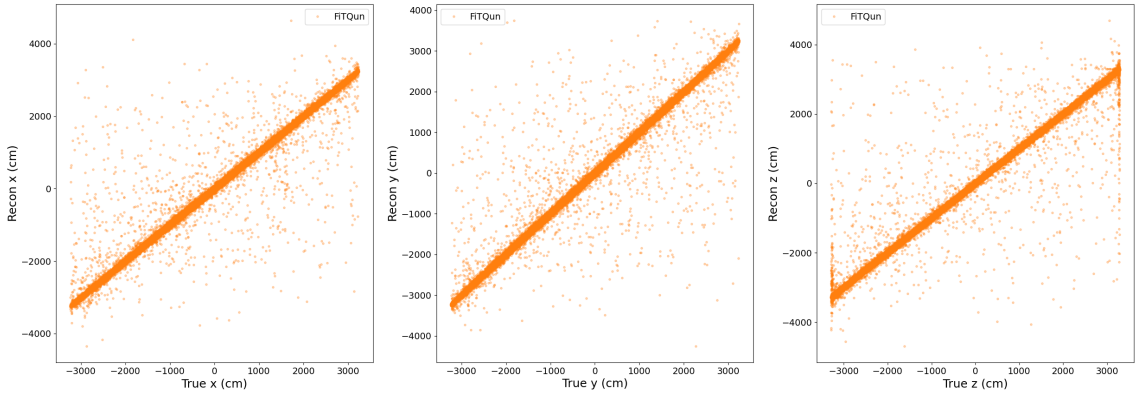


**(b)** After bad FiTQun position reconstruction cut

**Figure 6.23:** The effect of bad FiTQun position reconstruction cut on the reconstructed against true vertex coordinate distributions for FiTQun result. There are many events with mis-reconstructed $x$ and $y$ coordinates in (a), and as seen in (b), the designed cut has effectively removed all outliers.

examine the impact of the cut on the distribution of the absolute momentum resolutions. For instance, Figure 6.24c and 6.24d show the content of bin $0 - 324$ cm in true vertex $x$ position, before and after the cut. It is clear to see the outliers in both result distributions, especially in the PointNet case, are removed as the cut applies.

The comparison between the reconstructed and true momentum for electron events after all three cuts can be seen in Figure 6.22c.

Similar to the momentum reconstruction analysis, two critical data quality cuts are applied to reduce bad events included in the dataset for the vertex position reconstruction resolution analysis. The first cut addresses 'empty' events, where there are no

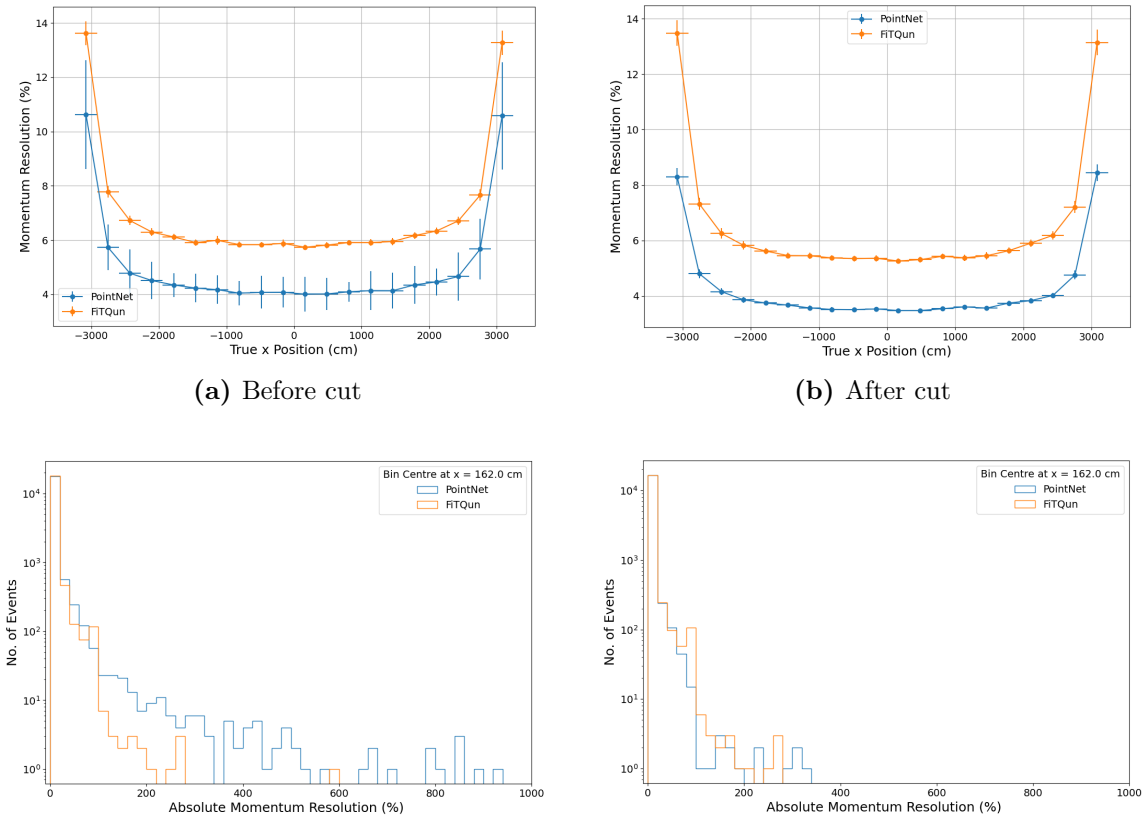


**(a)** Before cut **(b)** After cut

**(c)** Before cut **(d)** After cut

**Figure 6.24:** The impact of applying a low-energy event cut on the $e^-$ momentum resolution uncertainty across true $x$ vertex positions for PointNet and FiTQun results is illustrated in figures (a) (before the cut) and (b) (after the cut). To assess the influence of this cut, the content of each bin was studied. For instance, the content in bin $0 - 324$ cm is shown in figure (c) before the cut and in figure (d) after the cut. It is evident that the cut significantly reduces outliers in the PointNet event distribution and enhances the precision of the momentum resolution.

true PMT hits, identified by the horizontal lines in the reconstructed v.s. true vertex coordinates shown in Figure 6.25a. These events are excluded to prevent skewed analysis results, and resultant distributions are displayed in Figure 6.25b. The second cut targets events where FiTQun inaccurately reconstructs vertex positions, manifesting as values beyond the detector's physical limits. Such events, identified by their unrealistic vertex coordinates, are similarly removed.

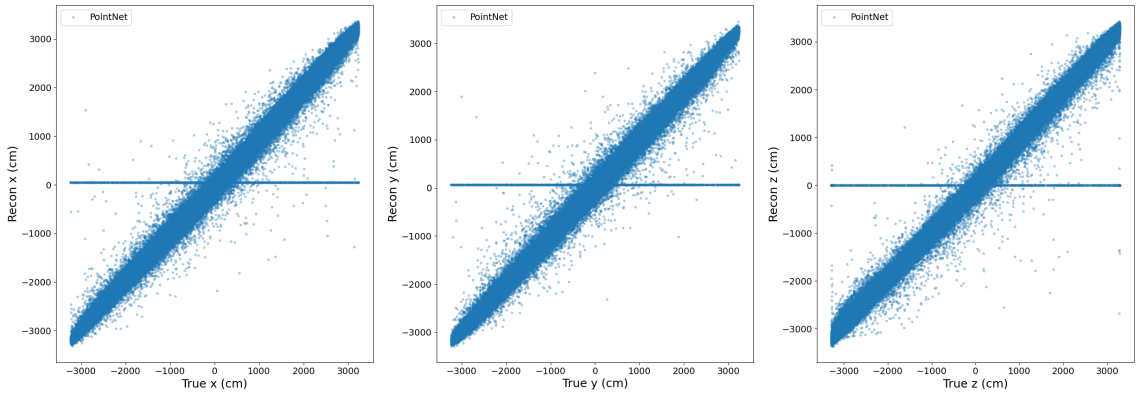


**(a)** Before cut

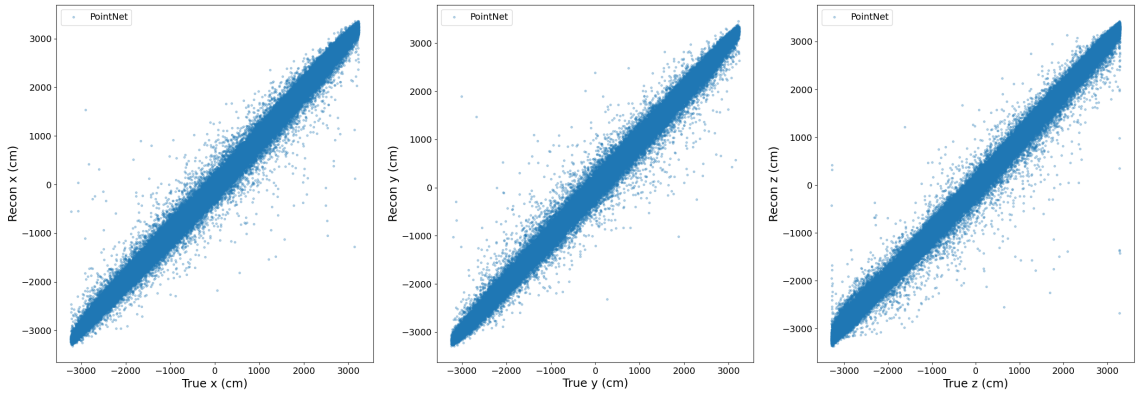


**(b)** After bad PointNet position reconstruction cut

**Figure 6.25:** PointNet reconstructed vertex positions against true for electron events 6.25a before and 6.25b after a cut. As one can see, the horizontal line that most likely consists of empty events has disappeared after the cut is applied.

### 6.5.2 $e^-$ Energy Reconstruction

Figure 6.26 illustrates the momentum resolution of reconstructed electron events from PointNet, using two distinct training-validation-test (TVT) ratios, i.e. 7 : 2 : 1 and

5 : 1 : 4. The wider ML field more commonly uses the 7 : 2 : 1 ratio, whereas 5 : 1 : 4 is a ratio inherited from WatChMaL's previous PointNet project, where the model trained on the IWCD MC data.

To contextualise the results of PointNet kinematic reconstructions, FiTQun's results are also presented. Note that the number of events processed by FiTQun can be adjusted to match PointNet's test event count, ensuring a direct one-to-one comparison. It is clear from the figure that the PointNet performance between the two TVT ratios is fairly similar, although the resolution from the 7 : 2 : 1 ratio has less fluctuation, leading to a more stable performance. Thus the TTV = 7 : 2 : 1 data distribution ratio has been chosen for the PointNet reconstruction task.

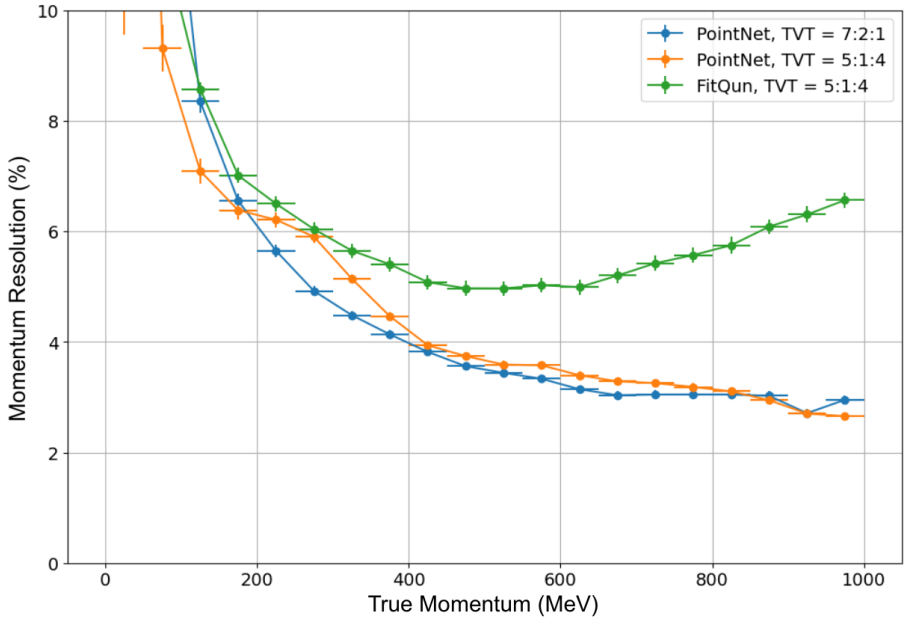


**Figure 6.26:** Comparing the performance between different training, validation, and testing event ratios for PointNet. The FiTQun result is included as a reference.

Figure 6.27 shows the momentum resolution as a function of true momentum for electron events, which indicates that FiTQun is much better at reconstructing lower energy events than PointNet. Conversely, once the $e^-$ event momentum surpasses 150 MeV, the performance of PointNet exceeds that of FiTQun. This shift in relative performance is likely caused by the reduction in the number of hits and charges recorded per hit PMT at low particle energy. As PointNet only learns from the hit PMT information, the lower the energy, the less available data per event, and subsequently,

the less accurate PointNet becomes. On the other hand, as described by Equation 6.2, FiTQun accounts for both the hit and unhit PMTs and, therefore does not have the same 'lack of event information' issue faced by PointNet.

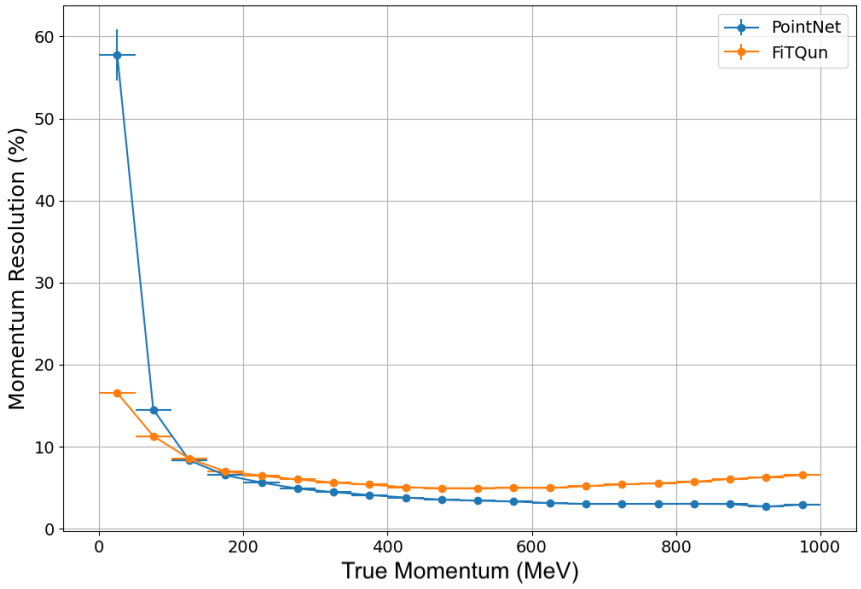


**Figure 6.27:** The momentum dependence of the momentum resolution of $e^-$ events from PointNet (blue) and FiTQun (orange) reconstructions.

As the particle energy increases, the advantage of PointNet starts to show in the plot. Contrary to FiTQun, which minimises the NLL value for all seven parameters ($x$, $y$, $z$, $t$, $q$, $\theta$ and $\phi$) of a particle hypothesis simultaneously, a PointNet model is dedicated to only perform electron energy reconstruction, which leads to less complexity and thus better performance.

Figure 6.28 and 6.29 explore the correlation, or lack thereof, between the particle vertex and the momentum resolution of the two reconstruction tools. Looking at Figure 6.28a, 6.28b and 6.28c, it is clear that the momentum resolutions are worse closer to the ID walls while remaining at a lower and roughly constant value in the middle of the tank. This trend still holds when the coordinates are translated into the towall and dwall parameters. The observation can be corroborated with the reconstruction experience gained from the Super-K [152], where the particle parameters are known to be less accurately reconstructed the closer the particle vertex is to the wall.

Conventionally, the resolution is only examined in the $[0, 4000]$ cm range of the

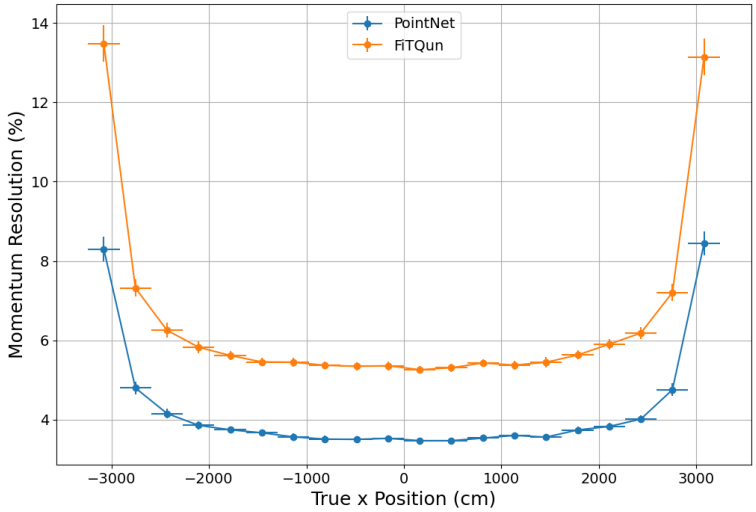


**(a)** x

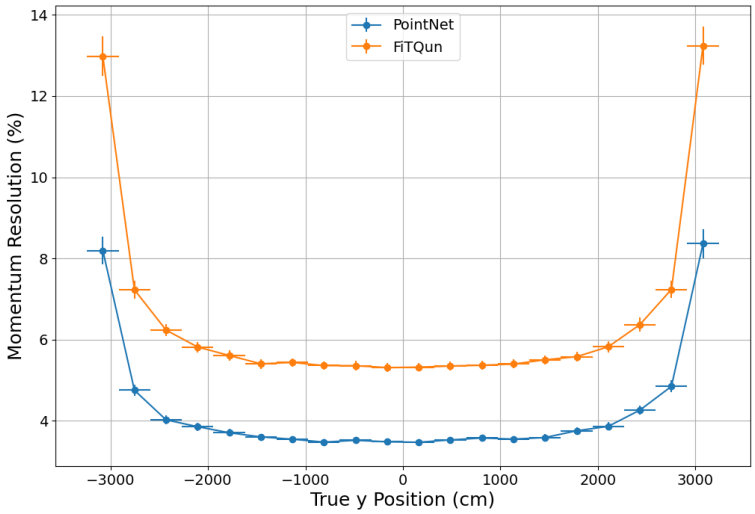


**(b)** y

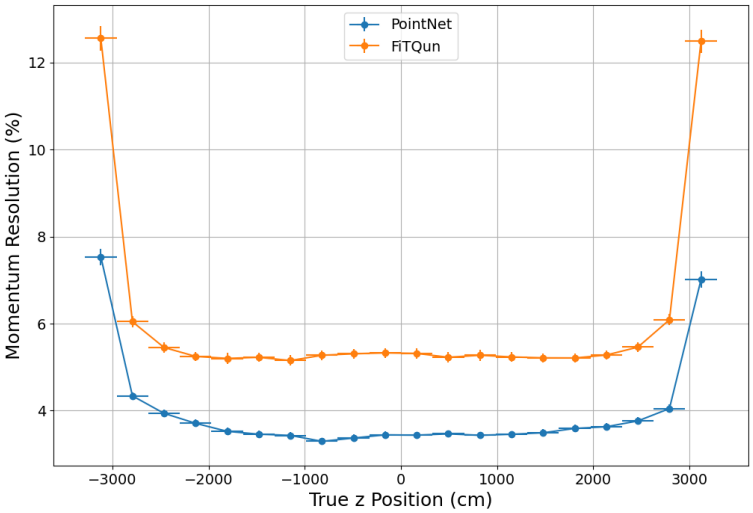


**(c)** z

**Figure 6.28:** The Cartesian coordinate dependence of the momentum resolution of $e^-$ events from PointNet (blue) and FiTQun (orange) reconstructions.

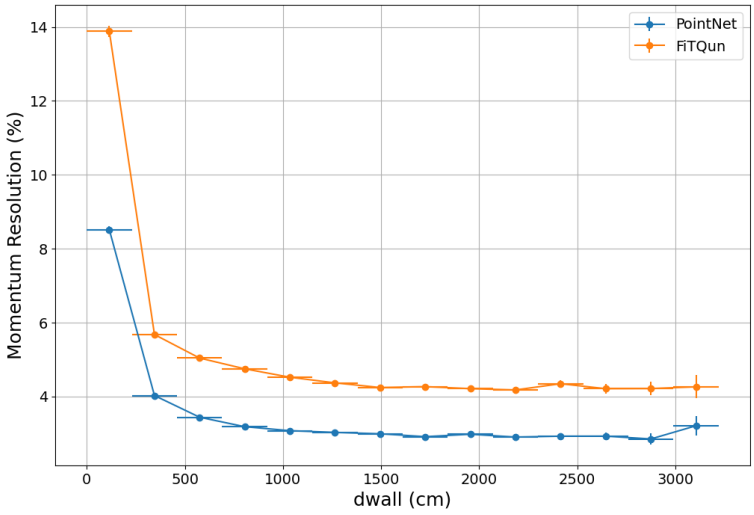


**(a)** dwall

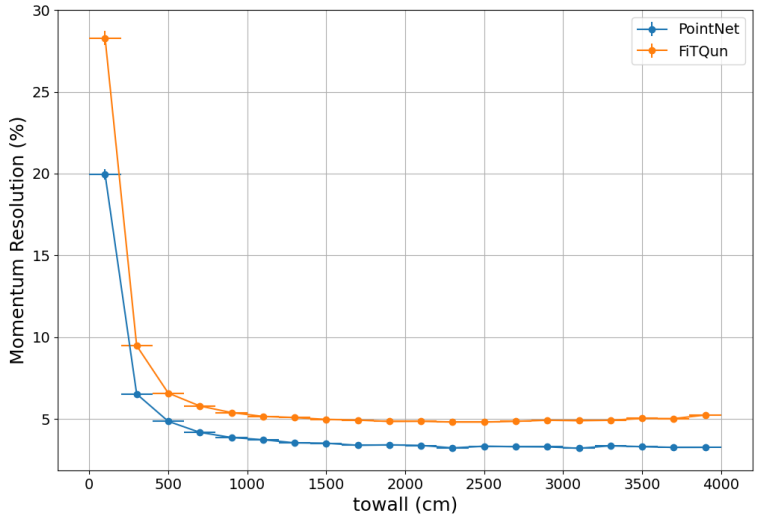


**(b)** towall (0 - 4000 cm)

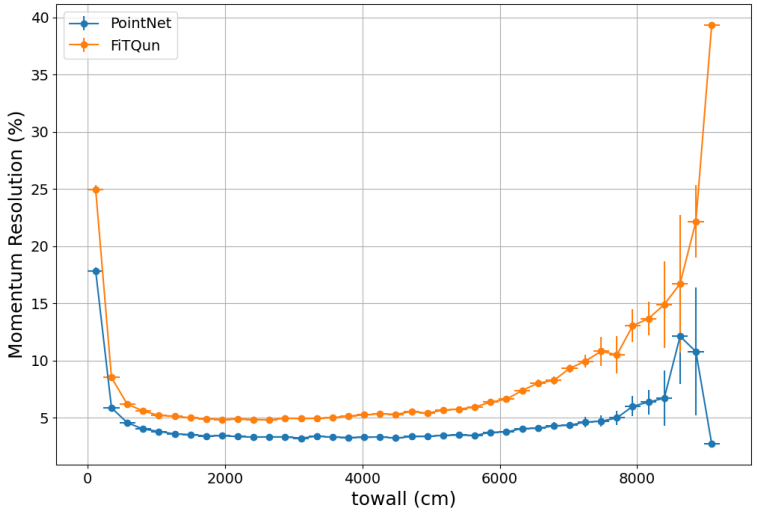


**(c)** towall (Full Range)

**Figure 6.29:** The 3D positional dependence of the momentum resolution of $e^-$ events from PointNet (blue) and FiTQun (orange) reconstructions.

towall value. However, interesting trends can be observed if the resolution is plotted for the full range of towall, where the PointNet and FiTQun reconstruction resolutions both worsen in the high towall region. Naively, one may assume that a particle would always produce a clearer Cherenkov ring as it travels a further distance to reach the detector wall, leading to better reconstruction results at a higher towall value. Nevertheless, this accuracy is not maintained as the towall value of a particle reaches the maximum, i.e. the scenario where the particle starts from a corner of the ID and travels towards the other corner. In these cases where the charged particles are tucked into a corner, their generated Cherenkov rings would be distorted and obscured when projected onto multiple tank surfaces, confusing the reconstruction algorithms and leading to worse reconstruction results.

Figure 6.30 illustrates the near-wall momentum resolutions from PointNet (left) and FiTQun (right) reconstructions. The darker regions represent worse reconstruction performance. The reconstruction results from both tools do not seem to depend on the towall variable as much as the dwall within the range of $[0, 1000]$ cm. This observation has been reported previously, as seen in the left plot Figure 2 in Ref. [153].

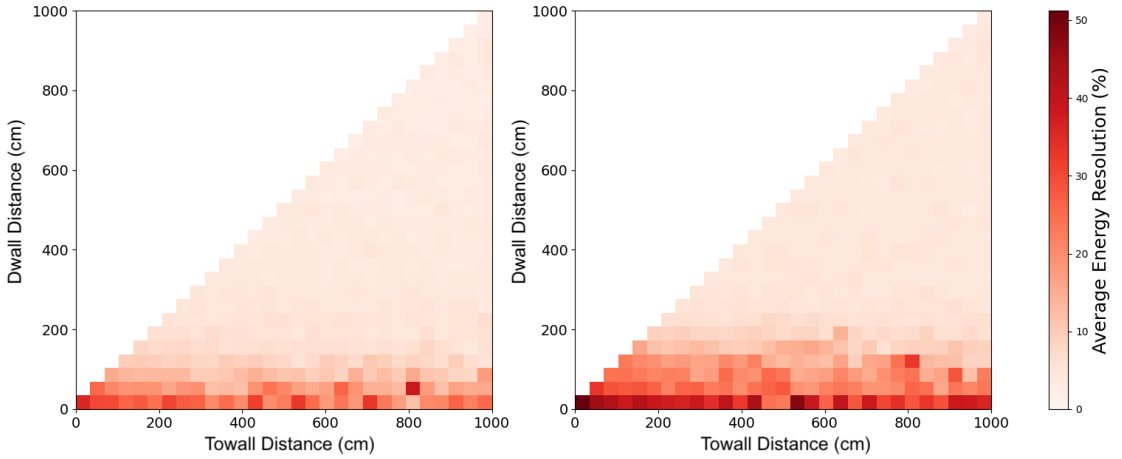


**Figure 6.30:** Momentum resolutions for $e^-$ events in percentage for PointNet (left) and FiTQun (right) reconstructed results in various fiducial volume regions. The darker the bin, the worse the momentum reconstruction result.

The directional dependence of the momentum resolution is explored in Figure 6.31, where the resolution is plotted against the cosine of the zenith angle and azimuth angle. Although there are slight fluctuations across the two kinematics, they are within the

error bar. Thus, it is safe to conclude that the resolutions are independent of the direction of travel of the electron.

### 6.5.3 $\mu^-$ Energy Reconstruction

Figure 6.32 displays the muon momentum reconstruction results from PointNet and FiTQun. The trends of both lines are unexpected, where the expected momentum resolution as a function of true muon momentum should follow the same trend as displayed in Figure 6.27 - worse resolution at low momentum and an improved resolution for higher momentum events. The reason for these unforeseen resolution results is unknown, but the underlying cause of this bad reconstruction is thought to be confined only to the true momentum variable. As Figure 6.33, 6.34 and 6.35 show, the muon momentum resolution is largely independent and the vertex positions or particle travelling directions.

### 6.5.4 $e^-$ Positions Reconstruction

The vertex resolutions, which measure the distance between the true and reconstructed vertex of an event, as a function of true electron momentum, reconstructed by the PointNet and FiTQun model are shown in Figure 6.36a. Both models have shown worse resolutions at momentum lower than around 100 MeV compared to the rest of the range, but the general performance of PointNet is overwhelmingly worse than that of the FiTQun. The possible causes of such discrepancy are two-fold: for PointNet, it has been shown previously that its performance becomes worse in multi-variate regression tasks, e.g. when the model is tasked to classify more than two types of particle events [154]. For the vertex resolutions displayed in Figure 6.36a, the 3D coordinates of the vertex were supplied to PointNet at once, and thus it reconstructed the $x$, $y$ and $z$ variables simultaneously. From previous results obtained with the IWCD geometry, it was shown that the vertex resolution would improve when every position coordinate was inferred individually. As for FiTQun, its reconstruction power reported here is seemingly beyond what is realistically plausible. Comparing across the FiTQun-reconstructed low energy ($< 15$ MeV) region with the 20% B&L benchmark

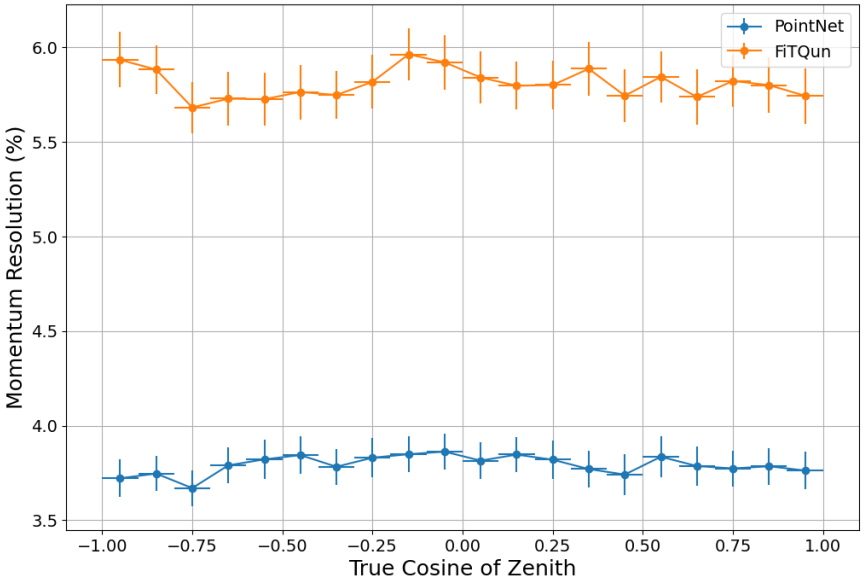


**(a)**

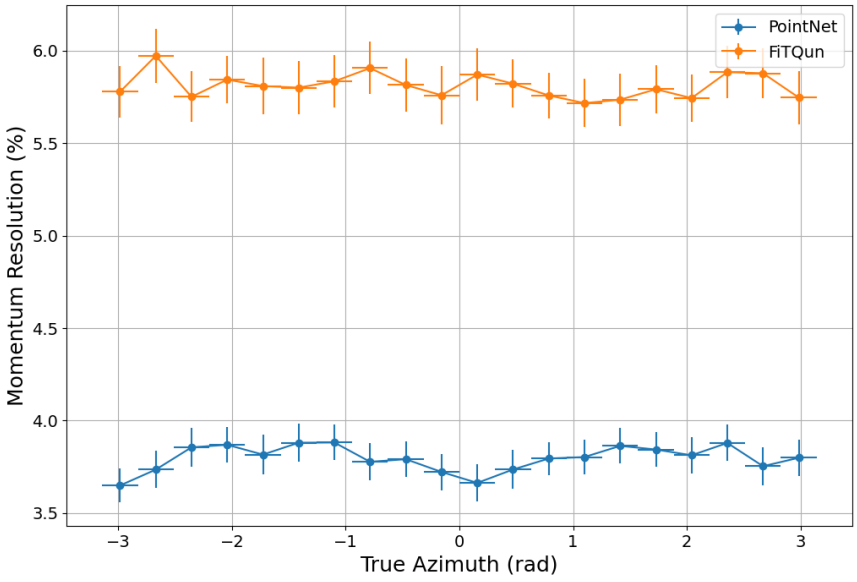


**(b)**

**Figure 6.31:** The directional dependence of the momentum resolution of $e^-$ events from PointNet (blue) and FiTQun (orange) reconstructions. The directional dependence of performance is explored as a function of (a) the cosine of zenith angle and (b) the azimuth angles.

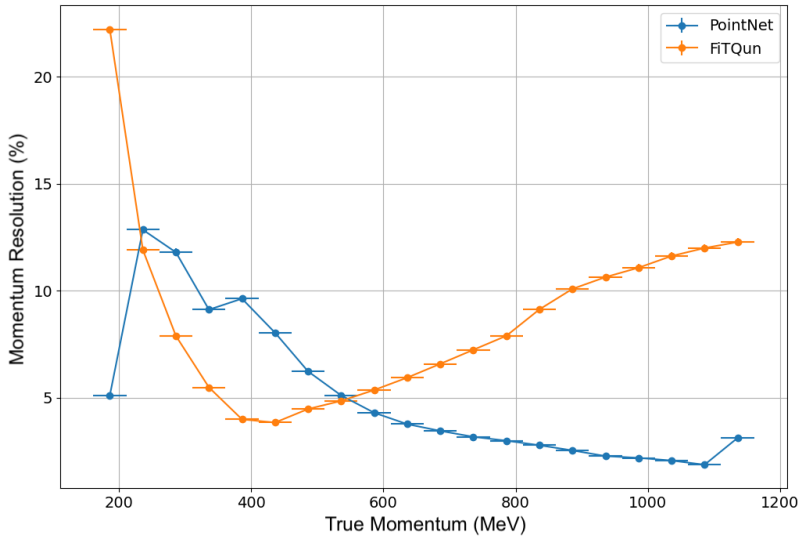


**Figure 6.32:** The momentum dependence of the momentum resolution of $\mu^-$ events from PointNet (blue) and FiTQun (orange) reconstructions.

data shown in Figure 6.36b, which was published in 2019 [155], it is clear that the benchmark resolution is never more accurate than 50 cm, while the first bin of the FiTQun position reconstruction result reported in this thesis is below such threshold. As a reference, the vertex resolution of events reconstructed by FiTQun in Super-K is approximately 20 cm for single-ring true $e^-$ events and 15 cm for single-ring $\mu^-$ events within the energy range of $[200, 1000]$ MeV [156, p. 13].

After troubleshooting, it was found that the simulation geometry version used in the WCSim, nuPRISM, is the cause of overly accurate vertex position reconstructions using FiTQun [157].

In any case, the position resolution for fully-contained events in Hyper-K should be better than the partially-contained ones, however, more study is needed to conclude on the resolution of through-going events.

### 6.5.5 $\mu^-$ Positions Reconstruction

The vertex position reconstruction for the $\mu^-$ events has very similar performance to those of the electron position recons. These results bear minimal meaning without a detailed examination of the simulation geometry and the PointNet training conditions

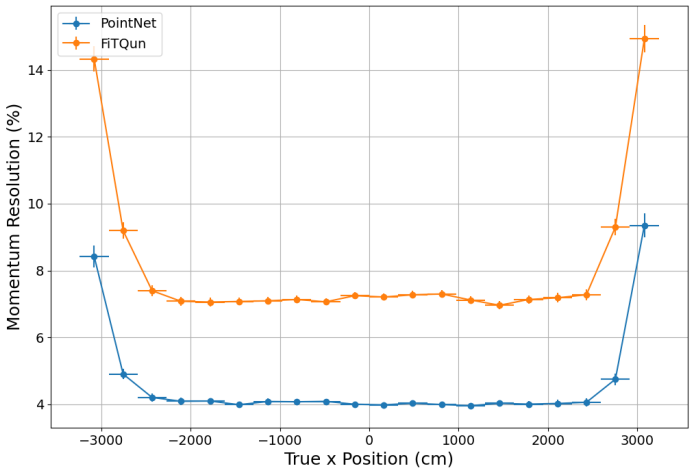


**(a)** x

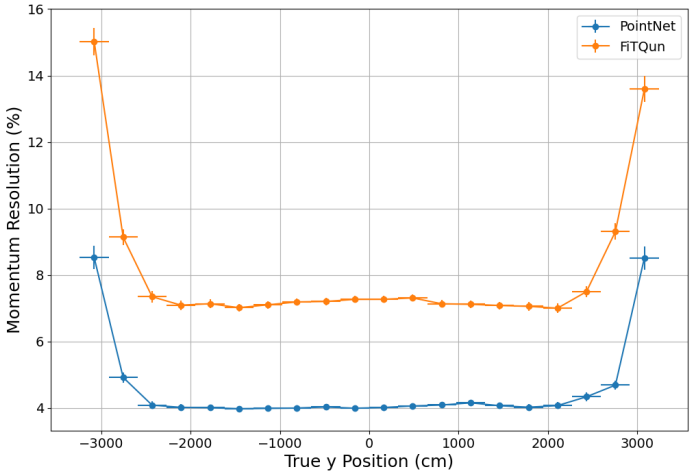


**(b)** y

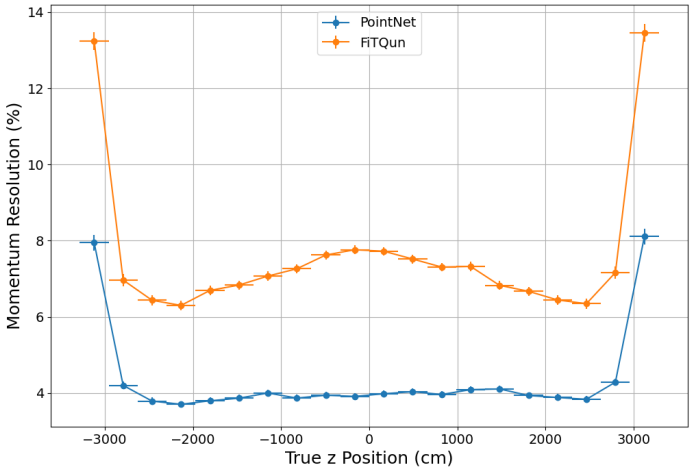


**(c)** z

**Figure 6.33:** The Cartesian coordinate dependence of the momentum resolution of $\mu^-$ events from PointNet (blue) and FiTQun (orange) reconstructions.

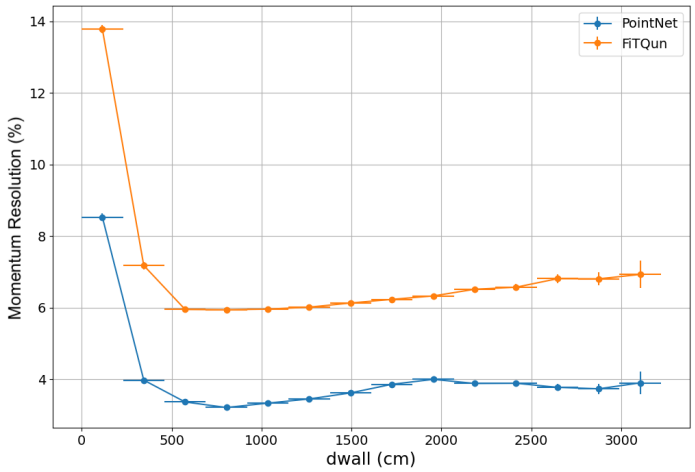


**(a)** dwall

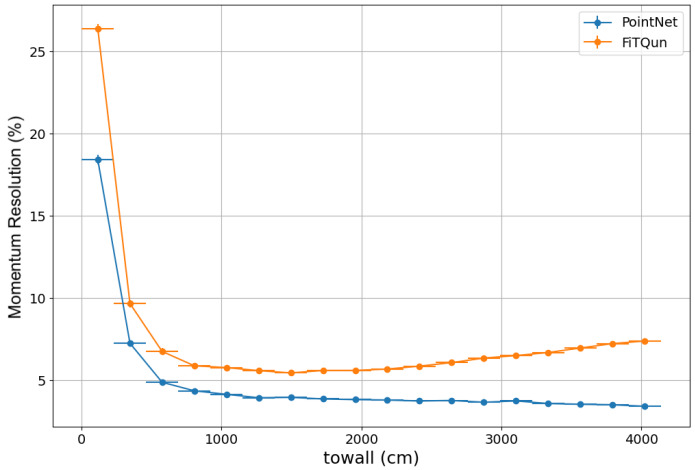


**(b)** towall (0 - 4000 cm)

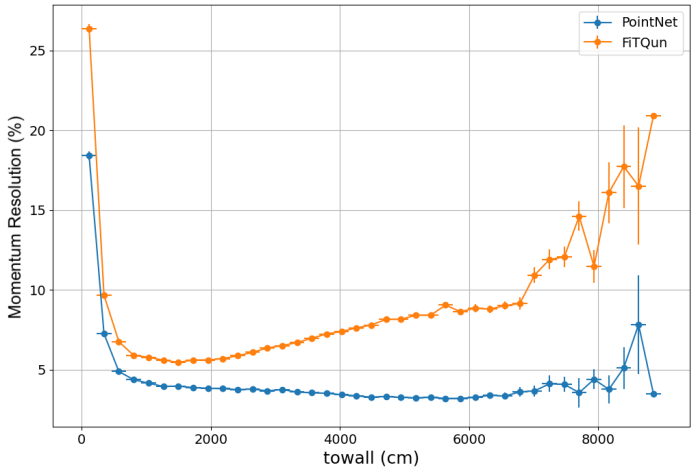


**(c)** towall (Full Range)

**Figure 6.34:** The 3D positional dependence of the momentum resolution of $\mu^-$ events from PointNet (blue) and FiTQun (orange) reconstructions.

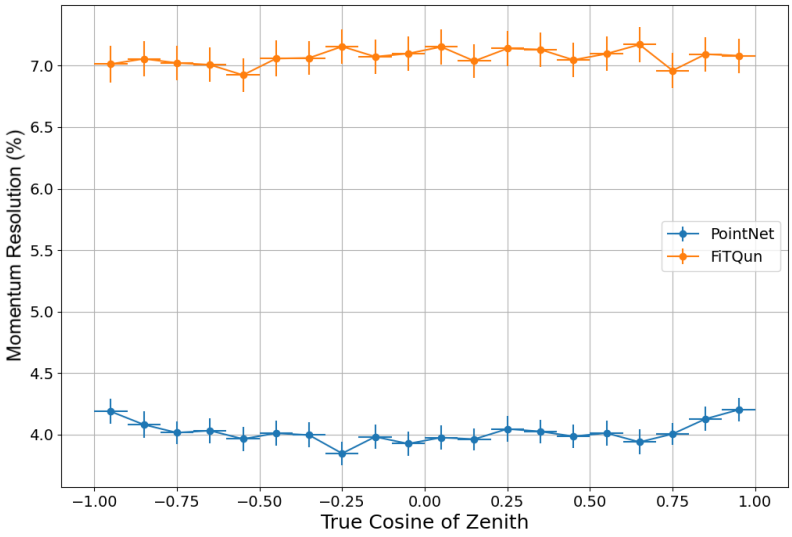


**(a)**

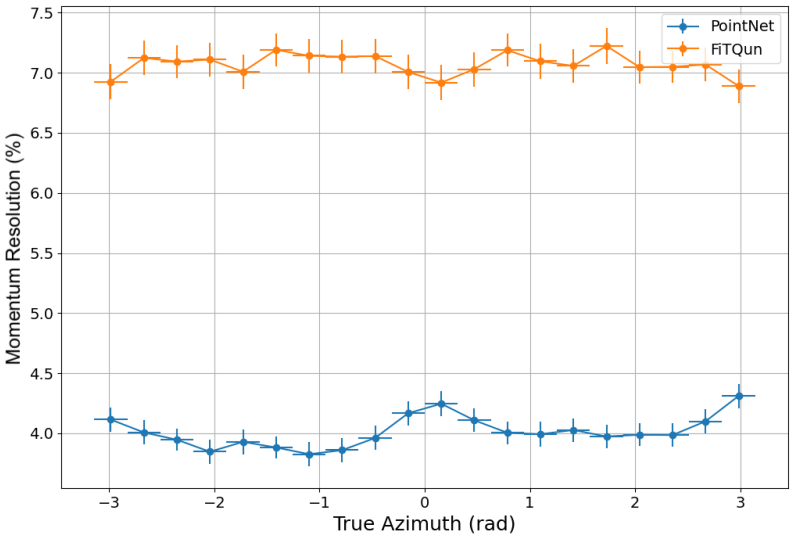


**(b)**

**Figure 6.35:** The directional dependence of the momentum resolution of $\mu^-$ events from PointNet (blue) and FiTQun (orange) reconstructions. The directional dependence of performance is explored as a function of (a) the cosine of zenith angle and (b) the azimuth angles.

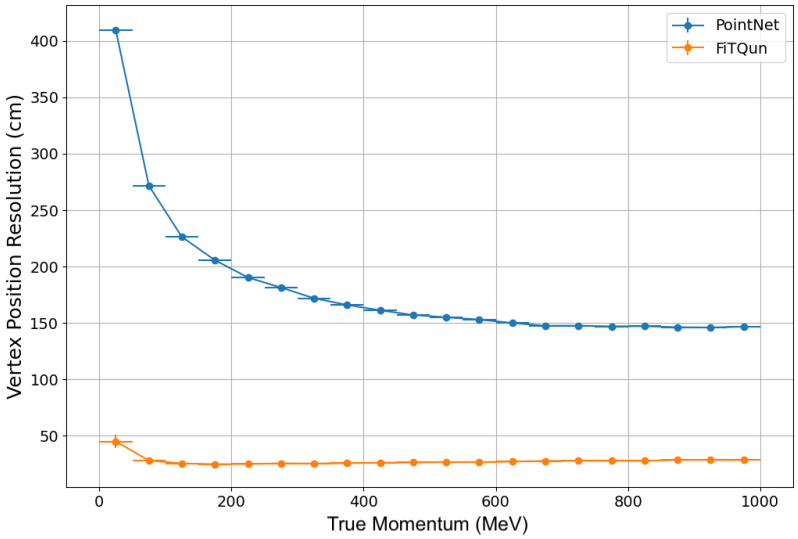


(a)

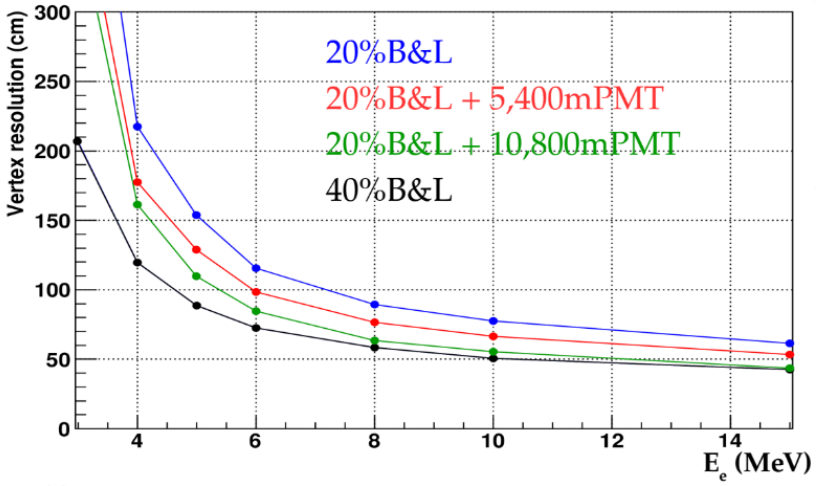


(b)

**Figure 6.36:** (a) The momentum dependence of the momentum resolution of $e^-$ events from PointNet (blue) and FiTQun (orange) reconstructions. (b) First reported vertex resolution of low energy electron events reconstructed using FiTQun for Hyper-K (2019) [155], the results in (a) should be benchmarked against the 20% B&L data (blue).

in further studies. Thus, the results are not shown explicitly here.

## 6.6 Discussions

### 6.6.1 Comparative Analysis of PointNet and FiTQun in Event Reconstruction

The application of PointNet, a machine learning method, and FiTQun, a traditional statistical approach, each has its own merits in reconstructing Hyper-K event kinematics. One of the outstanding features of PointNet is its flexibility and independence from prior assumptions about the data. This attribute allows PointNet to adapt seamlessly to various detector geometries, including changes in the dimensions or shape of the tank or the number of PMTs used. This starkly contrasts with FiTQun, which requires significant re-tuning to accommodate new geometries, consuming valuable time and resources.

Moreover, the efficiency of PointNet is remarkable once trained. It can classify or reconstruct events in roughly $10^{-5}$ seconds per event on a GPU. This performance vastly outstrips that of FiTQun, which processes an event every two minutes on a CPU, highlighting the potential for significant time savings in data analysis phases. Additionally, PointNet has demonstrated superior capabilities in anomaly detection. The model effectively identifies 'empty' events by comparing results with truth information, thereby facilitating the generation of more accurate cuts applied to events. This capability was found to be non-trivial with FiTQun, where identifying such anomalies proved more challenging.

On the other hand, FiTQun maintains its strengths, particularly in the clarity of its process from input data to output results. The conventional statistical tool has clear physical ramifications, making the pipeline easier to understand and interpret in physical terms. Adding to its advantages, it is also less complicated to estimate uncertainties with FiTQun reconstructions compared to using PointNet. Furthermore, FiTQun requires significantly less data for training compared to PointNet, which is advantageous in scenarios where data availability is limited. The need for less data pre-processing is another benefit, as FiTQun can directly process ROOT files from the WCSim output without the time-consuming conversion to hdf5 formats required by PointNet.

Despite the advantages listed above, PointNet's potential for overtraining or overfitting poses a risk to the model's generalisability to unseen data, a factor that requires careful consideration during its training phase. In contrast, FiTQun's simpler, more transparent approach mitigates such risks, although it does not match the speed and adaptability of PointNet. Each method's unique strengths and limitations underscore the importance of selecting the appropriate tool based on the specific requirements of the task at hand.

### 6.6.2 Directions for Future Research

Before the PointNet reconstruction tool can be deemed suitable for the application of reconstructing real Hyper-K data, it requires further refinement across five areas: performance analysis on new simulated data, introducing fiducial volume cuts, enhancing vertex resolution by reconstructing coordinates individually, integrating particle direction reconstruction, and improving model accuracy through hyperparameter optimisation. The following sections will systematically explore each of these areas.

An essential area for PointNet performance enhancement concerns training the model using newer MC data produced from the latest official Hyper-K geometry configurations. As mentioned earlier in this chapter, the data used for analysis reported in this thesis was produced at the end of 2021, using a geometry version named nuPRISM, which is no longer an accurate description of the latest Hyper-K detector design at the writing of this thesis at the end of 2023 and contains the wrong number of 20-in PMTs and mPMTs placed at an incorrect location. Thus, retraining the PointNet model and reprocessing data with FiTQun using updated simulation parameters is pivotal for accurately assessing their relative accuracies. These updates are imperative not only for preserving the analysis's relevance but also for potentially unveiling insights previously obstructed by obsolete simulation geometry.

Implementing fiducial volume (FV) cuts on processed events offers a promising strategy for enhancing classification and reconstruction accuracy. These cuts are crucial for filtering out poorly reconstructed events, especially since reconstruction software tends to underperform near the ID's wall regions. Adopting FV cuts could not only improve the tasks where PointNet and FiTQun excel but also boost their effectiveness

in weaker areas.

One avenue for improving PointNet vertex position reconstruction resolution is to focus on individual dimensions of the vertex coordinate, as multi-variate reconstruction had shown worse results previously. Although it takes more time to train the model on every coordinate dimension individually, the overall reconstruction speed should not be hugely impacted once trained. Moreover, with the already established WatChMaL framework, direction reconstruction for the events is fairly easily achievable, which, once established, could pave the way for a more comprehensive comparison to the FiTQun results.

Furthermore, optimising hyperparameters within the PointNet model offers a considerable prospect for advancement. Adjusting these hyperparameters, notably the learning rate and data sampling method, holds the potential for further improvements in model performance. This study would not only improve PointNet's predictive accuracy but also possibly expedite the training process by reducing computational demands and enabling more rapid cycles of testing and refinement.

# Chapter 7

# Conclusion

Since the addition of gadolinium into the Super-K detector, significant enhancements in operational oversight and procedural efficiency have been realised, particularly within the Super-K OD domain. The implementation of daily monitoring for the Super-K OD PMT gain has significantly enhanced the performance oversight of the OD. Moreover, with the processing time for the timing constant being reduced by more than a factor of 36, the capability for timely monitoring has markedly improved. These advancements have been crucial in analysing the impact of consecutive geomagnetic compensation coil failures at the end of 2023, facilitating a much faster impact analysis. It was observed that, unlike the Super-K ID, these coil failures did not significantly affect the operations of the OD PMTs due to the OD PMTs being smaller in volume, thus the geomagnetic field has less impact on the charged particle trajectories within.

Accompanying these operational advancements, this thesis provides a comprehensive documentation of the OD laser light injection system, which serves as a record for future reference. In addition, the data from the SK-VII OD laser calibration campaign, which commenced in September 2022, was analysed and compared to the SK-V data obtained using the same method. The result has confirmed the significant weakening of the OD laser light intensity, first observed in the OD fibre 51 and 52 data; and the result also demonstrated the necessity of a replacement laser. Moreover, the laser data also facilitated a health checkup of the OD light injection fibres and found three of the 52 fibres have seen a worsening in condition compared to their health reported at the end of 2019 during the SK-V period. Lastly, the analysis of new laser requirements

has laid the groundwork for selecting a replacement laser. Two of the most important requirements specify that the laser light injection system must emit over $10^9$ photons through the fibres fixed onto the OD wall, and that the output wavelength of the entire system should be close to 400 nm.

Furthermore, this thesis delves into the Hyper-K experiment, highlighting a pivotal aspect of neutrino physics analysis: the classification of particles and the reconstruction of their track kinematics. Utilising the hybrid tank geometry of Hyper-K, this work focuses on distinguishing between signal and background events by categorising four types of particles. Electron events are identified as signals, while muon, $\pi^0$, and photon events are treated as backgrounds. The investigation specifically explores the kinematic reconstructions of electrons and muons, underscoring their critical roles in the analysis.

The data used for the study was generated using the WCSim software, developed for the simulation of Hyper-K and IWCD detectors. The geometry chosen for the study presented in this thesis contains around 20,000 20-in PMTs and 5,000 mPMTs, with the number of mPMTs being an optimistic estimation. For each particle type mentioned in the paragraph above, three million events were generated. The energy, vertex position and direction distribution for each particle type was chosen as a uniform distribution between $[0, 1000]$ MeV above its Cherenkov energy threshold, uniformly distributed within the ID tank volume, and isotropically distributed, respectively.

A machine learning-based reconstruction framework, WatChMaL, has been developed for the upcoming IWCD detector, and ResNet18 and PointNet were two of the models employed. The PointNet model was adapted to the Hyper-K geometry. In the classification sector, the accuracy of the PointNet model in separating $e^-$ with $\mu^-$ and $\pi^0$ is on par with the traditional statistical method, FiTQun, which has been migrated from the Super-K reconstruction pipeline. However, PointNet, which runs on GPUs, is seven orders of magnitude faster than FiTQun, which currently can only be processed by CPUs. PointNet, as well as FiTQun, has no power to distinguish between $e^-$ and $\gamma$ events for now.

In terms of kinematics reconstruction, PointNet shows good performance as a function of all kinematic variables in electron momentum reconstruction above 100 MeV, but the resolution for muon momentum shows a weird trend as a function of true mo-

mentum. On the other hand, the vertex position reconstruction resolution of PointNet is worse than expected, while that of FiTQun is well over expectation. It is postulated that the low resolution of PointNet is due to the reconstruction of three dimensions of the position at the same time, as it was shown previously that the network is less accurate when trying to determine multiple variables together. As for the over-performance of FiTQun, it was possibly due to the geometry used for the simulated data.

Before implementing the PointNet model into the Hyper-K reconstruction framework, a few aspects should be further investigated. Firstly, the MC data generated for the analysis used out-of-date geometry from 2021; therefore, it would be hugely beneficial to retrain the model and reprocess using FiTQun with the latest simulation setup to draw a concrete conclusion on their relative performance. Secondly, incorporating fiducial volume cuts could notably enhance classification and reconstruction performance, especially in mitigating poorly reconstructed events near the ID's wall regions. Thirdly, the position resolution of a single dimension in vertex position should be investigated to verify whether reconstructing a single variable performs better than all at once. Fourthly, the direction reconstruction should be fairly easy to achieve using the existing framework. Lastly, the hyperparameters of the PointNet model, such as the learning rate, can be further optimised to improve model performance, as well as shortening the training time.

# Bibliography


[1] C. Jensen. *Controversy and Consensus: Nuclear Beta Decay 1911–1934*. Ed. by Finn Aaserud et al. 1st ed. Science Networks. Historical Studies. Springer Book Archive. Birkhäuser Basel, 2000, pp. XVII, 217. ISBN: 978-3-7643-5313-1. DOI: 10.1007/978-3-0348-8444-0.

[2] H.E. Mahnke. "Lise Meitner, $\beta$-decay and non-radiative electromagnetic transitions". In: *Notes and Records* 76 (2022), pp. 107–116. DOI: 10.1098/rsnr.2020.0036.

[3] P. Wolfgang. "Dear radioactive ladies and gentlemen". In: *Phys. Today* 31N9 (1978), p. 27.

[4] J. Chadwick. "The existence of a neutron". In: *Proceedings of the Royal Society of London. Series A, Containing Papers of a Mathematical and Physical Character* 136 (1932), pp. 692–708. DOI: 10.1098/rspa.1932.0112.

[5] H. Bethe and R. Peierls. "The Neutrino". In: *Nature* 133 (1934), pp. 689–690. DOI: 10.1038/133689b0.

[6] C.L. Cowan et al. "Detection of the Free Neutrino: a Confirmation". In: *Science* 124.3212 (1956), pp. 103–104. DOI: 10.1126/science.124.3212.103.

[7] G. Danby et al. "Observation of High-Energy Neutrino Reactions and the Existence of Two Kinds of Neutrinos". In: *Phys. Rev. Lett.* 9 (1 1962), pp. 36–44. DOI: 10.1103/PhysRevLett.9.36.

[8] M.L. Perl. "The Discovery of The Tau Lepton". In: *NATO Sci. Ser. B* 352 (1996). Ed. by H.B. Newman and T. Ypsilantis, pp. 277–302. DOI: 10.1007/978-1-4613-1147-8_15.

[9] K. Kodama et al. "Observation of tau neutrino interactions". In: *Physics Letters B* 504.3 (2001), pp. 218–224. ISSN: 0370-2693. DOI: https://doi.org/10.1016/S0370-2693(01)00307-0.

[10] The ILC Store. *Standard Model Plastic Folder*. Available from: https://aaasentan.thebase.in/items/41243686. [Accessed on 15 January 2024].

[11] M. Tanabashi et al. "Review of Particle Physics". In: *Phys. Rev. D* 98 (3 2018), p. 030001. DOI: 10.1103/PhysRevD.98.030001.

[12] M. Ahlers, K. Helbing, and C. Pérez de los Heros. "Probing particle physics with IceCube". In: *Eur. Phys. J. C* 78 (2018), p. 924. DOI: 10.1140/epjc/s10052-018-6369-9.

[13] CERN. *The origins of the Brout-Englert-Higgs mechanism*. European Organization for Nuclear Research. 2024. Available from: https://home.cern/science/physics/origins-brout-englert-higgs-mechanism. [Accessed on 12 January 2024].

[14] R. Davis, D.S. Harmer, and K.C. Hoffman. "Search for Neutrinos from the Sun". In: *Phys. Rev. Lett.* 20 (21 1968), pp. 1205–1209. DOI: 10.1103/PhysRevLett.20.1205.

[15] Y. Fukuda et al. "Evidence for Oscillation of Atmospheric Neutrinos". In: *Phys. Rev. Lett.* 81 (8 1998), pp. 1562–1567. DOI: 10.1103/PhysRevLett.81.1562.

[16] S. Fukuda et al. "The Super-Kamiokande detector". In: *Nuclear Instruments and Methods in Physics Research Section A: Accelerators, Spectrometers, Detectors and Associated Equipment* 501.2 (2003), pp. 418–462. ISSN: 0168-9002. DOI: https://doi.org/10.1016/S0168-9002(03)00425-X.

[17] B. Aharmim et al. "Combined analysis of all three phases of solar neutrino data from the Sudbury Neutrino Observatory". In: *Physical Review C* 88.2 (2013), p. 025501.

[18] B. Pontecorvo. "Mesonium and Antimesonium". In: *Journal of Experimental and Theoretical Physics* 33 (1957), pp. 549–551. Available from: http://jetp.ras.ru/cgi-bin/dn/e_006_02_0429.pdf.

[19] Z. Maki, M. Nakagawa, and S. Sakata. "Remarks on the Unified Model of Elementary Particles". In: *Progress of Theoretical Physics* 28.5 (1962), pp. 870–880. ISSN: 0033-068X. DOI: 10.1143/PTP.28.870.

[20] A.Y. Smirnov. "The MSW Effect and Matter Effects in Neutrino Oscillations". In: *Physica Scripta* 2005.T121 (2005), p. 57. DOI: 10.1088/0031-8949/2005/T121/008.

[21] Q. R. Ahmad et al. "Direct Evidence for Neutrino Flavor Transformation from Neutral-Current Interactions in the Sudbury Neutrino Observatory". In: *Phys. Rev. Lett.* 89 (1 June 2002), p. 011301. DOI: 10.1103/PhysRevLett.89.011301.

[22] E. Vitagliano, I. Tamborra, and G. Raffelt. "Grand unified neutrino spectrum at Earth: Sources and spectral components". In: *Reviews of Modern Physics* 92.4 (2020). ISSN: 1539-0756. DOI: 10.1103/revmodphys.92.045006.

[23] A. Goldsack. "Reactor Neutrinos in a Gadolinium-Loaded Super-Kamiokande". PhD thesis. University of Oxford, 2022. Available from: https://ora.ox.ac.uk/objects/uuid:0a1e9c97-a037-42e3-b175-26495a0e7ed2/download_file?file_format=application%2Fpdf&safe_filename=Goldsack_2022_Reactor_neutrinos_in.pdf&type_of_work=Thesis.

[24] A. Letourneau et al. "Origin of the Reactor Antineutrino Anomalies in Light of a New Summation Model with Parametrized $\beta$- Transitions". In: *Physical Review Letters* 130.021801 (2023). DOI: 10.1103/PhysRevLett.130.021801.

[25] O. Smirnov. "Experimental aspects of geoneutrino detection: Status and perspectives". In: *Progress in Particle and Nuclear Physics* 109 (2019), p. 103712. ISSN: 0146-6410. DOI: https://doi.org/10.1016/j.ppnp.2019.103712.

[26] C.V. Achar et al. "Detection of muons produced by cosmic ray neutrinos deep underground". In: *Physics Letters* 18.2 (1965), pp. 196–199. ISSN: 0031-9163. DOI: https://doi.org/10.1016/0031-9163(65)90712-2.

[27] F. Reines et al. "Evidence for High-Energy Cosmic-Ray Neutrino Interactions". In: *Phys. Rev. Lett.* 15 (9 Aug. 1965), pp. 429–433. DOI: 10.1103/PhysRevLett.15.429.

[28] K. Abe et al. "The T2K experiment". In: *Nuclear Instruments and Methods in Physics Research Section A: Accelerators, Spectrometers, Detectors and Associated Equipment* 659.1 (2011), pp. 106–135. ISSN: 0168-9002. DOI: 10.1016/j.nima.2011.06.067.

[29] M. D. Haigh. "Beam Extrapolation and Photosensor Testing for the T2K Experiment". PhD thesis. The University of Warwick, 2010.

[30] The JUNO Collaboration. *Potential to Identify the Neutrino Mass Ordering with Reactor Antineutrinos in JUNO*. 2024. arXiv: 2405.18008 [hep-ex].

[31] The KATRIN collaboration et al. "The Design, Construction, and Commissioning of the KATRIN Experiment". In: *Journal of Instrumentation* 16.08 (2021), T08015. DOI: 10.1088/1748-0221/16/08/T08015.

[32] The KATRIN Collaboration. "Direct neutrino-mass measurement with sub-electronvolt sensitivity". In: *Nature Physics* 18 (2022), pp. 160–166. DOI: https://doi.org/10.1038/s41567-021-01463-1.

[33] R. L. Workman et al. "Review of Particle Physics". In: *PTEP* 2022 (2022), p. 083C01. DOI: 10.1093/ptep/ptac097.

[34] A. Himmel. *New oscillation results from the NOvA experiment*. Tech. rep. Fermi National Accelerator Lab. (FNAL), Batavia, IL (United States), 2020.

[35] B. Abi et al. *Deep Underground Neutrino Experiment (DUNE), Far Detector Technical Design Report, Volume I: Introduction to DUNE*. 2020. arXiv: 2002.02967.

[36] I. Esteban et al. "The fate of hints: updated global analysis of three-flavor neutrino oscillations". In: *Journal of High Energy Physics* 2020.9 (2020), pp. 1–22.

[37] T. Kajita, M. Koshiba, and A. Suzuki. "On the origin of the Kamiokande experiment and neutrino astrophysics". In: *European Physical Journal H* 37 (2012). DOI: https://doi.org/10.1140/epjh/e2012-30007-y.

[38] T. Kajita. "Professor Koshiba and atmospheric neutrinos". In: *Progress of Theoretical and Experimental Physics* (2023), ptad013. ISSN: 2050-3911. DOI: 10.1093/ptep/ptad013.

[39] M. Nakahata. *History of Solar Neutrino Observations*. 2022. arXiv: 2202.12421 [hep-ex].

[40] M. Nakahata et al. "Atmospheric Neutrino Background and Pion Nuclear Effect for KAMIOKA Nucleon Decay Experiment". In: *Journal of the Physical Society of Japan* 55.11 (1986), pp. 3786–3805. DOI: 10.1143/JPSJ.55.3786.

[41] T.J. Haines et al. "Calculation of Atmospheric Neutrino-Induced Backgrounds in a Nucleon-Decay Search". In: *Phys. Rev. Lett.* 57 (16 1986), pp. 1986–1989. DOI: 10.1103/PhysRevLett.57.1986.

[42] K.S. Hirata et al. "Observation in the Kamiokande-II detector of the neutrino burst from supernova SN1987A". In: *Phys. Rev. D* 38 (2 1988), pp. 448–458. DOI: 10.1103/PhysRevD.38.448.

[43] R. Svoboda et al. "Neutrinos from Supernova 1987A in the IMB Detector". In: *European Southern Observatory Conference and Workshop Proceedings*. Vol. 26. European Southern Observatory Conference and Workshop Proceedings. 1987, p. 229. Available from: https://ui.adsabs.harvard.edu/abs/1987ESOC...26..229S.

[44] T. Araki et al. "Measurement of Neutrino Oscillation with KamLAND: Evidence of Spectral Distortion". In: *Phys. Rev. Lett.* 94 (8 2005), p. 081801. DOI: 10.1103/PhysRevLett.94.081801.

[45] T. Kajita, E. Kearns, and M. Shiozawa. "Establishing atmospheric neutrino oscillations with Super-Kamiokande". In: *Nuclear Physics B* 908 (2016). Neutrino Oscillations: Celebrating the Nobel Prize in Physics 2015, pp. 14–29. ISSN: 0550-3213. DOI: https://doi.org/10.1016/j.nuclphysb.2016.04.017.

[46] Hyper-Kamiokande Proto-Collaboration et al. *Hyper-Kamiokande Design Report*. 2018. arXiv: 1805.04163 [physics.ins-det].

[47] K. Hiraide. *Status of the Hyper-Kamiokande Experiment*. 2023. Available from: https://agenda.infn.it/event/33778/contributions/207825/attachments/111335/158814/231011-NNN23-hiraide-HK-v2.pdf.

[48] P. A. Čerenkov. "Visible Radiation Produced by Electrons Moving in a Medium with Velocities Exceeding that of Light". In: *Phys. Rev.* 52 (4 1937), pp. 378–379. DOI: 10.1103/PhysRev.52.378.

[49] I. Frank and Ig. Tamm. "Coherent Visible Radiation of Fast Electrons Passing Through Matter". In: *Selected Papers*. Ed. by Boris M. Bolotovskii, Victor Ya. Frenkel, and Rudolf Peierls. Berlin, Heidelberg: Springer Berlin Heidelberg, 1991, pp. 29–35. ISBN: 978-3-642-74626-0. DOI: 10.1007/978-3-642-74626-0_2.

[50] Kamioka Observatory, ICRR, University of Tokyo. *Super-Kamiokande Detector*. [Internet]. 2023. Available from: https://www-sk.icrr.u-tokyo.ac.jp/en/sk/about/detector/. [Accessed on 25 December 2023].

[51] Hamamatsu Photonics. *Photomultiplier Tubes: Basics and Applications*. 4th ed. Hamamatsu Photonics K.K. Hamamatsu City, Japan, 2023. Available from: https://www.hamamatsu.com/content/dam/hamamatsu-photonics/sites/documents/99_SALES_LIBRARY/etd/PMT_handbook_v4E.pdf. [Accessed on 26 December 2023].

[52] Hamamtsu Photonics. *Photomultiplier Tube R3600-02, -06*. 1999. Available from: http://hep.ucsb.edu/people/hnn/n/pmt_info/R3600-02_20inch_superKmain.pdf. [Accessed on 26 December 2023].

[53] *The dynode structure of the Hamamatsu R1408 8-inch PMT used in the IMB experiment*. Private communication with Baran Bodur from Duke University.

[54] Hamamatsu. *Large Photocathode Area Photomultiplier Tubes*. [Internet]. [8 Screens]. 2019. Available from: https://hep.hamamatsu.com/content/dam/hamamatsu-photonics/sites/documents/99_SALES_LIBRARY/etd/LARGE_AREA_PMT_TPMH1376E.pdf. [Accessed on 16 September 2023].

[55] T. Wester. "Discerning the Neutrino Mass Ordering Using Atmospheric Neutrinos in Super-Kamiokande I-V". PhD thesis. Boston University, 2023. Available from: https://www-sk.icrr.u-tokyo.ac.jp/sk/_pdf/articles/2023/twester_thesis_2023_embedded.pdf.

[56] K. Abe et al. "Calibration of the Super-Kamiokande detector". en. In: *Nuclear Instruments and Methods in Physics Research Section A: Accelerators, Spectrometers, Detectors and Associated Equipment* 737 (2014), pp. 253–272. ISSN: 0168-9002. DOI: 10.1016/j.nima.2013.11.081. [Accessed on 20 January 2020].

[57] J. A. Formaggio and G. P. Zeller. "From eV to EeV: Neutrino cross sections across energy scales". In: *Rev. Mod. Phys.* 84 (3 2012), pp. 1307–1341. DOI: 10.1103/RevModPhys.84.1307.

[58] J.N. Bahcall and C. Peña-Garay. "Solar models and solar neutrino oscillations". In: *New Journal of Physics* 6.1 (2004), p. 63. DOI: 10.1088/1367-2630/6/1/063.

[59] *The death rate of IMB PMTs in the Super-Kamiokande outer detector volume.* Private communication with Rory Ramsden from King's College London.

[60] R. Becker-Szendy et al. "IMB-3: a large water Cherenkov detector for nucleon decay and neutrino interactions". In: *Nuclear Instruments and Methods in Physics Research Section A: Accelerators, Spectrometers, Detectors and Associated Equipment* 324.1 (1993), pp. 363–382. ISSN: 0168-9002. DOI: https://doi.org/10.1016/0168-9002(93)90998-W.

[61] H. de Kerret et al. "The Double Chooz antineutrino detectors". In: *The European Physical Journal C* 82.9 (2022). ISSN: 1434-6052. DOI: 10.1140/epjc/s10052-022-10726-x.

[62] M. Nakahata. "Geomagnatic Compensation Coil (Status and Prospects)". Presented on 28 November 2023 in the Super-Kamiokande Collaboration Meeting. Available from: https://indico-sk.icrr.u-tokyo.ac.jp/event/8486/contributions/27481/attachments/24211/32194/SK-meeting-coil-cable-problem-231128-v4.pdf. [Accessed on 27 December 2023].

[63] K. Abe et al. "First gadolinium loading to Super-Kamiokande". In: *Nuclear Instruments and Methods in Physics Research Section A: Accelerators, Spectrometers, Detectors and Associated Equipment* 1027 (2022), p. 166248. DOI: 10.1016/j.nima.2021.166248.

[64] J. Zoll et al. "ZEBRA : Overview of the ZEBRA System". In: (1995). CERN Program Library Long Writeups. Available from: https://cds.cern.ch/record/2296399.

[65] R. Brun and F. Rademakers. *ROOT*. Version 6.26/04. CERN, Dec. 27, 2023. [Accessed on 27 December 2023].

[66] R. Brun et al. "GEANT Detector Description and Simulation Tool". In: (1994). DOI: 10.17181/CERN.MUHF.DMJ1.

[67] Y. Hayato. "Neut". In: *Nuclear Physics B - Proceedings Supplements* 112.1 (2002), pp. 171–176. ISSN: 0920-5632. DOI: https://doi.org/10.1016/S0920-5632(02)01759-0.

[68] M. Honda et al. "New calculation of the atmospheric neutrino flux in a three-dimensional scheme". In: *Physical Review D* 70.4 (2004). ISSN: 1550-2368. DOI: 10.1103/physrevd.70.043008. Available from: http://dx.doi.org/10.1103/PhysRevD.70.043008.

[69] M. Honda et al. "Atmospheric neutrino fluxes". In: *Phys. Lett. B* 248 (1990), pp. 193–198. DOI: 10.1016/0370-2693(90)90038-8.

[70] M. Honda et al. "Calculation of the flux of atmospheric neutrinos". In: *Phys. Rev. D* 52 (9 1995), pp. 4985–5005. DOI: 10.1103/PhysRevD.52.4985.

[71] G. Battistoni et al. "High-energy extension of the FLUKA atmospheric neutrino flux". In: *28th International Cosmic Ray Conference*. 2003. arXiv: hep-ph/0305208.

[72] G. D. Barr et al. "Three-dimensional calculation of atmospheric neutrinos". In: *Phys. Rev. D* 70 (2 2004), p. 023006. DOI: 10.1103/PhysRevD.70.023006.

[73] M. Harada, Y. Koshio, and K. Hagiwara. "Development of Geant4 based simulation for Super-Kamiokande". In: 2019, p. 049. DOI: 10.22323/1.356.0049.

[74] S. Agostinelli et al. "GEANT4–a simulation toolkit". In: *Nucl. Instrum. Meth. A* 506 (2003), pp. 250–303. DOI: 10.1016/S0168-9002(03)01368-8.

[75] M. Harada. "Geant4 based Simulation Study for Super-Kamiokande". In: *Journal of Physics: Conference Series* 1468.1 (2020), p. 012255. DOI: 10.1088/1742-6596/1468/1/012255. Available from: https://dx.doi.org/10.1088/1742-6596/1468/1/012255.

[76] S Moriyama. *Report from University of Tokyo*. 2023. Available from: https://hkdbweb.in2p3.fr/doc/meetingfiles/A00031706/231025-UTstatus-moriyama-v2.pdf. [Accessed on 5 January 2023].

[77] Kamioka Observatory, ICRR, University of Tokyo. *Hyper-Kamiokande Detector*. [Internet]. 2024. Available from: https://www-sk.icrr.u-tokyo.ac.jp/en/hk. [Accessed on 5 January 2024].

[78] B. Jamieson. *Future Neutrino Experiments*. 2022. arXiv: 2207.05044 [hep-ex].

[79] J. Bian et al. *Hyper-Kamiokande Experiment: A Snowmass White Paper*. 2022. arXiv: 2203.02029.

[80] T. Zhu. "Long-baseline neutrino oscillation sensitivities with Hyper-Kamiokande and impact of Intermediate Water Cherenkov Detector". In: *Proceedings of Neutrino Oscillation Workshop — PoS(NOW2022)*. Vol. 421. 2023, p. 028. DOI: 10.22323/1.421.0028.

[81] *Apache Subversion (SVN)*. Apache Software Foundation. 2023. Available from: https://subversion.apache.org/. [Accessed on 16 January 2024].

[82] B. Bodur. "Measurements of Atmospheric Flux-Weighted ve-16O Cross Section with the Super-Kamiokande Experiment". PhD thesis. Duke University, 2023.

[83] S. Nakayama. "Status of ID electronics". Presented on 17 May 2022 in the Super-Kamiokande Collaboration Meeting. Available from: https://indico-sk.icrr.u-tokyo.ac.jp/event/7212/contributions/22153/attachments/20704/26473/20220517-Nakayama-IDelec.pdf. [Accessed on 14 February 2024].

[84] Y. Byeongsu. "AutoLaser (TQ) status and timing stability in SK-5/6". Presented on 17 May 2022 in the Super-Kamiokande Collaboration Meeting. Available from: `https://indico-sk.icrr.u-tokyo.ac.jp/event/7212/contributions/22193/attachments/20697/26454/20220517%5C_yang%5C_Timing%5C_calibration.pdf`. [Accessed on 14 February 2024].

[85] Labarga L. "SK-V, -VI, -VII Detector Monitoring with Auto-Xenon and Nickel Data". Presented on 29 November 2023 in the Super-Kamiokande Collaboration Meeting. Available from: `https://indico-sk.icrr.u-tokyo.ac.jp/event/8451/contributions/27648/attachments/24130/32173/reportAt-sk_CM_20231129_autoXenonNiAtSKV-VII_v2.pdf`. [Accessed on 29 November 2023].

[86] M. Nakahata. "Geomagnetic Compensation coil #2 Problem". Presented on 30 October 2023 in the T2K Collaboration Meeting. [Accessed on 27 November 2023].

[87] A. Kibayashi. *Super-K Laser System Manual*. [Internet]. Dec. 2000. Not available on the public internet. [Accessed on 19 June 2023].

[88] O. Svelto. "Introductory Concepts". English. In: *Principles of Lasers*. Fourth edition. New York: Springer+ Science Business Media, 1998, pp. 1–14. ISBN: 9781475762662.

[89] Market Tech. *Overview of Modulated and Pulsed Diode Laser Systems*. Internet. 2018. Available from: `https://www.markettechinc.net/wp-content/uploads/2018/05/Modulated-and-Pulsed-Diode-Lasers.pdf`. [Accessed on 19 June 2023].

[90] O. Svelto. "Pumping Processes". English. In: *Principles of Lasers*. Fourth edition. New York: Springer+ Science Business Media, 1998, pp. 201–244. ISBN: 9781475762662.

[91] O. Svelto. "Introduction to Gas, Chemical, Free-Electron, and X-Ray Lasers". English. In: *Principles of Lasers*. Fourth edition. New York: Springer+ Science Business Media, 1998, p. 419. ISBN: 9781475762662.

[92] O. Svelto. "Nitrogen Lasers". English. In: *Principles of Lasers*. Fourth edition. New York: Springer+ Science Business Media, 1998, pp. 444–445. ISBN: 9781475762662.

[93] O. Svelto. "Molecular Gas Lasers". English. In: *Principles of Lasers*. Fourth edition. New York: Springer+ Science Business Media, 1998, pp. 432–445. ISBN: 9781475762662.

[94] O. Svelto. "Threshold Conditions and Output Power: Four-Level Laser". English. In: *Principles of Lasers*. Fourth edition. New York: Springer+ Science Business Media, 1998, p. 258. ISBN: 9781475762662.

[95] O. Svelto. "Dye Lasers". English. In: *Principles of Lasers*. Fourth edition. New York: Springer+ Science Business Media, 1998, pp. 386–394. ISBN: 9781475762662.

[96] J. Hecht. "Laser Characteristics". In: *Understanding lasers: an entry-level guide*. 3rd ed. IEEE Press Understanding Science & Technology Series. Piscataway, New Jersey: IEEE Press, 2008, pp. 93–119. ISBN: 0-470-33581-5.

[97] D.M. Pozar. "Transmission Line Theory". eng. In: *Microwave Engineering*. 3rd ed. New York: Wiley, 2004, pp. 62–63. ISBN: 0471448788.

[98] Laser Science, Inc. *VSL-337 Nitrogen Laser*. [Internet]. [1 screen]. 2000. Available from: `http://host.web-print-design.com/laserscience/vsl_337.html`. [Accessed on 19 June 2023].

[99] Exciton of Luxottica. *Exalite 384*. [Internet]. [2 screens]. Date Unknown. Available from: `https://exciton.luxottica.com/media/productattach/Datasheet/03840.pdf`. [Accessed on 28 June 2023].

[100] R. A. Zângaro et al. "Rapid multiexcitation fluorescence spectroscopy system for in vivo tissue diagnosis". In: *Appl. Opt.* 35.25 (1996), pp. 5211–5219. DOI: `10.1364/AO.35.005211`.

[101] Sirah Lasertechnik. *Exalite 384*. [Internet Webpage]. 2023. Available from: `https://www.sirah.com/accessories/dyes/dye-exalite-384/#hrr-355/`. [Accessed on 19 October 2023].

[102] G.H. Pujar et al. "A combined experimental and computational investigation of solvatochromism of nonpolar laser dyes: Evaluation of ground and singlet excited-state dipole moments". In: *Journal of Molecular Liquids* 244 (2017), pp. 453–463. ISSN: 0167-7322. DOI: https://doi.org/10.1016/j.molliq.2017.08.078.

[103] Thorlabs, Inc. *Manual Filter Wheels*. [Internet]. [1 screen]. 2023. [Accessed on 5 October 2023].

[104] UniGreenScheme. *LSI Laser Science VSL-337ND-S Pulsed Nitrogen Laser Head*. [Internet]. [1 screen]. Date Unknown. [Accessed on 10 October 2022].

[105] J.W. Flanagan. "A Study of Atmospheric Neutrinos at Super-Kamiokande". PhD thesis. University of Hawaii, 1997. Available from: https://www-sk.icrr.u-tokyo.ac.jp/sk/_pdf/articles/johnf_thesis.pdf.

[106] S. Matsuno. *Details on OD Calibration Fiber*. [Internet]. [5 screens]. Oct. 2016. [Accessed on 14 September 2023].

[107] S. Matsuno. *OD calibration system (in preparation for SK tank opening)*. [Internet]. [11 screens]. Sept. 2016. [Accessed on 13 October 2023].

[108] Silvano Donati. "Photomultipliers". eng. In: *Photodetectors: Devices, Circuits and Applications*. Wiley-IEEE Press, 2021, pp. 31–102. DOI: 10.1002/9781119769958.ch4.

[109] J. McElwee. "Tuning Neutrino Interaction Models to Inclusive Electron Scattering Data". PhD thesis. University of Sheffield, 2022. Available from: https://etheses.whiterose.ac.uk/32248/1/mcelwee_thesis.pdf.

[110] The Korean Group within the Super-Kamiokande Collaboration. "Auto TQ Monitor". [Internal Website]. Oct. 2023. Available from: https://www-sk1.icrr.u-tokyo.ac.jp/~calib/auto_tq_mon.html. [Accessed on 17 October 2023].

[111] Hamamatsu Photonics. *PLP-10 Laser Diode Head Series*. [Internet]. [2 screens]. 2023. Available from: https://www.hamamatsu.com/content/dam/hamamatsu-

photonics/sites/documents/99_SALES_LIBRARY/sys/SOCS0003E_PLP-10.pdf. [Accessed on 24 October 2023].

[112] *The usage of Hamamatsu PLP-10 laser in the Super-Kamiokande*. Private communication with Motoyasu Ikeda from ICRR, University of Tokyo.

[113] mrongen. *Ultrafast VCSEL/LED Triggered Light Source*. [Internet]. [2 screens]. 2023. Available from: https://mrongen.de/wp-content/uploads/2018/05/LightPulser.pdf. [Accessed on 24 October 2023].

[114] Thorlabs. *Power and Energy Meter Interfaces with External Readout*. [Internet]. [1 screen]. 2023. Available from: https://www.thorlabs.com/newgrouppage9.cfm?objectgroup_id=4037. [Accessed on 23 October 2023].

[115] Spectra Physics. *Explorer® One™ Compact and Lightweight UV and Green ns Lasers*. [Internet]. [8 Screens]. 2023. Available from: https://www.spectra-physics.com/mam/celum/celum_assets/sp/resources/Explorer-One-Datasheet_0315.pdf?0. [Accessed on 15 May 2023].

[116] LaserTechnik Berlin. *MNL 100 Mini-Nitrogen-Laser*. [Internet]. [2 Screens]. 2023. Available from: https://www.photonicsolutions.co.uk/upfiles/MNL100.pdf. [Accessed on 16 May 2023].

[117] D. Guest, K. Cranmer, and D. Whiteson. "Deep Learning and Its Application to LHC Physics". In: *Annual Review of Nuclear and Particle Science* 68.1 (2018), pp. 161–181. ISSN: 1545-4134. DOI: 10.1146/annurev-nucl-101917-021019.

[118] J. Barhen, R. Cogswell, and V. Protopopescu. "Single-Iteration Training Algorithm for Multi-Layer Feed-Forward Neural Networks". In: *Neural Processing Letters* 11 (2 2000), pp. 113–129. DOI: 10.1023/A:1009682730770.

[119] K. Hornik, M. Stinchcombe, and H. White. "Multilayer feedforward networks are universal approximators". In: *Neural Networks* 2.5 (1989), pp. 359–366. ISSN: 0893-6080. DOI: https://doi.org/10.1016/0893-6080(89)90020-8.

[120] Y. Guo et al. "Deep learning for visual understanding: A review". In: *Neurocomputing* 187 (2016). Recent Developments on Deep Big Vision, pp. 27–48. ISSN: 0925-2312. DOI: https://doi.org/10.1016/j.neucom.2015.09.116.

[121] Y. Lecun et al. “Gradient-Based Learning Applied to Document Recognition”. In: *Proceedings of the IEEE* 86 (1998), pp. 2278–2324. DOI: 10.1109/5.726791.

[122] F. Psihas et al. “A review on machine learning for neutrino experiments”. In: *International Journal of Modern Physics A* 35.33 (2020), p. 2043005. ISSN: 1793-656X. DOI: 10.1142/s0217751x20430058.

[123] M.D. Zeiler. “Hierarchical Convolutional Deep Learning in Computer Vision”. PhD thesis. New York University, 2013. Available from: https://api.semanticscholar.org/CorpusID:5426209.

[124] K. Fukushima. “Neocognitron: A self-organizing neural network model for a mechanism of pattern recognition unaffected by shift in position”. In: *Biological Cybernetics* 36 (1980), pp. 193–202. Available from: https://api.semanticscholar.org/CorpusID:206775608.

[125] C. SSzegedy et al. “Going deeper with convolutions”. In: *Proceedings of the IEEE conference on computer vision and pattern recognition*. 2015, pp. 1–9.

[126] M. Oquab et al. “Is object localization for free?-Weakly-supervised learning with convolutional neural networks”. In: *Proceedings of the IEEE conference on computer vision and pattern recognition*. 2015, pp. 685–694.

[127] M. Lin, Q. Chen, and S. Yan. “Network In Network”. In: vol. abs/1312.4400. 2013. Available from: https://api.semanticscholar.org/CorpusID:16636683.

[128] Y.L. Boureau, J. Ponce, and Y. Lecun. “A Theoretical Analysis of Feature Pooling in Visual Recognition”. In: 2010, pp. 111–118.

[129] K. Jarrett et al. “What is the best multi-stage architecture for object recognition?” In: *2009 IEEE 12th International Conference on Computer Vision*. 2009, pp. 2146–2153. DOI: 10.1109/ICCV.2009.5459469.

[130] M.C. Chon. “Muon physics and neural network event classifier for the Sudbury Neutrino Observatory”. PhD thesis. University of Guelph, 1998. Available from: https://ui.adsabs.harvard.edu/abs/1998PhDT.....227C/abstract.

[131] C. Adams et al. "Deep neural network for pixel-level electromagnetic particle identification in the MicroBooNE liquid argon time projection chamber". In: *Physical Review D* 99.9 (2019). ISSN: 2470-0029. DOI: 10.1103/physrevd.99.092001.

[132] P. Adamson et al. "Constraints on Oscillation Parameters from $\nu_e$ Appearance and $\nu_\mu$ Disappearance in NOvA". In: *Phys. Rev. Lett.* 118 (23 2017), p. 231801. DOI: 10.1103/PhysRevLett.118.231801.

[133] E. Drakopoulou et al. "Application of Machine Learning Techniques to Lepton Energy Reconstruction in Water Cherenkov Detectors". In: *Journal of Instrumentation* (2018).

[134] K. He et al. *Deep Residual Learning for Image Recognition*. 2015. arXiv: 1512.03385 [cs.CV].

[135] N. Prouse. "Advances in Simulation and Reconstruction for Hyper-Kamiokande". In: vol. ICHEP2020. 2021, p. 919. DOI: 10.22323/1.390.0919.

[136] S. Tobayama. "An analysis of the oscillation of atmospheric neutrinos". PhD thesis. University of British Columbia, 2016. DOI: http://dx.doi.org/10.14288/1.0340615.

[137] C.R. Qi et al. *PointNet: Deep Learning on Point Sets for 3D Classification and Segmentation*. 2017. arXiv: 1612.00593 [cs.CV].

[138] WatChMaL. [Internet].

[139] M. Jaderberg et al. *Spatial Transformer Networks*. 2016. arXiv: 1506.02025 [cs.CV].

[140] V. Nair and G. Hinton. "Rectified Linear Units Improve Restricted Boltzmann Machines Vinod Nair". In: vol. 27. 2010, pp. 807–814.

[141] T. Oliphant. *NumPy: A guide to NumPy*. USA: Trelgol Publishing. 2006.

[142] J. Gao. "Developing Machine Learning Techniques for Simplified Template Cross Section Measurements in the Higgs Boson to Two-photon Decay Channel at CMS". 2019.

[143] P. De Perio. *Progress on Analysis Technologies for the Hyper-Kamiokande Water Cherenkov Detectors*. Presented at The 21st international workshop on Next Generation Nucleon Decay and Neutrino Detectors (NNN22). 2022.

[144] R.B. Patterson et al. "The extended-track event reconstruction for MiniBooNE". In: *Nuclear Instruments and Methods in Physics Research Section A: Accelerators, Spectrometers, Detectors and Associated Equipment* 608.1 (2009), pp. 206–224. ISSN: 0168-9002. DOI: 10.1016/j.nima.2009.06.064.

[145] B Quilain. *Readiness of fiTQun for 2023/24 production*. 2023. Available from: https://hkdbweb.in2p3.fr/doc/meetingfiles/A00031487/HyperK_20231023_StatusOfFiTQunFD_HKPhysicsSoftwarePreMeeting_Quilain.pdf.

[146] J Gao. *Fitqun cut generation for e-mu- PID*. 2023.

[147] WCSim Development Group. *WCSim Software on GitHub*. 2024.

[148] R. Brun and F. Rademakers. "ROOT - An Object Oriented Data Analysis Framework". In: *Proceedings of the AIHENP'96 Workshop*. Vol. 389. Workshop held in September 1996. Lausanne: Nucl. Inst. & Meth. in Phys. Res. A, 1997, pp. 81–86.

[149] B. Quilain. *nuPRISM simulation used for data generation for this thesis*. Available from: https://github.com/nuPRISM/WCSim/tree/nuPRISM/develop. [Accessed on 2 January 2024].

[150] WCSim Development Group. *WCSim v1.11.0*.

[151] M. Smy. "Low Energy Event Reconstruction and Selection in Super-Kamiokande-III". In: *30th International Cosmic Ray Conference*. Vol. 5. 2007, pp. 1279–1282.

[152] M. Jiang et al. "Atmospheric neutrino oscillation analysis with improved event reconstruction in Super-Kamiokande IV". In: *Progress of Theoretical and Experimental Physics* 2019.5 (2019). ISSN: 2050-3911. DOI: 10.1093/ptep/ptz015.

[153] Missert A.D. on behalf of the T2K Collaboration. "Improving the T2K Oscillation Analysis With fiTQun: A New Maximum-Likelihood Event Reconstruction for Super-Kamiokande". In: *Journal of Physics: Conference Series* 888.1 (2017),

p. 012066. DOI: 10.1088/1742-6596/888/1/012066. Available from: https://dx.doi.org/10.1088/1742-6596/888/1/012066.

[154] *The performance of multi-variate reconstruction using PointNet*. Private communication with Nicholas Prouse from Imperial College London.

[155] B Quilain. *First simulation results using multi-PMTs for Hyper-Kamiokande far detector*. 2019. Available from: https://www.dropbox.com/scl/fi/8sualssga75g8wli7kbwj/HyperK%5C_20190905%5C_HyperKamiokandeCMPlenary%5C_SimulationStudiesWithmPMTs%5C_Quilain.pdf?rlkey=wo5u1jgiayvfn0udw5owc8zsj&dl=0. [Accessed on 11 February 2024].

[156] M Jiang et al. "Atmospheric neutrino oscillation analysis with improved event reconstruction in Super-Kamiokande IV". In: *Progress of Theoretical and Experimental Physics* (2019). DOI: https://doi.org/10.1093/ptep/ptz015.

[157] *The overly accurate vertex reconstruction using FiTQun*. Private communication with Benjamin Quilain from Laboratoire Leprince-Ringuet, CNRS/Ecole Polytechnique, France.

[158] O. Svelto. *Principles of Lasers*. English. Fourth edition. New York: Springer+ Science Business Media, 1998. ISBN: 9781475762662.

# Appendix A

# Notes and Instructions from the September 2022 OD Laser Data Taking Campaign

This appendix documents the steps taken to perform a successful OD laser data-taking campaign. Simply speaking, a complete OD laser data-taking process involves flashing light through all 52 OD fibres with 10 different filter intensity settings ('settings'), and each fibre at each setting is flashed 400 times. There is an option to have 11 settings for fibre 51 and 52, which will also be discussed in this chapter.

A few things to note:

- Change into a *test run* first before amending any hardware/software configurations!
- The signal input cable is left **plugged into Switch 1** as of October 2022. This is due to fibre 51 and 52 being included in the autocalib process to monitor water quality while the Gd compound was loaded into the Super-K tank at the beginning of June 2022. There is a plan to remove the two fibres from the autocalib process as of 14 October 2022 since the Gd loading has finished and the water quality seems stable at the bottom of the OD.
- To switch between using fibre 51/52 (Switch 1) and fibre 1-50 (Switch 2), the signal input cable to the switch box has to be plugged **manually**. This is the only work that needs to be performed in person in the mine concerning the laser data-taking process. If one only wants to change the filter intensity of the current fibres, it can

be done remotely.

- To use `vi` on `sukcal`, run command `setenv TERM xterm` to get rid of the error message the machine throws otherwise.
- Keep watching the OD trigger histogram throughout the data-taking process to ensure the fibres are working as intended.
- Beware that the filter settings in the analysis code are hard-coded to be five times less than the numbers in the program control, i.e. they range from 10 to 480 instead of 50 to 2400.

For a detailed record of what was done during the last data taking, check the log book for 22 September 2022. To perform a complete laser data taking (flashing all the fibres), follow the steps below.

1. Inform the person on shift so that they would not accidentally kill the process that is running. Ask the current shifter to inform the next shifter as well.
2. Create new schedule files on `sukcal`:
   (a) `ssh` into `sukap` using any account;
   (b) Log into `sukcal` using the `calib` account. Do `telnet sukcal`, then the terminal will prompt for username (`calib`) and password. Please consult Hidekazu Tanaka or Shunichi Mine for the passwords of the `calib` account;
   (c) Go to `/vme_test`, copy either folder `/20210128` or `/20220922` and rename it.

   The content in both folders is the same; the extensions of the schedule files indicate the location of the fibres included in the file:

   **schedule.bar1** Operates fibre 1 to 12 on the barrel;

   **schedule.bar2** Operates fibre 13 to 24 on the barrel;

   **schedule.top** Operates fibre 25 to 38 on the top cap;

   **schedule.bot-sw2** Operates fibre 39 to 50 on the bottom cap, the end of all channels on Switch 2;

   **schedule.bot-sw1.org** Operates fibre 51 and 52 on the bottom cap. Only two channels are used for the OD fibres on Switch 1. This file does **not** contain filter setting 1000, which is used in the autocalib process (not used in the 22 September 2022 campaign);

   **schedule.bot-sw1** Same as above, the only difference is that this file **does** contain

filter setting 1000 (i.e. fibre 51 and 52 each has 11 settings). This file was used in the 22 September 2022 campaign;

**schedule.bot-sw1-reset** This file does not take any data but it sets the fibre 51 and 52 filter setting to 1000 for autocalib purposes.

3. Before switching to *test run*, write down all the different trigger conditions displayed in the run control window just in case the conditions do not remain the same after switching back to the normal run at the end of the campaign.

   Before the *test run*, OD trigger rate histogram (5 minutes) as observed on the shift machine is around 2-3 Hz, and the autocalib trigger rate histogram is around 1.7 Hz.

4. Change into a *test run*. Note that sometimes the run number doesn't automatically increment by 1 going into a *test run*, in such case edit manually.

   When pressing the change run button, it would occasionally have a pop-up window warning, call relevant experts if in doubt. Example pop-up window seen on 22 September 2022: 'Trigger threshold for trigger ID 2 is different from default, are you sure?'. The expert said it was okay to ignore this message as long as we check the trigger conditions after going back to a normal run.

   ! Use a new *test run* every time the system configuration is changed and for every schedule file.

5. Stop the autocalib process:

   (a) `ssh` into `sukap` using any account;

   (b) Log into `sukcal` using the `shift` account. Do `telnet sukcal`, then the terminal will prompt for username (`calib`) and password. Please consult Hidekazu Tanaka or Shunichi Mine for the passwords of the `calib` account;

   (c) Check the autocalib process id with command `ps -ef | grep schedule`;

   (d) Terminate the process with command `kill [job id]`;

   (e) Double check that the autocalib process is killed with `ps -ef | grep schedule`, and check the autocalib trigger rate in the histogram goes to zero.

6. Plug the signal input cable into Switch 2, since it is advised to take data in the ascending order of the fibre number.

7. Start a new *test run*. In the `/vme_test/[new_name]` folder, run the schedule file

that starts from fibre 1 using command `smtest < schedule.bar1`. The command has to be executed by the `calib` account.

The autocalib trigger rate shown on the histogram is around 8-10 Hz when the fibres are flashing. To see the laser events on the live event display, set cut to OD only, select low E, and change to display OD in the foreground.

8. Repeat Step 7 for the barrel and top cap files in the following order: schedule.bar2 → schedule.top

! Remember to start a new test run for every new file.

It takes about 2 to 2.5 hours to run each file.

9. Due to the cables going to the OD bottom (110m) being longer than the rest of the cables (70m), need to turn off two trigger conditions for timing reasons, otherwise no hits would be recorded. A slightly more complicated procedure has to be followed to start the bottom cap data taking. This is one of two places that will cause Supernovae detection downtime (about 1.5 minutes each if done quickly).

   (a) Before changing to a *test run* for the bottom, turn off (untick) 2 software trigger conditions in the run control: #4 cailib trigger cable #15001, and #15 ID laser trigger cable #15012;

   (b) Click **Stop** button;

   (c) Click **Abort** button;

   (d) Double check the run mode is 'test' before this step, sometimes it jumps back to 'normal' for some reason. After double-checking the mode is 'test', click **Start** button.

10. After turning off two trigger conditions, run schedule.bot-sw2.

! With the two trigger conditions off, the autocalib trigger histogram should be blank.

11. Wait till schedule.bot-sw2 finishes running, change to a new *test run*, plug the signal input cable back into Switch 1.

12. In a new *test run*, run schedule.bot-sw1(.org)

! Use schedule.bot-sw1 file if there is an intention to compare fibre 51/52 data from this dedicated data-taking campaign with autocalib data, otherwise can use schedule.bot-sw1.org.

13. After the OD bottom data taking has finished, revert the software trigger conditions

and start a new *test run*. This is the other place that will cause Supernovae detection downtime (about 1.5 minutes if done quickly):

(a) Turn on (tick) the software trigger conditions in the run control: #4 calib trigger cable #15001, and #15 ID laser trigger cable #15012;

(b) Click **Stop** button;

(c) Click **Abort** button;

(d) Double check the run mode is 'test' before this step, sometimes it jumps back to 'normal' for some reason. After double-checking the mode is 'test', click **Start** button.

14. Depending on if the autocalib process includes fibre 51 and 52, decide whether to run file schedule.bot-sw1-reset.

15. Restart the autocalib process:

(a) `ssh` into `sukcal` using the `shift` account, i.e. `ssh shift@sukcal`;

(b) Check the command needed to run with `crontab -l`. The command should look something like `/home/shift/bin/start_scaler_scheduler`;

(c) Put `/home/shift/bin/start_scaler_scheduler` into the terminal and run;

(d) Check that the autocalib process is running with `ps -ef | grep schedule`, note that the name shown in `ps` is different from the executed command name, i.e. as of October 2022 you should see something in the vicinity of `/home/online/calib-schedule/test_20200127_Gd-loading_uk_light_injector/schedule` in `ps`. In addition, check the autocalib trigger rate in the histogram.

16. Confirm all the trigger condition values with the values noted down in Step 3. Note that the SLE trigger threshold has to be set to 36 manually for a normal run (it defaults to 34 which is too low). Select 'normal' mode, and check the run number has incremented. Change back to normal run.

17. Inform the current shifter that all work is done.

Note: only *normal runs* counts towards the live-time of a shift. Hence, this shift should have very little live-time.

# Appendix B

# Time and Charge Distributions for Fibre 2, 4-52 from SK-V and SK-VII Laser Data Taking Campaigns

The following figures compare the hit time and charge distributions of fibre 2 and $4-52$ for SK-V and SK-VII period. (No cuts were applied to the plotting data.)

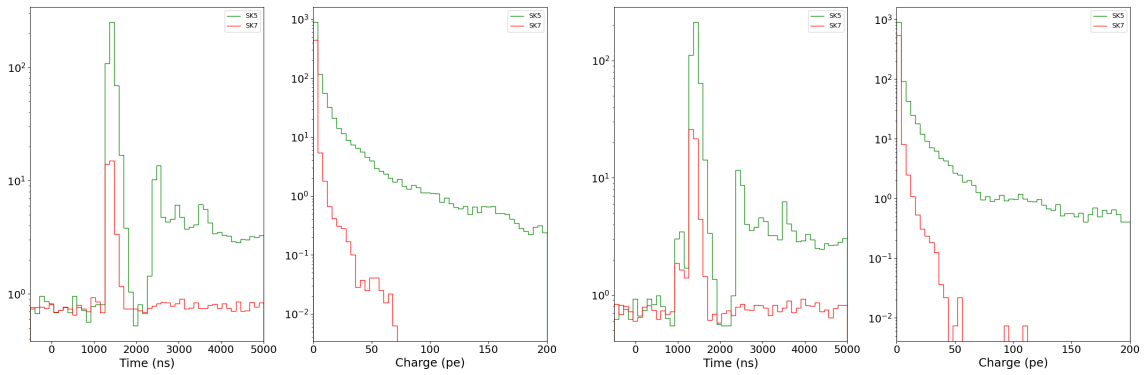


**(a)** Fibre 2 **(b)** Fibre 4

**Figure B.1:** Comparison of hit time and charge distributions between SK-V and SK-VII data periods for two fibres.

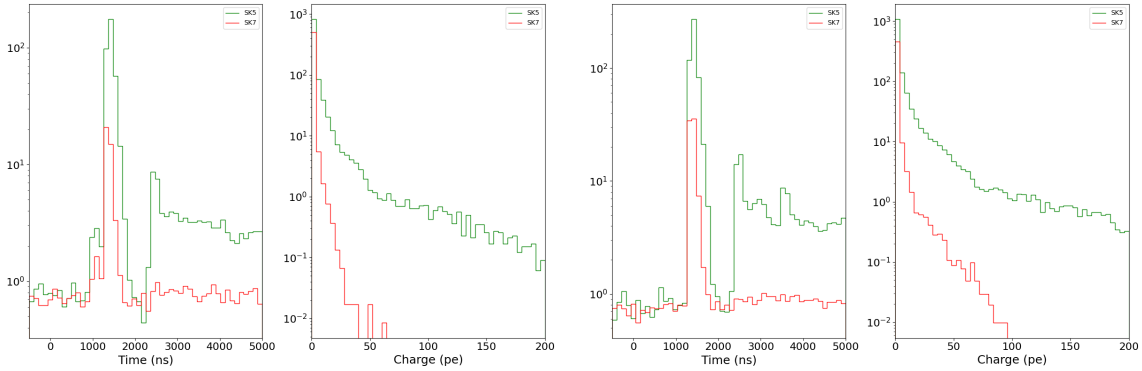


**(a)** Fibre 5




**(b)** Fibre 6

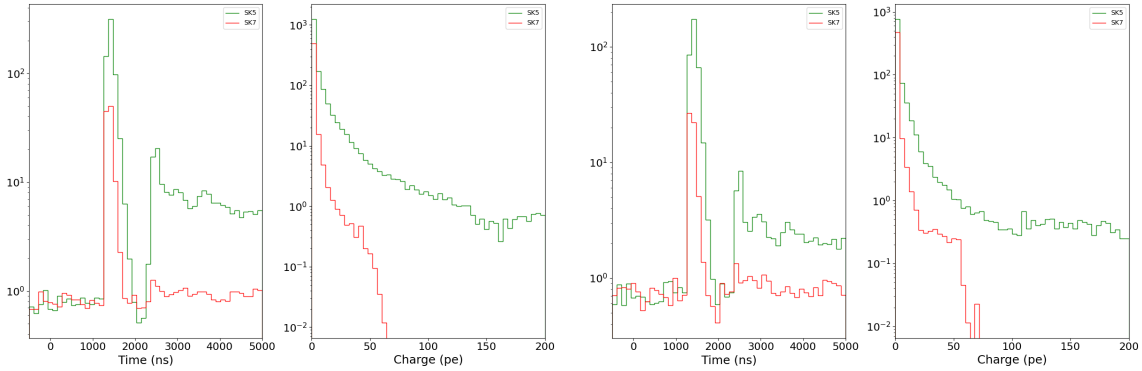


**(c)** Fibre 7




**(d)** Fibre 8

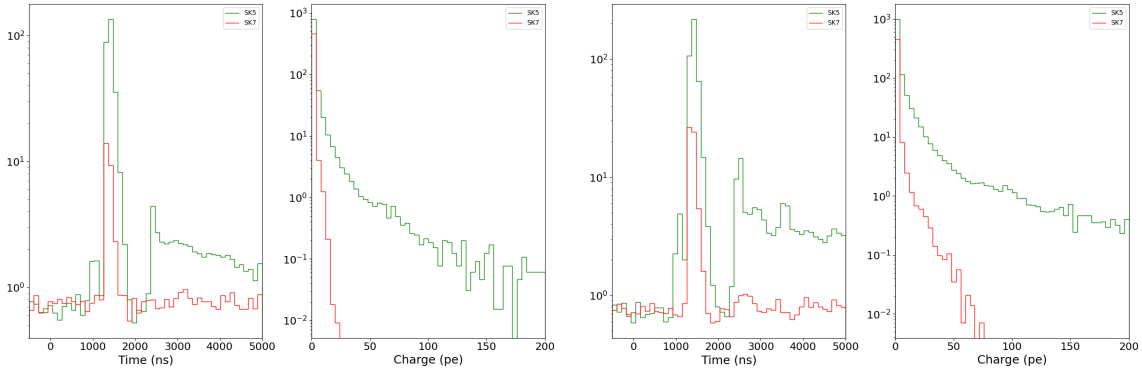


**(e)** Fibre 9




**(f)** Fibre 10

**Figure B.2:** Comparison of hit time and charge distributions between SK-V and SK-VII data periods for six fibres.

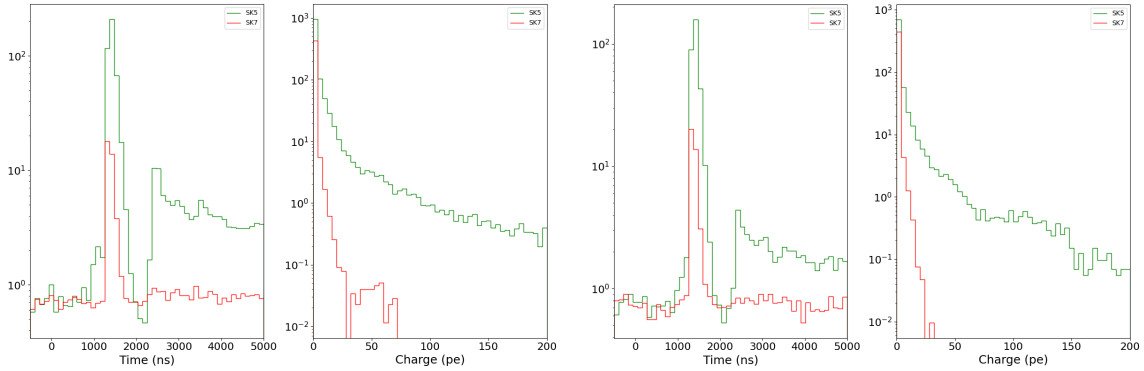


**(a)** Fibre 11 **(b)** Fibre 12

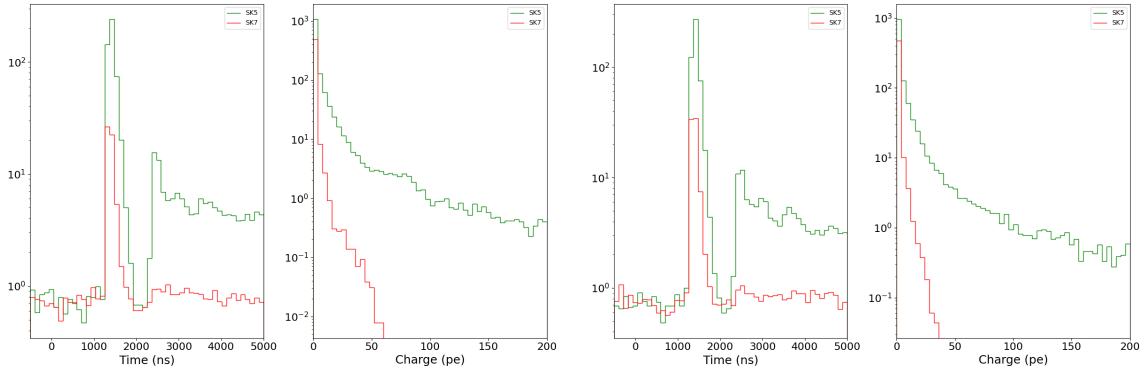


**(c)** Fibre 13 **(d)** Fibre 14

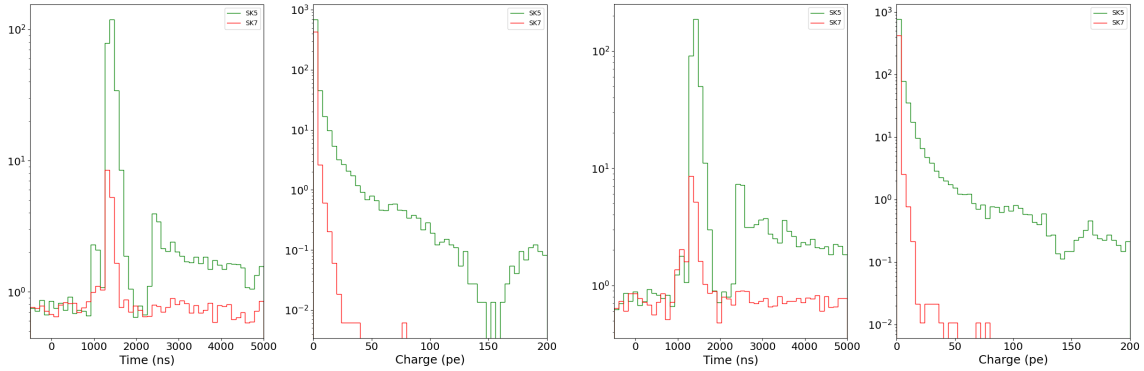


**(e)** Fibre 15 **(f)** Fibre 16

**Figure B.3:** Comparison of hit time and charge distributions between SK-V and SK-VII data periods for six fibres.

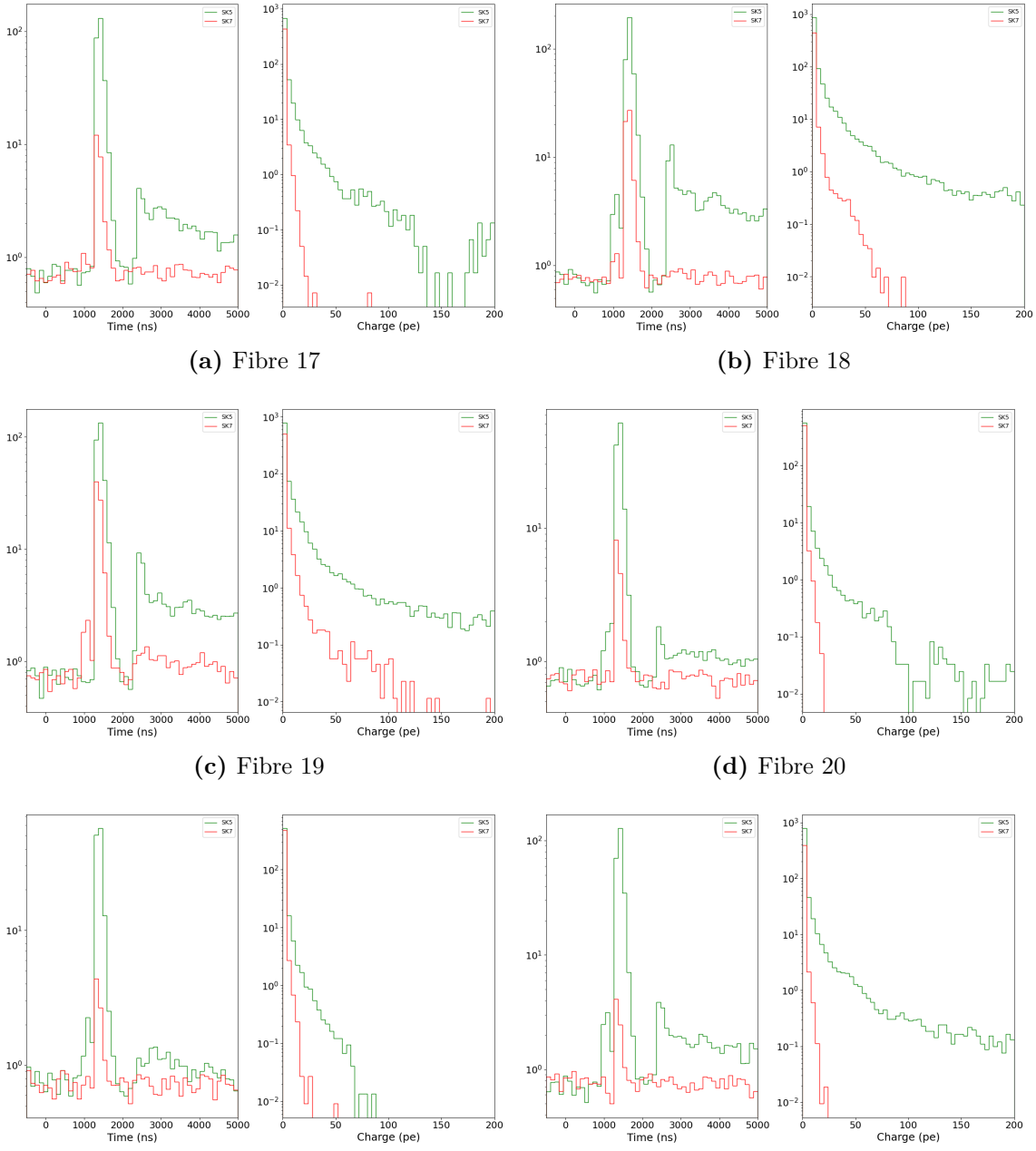


**(a)** Fibre 17 **(b)** Fibre 18

**(c)** Fibre 19 **(d)** Fibre 20

**(e)** Fibre 21 **(f)** Fibre 22

**Figure B.4:** Comparison of hit time and charge distributions between SK-V and SK-VII data periods for six fibres.

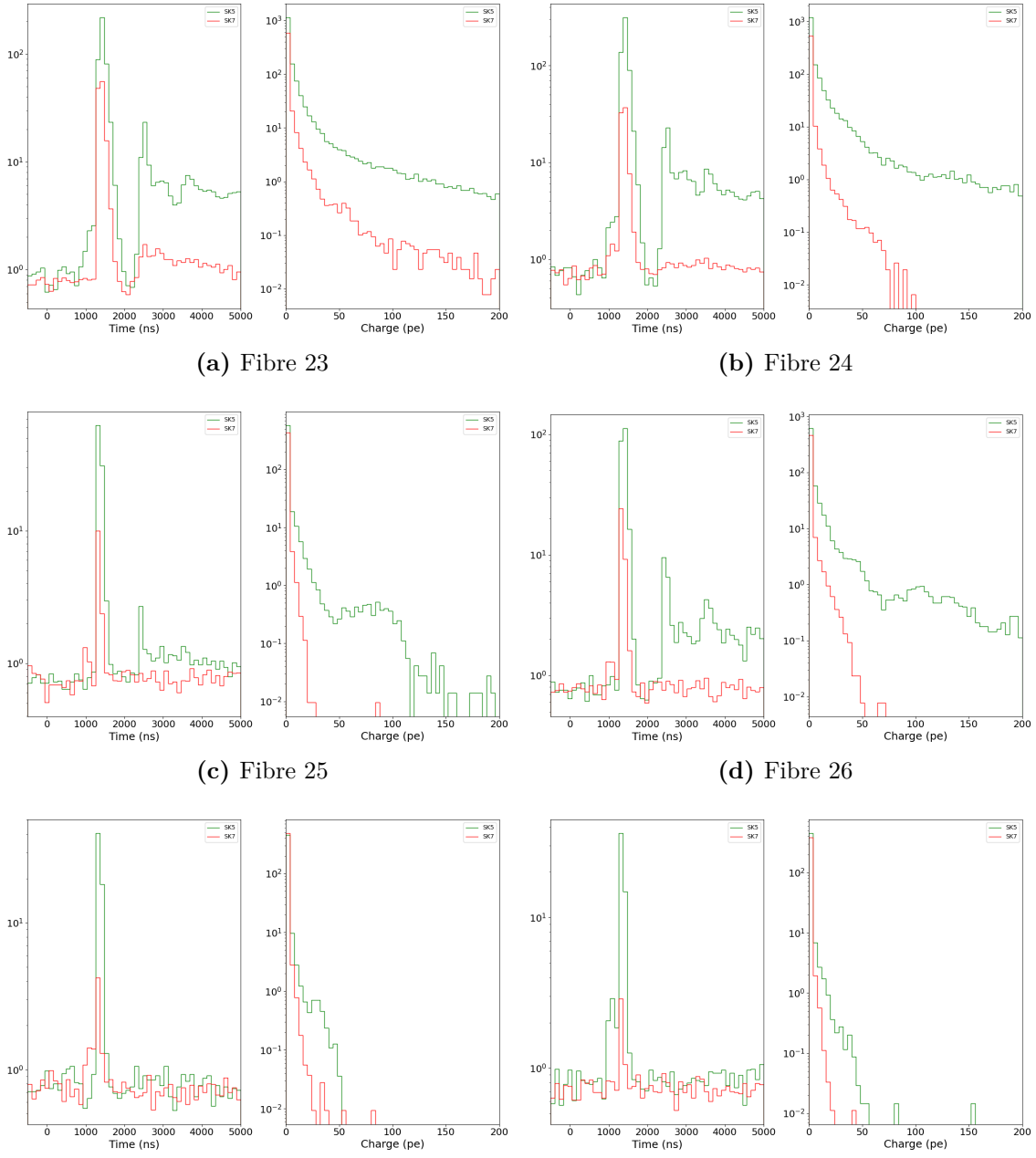


**(a)** Fibre 23 **(b)** Fibre 24

**(c)** Fibre 25 **(d)** Fibre 26

**(e)** Fibre 27 **(f)** Fibre 28

**Figure B.5:** Comparison of hit time and charge distributions between SK-V and SK-VII data periods for six fibres.

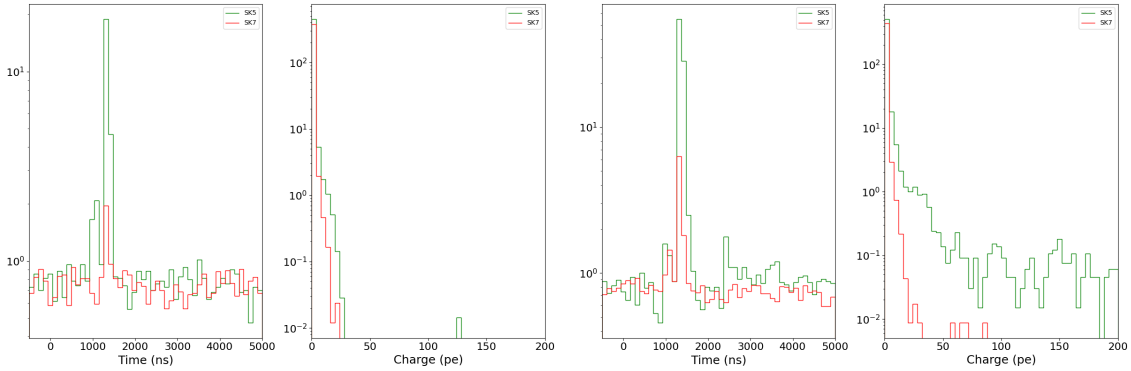


**(a)** Fibre 29 **(b)** Fibre 30

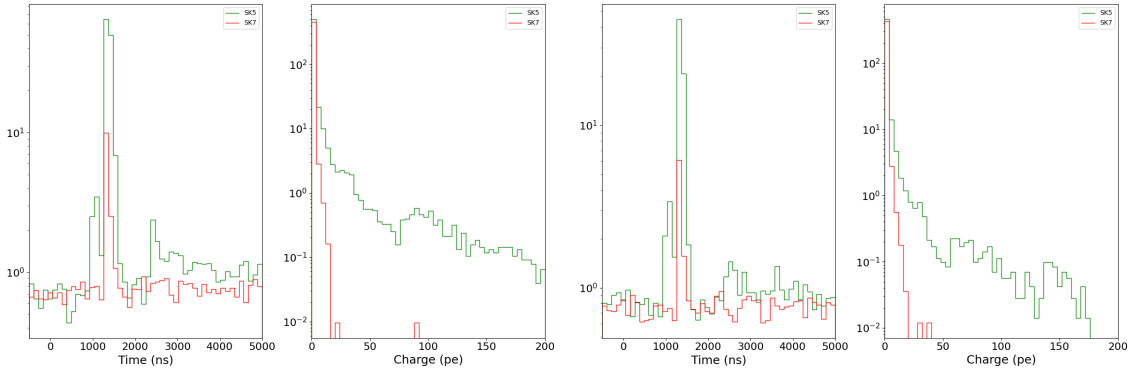


**(c)** Fibre 31 **(d)** Fibre 32

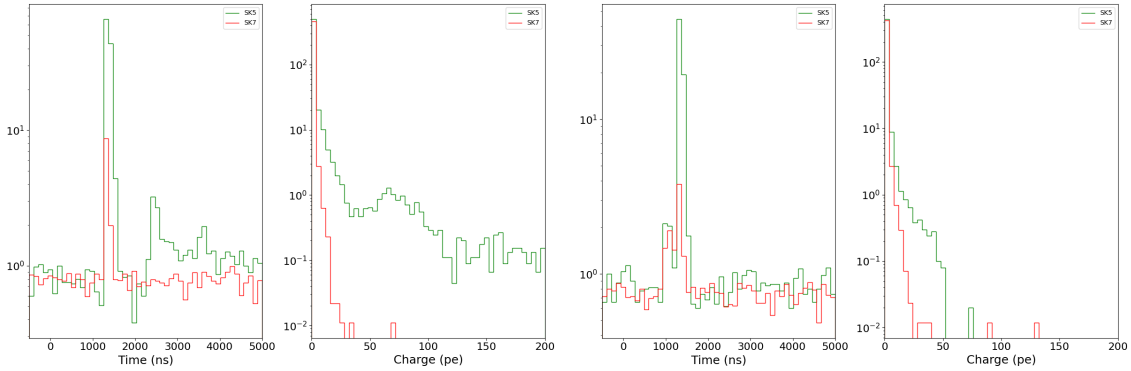


**(e)** Fibre 33 **(f)** Fibre 34

**Figure B.6:** Comparison of hit time and charge distributions between SK-V and SK-VII data periods for six fibres.

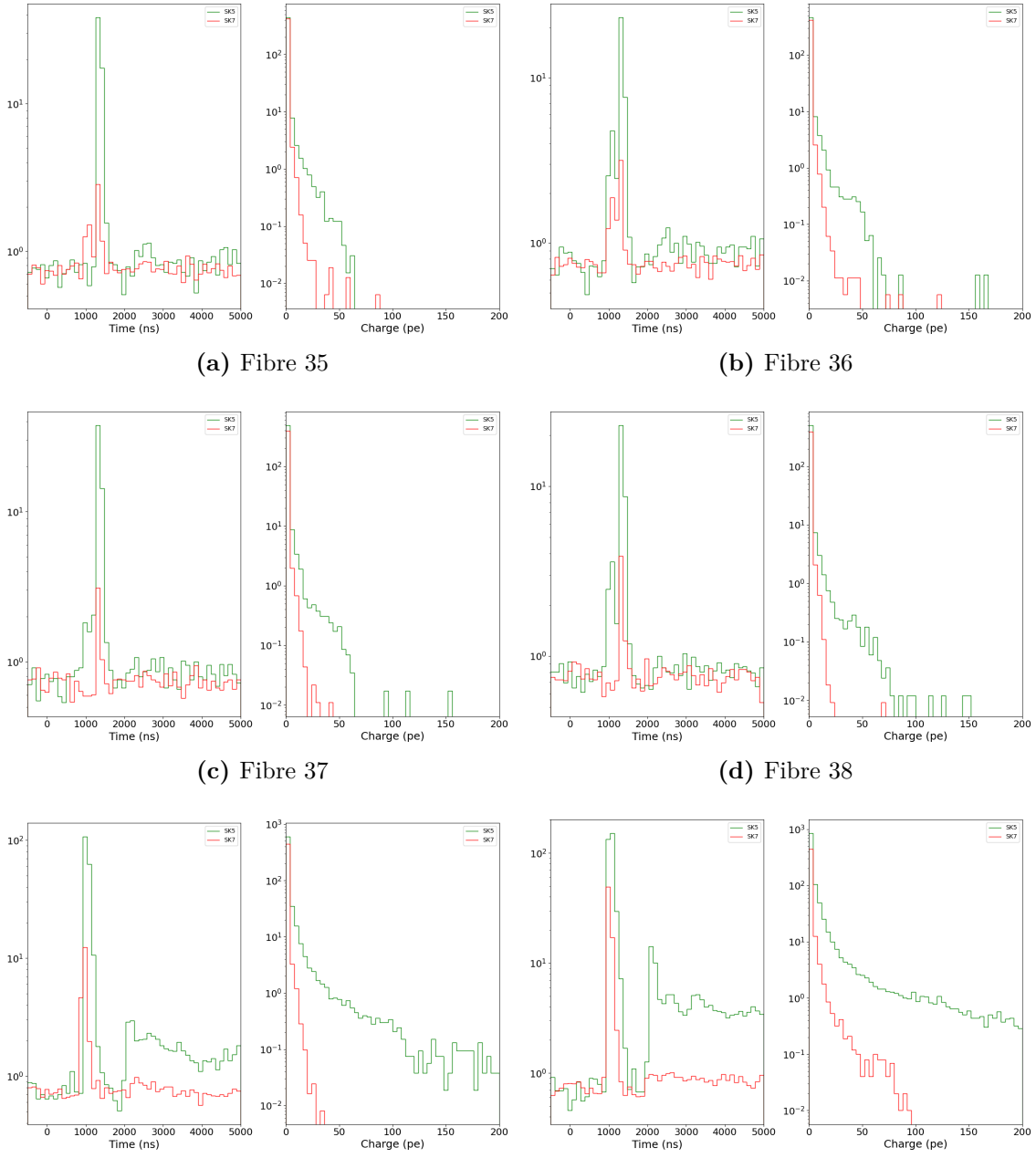


**(a)** Fibre 35 **(b)** Fibre 36

**(c)** Fibre 37 **(d)** Fibre 38

**(e)** Fibre 39 **(f)** Fibre 40

**Figure B.7:** Comparison of hit time and charge distributions between SK-V and SK-VII data periods for six fibres.

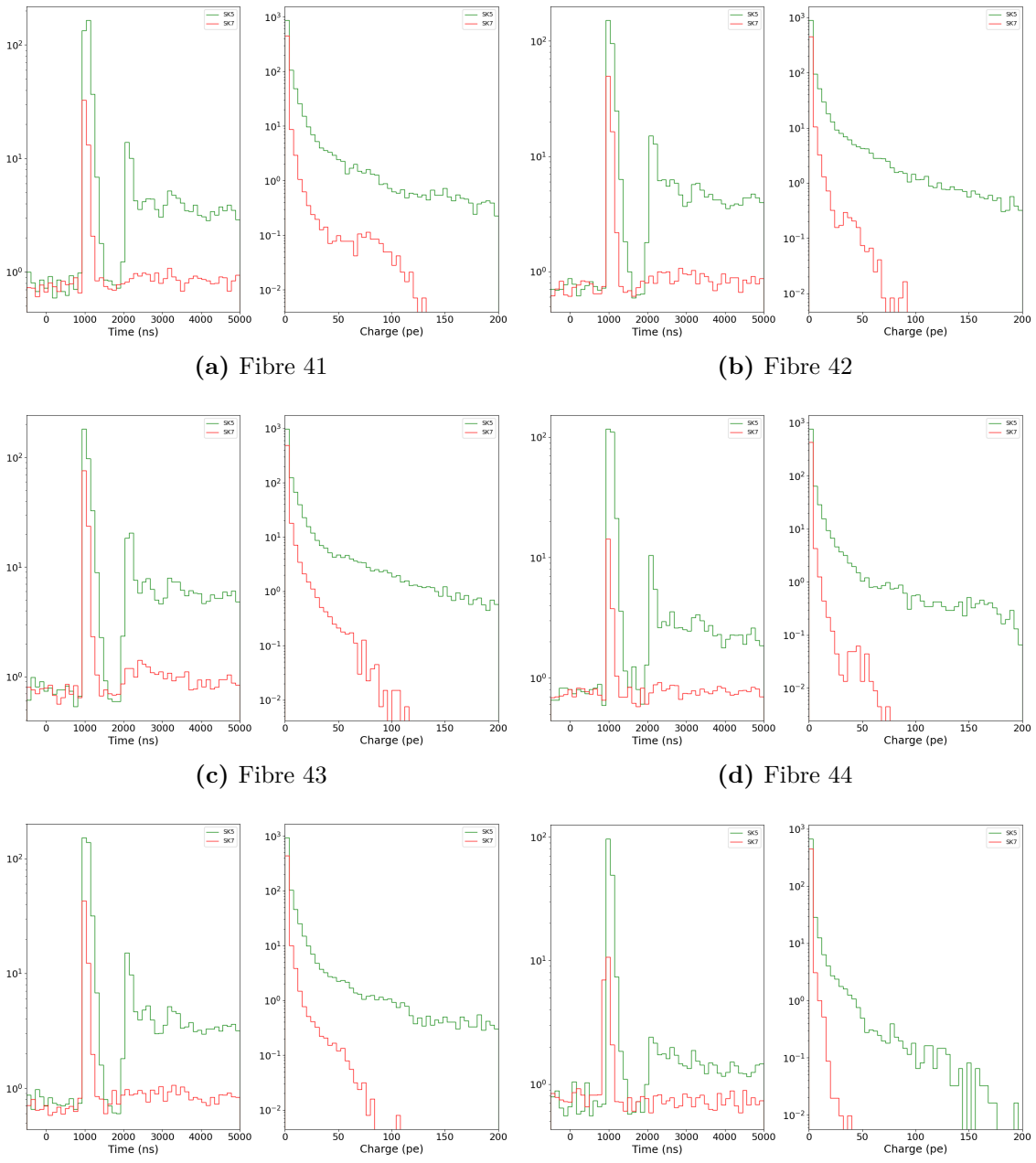


**(a)** Fibre 41 **(b)** Fibre 42

**(c)** Fibre 43 **(d)** Fibre 44

**(e)** Fibre 45 **(f)** Fibre 46

**Figure B.8:** Comparison of hit time and charge distributions between SK-V and SK-VII data periods for six fibres.

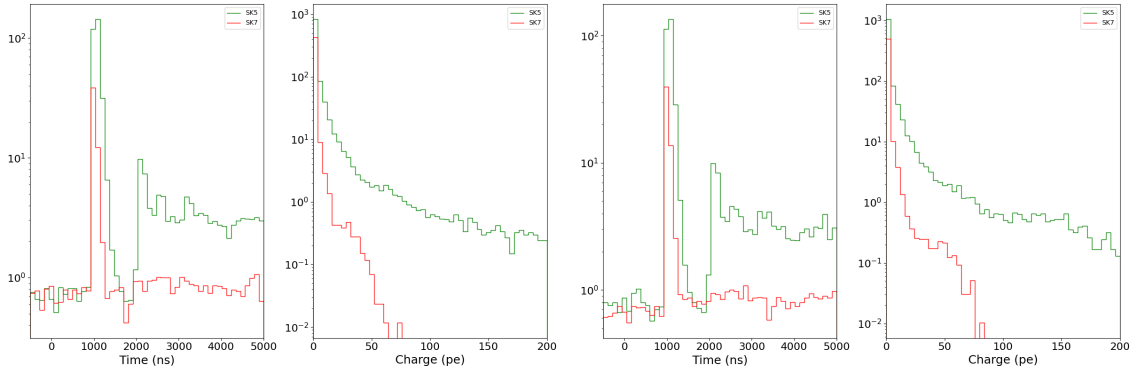


**(a)** Fibre 47 **(b)** Fibre 48

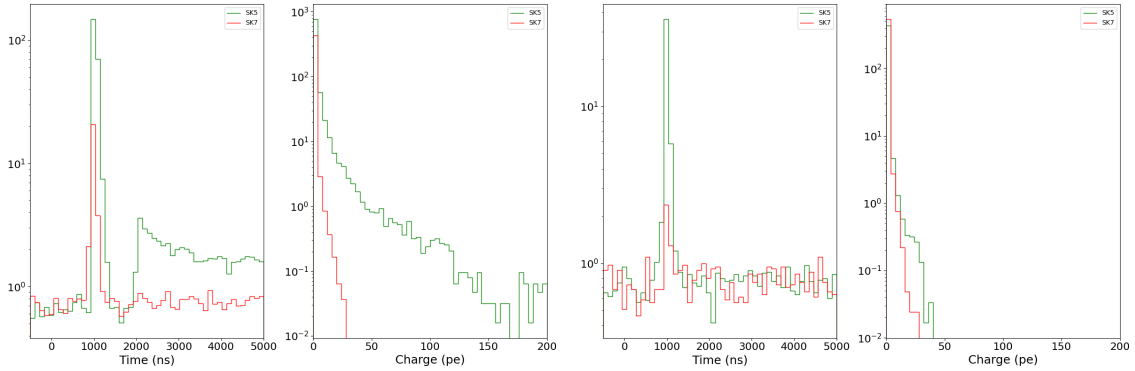


**(c)** Fibre 49 **(d)** Fibre 50

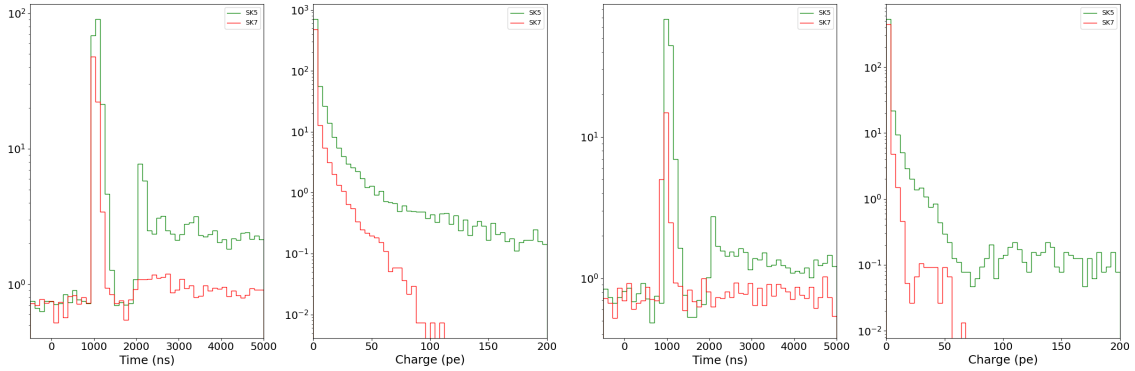


**(e)** Fibre 51 **(f)** Fibre 52

**Figure B.9:** Comparison of hit time and charge distributions between SK-V and SK-VII data periods for six fibres.